

UNCLASSIFIED

AD NUMBER

AD900517

NEW LIMITATION CHANGE

TO

Approved for public release, distribution
unlimited

FROM

Distribution authorized to U.S. Gov't.
agencies only; Test and Evaluation; MAY
1972. Other requests shall be referred to
Air Force Materials Lab., AFSC,
Wright-Patterson AFB, OH 45433.

AUTHORITY

AFML ltr, 13 Sep 1974

THIS PAGE IS UNCLASSIFIED

AD 900517

AFML-TR-72-85

SUPersonic RAIN AND SAND EROSION RESEARCH:
CHARACTERIZATION AND DEVELOPMENT OF
EROSION RESISTANT MATERIALS

William F. Adler

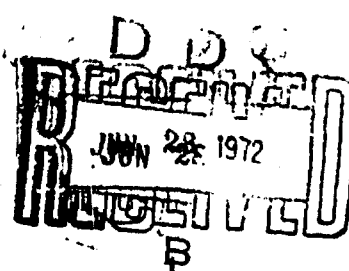
John W. Morris, Jr.

Norman E. Wahl

TEXTRON'S BELL AEROSPACE COMPANY

TECHNICAL REPORT AFML-TR-72-85

MAY 1972



Distribution limited to U.S. Government agencies only;
(test and evaluation). May 1972. Other requests for
this document must be referred to Air Force Materials
Laboratory, Nonmetallic Materials Division, Elastomers
and Coatings Branch, AFML/LNE, Wright-Patterson AFB,
Ohio 45433.

Air Force Materials Laboratory

Air Force Systems Command

Wright-Patterson Air Force Base, Ohio

Best Available Copy

NOTICES

When Government drawings, specifications, or other data are used for any purpose other than in connection with a definitely related Government procurement operation, the United States Government thereby incurs no responsibility for any obligation whatsoever; and the fact that the Government may have formulated, furnished, or in any way supplied the said drawings, specifications, or other data, is not to be regarded by implication or otherwise as in any manner licensing the holder or any other person or corporation, or conveying any rights or permission to manufacture, use, or sell any patented invention that may in any way be related thereto.

Copies of this report should not be returned unless return is required by security considerations, contractual obligations, or notice on a specific document.

This progress report is not part of the scientific literature and must not be cited, abstracted, reprinted or given further distribution.

SUPersonic RAIN AND SAND EROSION RESEARCH:
CHARACTERIZATION AND DEVELOPMENT OF
EROSION RESISTANT MATERIALS

William F. Adler

John W. Morris, Jr.

Norman E. Wahl

Distribution limited to U.S. Government agencies only;
(test and evaluation). May 1972. Other requests for
this document must be referred to Air Force Materials
Laboratory, Nonmetallic Materials Division, Elastomers
and Coatings Branch, AFML/LNE, Wright-Patterson AFB,
Ohio 45433.

FOREWORD

This report was prepared by Bell Aerospace Company, Buffalo New York 14240, under Air Force Contract F33615-71-C-1219. It was initiated under Project No. 7340 "Nonmetallic and Composite Materials," Task No. 734007 "Coatings for Energy Utilization, Control and Protective Functions." The work was administered under the direction of the Air Force Materials Laboratory, Air Force Systems Command, Wright-Patterson Air Force Base, Ohio with George F. Schmitt, Jr. of the Elastomers and Coatings Branch, Nonmetallic Materials Division, acting as project engineer.

This report covers the work carried out during the period from January 1971 through January 1972.

The following Bell Aerospace Company personnel were major contributors to the program in the capacity noted:

F. E. Flint	Test Operations Engineer
W. N. Mehlik	Blade Design and Structural Engineer
E. J. Morris, Jr.	Instrumentation
(W. F. Adler	
(J. W. Morris, Jr.*	Mechanics of Erosion
N. E. Wahl	Project Manager

*Present address University of California at Berkeley

This report was submitted by the authors in April 1972.

This technical report has been reviewed and is approved.


WARREN P. JOHNSON, Chief
Elastomers and Coatings Branch
Nonmetallic Materials Division

ABSTRACT

Development and evaluation of electro-deposited, sprayed and diffusion coatings capable of providing erosion protection for titanium compressor and fan blades on gas turbine engines were carried out. Recently developed hard coatings of carbides and borides exhibited sand erosion resistance 2.5 - 5 times that of uncoated titanium.

Results are outlined on comparative erosion characteristics of thermoplastic polymers that might be used as coatings and might possess satisfactory rain erosion resistance. Correlation of the physical and mechanical properties of these polymers with erosion resistance, are discussed.

The mechanism of erosion damage caused by plastic deformation and progressive fracture is discussed in detail.

The erosion process occurring by these two methods considers ductile pitting, abrasion, polishing, fatigue, tearing and brittle fracture.

TABLE OF CONTENTS

SECTION	PAGE
I INTRODUCTION	1
II SUMMARY	3
III EROSION RESISTANT COATINGS RESEARCH	12
IV EXPERIMENTAL WORK ON TITANIUM COATINGS	17
V MATERIALS CHARACTERIZED FOR SAND EROSION BEHAVIOR	
A. Turbine Shaped Specimens	39
B. Airfoil Shaped Specimens	40
VI RESULTS OF SAND EROSION TESTS	41
VII MATERIALS CHARACTERIZED FOR RAIN EROSION BEHAVIOR	100
VIII RESULTS OF RAIN EROSION TESTS	106
IX MECHANICS OF EROSION STUDIES	
A. The Mechanisms of Erosion	
1. Ductile Pitting	164
2. Abrasion	166
3. Polishing	169
4. Fatigue	170
5. Tearing	171
6. Brittle Fracture	173
B. Mechanisms of Sand Erosion	
1. Ductile Metals	174
2. Ceramic Coatings	176
3. Fiber-reinforced Composites	179
C. Mechanisms of Rain Erosion	185
1. Erosion of Ductile Metals	186
2. Erosion of Polymeric Materials	216

TABLE OF CONTENTS

SECTION	PAGE
X MAINTENANCE WORK	270
XI RECOMMENDATIONS	273
XII REFERENCES	274

LIST OF ILLUSTRATIONS

FIGURE		PAGE
1	ALUMINA-COLUMBIUM COATING	19
2	ALUMINA COATINGS OF TEST SPECIMENS - 25X	20
3	TYPICAL CROSS SECTION OF Cb/Al ₂ O ₃ AND Al ₂ O ₃ COATINGS ON AIRFOIL SHAPED TEST SPECIMEN - 110X	22
4	EFFECTS OF VARIOUS HEAT TREATMENTS OF NICKEL-TITANIUM - 200X	31
5	COBALT-TUNGSTEN COATING ELECTRODEPOSITED ON TITANIUM-6Al-4V AND HEAT TREATED TO 800°C FOR 1/2 HOUR - 440X	36
6	COMPARISON OF SAND EROSION OF TITANIUM AND NICKEL AT 880 FT/SEC.	43
7	SAND EROSION TITANIUM ALLOYS - 880 FT/SEC.	45
8	SAND EROSION Ti-6Al-4V AT VARIOUS VELOCITIES	46
9	PROFILE VIEW OF NICKEL COATED BORSIC ALUMINUM COMPOSITE SHOWING LEADING EDGE AFTER 18 MIN. EROSION BY SAND AT 880 FT/SEC. 15X	48
10	VIEW OF EROSION OF COMPOSITE MATERIALS	51
11	EROSION OF BORON-ALUMINUM COMPRESSOR BLADE SECTIONS	53
12	RATE OF SAND EROSION OF BORSIC-ALUMINUM COMPOSITE AT 1100 FT/SEC.	55
13	EROSION OF 2-3 MIL S-183 SOLAR BORIDE COATING	58
14	EROSION OF TITANIUM CARBIDE COATING ON LEADING EDGE OF TEST SPECIMEN - 15X	59

LIST OF ILLUSTRATIONS

FIGURE		PAGE
15	EROSION OF TITANIUM CARBIDE COATING FROM 403 STAINLESS SUBSTRATE	60
16	COMPARISON OF SAND EROSION RESISTANCE OF COATINGS ON 403 STAINLESS STEEL 880 FT/SEC	65
17	COMPARISON OF SAND EROSION RESISTANCE OF COATINGS ON Ti-6Al-4V (880 FT/SEC)	66
18	EROSION OF TIP OF SPECIMEN IN SAND AT 880 FT/SEC - 15X	69
19	BORIDE COATING ON TITANIUM 6Al-4V BEFORE AND AFTER EXPOSURE TO SAND EROSION SEM - 650X	70
20	ELECTRON MICROGRAPH - 7000X VIEW OF FRACTURED BORIDE COATING AFTER 50 MINUTES EXPOSURE TO SAND PARTICLE IMPACT	71
21	NRC BORON CARBIDE COATING ON Ti-6Al-4V AFTER 30 MINUTES EXPOSURE	75
22	SAND ERODED AREAS IN ALUMINA COATING AFTER 22 MINUTES OF TESTING 880 FT/SEC 25X	81
23	PHOTOMICROGRAPHS OF BELL ALUMINA COATING	82
24	EROSION OF LEAD	84
25	SAND ERODED SURFACE SAE 13 LEAD ALLOY 3X MAGNIFICATION	85
26	EROSION OF PLASTIC MATERIALS	89
27	SAND EROSION OF BULK POLYMER (KYDEX) AT 880 FT/SEC VELOCITY	90

LIST OF ILLUSTRATIONS

FIGURE		PAGE
28	SCANNING ELECTRON MICROGRAPH AT 160X SHOWING DAMAGE TO SURFACE OF BULK POLYMER (KYDEX) AFTER 15 MINUTES EXPOSURE TO SAND EROSION AT 880 FT/SEC	91
29	RATE OF SAND EROSION OF MATERIALS AT 880 FT/SEC	92
30	RATE OF SAND EROSION OF ALUMINA - ALSIMAG 753 AT 1100 FT/SEC	94
31	EROSION OF CERAMIC MATERIALS	95
32	EROSION OF ELECTROPIATED NICKEL ON FIBER- GLASS LAMINATE	97
33	ASTROCOAT-COMPOSITE POLYURETHANE COATING SYSTEM FOR SAND EROSION - 18 MIL THICKNESS ON ALUMINUM SUBSTRATE	99
34	PHILCO-FORD - 3D - SILICA - SILICA FIBER COMPOSITE SPECIMENS BEFORE TEST	105
35	PLASMA SPRAYED ALUMINA ON ALUMINUM SUBSTRATE	108
36	PLASMA SPRAYED ALUMINA ON ALUMINUM SUBSTRATE	110
37	PLASMA SPRAYED ALUMINA ON POLYIMIDE-GLASS FABRIC SUBSTRATE	111
38	SLIP CAST ALUMINA ON GLASS REINFORCED PHENOLIC SUBSTRATE	113
39	SLIP CAST ALUMINA ON GLASS REINFORCED PHENOLIC SUBSTRATE	114
40	RAIN EROSION OF PURE NICKEL 270 AT 1120 FT/ SEC	117

LIST OF ILLUSTRATIONS

FIGURE		PAGE
41	EROSION OF 12 MIL AFML FLUOROCARBON COATING ON ALUMINUM SUBSTRATE	119
42	TYPICAL EROSION OF RADOME COATINGS ON ALUMINUM SUBSTRATE	120
43	TYPICAL EROSION OF RADOME COATINGS ON ALUMINUM SUBSTRATE	121
44	EROSION OF 11.5 MIL AFML FLUOROELASTOMER TYPE I ON GLASS FIBER REINFORCED LAMINATE	123
45	EROSION OF 12 MIL AFML FLUOROELASTOMER ANTISTATIC TYPE II - ON GLASS FIBER REINFORCED LAMINATE	124
46	EROSION OF HIGH MOLECULAR WEIGHT POLY-ETHYLENE PLASTIC	128
47	EROSION OF HIGH MOLECULAR WEIGHT POLY-ETHYLENE PLASTIC	129
48	EROSION OF ACRYLIC-POLYVINYL CHLORIDE PLASTIC	131
49	EROSION OF ACRYLIC-POLYVINYL CHLORIDE PLASTIC	132
50	EROSION OF POLYURETHANE W-121	136
51	EROSION OF POLYURETHANE W-134	137
52	EROSION OF POLYURETHANE W-612	138
53	EROSION OF POLYURETHANE W-612	139
54	EROSION OF POLYARYLSULFONE (ASTRAL 360)	141
55	EROSION OF POLYARYLSULFONE (ASTRAL 360)	142

LIST OF ILLUSTRATIONS

FIGURE		PAGE
56	EROSION OF NYLON (ZYTEL 7110-13)	146
57	EROSION OF NYLON (ZYTEL 7110-13)	147
58	EROSION OF POLYPHENYLENE OXIDE (NORYL-731)	151
59	EROSION OF GLASS FILLED PPO (NORYL-GFN-3)	152
60	EROSION OF POLYPHENYLENE OXIDE (NORYL-731)	153
61	EROSION OF GLASS FILLED PPO (NORYL-GFN-3)	154
62	EROSION OF ACETAL (DELRIN 550)	157
63	EROSION OF ACETAL (DELRIN 550)	158
64	GLASS REINFORCED EPOXY LAMINATES	161
65	PHILCO-FORD SILICA - SILICA FIBER COMPOSITE	163
66	RAIN EROSION OF NICKEL AT 1120 FT/SEC	165
67	MICROGRAPH OF SAND EROSION OF DUCTILE MATERIAL	167
68	MICROGRAPH OF SAND EROSION OF TITANIUM ALLOY	168
69	EROSION OF Ti- β Al-4V AT 1120 FT/SEC SHOWING SUBSURFACE CRACKS	172
70	MICROGRAPH OF SAND EROSION OF TITANIUM CARBIDE COATING	177
71	MICROGRAPH OF SAND EROSION OF GRAPHITE- EPOXY COMPOSITE	180

LIST OF ILLUSTRATIONS

FIGURE		PAGE
72	MICROGRAPH OF SAND EROSION OF ALUMINUM-BORONIC COMPOSITE	181
73	SCANNING ELECTRON MICROGRAPH SHOWING SAND EROSION OF A COMPOSITE OF BORON FIBERS IN ALUMINUM MATRIX	182
74	VIEW OF FRACTURED FIBER OF BORON IN ALUMINUM MATRIX AFTER 1-MINUTE EXPOSURE TO SAND IMPACT	183
75	SCANNING ELECTRON MICROGRAPH SHOWING VOID IN SURFACE OF BORON-ALUMINUM COMPOSITE	184
76	RAIN EROSION OF FOUR DUCTILE METALS AT 1120 FT/SEC	188
77	MICROGRAPHS OF EROSION DAMAGE ON ETCHED NICKEL SAMPLE	190
78	RAIN EROSION TESTS OF 403 STAINLESS STEEL	193
79	STRUCTURE OF 403 STAINLESS STEEL SHOWING PLANAR PRECIPITATES AND FLAWS	195
80	PITS IN SURFACE OF 403 STAINLESS STEEL EXPOSED AT 1120 FT/SEC for 45 MINUTES	196
81	EROSION OF Ti-6Al-4V AT 1120 FT/SEC	198
82	EROSION DAMAGE ON Ti-6Al-4V AFTER 30-MINUTE EXPOSURE TO 1 IN/HR RAINFALL AT 1120 FT/SEC	199
83	EROSION OF Ti-6Al-4V AT 1120 FT/SEC	200
84	CRACKING ON SURFACE OF Ti-6Al-4V	205
85	LOCALIZED CRACKING AT PRECIPITATES ON SURFACE OF Ti-6Al-4V	206
86	SCANNING ELECTRON MICROGRAPHS OF SMALL PITS CONFIGURATIONS ON Ti-6Al-4V AFTER 30-MINUTE EXPOSURE TO RAIN AT 1120 FT/SEC	208

LIST OF ILLUSTRATIONS

FIGURE		PAGE
87	SCANNING ELECTRON MICROGRAPH SHOWING DETAIL OF SMALL PIT IN Ti-6Al-4V	209
88	ETCHED CROSS-SECTION OF SHALLOW PIT IN Ti-6Al-4V	209
89	ETCHED CROSS SECTION OF TUNNELING WITH SHALLOW PITS IN Ti-6Al-4V	210
90	SURFACE UPHEAVAL IN Ti-6Al-4V	211
91	ETCHED CROSS SECTION OF TUNNELING AND SURFACE UPHEAVAL IN Ti-6Al-4V	213
92	SUBSURFACE CRACKING IN Ti-6Al-4V	214
93	EROSION OF CAST URETHANE IN 1 IN/HR RAINFALL AT 730 FT/SEC	218
94	TYPICAL SURFACE CONDITION OF POLYURETHANE W-121 BEFORE TESTING	220
95	TYPICAL SURFACE CONDITION OF POLYURETHANE W-612 BEFORE TESTING	223
96	ERODED SURFACES OF CAST URETHANE IN 1 IN/HR RAINFALL AT 730 FT/SEC	224
97	TRANSMISSION ELECTRON MICROGRAPHS SHOWING THE INITIATION OF PITTING IN POLYURETHANE W121 AFTER AN EXPOSURE TIME OF 5 MINUTES	225
98	IDEALIZATION OF HINGE MECHANISM IN POLY- URETHANE	227
99	EXAMPLE OF HINGE MECHANISM IN POLYURETHANE W-612	227
100	SCALLOPED FRACTURE SURFACES IN POLYURETHANE W121 AFTER AN EXPOSURE TIME OF 5 MINUTES	228

LIST OF ILLUSTRATIONS

FIGURE		PAGE
101	SCANNING ELECTRON MICROGRAPH OF GENERAL SURFACE FEATURES AND DETAIL OF SCALLOPED FRACTURE SURFACE IN POLYURETHANE W-612 AFTER 6 MINUTE EXPOSURE	230
102	SCANNING ELECTRON MICROGRAPH OF SCALLOPED FRACTURE SURFACES IN POLYURETHANE W-121	232
103	DEVELOPMENT OF LARGE-SCALE SURFACE CRACKING IN POLYURETHANE W-121 AFTER 9-MINUTE EXPOSURE TO 1 IN/HR RAINFALL AT 730 FT/SEC	233
104	GENERAL APPEARANCE OF POLYURETHANE W-13 ⁴ AFTER 20MINUTE EXPOSURE TO 1 IN/HR RAINFALL AT 730 FT/SEC	234
105	RAIN EROSION OF POLYMETHYL METHACRYLATE AFTER 15-SECOND EXPOSURE AT 730 FT/SEC	252
106	RAIN EROSION OF POLYMETHYL METHACRYLATE AFTER 45-SECOND EXPOSURE AT 730 FT/SEC	253
107	RAIN EROSION OF 181 GALSS-FIBER REINFORCED EPOXY (4617) AT 730 FT/SEC	255
108	UNERODED SURFACE OF GLASS-FIBER REINFORCED EPOXY	257
109	RAIN EROSION OF GLASS-FIBER REINFORCED EPOXY AT 730 FT/SEC	258
110	CHARACTERISTIC FRACTURE SURFACES IN GLASS-FIBER REINFORCED EPOXY AFTER 10-SECOND EXPOSURE TO RAIN AT 730 FT/SEC	259
111	MATERIAL REMOVAL FROM FIBERS AT SURFACE AND MATRIX IN GLASS-FIBER FRINFORCED EPOXY	261
112	EXPOSURE OF GLASS FIBERS LYING NEAR THE SURFACE OF GLASS-FIBER REINFORCED EPOXY SPECIMEN	262

LIST OF ILLUSTRATIONS

FIGURE		PAGE
113	ADVANCED STAGE OF EXPOSURE OF GLASS-FIBER LYING NEAR THE SURFACE OF GLASS-FIBER REINFORCED EPOXY SPECIMENS	263
114	CROSS SECTION OF GLASS-FIBER REINFORCED EPOXY	265
115	CROSS SECTION OF GLASS-FIBER REINFORCED EPOXY SHOWING TWILL WEAVE PATTERN	265
116	INITIATION OF MATERIAL REMOVAL BELOW THE SURFACE LAYER IN GLASS-FIBER REINFORCED EPOXY	266
117	INTERMEDIATE STAGE OF MATERIAL REMOVAL BELOW SURFACE LAYER IN GLASS-FIBER REINFORCED EPOXY	267
118	ADVANCED STAGE OF SEPARATION OF EPOXY FROM FIBERS IN GLASS-FIBER REINFORCED EPOXY	268
119	FRACTURING OF TRANSVERSE FIBERS IN GLASS-FIBER REINFORCED EPOXY	268
120	SPECIMEN HOLDER BEFORE AND AFTER REPAIR	272

LIST OF TABLES

TABLE		PAGE
I	SUMMARY DATA ON FABRICATION OF CERAMIC COATED TEST SPECIMENS	23
II	SAND EROSION OF PURE NICKEL (270) CUMULATIVE WEIGHT LOSS - MILLIGRAMS - 880 FT/SEC	42
III	SAND EROSION OF AFML-BORSIC ALUMINUM COMPOSITE SPECIMENS COATED WITH SOFT NICKEL - 880 FT/SEC	49
IV	BORSIC-ALUMINUM COMPOSITES CUMULATIVE WEIGHT LOSS - MILLIGRAMS - 1100 FT/SEC	52
V	NICKEL COATED GRAPHITE EPOXY CUMULATIVE WEIGHT LOSS - MILLIGRAMS - 1100 FT/SEC	52
VI	BORON-ALUMINUM 2024-T6 CUMULATIVE WEIGHT LOSS - MILLIGRAMS - 1100 FT/SEC	54
VII	ALUMINUM 2024-T6 CUMULATIVE WEIGHT LOSS - MILLIGRAMS - 1100 FT/SEC	54
VIII	403 STAINLESS-SOLAR 183 COATING CUMULATIVE WEIGHT LOSS - MILLIGRAMS - 880 FT/SEC	57
IX	SAND EROSION TESTS 403 STAINLESS COATED WITH 1 MIL TITANIUM CARBIDE CUMULATIVE WEIGHT LOSS - MILLIGRAMS - 880 FT/SEC	61
X	SINGLE NICKEL PHOSPHIDE COATING ON Ti-6Al-4V CUMULATIVE WEIGHT LOSS - MILLIGRAMS - 880 FT/SEC	63
XI	DUPLEX NICKEL COATING ON Ti-6Al-4V CUMULATIVE WEIGHT LOSS - MILLIGRAMS - 880 FT/SEC	64
XII	CHROMALLOY-NICKEL COATING ON Ti-6Al-4V CUMULATIVE WEIGHT LOSS - MILLIGRAMS - 880 FT/SEC	68
XIII	CHROMALLOY-BORIDE COATING ON Ti-6Al-4V CUMULATIVE WEIGHT LOSS - MILLIGRAMS - 880 FT/SEC	72

LIST OF TABLES

TABLE	PAGE
XIV SAND EROSION - NRC BORON CARBIDE COATING ON Ti-6Al-4V CUMULATIVE WEIGHT LOSS - MILLIGRAMS - 880 FT/SEC	73
XV TIDURAN PROCESS - NITRIDE COATING ON Ti-6Al-4V CUMULATIVE WEIGHT LOSS - MILLIGRAMS - 880 FT/SEC	76
XVI SAND EROSION UCAR COATINGS ON Ti-6Al-4V CUMULATIVE WEIGHT LOSS - MILLIGRAMS - 880 FT/SEC	79
XVII SAND EROSION SAE 13 LEAD ALLOY CUMULATIVE WEIGHT LOSS - MILLIGRAMS - 880 FT/SEC	87
XVIII PLASMA SPRAYED ALUMINA ON ALUMINUM CUMULATIVE WEIGHT LOSS - MILLIGRAMS - 730 FT/SEC	107
XIX PLASMA SPRAYED ALUMINA ON ALUMINUM CUMULATIVE WEIGHT LOSS - MILLIGRAMS - 1120 FT/SEC	107
XX RAIN EROSION TESTS ON ALUMINA COATING	115
XXI RAIN EROSION TESTS ON PURE NICKEL (270) CUMULATIVE WEIGHT LOSS - MILLIGRAMS - 1120 FT/SEC	118
XXII IZOD IMPACT STRENGTH OF POLYMERS	125
XXIII RAIN EROSION TESTS ON HMW POLYETHYLENE CUMULATIVE WEIGHT LOSS - MILLIGRAMS - 730 FT/SEC	127
XXIV RAIN EROSION TESTS ON HMW POLYETHYLENE CUMULATIVE WEIGHT LOSS - MILLIGRAMS - 1130 FT/SEC	127
XXV RAIN EROSION TESTS ON ACRYLIC-POLYVINYL CHLORIDE CUMULATIVE WEIGHT LOSS - MILLIGRAMS - 730 FT/SEC	130
XXVI RAIN EROSION TESTS ON ACRYLIC-POLYVINYL CHLORIDE CUMULATIVE WEIGHT LOSS - MILLIGRAMS - 1130 FT/SEC	130

LIST OF TABLES

TABLE		PAGE
XXVII	RAIN EROSION TESTS ON POLYURETHANE (W-134) CUMULATIVE WEIGHT LOSS - MILLIGRAMS - 730 ft/sec.	134
XXVIII	RAIN EROSION TESTS ON POLYURETHANE (W-121) CUMULATIVE WEIGHT LOSS - MILLIGRAMS - 730 ft/sec.	134
XXIX	RAIN EROSION TESTS ON POLYURETHANE (W-612) CUMULATIVE WEIGHT LOSS - MILLIGRAMS - 730 ft/sec.	135
XXX	RAIN EROSION TESTS ON POLYURETHANE (W-612) CUMULATIVE WEIGHT LOSS - MILLIGRAMS - 1120 ft/sec.	135
XXXI	RAIN EROSION TESTS ON POLARYLSULFONE (ASTREL 360) CUMULATIVE WEIGHT LOSS - MILLIGRAMS - 730 ft/sec.	143
XXXII	RAIN EROSION TESTS ON POLARYLSULFONE (ASTREL 360) CUMULATIVE WEIGHT LOSS - MILLIGRAMS - 1120 ft/sec.	144
XXXIII	RAIN EROSION TESTS ON NYLON (ZYTEL-7110-13) CUMULATIVE WEIGHT LOSS - MILLIGRAMS - 1120 ft/sec.	144
XXXIV	RAIN EROSION TESTS ON NYLON (ZYTEL-7110-13) CUMULATIVE WEIGHT LOSS - MILLIGRAMS - 730 ft/sec.	145
XXXV	RAIN EROSION TESTS ON POLYPHENYLENE OXIDE (NORYL-731) CUMULATIVE WEIGHT LOSS - MILLIGRAMS - 730 ft/sec.	149
XXXVI	RAIN EROSION TESTS ON GLASS FILLED PPO (NORYL-GFN-3) CUMULATIVE WEIGHT LOSS - MILLIGRAMS - 730 ft/sec.	149
XXXVII	RAIN EROSION TESTS ON POLYPHENYLENE OXIDE (NORYL-731) CUMULATIVE WEIGHT LOSS - MILLIGRAMS - 1120 ft/sec.	150
XXXVIII	RAIN EROSION TESTS ON GLASS FILLED PPO (NORYL-GFN-3) CUMULATIVE WEIGHT LOSS - MILLIGRAMS - 1120 ft/sec.	150
XXXIX	RAIN EROSION TESTS ON ACETAL (DELRIN 550) CUMULATIVE WEIGHT LOSS - MILLIGRAMS - 730 ft/sec.	156
XL	RAIN EROSION TESTS ON ACETAL (DELRIN 550) CUMULATIVE WEIGHT LOSS - MILLIGRAMS - 1120 ft/sec.	156

LIST OF TABLES

TABLE		PAGE
XLI	COMPARISON OF EROSION RESISTANCE OF THERMOPLASTIC POLYMERS	159
XLII	MECHANICAL PROPERTIES OF METALS TESTED	187
XLIII	COMPARISON OF TENSILE IMPACT STRENGTHS WITH REPEATED IMPACT DATA	242
XLIV	PROPERTIES OF SELECTED THERMOPLASTIC RESINS	248

I. INTRODUCTION

Damage caused by the impact of rain drops and/or dust particles on the leading edges of various components of aerospace vehicles has become a serious problem as the speeds of these vehicles have attained supersonic velocities. This phenomenon has been the subject of research studies by various investigators for many years. A state-of-art survey was published in 1965. (1)

In order to obtain a solution to this problem the Air Force Materials Laboratory is currently conducting in-house research (2,3,4,5) and has sponsored not only development studies on erosion resistant materials (6,7) but also studies of the erosion characteristics of aerospace materials in rain and sand environments (8).

The goals of the research that was carried out on this program were threefold: one to determine the response of various classes of materials to rain and sand particle impact at supersonic velocities and to relate this behavior to the physical and mechanical properties of the materials through analytical and empirical relationships; two, the development of coatings which will provide resistance to rain and sand erosion; three, the micro-mechanical investigation of the erosion caused by the impingement of water and dust particles at high velocities

which will provide a fundamental understanding of the erosion damage under specific environments and in the development of improved erosion resistant materials.

II. SUMMARY

An investigation was carried out on the protective capability of coatings of electrodeposited nickel, against sand erosion, on advanced fiber reinforced fan blade materials of graphite-epoxy and boron aluminum composites and titanium 6Al-4V. It was found that in general, the time to lose a given weight of electrodeposited nickel coating (100 milligrams) was comparable to the time to lose the same weight of bulk, pure nickel. This indicates that the erosion resistance of electroplated nickel on various substrates will probably be no greater than bulk nickel.

A comparison of the sand erosion resistance of boron aluminum 2024-T6 composite with the same bulk aluminum alloy (2024-T6) shows that which has been previously observed for other non-metallic composites, i.e., the use of a reinforcement reduces the erosion resistance of a bulk material.

Based upon the volume of material lost due to sand erosion, Ti-6Al-4V alloy is only approximately six percent greater in erosion resistance than pure nickel.

The sand erosion rates of three different titanium alloys determined at 880 ft/sec were found to be comparable, for all practical purposes.

Comparison of the sand erosion resistance of eleven newly developed protective coatings for titanium alloy compressor blades indicated that only five coatings

merited further evaluation. These five coatings were Chromalloy boride, Solar boride coating, NRC boron carbide coating, TI titanium carbide and the Bell alumina-columbium coating.

These coatings will be evaluated further for sand erosion at supersonic velocities and for the effect of these coatings on the fatigue and structural strength of the Ti-6Al-4V alloy.

Comparison of the sand erosion characteristics of bulk ceramic materials at 1100 ft/sec shows that high density alumina possessed the greatest resistance to erosion.

Investigations of the rain erosion behavior of elastomeric radome coating materials indicates that polyurethane coating (Astrocoat 115) has approximately 2.5 - 3 times the erosion resistance of neoprene (1801-C).

The advanced high temperature AFML fluorocarbon elastomer coating does not deteriorate in erosion resistance after previous aging for one hundred hours at 400°F.

Special radome constructions of fiber reinforced composites investigated for rain erosion resistance consisted of glass fibers oriented perpendicular to the impacted surface and 3D orthogonal and angle interlock silica fibers in a silica matrix. These constructions did not exhibit any improvement in rain erosion resistance over standard non-metallic fiber reinforced composites.

Ceramic coated (alumina) composites prepared by spraying and slip casting methods were evaluated for rain erosion resistance. The plasma sprayed coatings on aluminum exhibited good rain erosion resistance at 730 and 1120 ft/sec. The plasma sprayed alumina coatings on polyimide fractured very quickly at similar velocities and lost adhesion. Slip cast alumina on phenolic laminate substrates exhibited good erosion resistance at 770 and 880 ft/sec impact velocities.

Polymeric materials that might be used as coatings having improved rain erosion resistance were tested in their bulk form. An acetal resin (Delrin) exhibited good erosion resistance at 720 and 1120 ft/sec, however, because the acetal did not appear to be significantly better than the currently used polyurethane coating (Astrocoat) no attempts were made to test it as a coating on various substrates.

Micrographic studies were carried out to identify the principal mechanisms of erosion in materials whose rain and sand erosion had been characterized on the AFML-Bell rotating-arm apparatus. The materials studied from sand erosion tests included three ductile metals: 6061-T6 aluminum, Ti-6Al-4V titanium, and type 403 stainless steel; two types of ceramic coatings on type 403 stainless steel: titanium carbide and a boride proprietary to Solar Aircraft; and two filament-reinforced composite materials: aluminum-borsic and graphite-epoxy. The materials studied from rain erosion tests included three ductile metals: pure nickel (Inco 270), Ti-6Al-4V titanium, and type 403 stainless steel; three formulations of bulk

polyurethane; urethane coating materials; a group of nine thermoplastics; and a glass-fiber reinforced epoxy. In addition, a series of short-duration rain erosion tests were conducted on well-characterized specimens of Ti-6Al-4V, bulk polyurethane, and a glass-fiber reinforced epoxy for in-depth studies of the erosion mechanisms in these materials.

The investigation of sand erosion of ductile alloys at approximately 900 ft/sec indicates that dispersion hardening may be an effective technique for increasing the resistance of ductile alloys; especially if the hardened particles are densely arrayed and if they are small compared to the size of the grains of impacting sand.

The principal mechanism for erosion of the ceramic coating materials was brittle fracture. The uneroded surface of the titanium carbide was found to contain a network of microcracks of significant depth. The boride coating also contained a network of flaws, but on a finer scale than those observed in the titanium carbide. Erosion pits are nucleated through the local growth and juncture of these microflaws. Both materials eroded through the nucleation and growth of pits, but the nucleation and growth rates were less in the boride.

Observations on the sand erosion of the composite materials tested are similar to those made for dispersion-hardened alloys. Candidate filament materials are brittle, and they are used in a geometry which virtually ensures filament fracture on sand impact. Sand erosion resistance

can be improved by changing the matrix material, but the behavior of the matrix material must lead to desirable composite strength: hence the available options in choice of matrix material are limited. It seems clear that erosion research should concentrate on the development of coating materials to protect composites rather than on material manipulation to improve the native erosion resistance of the composite.

The studies of rain erosion of ductile alloys at 1120 ft/sec showed that there is no obvious relation between selected mechanical properties and erosion resistance. In particular, the high erosion resistance found for pure nickel is anomalous. Morphologically, the high erosion resistance of the nickel seems attributable to the fact that the pits formed in the nickel are broad and shallow. Such pits tend to minimize the likelihood that high velocity water jets will be formed in raindrop impact and decrease the velocity of those jets which do form. Both factors are expected to give a significant reduction in the rate of ductile erosion. The results of the tests on stainless steel and titanium seem to indicate profitable directions for the development of other rain erosion resistant alloys, particularly steel and nickel-base alloys. Drawing on these results, the rain erosion resistant metal should have the yield strength and hardness to resist the accumulation of plastic damage. Results to date indicate that a yield strength of about 90 ksi is sufficient to resist damage at Mach 1.0 if the surface is free of gross flaws. One must, however, ensure that this strength is available to resist fine fluid flows, which dictates a fine grain size

and thorough dispersion of hardening agents. In the case of high strength steels or titanium alloys it appears that one can profitably trade some bulk strength for fracture toughness. If we begin from the position that it is mandatory to prevent surface roughening, the material must have the toughness to resist quasi-brittle crack propagation normal to the surface and should have an effective fatigue limit high enough to ensure that only that material in the immediate surface layer is liable to fatigue failure.

In-depth micrographic studies were made of the rain erosion mechanisms in Ti-6Al-4V and a homologous series of three polyurethane elastomers. The erosion mechanisms in these materials have been identified over a period spanning the initiation of the erosion process through large-scale material removal during the later stages of the erosion process. The change in the form of the erosion mechanism from the early to the later stages of the erosion process has been correlated with the abrupt change in the rate of material removal seen in plots of weight loss as a function of time. A direct correlation is evident between the static stress-strain behavior of the three urethanes and their long-term erosion resistance.

The observations pertaining to the bulk polyurethane specimens used in this research are only indirectly applicable to elastomeric coatings. Differences arise due to the initial condition of the exposed surface in each case, the presence of bubbles in the coatings as seen in microscopic examinations of samples of non-pigmented Astrocoat 115, and the presence of the substrate. The work on polyurethane coatings indicates that pits originate

at sites where the coating is not properly bonded to the substrates. Coating removal takes place through the growth of one or only a few pits. The erosion resistance of Astrocoat 115 is very impressive; even after exposure to raindrop impacts at 730 ft/sec for over an hour, large areas of coating surface showed almost no evidence of damage. The outstanding erosion resistance can be attributed to the virtual absence of initial flaws on the exposed surface of the coating.

An attempt to correlate the erosion resistance of a diverse group of eight thermoplastics with their mechanical properties as found in existing tabulations did not produce any general trends. Significant differences were observed in the erosion behavior of the thermoplastics tested; however, further microscopic investigations in conjunction with controlled tests will be required to identify the erosion mechanisms contributing to the gross erosion characteristics of selected thermoplastics.

Detailed microscopic investigations were undertaken for 181 glass-fiber reinforced epoxy specimens exposed to a 1 in/hr rainfall at 730 ft/sec for a total exposure time slightly in excess of one minute. These studies indicate that from the standpoint of erosion resistance the epoxy matrix is the weakest component in the composite. The droplet impacts preferentially remove the epoxy from areas which form interstices in the woven fabric; brittle chipping of the epoxy continues down to the underlying fiber bundles. The composite fractures at the epoxy/fiber interface; however, the glass fibers resist this initial failure mode and exhibit minimal fracturing of

the fibers in a fiber bundle. Even after several layers of fiber bundles are exposed to direct droplet impacts, relatively few pits can be found along the exposed fibers. A limited number of fibers are removed by localized cracking in one area with subsequent removal from the fiber bundle by lateral jetting. The primary erosion mechanism is the progressive removal of epoxy from around entire fiber bundles. Segments of the fiber bundles are removed when they can be fractured in bending or shear.

From these investigations it is clear that the erosion resistance of glass-fiber reinforced composites could be increased if the bonding between the fibers and the matrix material could be improved in order to avoid delamination at the matrix/fiber interface and if the matrix had more inherent erosion resistance than the brittle epoxy used in the specimens tested.

The differentiation of the erosion mechanisms in the early stage of the erosion process from those in the later stages has far-reaching significance. Understanding the initial mechanisms for material removal serves as the basis for mechanistic analyses of the effect changes in material properties will have on the erosion behavior of the bulk material. Comparative predictions of the erosion behavior for a class of materials can be made in a rational manner. For example, a simple mathematical representation for the initiation of the erosive process in bulk polyurethane is the opening of a crack under a mode I deformation in a plane strain state. The mechanical properties of the polyurethanes, and possibly other elastomers, can be used in conjunction with this simple

model to evaluate their erosion resistance. The complexity of the model and the mechanical characteristics can be progressively increased.

It has been seen repeatedly in a homologous series of materials that one or more materials in the group will exhibit good erosion resistance up to the time the later-stage mechanisms become dominant as evidenced by a noticeable change in the weight-loss data, ther. the erosion resistance of these particular materials will display an erosion resistance which is considerably less than other formulations of the same general material. The research on erosion mechanisms is progressing to the point where it is possible to specify modifications in material properties which will tend to delay the onset of the more rapid material removal which develops in the later stages of the erosion process.

III. EROSION RESISTANT COATINGS RESEARCH

The detrimental effects caused by the rain and/or sand erosion of the leading edges of helicopter blades, rotating at tip speeds up to 600 ft/sec., has been reduced to a practical degree by the development and use of elastomeric coatings or metal sheaths.

However, the operation of gas turbine engines in dusty environments highlights a major problem of sand and dust erosion of turbine blades, particularly in the compressor portion of the engine.

Titanium alloys are currently used in some compressor sections of jet engines for axial blades and vanes and are candidate metals for advanced turbine engine components where light weight, high strength and ductility are required. However, sand and dust erosion of turbine engine blades have so reduced the time between overhauls that this has become a problem of major concern.

The effort on this portion of the investigation involves the development of wear resistant coatings capable of providing sand erosion protection for titanium alloy compressor blades and vanes of gas turbine engines which would at least double the time between engine maintenance or overhaul due to sand and dust erosion damage.

The particular titanium alloy of interest for use in current and future compressor vanes and blades is Ti-6Al-4V.

The literature relating to surface treatment or coatings for titanium is well covered in a summary report by Wood (9). However, the treatments described, emphasize coatings for the prevention of galling of titanium used with other metals.

Recent reports by Levy and Morrosi (10) and Currie (11) indicate that coatings of diffusion bonded electroless and electroplated nickel give significantly improved wear resistances to titanium alloys.

Only one report by Green (12) is pertinent to the problem of erosion by sand. The work describes the development and testing of a carbide coating for stainless steel and titanium alloy compressor blades. The carbide coating increases the resistance of steel and titanium alloy compressor blades to sand erosion but problems with reduced mechanical properties and ductility of the coated blades, were experienced, making further development of erosion resistant coatings for aircraft gas turbine compressor blades highly desirable.

Coatings formed on the surface of titanium alloys by chemical reactions with interstitial elements to form oxides, carbides, nitrides or borides as well as electrochemical reactions with nickel, cadmium and chromium are generally referred to as hard coatings.

The interstitial elements form solid solutions and react readily with titanium at elevated temperatures to form wear resistant coatings which tend to have a deleterious effect on the mechanical properties and ductility of most titanium alloys.

Surface hardened titanium derives its brittleness from the notch-sensitive nature inherent in the highly stressed expanded coating that has been applied by a high temperature process. Cracks occurring in the hard coatings penetrating through the coating and extending down to the titanium core act as stress risers or as points of extreme notch sensitivity which is exhibited in the highly brittle character of coated titanium in bending or impact tests.

Another problem associated with the formation of hard coatings on titanium such as nitrides, carbides or borides which involve high temperature processing (1200° - 1800°F) springs from the fact that the coefficient of thermal expansion of the coating and titanium alloy are significantly different, resulting in spalling of the coating during cooling from the elevated temperature

Because of the reduction of fatigue strength and increased brittleness experienced with titanium alloys coated with 2-3 mils of carbides or nitrides using high temperature processes (9,12) it seemed desirable to investigate other coatings that would not have to be processed at high temperatures, i.e., the use of a ceramic or electrodeposited coatings.

The coating development work carried out was comprised of four separate tasks: (1) developing methods of applying an alumina coating to metal substrates with good adhesion (2) developing techniques of electrodeposition of nickel coatings on titanium and diffusion of nickelides into the titanium surface (3) electrodeposition of cobalt tungsten alloys and iron to form borides (4) determination of the comparative sand erosion resistance of borides, nitrides and carbides available from other sources.

The immediate problems with the addition of a thin ceramic coating, which would have satisfactory erosion resistance such as alumina, to a titanium alloy were concerned with obtaining satisfactory adhesion and obtaining sufficient density, as well as ductility in a 3-5 mil coating of ceramic to prevent cracking.

The concept of coating the titanium alloy with a metal binder that would bond layers of small spheres of alumina and which would tend to form a relatively ductile matrix offered considerable promise in reducing the wear and damage caused by sand erosion. After consideration of many metals for a binder material, columbium was selected because it is compatible with both alumina and titanium and forms a solid solution up to about 10% with Ti-6Al-4V.

The second approach which was explored was the use of electroless and electrodeposited nickel coatings on titanium with and without diffusion upon heating at relatively low temperatures. These nickel coatings have been shown to have very high surface hardnesses and excellent wear resistances (10,11,13,14,15).

The third approach being explored consisted of two phases; one, the electrodeposition of cobalt-tungsten coatings on titanium and the determination of their sand erosion resistance and two, the electrodeposition of cobalt-tungsten and iron coatings on titanium and the conversion of coatings to the borides. It is well known that cobalt and tungsten borides are very hard and wear resistant and that iron boride coatings have excellent resistance to sand erosion.

In addition to the three areas of exploratory development noted above commercially available coatings of borides, nitrides and carbides on Ti-6Al-4V specimens were obtained for evaluation of their erosion capabilities in a sand environment.

IV. EXPERIMENTAL WORK ON TITANIUM COATINGS

Major emphasis on the development of a new coating that would not have a detrimental influence on the mechanical behavior of titanium alloys (i.e., fatigue strength, ductility and stress rupture) was centered on the use of alumina particles bonded with columbium metal which would form a solid solution with the alpha-beta titanium alloy of interest, Ti-6Al-4V.

Ceramic Coating

In the ceramic coating process which was developed after considerable experimentation spheroidized alumina particles (44-74 microns in diameter) were coated with columbium metal (3-4 micron coating) by passing columbium pentachloride (CbCl_5) and hydrogen gas through a fluidized bed of alumina held at 1500°F in a furnace.

The alumina particles are held in a conical shaped quartz container in the furnace and the gas flows through the fluidized bed, coating the particles with columbium metal.

The columbium coated particles were then packed around the airfoil shaped test specimen to be coated, in a columbium can and subjected to a range of temperatures from 1000 to 1500°F, pressures from 1000 to 6000 psi and times from 6-8 hours. Optimum temperatures of 1400°F and pressure of 6000 psi for a period of six hours in an isostatic press were used in specimen preparation.

Figure 1a is a 440X photomicrograph of the compacted alumina particles bonded by the columbium metal. The metal phase in this combination was found to be in the range of 20 ± 2 percent by volume, based upon a weight determination.

Figure 1b is a 440X magnification of the bond between the test specimen and the alumina particles.

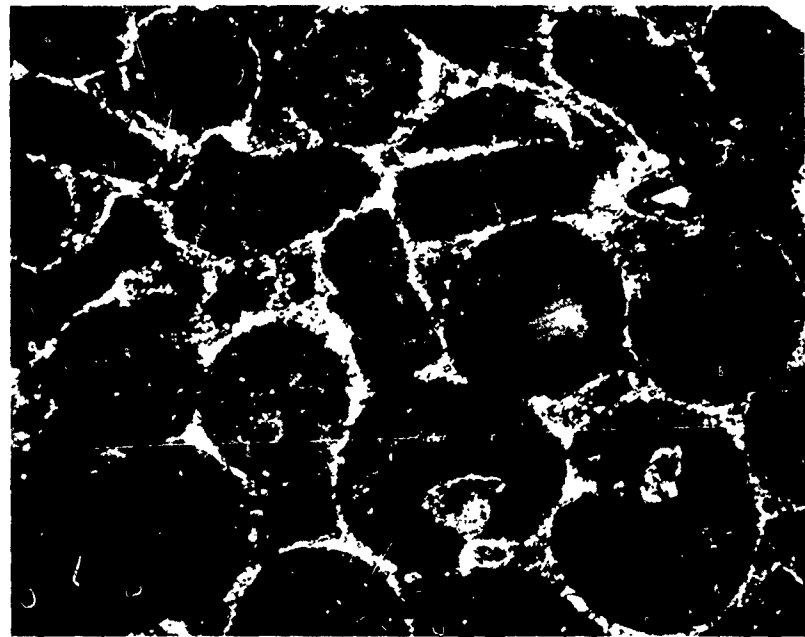
Three airfoil test specimens were prepared with approximately a 20 mil coating of alumina bonded in columbium.

The surface of the alumina bonded coating was rather rough and attempts were made to polish the surface with diamond paste which was only moderately successful.

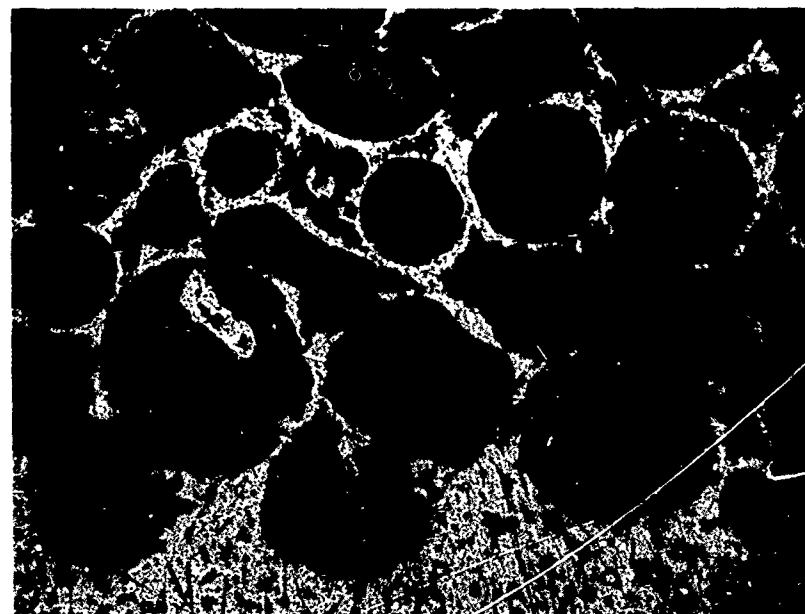
Flame spraying of alumina by Union Carbide Materials Research Division using their detonation gun to fill in the voids in the roughened surface resulted in the removal of all but 2-3 mils of the alumina-columbium coating, probably by abrasion of the supersonically sprayed alumina.

The remaining coating of alumina-columbium overcoated with pure alumina was compacted and densified in the isostatic press at 1400°C and 6000 psi for three hours.

Figure 2 shows two 25X photomicrographs of the surface of the densified Ucar alumina coating the two specimens which were tested for sand erosion resistance.



(a) Compacted Columbium coated Alumina - 440X



(b) Alumina Particles in Columbium - 440X

Figure 1. Alumina-Columbium Coating

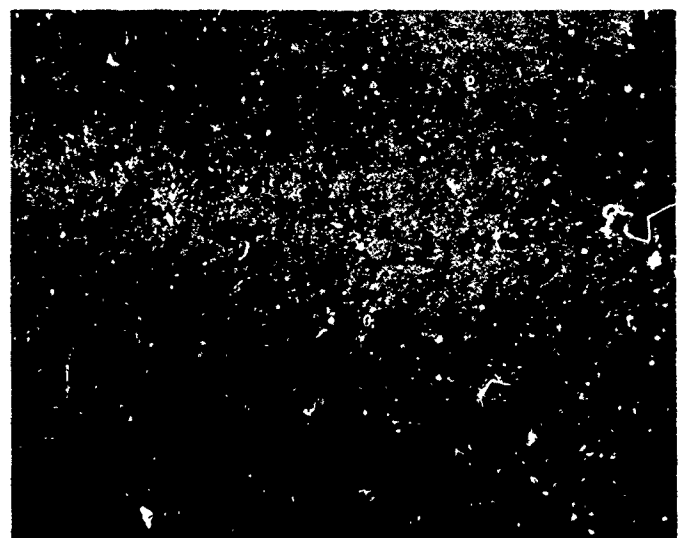
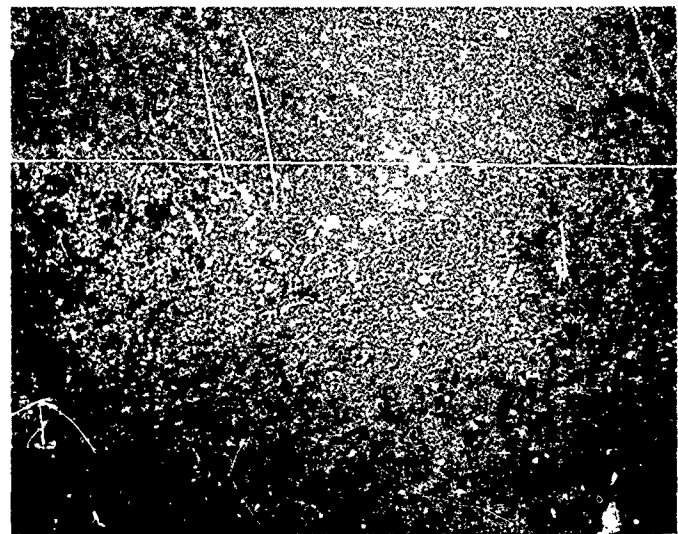


Figure 2. Alumina Coatings on Test Specimens - 25X

Two more airfoil shaped specimens were then coated with 10-12 mils of columbium coated alumina spheres approximately 50μ in diameter and overlayed with 4-5 mil coating of alumina of two different particle sizes to give a dense, very smooth outer layer of pure alumina. The 4-5 mil coating of fine particle alumina was consolidated and bonded to the coarser 12-15 mil columbium-alumina coating using the isostatic hot gas press at 1400°C and 6000 psi for three hours.

Figure 3 shows a typical cross section of the coating applied to the airfoil shaped test specimen.

Three airfoil shaped test specimens coated with Al_2O_3 as noted below were tested.

Specimen A-12	Densified Al_2O_3 , Ucar coating
Specimen A-13	Densified Al_2O_3 - 0.5 micron alumina 95% dense
Specimen A-14	Densified Al_2O_3 - 0.03 micron alumina 79% dense

Table I summarizes the work carried out on alumina coated specimens.

Nickel Coatings

Based upon the results of a previous investigation of hardened nickel coatings for application to titanium alloys (10,11) a single and a duplex nickel coating system were also investigated.

Specimens for adhesion, ductility and sand erosion tests were machined from titanium alloy 6Al-4V sheet .090 inches in thickness. The titanium metal was in the annealed condition before processing with the two types of nickel coatings.

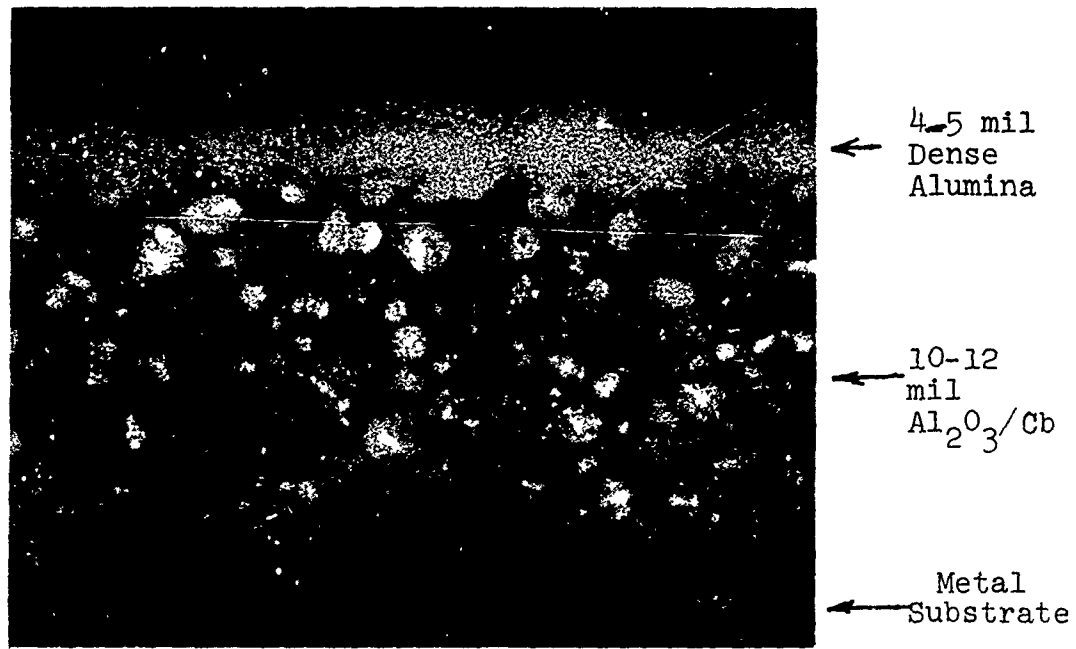


FIGURE 3 Typical Cross Section of Cb/Al₂O₃
and Al₂O₃ coatings on airfoil shaped
test specimen - 110X.

TABLE I
SUMMARY DATA ON FABRICATION OF CERAMIC COATED TEST SPECIMENS

SPECIMEN NO.	PROCESSING CONDITIONS FOR $\text{Cb}/\text{Al}_2\text{O}_3$	TYPE OF Al_2O_3	PROCESSING CONDITIONS FOR Al_2O_3	REMARKS
A-12	1350°C, 19 hrs, 5000 psi	44-74 microns	D-gun Spray	High speed Al_2O_3 particles from D-gun spray Eroded away the $\text{Cb}/\text{Al}_2\text{O}_3$ coating. D-gun Al_2O_3 coating removed and sample reprocessed as No. A-14.
A-13	1400°C, 6000 psi, 3 hrs.	44-74 microns	D-gun Spray	Same as No. A-12 Specimen reprocessed as No. A-13.
Trial	-	-	1400°C, 6000 psi, 3 hrs.	Trial run to assess quality of coating for the processing conditions. Coating had cracks but excellent density of 95%
A-14	1400°C, 6000 psi, 3 hrs.	(a)	1400°C, 6000 psi, 3 hrs. 1400°C, 6000 psi, 3 hrs.	Weld leaked, Al_2O_3 did not compact. Al_2O_3 coating is 95% dense but had cracks. Tested on Whirling Arm.
A-13	1400°C, 6000 psi, 3 hrs.	(b) Alon	1400°C, 6000 psi, 3 hrs. 1400°C, 6000 psi, 5.5 hrs.	Weld leaked, Al_2O_3 did not compact. Al_2O_3 coating 79% dense but had cracks. Tested on Whirling Arm.
A-12	-	-	D-gun Spray 1400°C, 6000 psi, 3 hrs.	Specimen canned and hot gas isostatic pressed. Al_2O_3 coating was greater than 98% dense. Tested on Whirling Arm.

(a) 0.5 micron diameter polishing alumina from Buchler Ltd., Chicago, Ill.
(b) >90% Al_2O_3 0.03 micron diameter from Clevet Corp.

The single coating process involved the use of a hardened electroless nickel-phosphite coating and the duplex process employed an initial electroless nickel coating with a second electrodeposited outer coating of nickel.

The nickel phosphorous alloy coating was deposited from an electroless nickel plating bath. Heat treatment of the coating causes the nickel-phosphite to precipitate and diffuse into the titanium surface and form a titanium intermetallic coating. The phosphorous assists in the diffusion process which has a hardening effect, but one which increases in hardness from the substrate to the coating surface.

The electroless nickel in the as-plated condition was found to have relatively low bond strength to the titanium 6Al-4V and low hardness. A diffusion treatment at temperatures ranging from 750°F for four hours to 1550°F for 1 hour was found to significantly improve the adhesion and hardness by producing Ni_3Ti and NiTi_2 intermetallic compounds which were identified by microprobe analysis.

The use of higher temperatures resulted in higher hardnesses of the coating therefore for the test specimens prepared a 1550°F diffusion temperature for 1 hour in a vacuum retort was used.

The specimens coated with the duplex nickel coatings were prepared with a one mil coating of electroless nickel then given a two minute sulfuric acid,

anodic etch to activate the electroless nickel surface at 100 amperes/ft² anodic current density prior to the electroplating with nickel.

Immediately following the acid anodic etch the specimen was transferred to the nickel sulfamate plating bath and a 1.5 mil nickel coating was obtained over the electroless nickel in approximately one hour, using a current density of 30 amperes/ft².

The duplex nickel coated titanium test specimens were then subjected to diffusion heat treatment at 1550°F in a vacuum retort for one hour.

On conducting microhardness tests on the duplex nickel coatings after diffusion heat treatment it was found that approximately 0.5 mil of the outer thickness of nickel was relatively soft and it had to be removed by a chemical etch in nitric acid (40 vol %) for two hours. The remaining outer coating had a Vickers hardness number of 890-900.

Initially prepared specimens of Ti-6Al-4V with a duplex nickel coating exhibited a tendency to blister during the diffusion heat treatment at 1550°F. After a considerable amount of experimentation and evaluation of the plating procedures it was found that if the anodic etching process did not remove all of the oxide from the titanium alloy before electroless plating this blistering of the duplex nickel coating occurred.

Bend tests through 180° angle over a 1/4" radius of diffusion coated electroless nickel coatings have demonstrated excellent adhesion of the nickel coating to titanium but small microcracks in the nickel were observed under 440X optical microscopic examination. The duplex coating system described above will do much to eliminate this problem of brittleness since the addition of an equally thick layer of nickel, cobalt-tungsten, or cobalt-rhenium on top of the nickel-phosphorous alloy before heat treatment will allow diffusion of all of the phosphorous into the metal outer layer and into the Ti-6Al-4V substrate. To date only specimens of Ti-6Al-4V with the electroless nickel and duplex nickel coating have been prepared for sand erosion testing.

The following process procedures were used. Titanium 6Al-4V specimens were thoroughly cleaned with an abrasive scrub cleaner until "water-break" free.

Specimens were then etched in a nitric-hydrofluoric acid mixture for 2 minutes at room temperature. This was followed by an anodic etch in glacial acetic-hydrofluoric acid mixture at 110°F for 2 minutes using a current density of 20 amps/ft². Immediately following the anodic etch the specimens were passed through a hot distilled water rinse and immersed in the electroless nickel plating bath with an initial current of 20 amps/ft² for approximately 20 seconds to initiate the chemical reaction. Current was then stopped and after one hour the specimens were removed from the bath with a nickel-phosphorous coating of 1 mils.

Four specimens of electroless nickel one mil thick were diffusion heat treated at 1550°F in vacuum.

Four specimens of electroless nickel one mil thick were anodically etched in sulfuric acid (50% vol) at 100 amps/ft² for five minutes, rinsed in distilled water and immersed in nickel sulfamate plating bath and plated with 1.5 mil of nickel for 1½ hours using a current density of 30 amp/ft².

The four duplex nickel coatings were then diffusion heat treated in vacuum at 1550°F for one hour and subsequently etched in nitric acid (40 vol %) for two hours at room temperature.

Plating bath conditions and etchant solutions used for nickel coatings are given below.

Etches:

Initial Etch

Nitric-hydrofluoric
10% (vol) HF (48%)
35% (vol) HNO₃ (conc)
Balance distilled water
Room Temperature

Anodic Etch

Glacial acetic-hydrofluoric
7 parts - HC₂H₃O₂ (conc)
1 part - HF (48%)
Temperature - 100° to 120°F.
Solution continuously sparged with dry nitrogen.

Baths: (15)

Electroless Nickel

NiSO ₄ .	6H ₂ O	- 2.8 oz/gal.
NaH ₂ PO.	H ₂ O	- 17.3 oz/gal.
pH		4.6 - 4.7
Temperature		204 - 206°F
Initial Current Density		- 20 amp/ft ²
Time	- Approx.	1 hr/mil

Electrolytic Nickel

Ni(NH ₂ SO ₃) ₂	- 43.6 oz/gal.	
NiCl ₂ .	2H ₂ O	- 0.4 oz/gal.
H ₃ BO ₃	- 4.5 oz/gal.	
Anti-Pit	- 0.05 oz/gal.	
pH	- 4.0	
Temperature	- 110°F	
Current Density	- 30 amps/ft ²	
Time	- 1 hour/mil	

Diffusion Process:

The nickel plated specimens were placed in a titanium retort and heated to 1550°F for 1 hour in a vacuum of 10⁻⁴ - 10⁻⁵ torr.

Iron Coating

Initial sand erosion tests on Solar boride coatings have indicated that this hard coating possessed outstanding erosion resistance when applied to 403 stainless steel.

Contacts with Solar regarding the possibility of applying their boride coating on titanium 6Al-4V revealed that the boride coating could only be applied to an iron substrate. Solar suggested brazing a 5 mil iron foil to

the titanium alloy and then forming the boride on the ferritic substrate. We suggested plating an iron coating on the titanium 6Al-4V in lieu of the brazing process which would allow Solar to form the boride coating. Because this idea was feasible (9,15) attempts were made to plate a 3 mil coating of iron on titanium 6Al-4V.

Several iron plating baths were investigated: ferrous sulfate, mixed ferrous sulfate-chloride, and ferrous ammonium sulfate. These baths were found to build up a deleterious concentration of ferric ions which caused an iron precipitation. This was especially true in the ammoniacal sulfate bath. Some plating did occur but the as-deposited iron on the titanium 6Al-4V was extremely brittle and stress-cracked.

The use of an iron fluoborate bath was then investigated and found to be quite resistant to oxidation. However, titanium and fluoborate solutions were not compatible.

It was then decided to coat the titanium-6Al-4V with nickel prior to plating with iron to eliminate the problems of dissolution of titanium and poor adhesion. The nickel layer served to protect the titanium during plating and also functioned as a bonding medium between the iron and titanium.

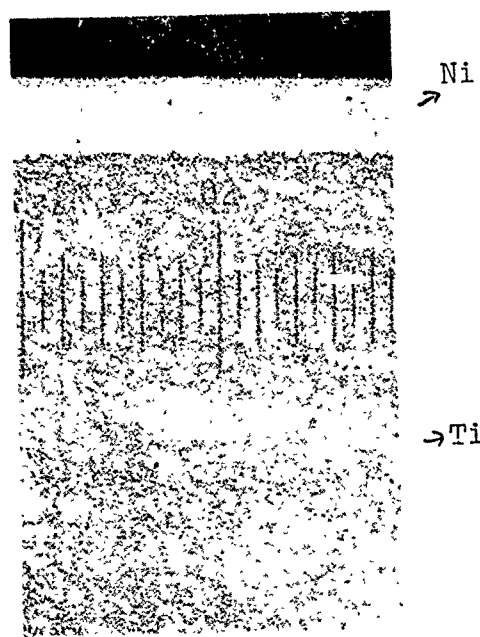
The titanium-nickel-iron system worked initially using a 0.2 - 0.3 mil nickel coating. Occasional localized delamination of the nickel from the titanium occurred, which was traced to blisters between the titanium and nickel. The blisters were induced by the sulfuric acid

anodic etch. A low temperature heat treatment of 400°C of the titanium-nickel prior to iron plating for 30 minutes eliminated this blistering but passivated the nickel surface for subsequent plating. The nickel surface was activated with the use of a nitric acid-ferric chloride etch for subsequent plating. This etch in combination with the usual sulfuric acid anodic etch prior to iron plating, caused dissolution of the nickel and the thinly plated areas of the titanium 6Al-4V specimen were exposed.

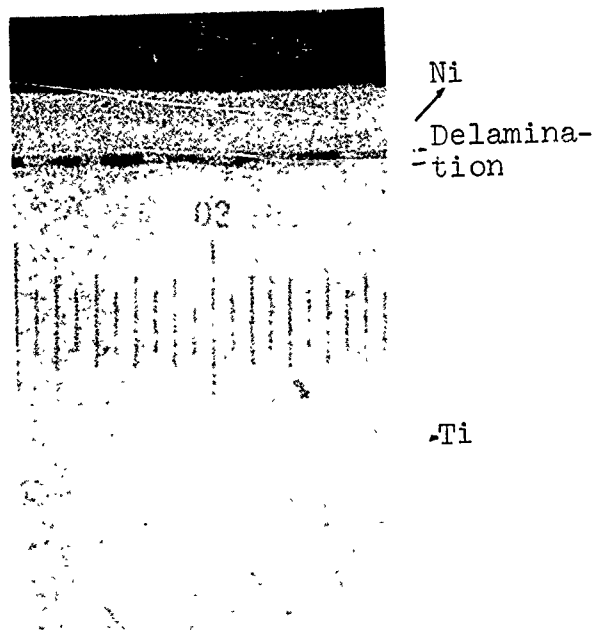
Several titanium 6Al-4V specimens were then prepared with a thicker, 1 mil nickel coating and a 3 mil iron coating. The "as plated" iron was shiny but brittle. An annealing heat treatment of 820°C for 2 hours was found to yield a ductile iron coating with good adhesion to the nickel undercoating but a brittle nickel layer was formed. Note Figure 4d.

However, because of the brittle intermetallic layer which forms between nickel and titanium under these conditions, a lower temperature with a longer heat treatment was examined. A heat treatment of 600°C for 4 hours resulted in cracking and delamination in the intermetallic nickel layer. Note Figure 4c.

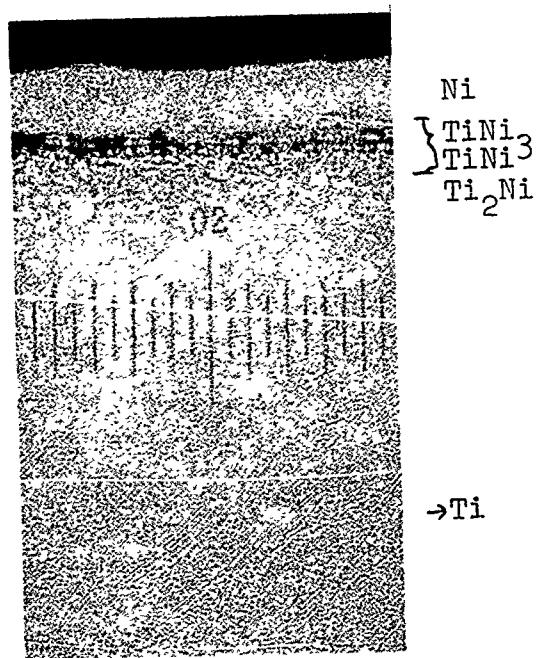
At this point a study of the influence of heat treatment on cracking and delamination of the iron coating was carried out. It was found that delamination even occurred after a heat treatment of 400°C for 2½ hours. Note Figure 4b. A short heat treatment of 400°C for 30 minutes resulted in satisfactory bonding of the nickel and titanium layers with no delamination of iron to the intermetallic layer being formed. Note Figure 4a.



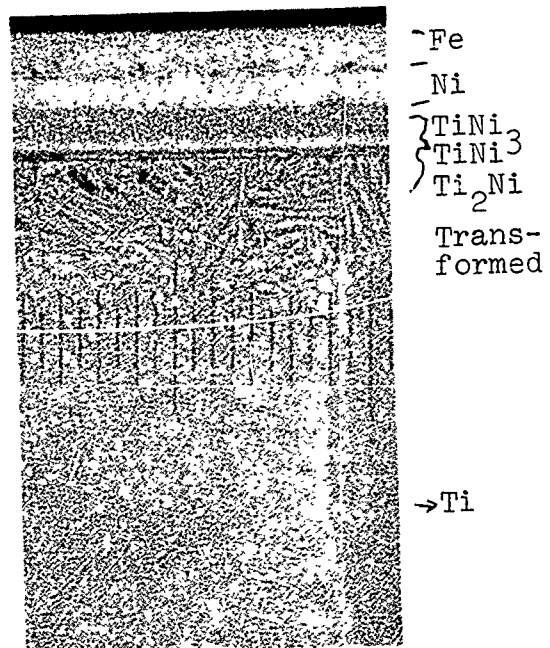
(a) 400°C - 1/2 hr.



(b) 400°C - 2 1/2 hrs.



(c) 600°C - 4 hrs.



(d) 820°C - 2hrs.

FIGURE 4 Effects of various heat treatments on nickel-titanium - 200X

This nickel coating could be plated with iron with no delamination or cracking. Because the nickel and iron coated titanium specimens were to be subsequently subjected to a long-high temperature boriding process, it was necessary to investigate a more suitable technique to deposit the iron directly on the titanium 6Al-4V without the use of a nickel inner layer.

Presently an iron chloride-calcium chloride bath is being examined for this purpose. Its advantageous low pH of 1.2 should retard ferric ion formation and precipitation. All baths investigated to date had higher pH values ranging from 3.0 to 5.0.

Details of exact plating processes and bath compositions are described below.

Titanium - 6Al-4V specimens, machined to the sand erosion configuration, were first degreased with an organic solvent and thoroughly cleaned with a pumice scrub cleaner until "water-break" free.

Each specimen was anodically etched in an oxalic acid-sodium fluoride mixture at 55°C for 5 minutes using a current density of 1.5 amps/ft². Following the anodic etch the specimens were quickly rinsed in distilled water and immediately immersed in a Barrett nickel plating bath for 1 hour using a current density of 30 amps/ft² and a temperature of 110°F. After nickel plating, the specimen was heat treated at 400°C for 2 hours in a vacuum of 10⁻⁵ Torr.

Anodic Etch for Titanium: (16)

Oxalic Acid	50 gm/l.
Sodium Fluoride	100 gm/l.
Hydrochloric Acid (conc.)	100 ml/l.
C.T.A.B. (Cetyl Trimethyl- Ammonium Bromide)	5 gm/l.
Current Density	1.5 amps/ft ²
Temperature	55-60°C.
Time	5 minutes

Nickel Plating Bath (Barrett):

Nickel Sulfamate	10.0 oz/gal.
Nickel Chloride	1.0 g/fal.
Boric Acid	4.5 oz/gal.
pH	4.0

Iron Plating Process:

The nickel coated specimens were etched in Nitric Acid-Ferric Chloride solution for 1 minute at room temperature. Following a thorough rinse and scrub cleaning, each specimen was anodically reversed at a current density of 75-100 amps/ft² in sulfuric acid for 2 minutes at room temperature and then immersed in the iron fluoborate bath for 2½ hours at 30 amps/ft² -135°F. Following plating, the specimen was heat treated to 400°C or 600°C in vacuum of 10⁻⁵ Torr.

Etch for Nickel:

Nitric Acid (conc.)	400 mls/l.
Distilled Water	Remainder
Ferric Chloride	20 g/l.

Anodic Etch for Nickel:

Sulfuric Acid (conc.)	500 mls/l.
Distilled Water	Remainder

Iron Fluoborate Bath: (19)

Iron Fluoborate	227 g/l.
Sodium Chloride	10 g/l.
Boric Acid	17 g/l.
pH	3.0 - 3.5
Temperature	135 - 145°F
Current Density	40 amps/ft ²

Cobalt-Tungsten Coatings

Cobalt-tungsten coating for titanium 6Al-4V offer considerable promise for sand erosion resistance because of their inherent hardness and wear resistance.

An electrodeposited cobalt-tungsten alloy coating was prepared on the titanium alloy using a ammoniacal bath of cobalt sulfate and sodium tungstate. This bath was selected because it resulted in a cobalt-tungsten coating having a ratio of approximately 85/15 ensuring some ductility. To avoid an oscillatory metal-iron concentration problem associated with the use of insoluble anodes, it was necessary to use 85/15 cobalt tungsten alloy anodes. Because these anodes were not available commercially they had to be prepared in the laboratory using compacted metal powders and an arc melting furnace.

The titanium alloy specimens were degreased with trichloroethylene and thoroughly cleaned with pumice scrub cleaner until "water break" free. Each titanium specimen was etched in the previously described anodic etch of oxalic acid-sodium fluoride mixture at 55°C for five minutes and an anodic current density of 1.5 amps/ft². Following

the anodic etch the specimens were rinsed in hot distilled water and immediately immersed in the cobalt-tungsten plating bath.

The plating operation was carried out in cobalt-tungsten plating bath for a period of three hours at 90°C, a cathodic current density of 30 amps/ft² and a pH of 9.0.

The plated cobalt-tungsten alloy was bright and smooth but on 180° bend tests was found to be brittle and have low adhesion to the titanium 6Al-4V alloy. Micro-probe analysis of the coating indicated the tungsten in the plated alloy to be about 15%, as expected.

Several heat treatments were evaluated to improve the adhesion of the cobalt-tungsten alloy coating to the titanium by diffusion.

Specimens were heat treated for 30 minutes at 400, 600 and 800°C in vacuum of 10⁻⁵ Torr. The specimens heat treated at 800°C had satisfactory adhesion and will be evaluated for sand erosion. Figure 5 shows the 4-5 mil coating of cobalt tungsten obtained on titanium that had a hardness of 740 VHN.

Recent literature (17) indicates that the cobalt and tungsten coatings can be converted to tungsten borides by immersion in a molten salt bath containing 40% carborundum and 60% borax by weight. Titanium specimens will be coated with cobalt-tungsten alloy, heat treated and conversion of the coating to borides by this means will be investigated.

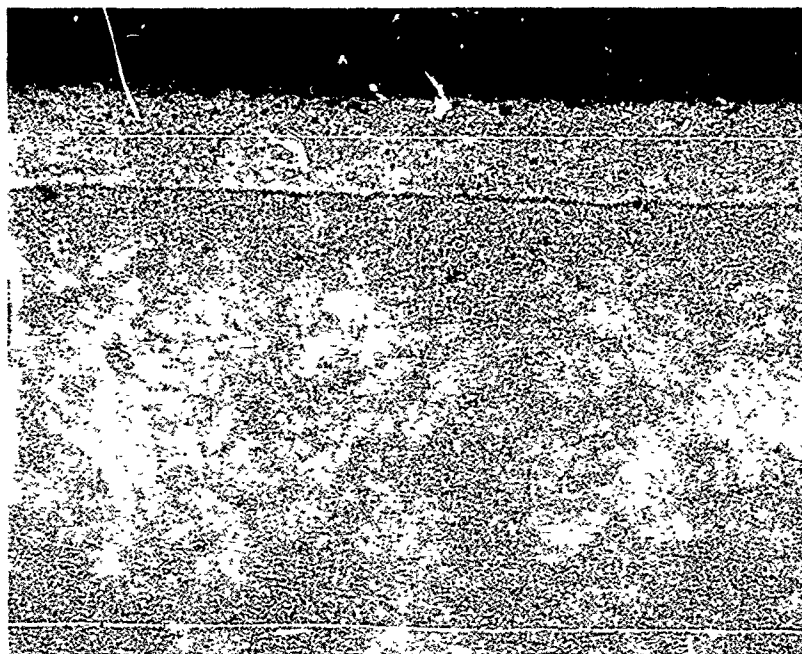


FIGURE 5. Cobalt-Tungsten Coating Electrodeposited
on Titanium-6Al-4V and heat treated to
800°C for 1/2 hour. (440X)

The cobalt-tungsten plating bath used was as follows:

Cobalt-Tungsten Plating Bath: (18)

Cobalt Sulfate 120 gm/l.

Sodium Tungstate 45 gm/l.

Sodium Potassium Tartrate 400 gm/l.

Ammonium Chloride 50 gm/l.

pH 9.0

Temperature 90 - 95°C

Anodes Co-20W

Current Density 20-40 A.S.F.

The following commercially available hard coatings applied to Ti-6Al-4V turbine shaped specimen were obtained for determination of their sand erosion resistance.

1. Boride

Atlantic Advanced Metals, Inc.
65 Aulton Street
Woburn, Massachusetts

2. Nitride Tiduran process

Kolene Corporation
12890 Westwood Avenue
Detroit, Massachusetts

3. Boride and Nickel

Chromalloy American Corporation
Turbine Support Division
4430 Director Drive
San Antonio, Texas

4. Mixed Carbides and Metallics

Union Carbide Corporation
Materials Systems Division
441 Sackett Point Road
North Haven, Connecticut

5. Boron Carbide

National Research Corporation
Cambridge, Massachusetts

In addition specimens of 410 stainless steel coated with approximately 1 mil of vapor deposited titanium carbide (Tikote C) applied by low temperature process (1000°F) were received from Texas Instruments for evaluation for sand erosion resistance.

V. MATERIALS CHARACTERIZED FOR SAND EROSION BEHAVIOR

Various classes of materials were evaluated for comparative sand erosion resistance at a 90° impact angle, various velocities, and a sand concentration of 2.3 grams/ft³ air flowing into the test chamber. Details of sand test conditions have been outlined in a previous report (8).

Two types of specimens were used for sand erosion tests. One, the flat turbine shaped specimen and two, the airfoil shaped specimen.

Because the geometry and area of impact is considerably different for the flat turbine specimen and the airfoil shaped specimen no good correlation, has been developed on the rate of erosion between the two types. The ranking of both types of specimens in their relative order of resistance to sand erosion, at a given velocity however can be obtained irregardless of their geometry.

A. Turbine Shaped Specimens

The following types of materials were tested for sand erosion using turbine shaped specimens:

1. Pure nickel (270)
2. Titanium alloys
3. Composites
4. Aluminum
5. Coatings on stainless steel
6. Coatings on titanium alloy

B. Airfoil Shaped Specimens

The following types of material were evaluated for sand erosion resistance using airfoil shaped specimens.

1. Lead (SAE 13)
2. Plastics
3. Ceramics
4. Coatings

VI. RESULTS OF SAND EROSION TESTS

A. Tests on Turbine Shaped Specimens

1. Pure Nickel

Previous comparative sand erosion tests (8) indicated that titanium 6Al-4V had sand erosion resistance comparable to high strength stainless steels and that nickel coated reinforced plastic composites had sand erosion resistance similar to that of the titanium alloys but no information was available on the sand erosion resistance of pure nickel.

Because nickel coatings both in the plated form and as foils are of considerable interest, sand erosion tests were conducted on six, annealed pure nickel, turbine shaped specimens at 880 ft/second.

The cumulative weight losses observed for the nickel specimens are outlined in Table II. The volume of nickel lost by erosion compared with Ti-6Al-4V alloy as a function of exposure time is graphically shown in Figure 6.

When the density of nickel 270 and Ti-6Al-4V are taken into account the volume of metal lost due to sand erosion is approximately the same for both materials but the actual weight loss per unit exposure time for nickel is greater.

TABLE II
 SAND EROSION OF
 PURE NICKEL (270)
 CUMULATIVE WEIGHT LOSS - MILLIGRAMS

880 ft/sec.

TIME MINUTES	SPECIMEN NO.					
	1	2	3	4	5	6
1	13	14	13	15	13	13
2	25	26	25	28	27	27
3	43	47	39	49	45	47
4	51	65	63	66	60	64
5	79	87	75	90	84	85
6	92	106	98	102	100	101
7	120	123	128	129	127	124
8	137	149	147	143	145	149
9	-	-	168	166	-	170
10	-	-	184	182	-	190

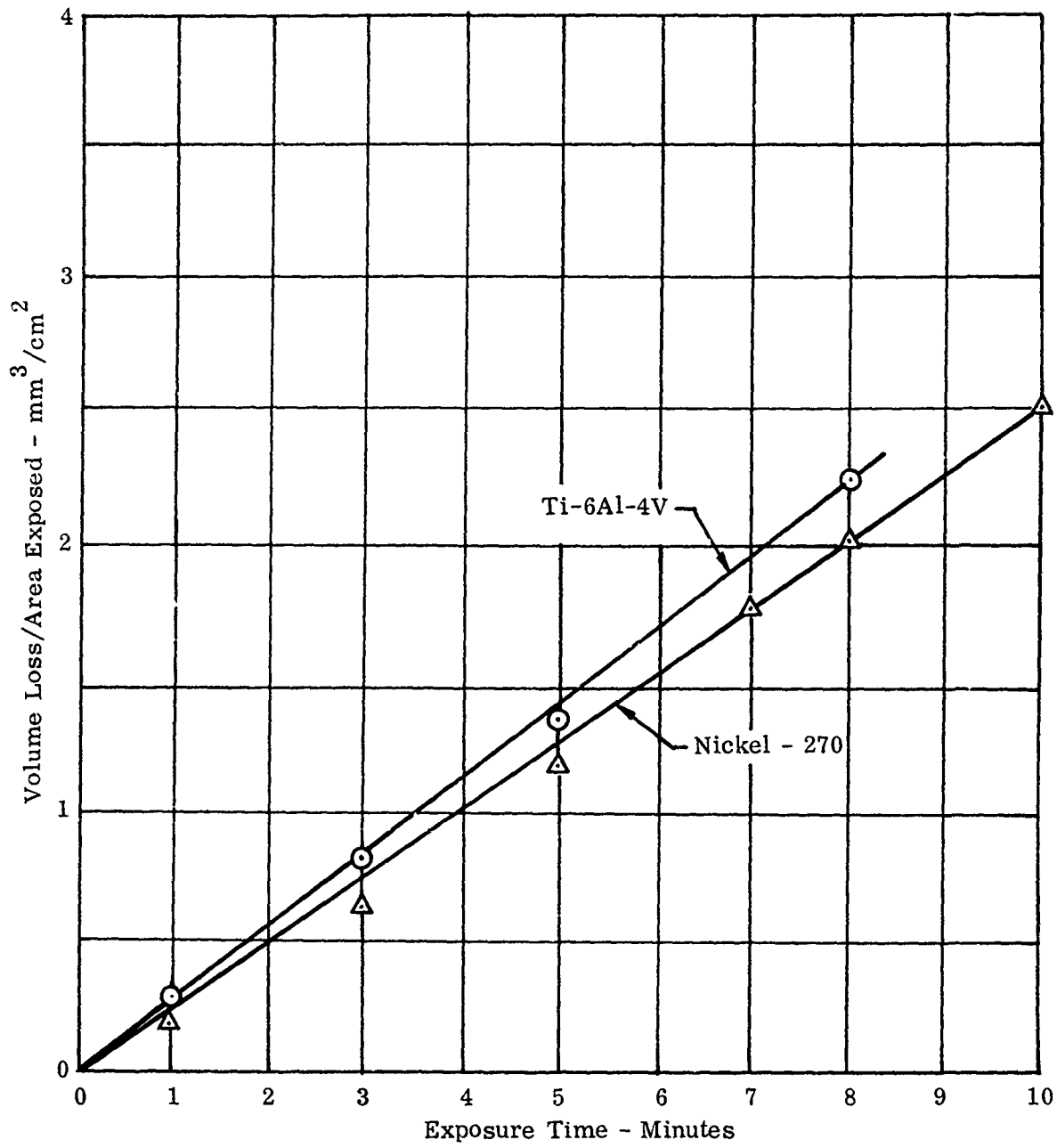


Figure 6. Comparison of Sand Erosion of Titanium and Nickel at 880 ft/sec.

2. Titanium Alloys

The volume loss in cubic millimeters per square centimeter of exposed area for three different titanium alloys exposed to a sand concentration of 2.3 grams/ft³ of air flow at impact velocities of 880 ft/sec is shown in Figure 7.

Figure 7 indicates that the three uncoated, annealed titanium alloys having Rockwell hardness of C-28-32 have comparable erosion rates at 880 ft/sec.

Figure 8 illustrates the change in sand erosion rate of Ti-6Al-4V at various velocities from 880 ft/sec to 1800 ft/sec.

3. Composites

AFML personnel coated six standard sand test specimens of a Borsic aluminum composite with soft nickel. The thickness of the electroplated nickel coating ranged from 11-17 mils.

The specimens were tested in sand at 880 ft/sec for periods ranging from 8 to 18 minutes.

After exposure to sand erosion for seven to eight minutes all of the six specimens had lost approximately one hundred milligrams in weight. Tests were continued on three specimens with the idea that we would erode through the nickel coating.

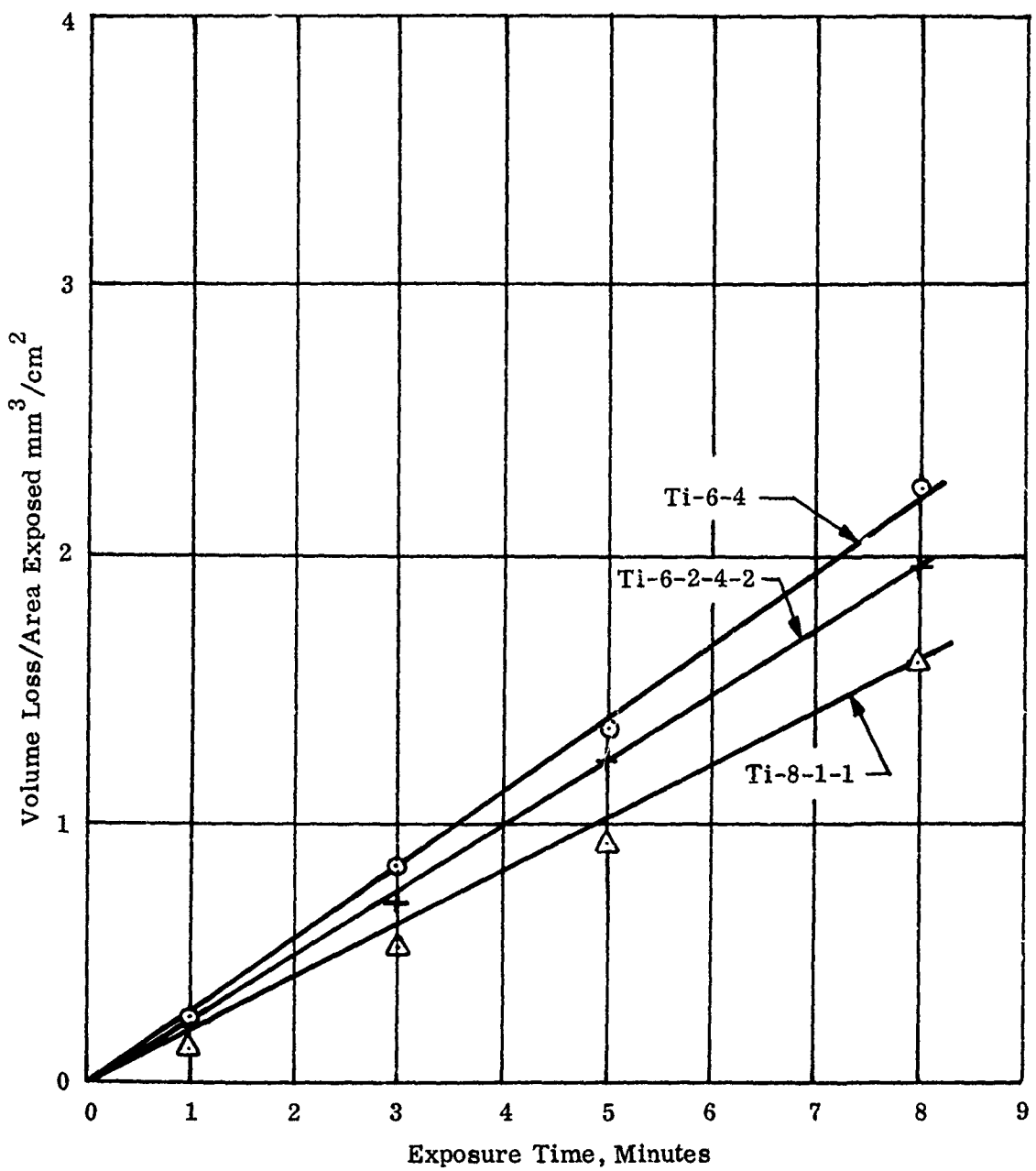


Figure 7. Sand Erosion Titanium Alloys - 880 ft/sec

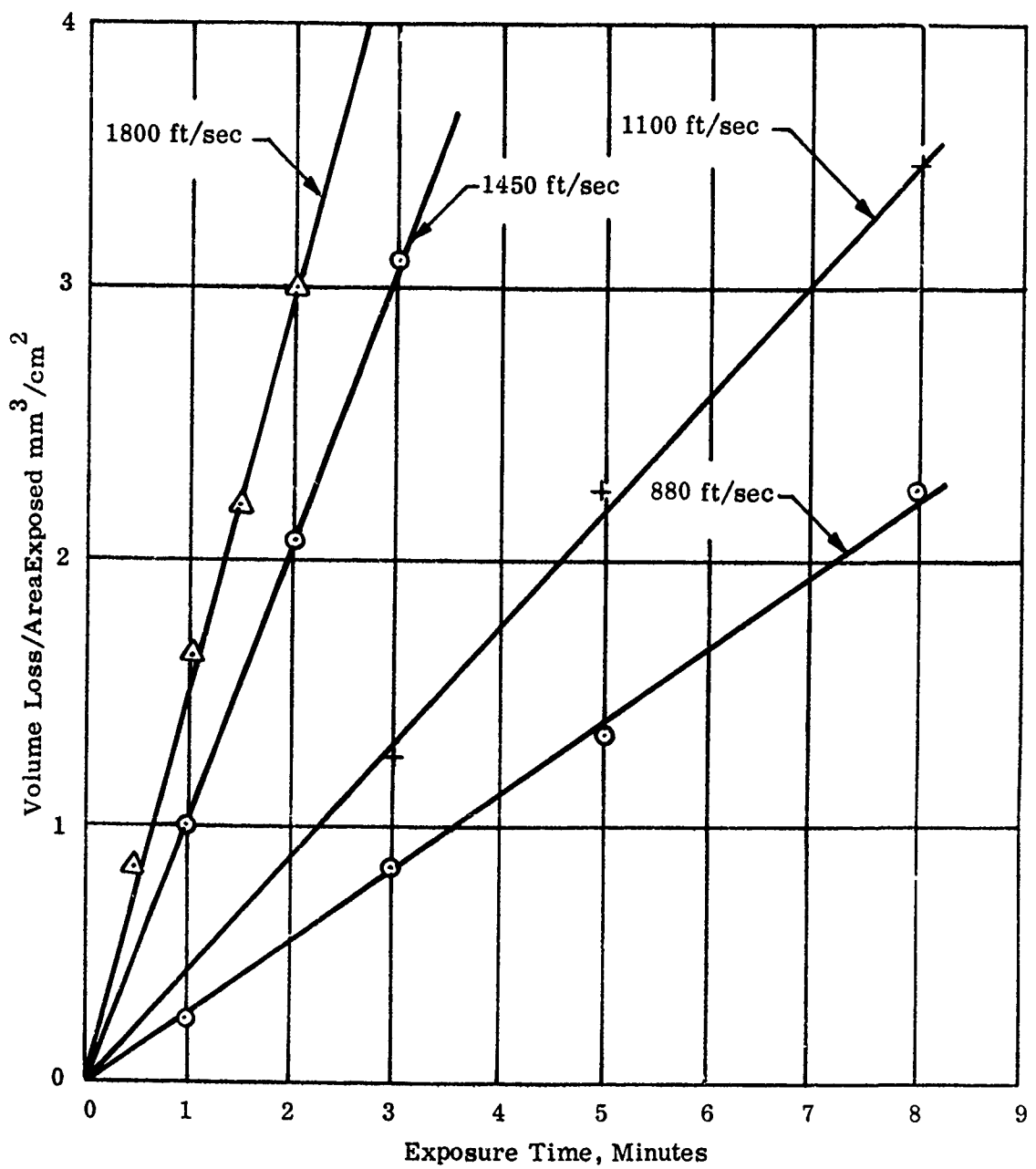


Figure 8. Sand Erosion Ti-6Al-4V at Various Velocities

However on these three specimens the nickel coating began to peel off due to the fact that the leading edge had been entirely eroded away after 10-18 minutes of exposure to sand erosion.

Figure 9 is a profile view of the leading edge of Specimen N-13 showing how the nickel had eroded away from the nose of the composite and the lifting of the nickel coat away from the Borsic-aluminum substrate.

Table III outlines the cumulative weight loss in milligrams of the nickel coated composite specimens.

Three specimens of boron-aluminum cut from a portion of an actual composite compressor blade were received from AFML and given specimen numbers BAP-4,5,6, and tested at 880 and 1100 ft/sec. Specimens of Borsic fiber with 2024T6 aluminum received from AFML were coded, BAS-4 and 5 and tested at 1100 ft/sec.

Samples of boron fiber aluminum composites prepared by General Electric were designated as specimens numbered 2Z2 through 2Z6.

Samples of Borsic fiber aluminum composite specimens coated with electroplated sulfamate nickel 8-10 mils in thickness by AFML personnel were given specimen numbers NBSAL-1 and 2 and tested at 1100 ft/sec.

Specimens of graphite-epoxy laminate coated by General Electric with 20 mils of nickel coating was designated NGE-1,2 and tested at 1100 ft/sec.

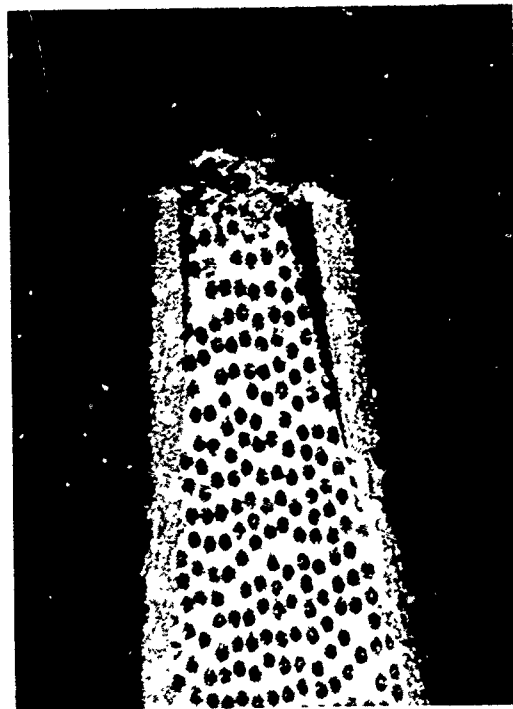


FIGURE 9. Profile view of nickel coated Borsic aluminum composite showing leading edge after 18 min. erosion by sand at 880 ft/sec - 15X.

TABLE III
 SAND EROSION
 AFML - BORSIC-ALUMINUM COMPOSITE SPECIMENS
 COATED WITH SOFT NICKEL

880 ft/sec.

TIME MINUTES	AFML SPECIMEN					
	N-1	N-2	N-7	N-8	N-13	N-14
1	10	11	10	12	11	10
2	24	26	24	23	25	24
3	36	38	35	36	36	38
4	49	54	48	51	52	56
5	66	67	62	63	65	64
6	80	83	76	81	73	86
7	90	92	89	94	80	98
8	104	113	104	113	96	118
9	112	---	116	---	112	---
10	134	---	135	---	146	---
12	162	---	---	---	172	---
14	193	---	---	---	209	---
16	222	---	---	---	240	---
18	250	---	---	---	269	---

* 1-2 -11 mils nickel

* 7-8 14 mils nickel

* 13-14 17 mils nickel

Of all the composites evaluated in this series of tests the nickel coated boron aluminum and graphite epoxy possessed the greatest resistance to sand erosion. Typical erosion observed is shown in Figure 10 and weight losses observed are outlined in Tables IV and V.

The specimens of boron aluminum composites taken from a section of an actual compressor blade exhibited very high rates of erosion after 1.5 and 2 minutes of exposure at 880 and 1100 ft/sec velocity. The results are shown in Figure 11. The rear side of specimen BAP-6 lost a large portion of the fiber and aluminum matrix after two minutes of testing.

4. Aluminum

The specimens of Borsic fiber with 2024-T6 aluminum matrix were compared with straight 2024-T6 aluminum at 1100 ft/sec to determine the influence of the boron fiber reinforcement on the rate of erosion. Based upon the comparative weight loss outlined in Tables VI and VII introduction of boron fiber into 2024-T6 increases the rate of erosion as shown in Figure 12.

5. Coatings on Stainless Steel

Fourteen standard sand erosion specimens of 403 stainless steel were coated by Solar Aircraft with 2-3 mil thickness of their S-183 boride coating. These samples were designated S1 through S-14.

SAND EROSION TEST

1100 ft/sec SPECIMEN VELOCITY

660 FT./SEC SAND-AT-VELOCITY

20 ± 0.05 LB SAND/MIN:

卷之三

SPECIMEN NO.	MATERIAL	MILLIGRAM WEIGHT	LOSS	TIME OF EXPOSURE	MINUTES
BAS-4	Borsic Fiber 2024T6Al	206	201	6	6
BAS-5	Boron Fiber Aluminum	191	191	6	6
ZA-2	ZA-3	210	217	9	9
NBSAL-1	Electro-Plated Borsic Fiber Aluminum	219	227	9	9
NBSAL-2	Nickel Coated Gra- phite Epoxy				
NGE-1					

Figure 10. View of Erosion of Composite Materials

TABLE IV
 BORSIC ALUMINUM COMPOSITES
 AFML NICKEL COATED 8-10 MILS
 CUMULATIVE WEIGHT LOSS MILLIGRAMS

TIME MINUTES	SPECIMEN NO.	
	NBSAL-1	NBSAL-2
1	15	17
2	33	40
3	58	64
5	105	119
7	158	169
9	217	219

TABLE V
 NICKEL COATED GRAPHITE EPOXY
 20 MILS
 CUMULATIVE WEIGHT LOSS - MILLIGRAMS
 1100 FT/SEC

TIME MINUTES	SPECIMEN NO.	
	NGE-1	NGE-2
1	15	14
3	62	70
5	109	131
6	147	158
9	227	221

SAND EROSION TEST
880 AND 1100 FT/SEC SPECIMEN VELOCITY
660 FT/SEC SAND-AIR VELOCITY
 2.0 ± 0.05 LB SAND/MIN

SPECIMEN NO.	BAP-4	BAP-6
SPECIMEN VELOCITY FT/SEC	1100	880
MILLIGRAM WEIGHT LOSS	124	71
TIME SECONDS	90	120

Figure 11. Erosion of Boron - Aluminum Compressor Blade Sections

TABLE VI
 BORON ALUMINUM
 2024Al-T6
 CUMULATIVE WEIGHT LOSS - MILLIGRAMS
 1100 ft/sec

TIME MINUTES	SPECIMEN NO.		
	BAS-4	BAS-5	BAS-6
1	30	34	30
2	66	67	63
3	102	98	99
6	206	201	204

TABLE VII
 2024-T6 ALUMINUM
 CUMULATIVE WEIGHT LOSS - MILLIGRAMS

1100 ft/sec

TIME MINUTES	SPECIMEN NO.				
	A-10	A-11	A-12	A-13	A-14
1	18	20	21	19	17
2	38	42	40	36	35
3	69	68	60	67	63
4	97	102	96	107	99
5	134	130	138	129	126
8	211	216	205	217	208

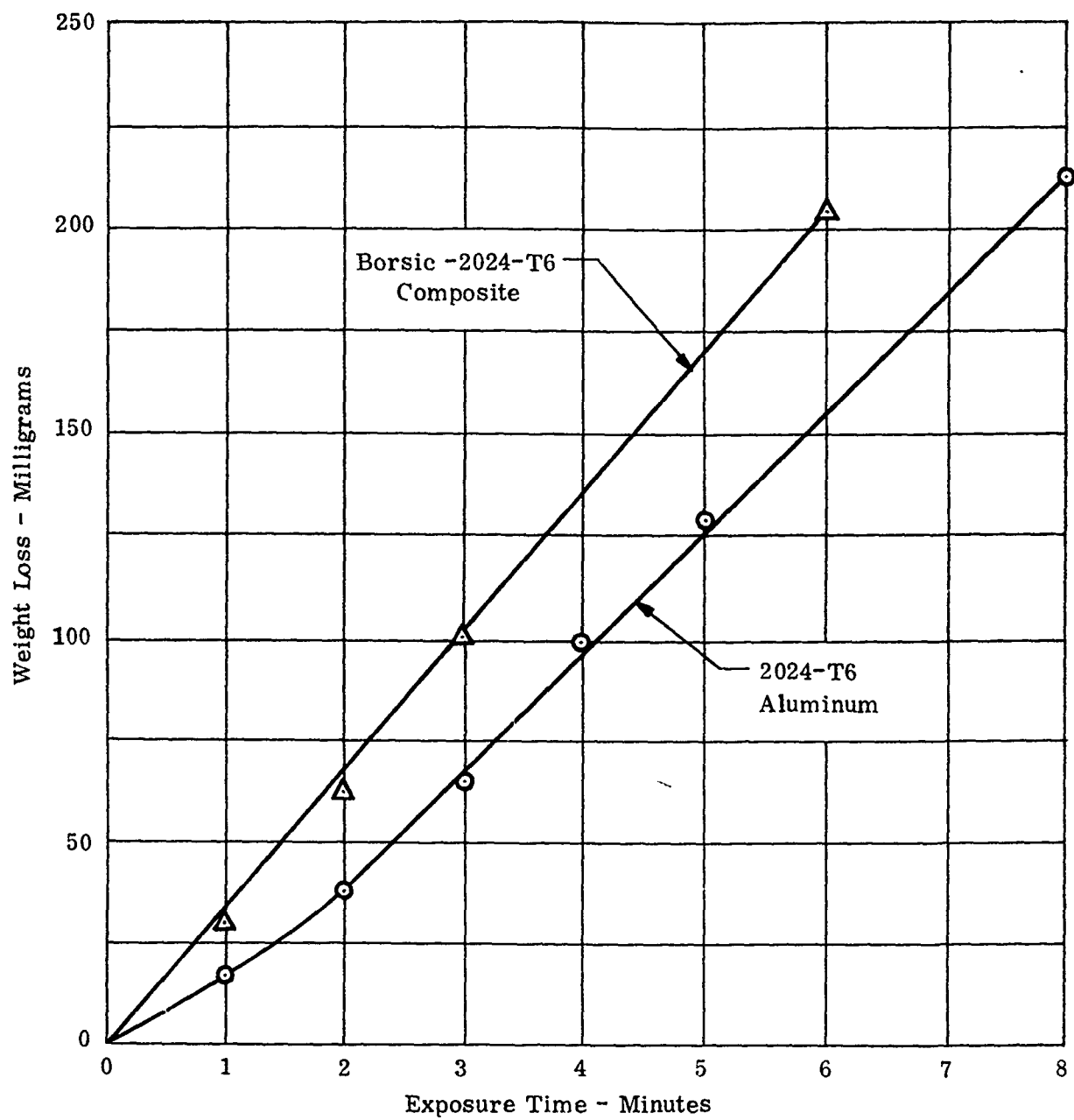


Figure 12. Rate of Sand Erosion of Basic Aluminum Composite at 1100 ft/sec

The Solar boride coating was evaluated for sand erosion for periods up to 20 minutes at velocities of 880 and 1100 ft/sec and at a velocity of 1450 ft/sec for five minutes to obtain approximately a 100 milligram weight loss.

The resultant weight losses are outlined in Table VIII. Approximately 100 milligram weight loss was experienced in 20 minutes at 880 ft/sec.

The typical pitting type erosion experienced in the coating at 880, 1100 and 1450 ft/sec are shown in Figure 13.

Six standard sand erosion test specimens of 403 stainless steel coated with approximately one mil thickness of Texas Instruments' vapor deposited titanium carbide applied by their low temperature process (1000°F) were tested at 880 ft/sec and $2.0 \pm .1$ lbs. sand/min.

Figure 14 is a low magnification (15X) which illustrates the brittle nature of the erosion of the titanium carbide coating on the leading edge of a standard turbine shaped sand erosion test specimen. Figure 15a is a scanning electron micrograph at 400X showing the eroded areas of the 403 substrate from which some of the titanium carbide coating has been removed. Figure 15b is an 800X SEM showing the brittle fracture of the titanium carbide coating from the stainless steel substrate after 10 minutes exposure to sand erosion at 880 ft/sec.

TABLE VIII
403 STAINLESS
SOLAR S-183 COATING
CUMULATIVE WEIGHT LOSS - MILLIGRAMS

TIME MINUTES	SPECIMEN NO.				
	S-6	S-7	S-8	S-9	S-10
5	18	18	20	20	19
10	38	43	55	40	40
15	60	64	73	62	61
20	92	94	98	95	83

880 ft/sec

TIME MINUTES	SPECIMEN NO.				
	S-1	S-2	S-3	S-4	S-5
5	32	29	36	37	42
10	71	63	76	78	81
15	114	105	125	123	123
20	172	154	179	171	172

1100 ft/sec

TIME MINUTES	SPECIMEN NO.			
	S-11	S-12	S-13	S-14
1	15	31	25	20
3	45	61	64	71
5	80	96	114	116

SAND EROSION TEST

880 - 1450 FT/SEC SPECIMEN VELOCITY
660 FT/SEC SAND-AIR VELOCITY
 2.0 ± 0.05 LB SAND/MIN

SPECIMEN NO.	SPECIMEN VELOCITY FT/SEC	MILLIGRAM-WEIGHT LOSS	TIME OF EXPOSURE MINUTES
S-183-10	880	1100	20
S-183-2	1100	106	15
S-183-12	1450	96	5

Figure 13. Erosion of 2-3 MIL S-183 Solar Boride Coating

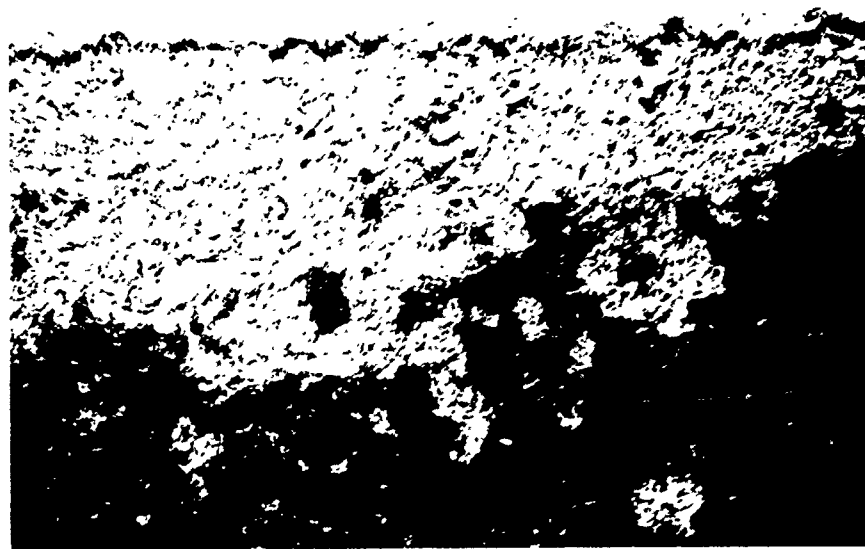
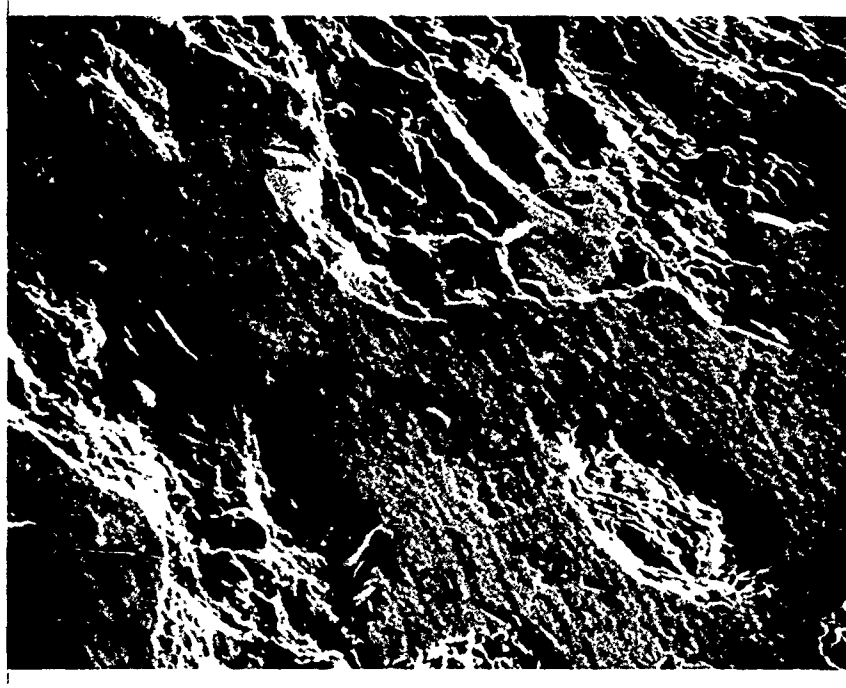
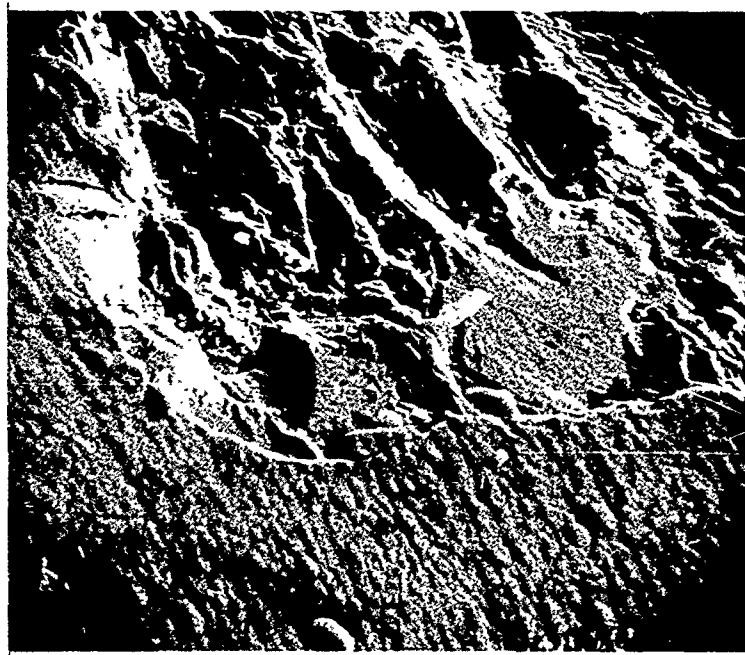


FIGURE 14. Erosion of titanium carbide coating
on leading of test specimen - 15X



(a) SEM 400X



(b) SEM 800X

FIGURE 15. Erosion of titanium carbide coating from 403 stainless substrate.

TABLE IX
SAND EROSION TESTS

403 STAINLESS-COATED 1 MIL TITANIUM CARBIDE

CUMULATIVE WEIGHT LOSS-MILLIGRAMS

1000°F PROCESS

880 ft/sec.

TIME MINUTES	SPECIMEN NO.					
	T2-8-1	T2-8-2	T2-8-3	T2-8-4	T2-8-5	T2-8-6
3	16	6	8	20	12	6
5	22	15	20	28	21	14
10	33	25	31	35	31	26
15	42	37	42	--	43	35
20	58	49	56	--	59	51
25	72	65	70	--	74	68
30	88	82	89	--	91	87
35	104	101	106	--	110	104

The cumulative weight losses obtained are outlined in Table IX. Approximately 100 milligrams weight loss of the coated specimen occurred in 35 minutes at 880 ft/sec velocity.

Figure 16 is a comparison of erosion of 403 with and without coatings.

6. Coatings on Titanium Alloy

The following coatings on metal alloy substrate were evaluated for sand erosion resistance at 880 ft/sec:

1. Nickel phosphite coating - Bell
2. Duplex nickel coating - Bell
3. Chromalloy nickel coating - Chromalloy
4. Chromalloy boride coating - Chromalloy
5. NRC - boron carbide coating - National Research
6. Tiduran Nitride coating - Kolene Corp.
7. Ucan - hard coatings - Union Carbide
8. Alumina-coating - Union Carbide
9. Alumina-Columbium substrate - Bell

The single and duplex nickel coatings prepared at Bell exhibited erosion resistance comparable to the straight titanium 6Al-4V metal.

The weight losses of the six nickel coated specimens are outlined in Tables X and XI and are compared with the other coatings in Figure 17.

Nine specimens of Ti-6Al-4V having the standard sand test configurations were coated with a proprietary nickel designated chromally series "N" by the Turbine Support Division of the Chromalloy American Corporation, San Antonio, Texas.

TABLE X

SINGLE NICKEL PHOSPHIDE COATING ON Ti-6Al-4V
CUMULATIVE WEIGHT LOSS - MILLIGRAMS

880 ft/sec.

TIME MINUTES	SPECIMEN NO.		
	NIP-1	NIP-2	NIP-6
1	17	16	20
2	35	32	34
3	46	44	49
4	58	57	59
5	66	68	72
6	73	78	82
7	80	88	94
8	88	99	105
9	96	109	116
10	112	119	129

TABLE XI

DUPLEX NICKEL COATING ON Ti-6Al-4V
 CUMULATIVE WEIGHT LOSS - MILLIGRAMS

880 ft/sec.

TIME MINUTES	SPECIMEN NO.		
	NP-5	NP-7	NP-8
1	19	22	20
2	33	39	37
3	49	54	51
4	60	61	67
5	67	70	79
6	74	81	96
7	82	91	110
8	91	97	127
9	101	108	135
10	122	119	147

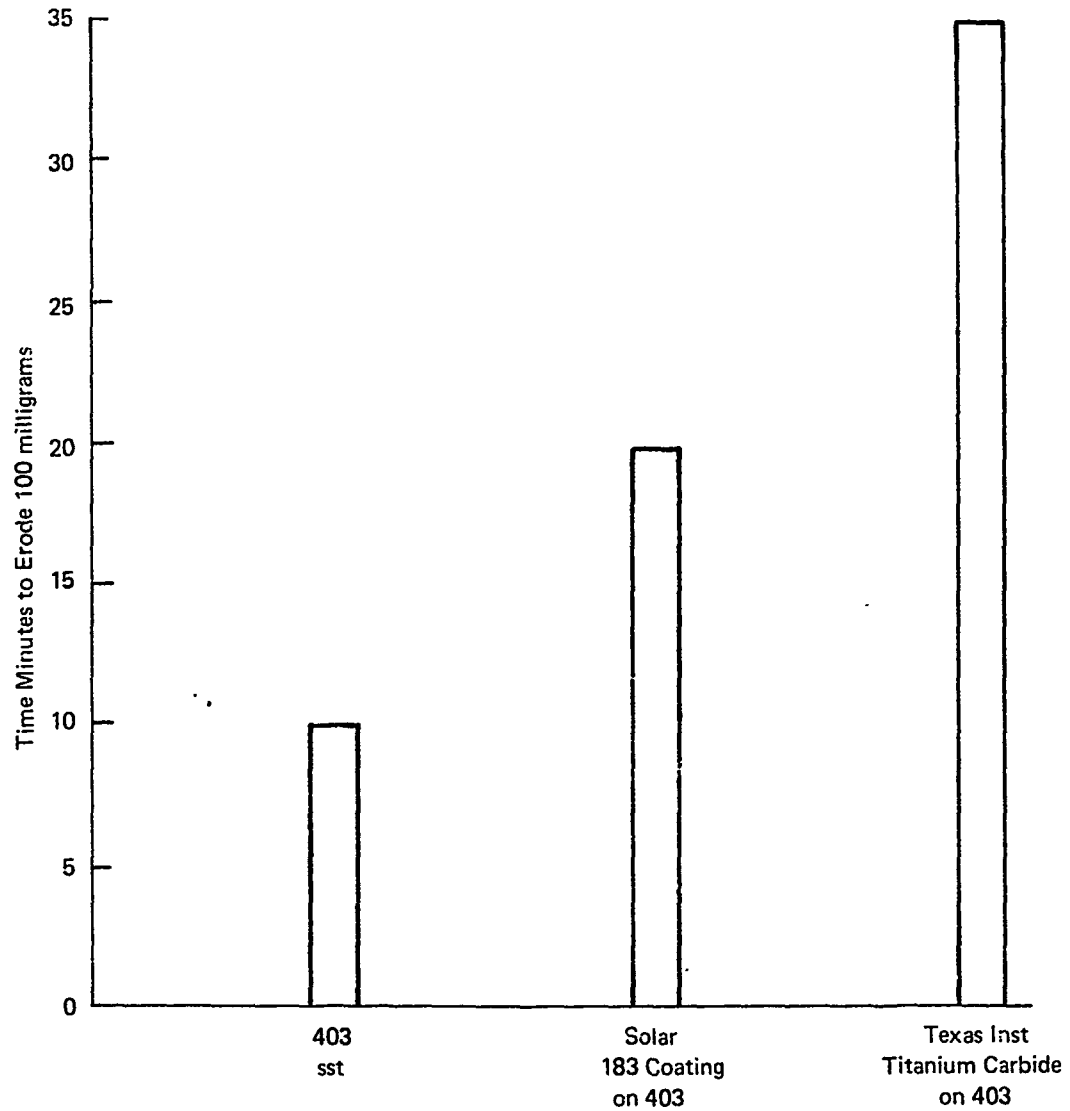


FIGURE 16 Comparison of sand erosion resistance of coatings on 403 stainless steel (880ft/sec.)

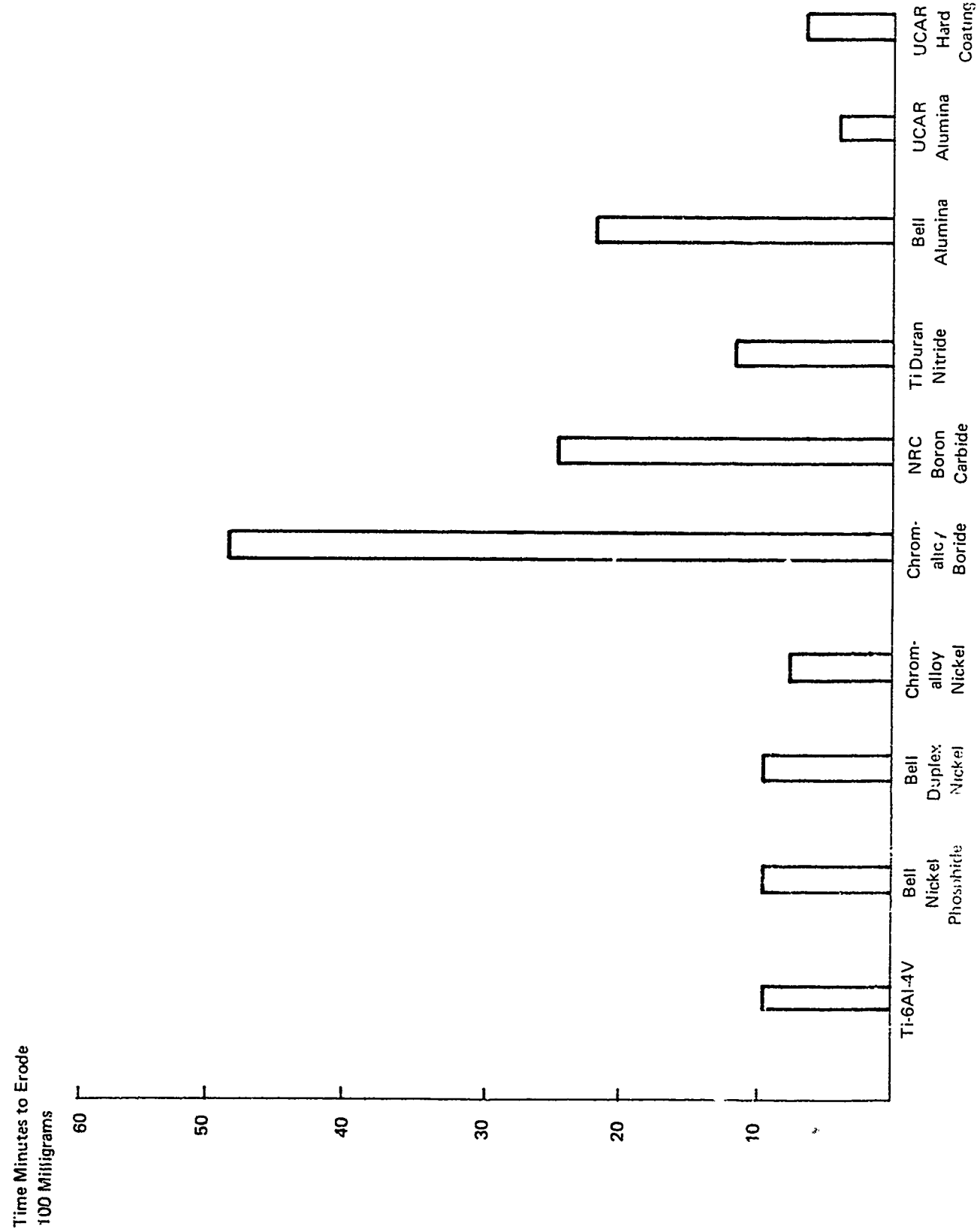


Figure 17 Comparison of Sand Erosion Resistance of Coatings on Ti-6Al-4V (880 ft/sec)

Three of these nickel coated titanium specimens were tested for sand erosion at 880 ft/sec.

As observed in Table XII the 5 mil nickel coating lost approximately 100 milligrams in 7-8 minutes.

Nine specimens of titanium 6Al-4V were coated with a three mil thickness of a proprietary boride coating by the Turbine Support Division of the Chromalloy American Corporation. This coating was designated Chromally Series "B" but no information was available as to the processing methods employed.

Of all of the coatings evaluated for sand erosion at 880 ft/second this coating was outstanding and merits further testing at higher velocities.

As noted in Table VIII the boride coating lost 100 milligrams in fifty minutes as compared to the other coatings and titanium of approximately 10 minutes. Figure 17 shows graphically the resistance to erosion compared to the other coatings. Figure 18(a) shows only slight pitting of the specimens after 20 minutes of test and Figure 18(b) exhibits the relatively small amount of erosion after 50 minutes of test. Figure 19 is a 650X scanning electron photomicrograph of the Chromalloy boride coating before and after testing in sand. Figure 19'(b) shows how the boride coating is scoured by the impacting sand particles. Figure 20 is an electron photomicrograph of the boride coating at 1000X showing how the boride coating has fractured due to solid particle impact.

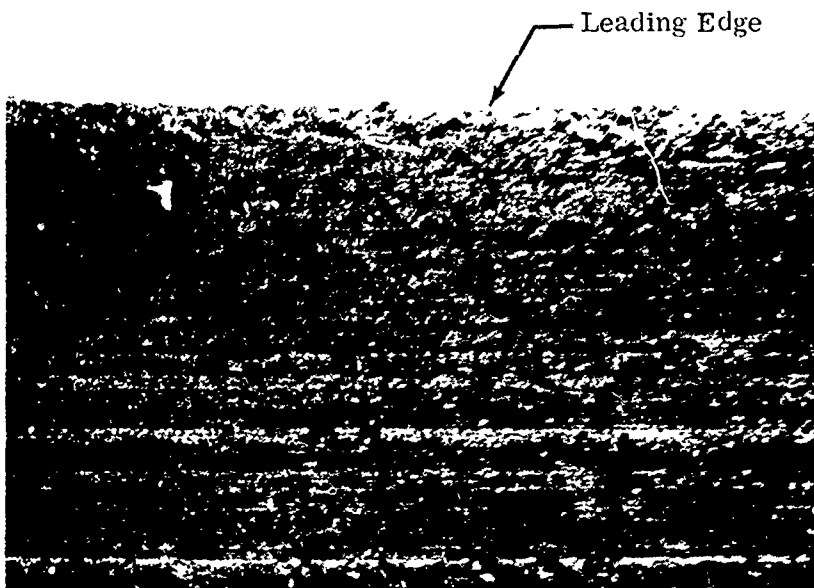
TABLE XII

CHROMALLOY-NICKEL COATING ON Ti-6Al-4V

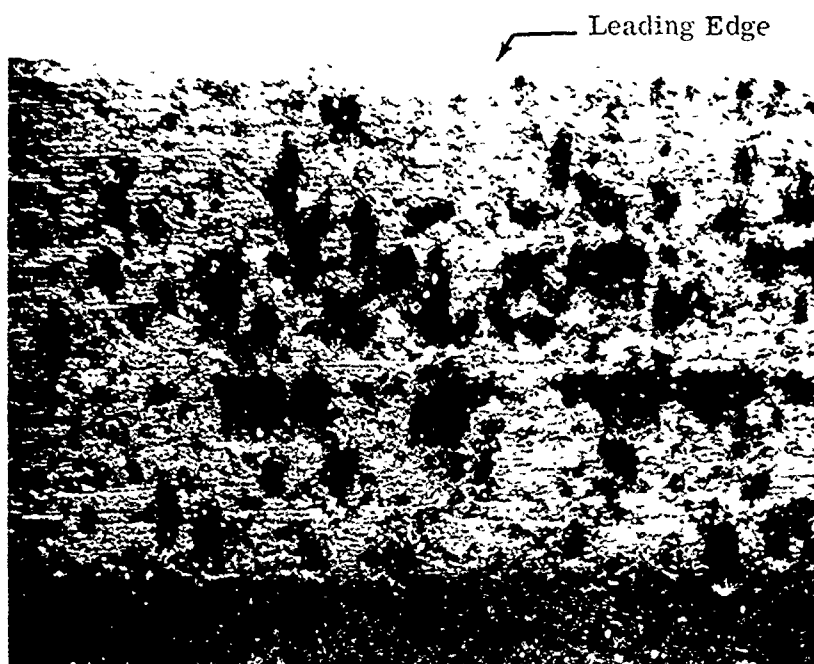
CUMULATIVE WEIGHT LOSS-MILLIGRAMS

880 ft/sec.

TIME MINUTES	SPECIMEN No.		
	CAC-N-1	CAC-C-2	CAC-N-3
1	10	15	2
2	32	39	25
3	53	52	45
4	65	66	56
5	77	76	65
6	86	88	76
7	97	96	87
8	106	104	96
9	117	112	105
10	137	124	115

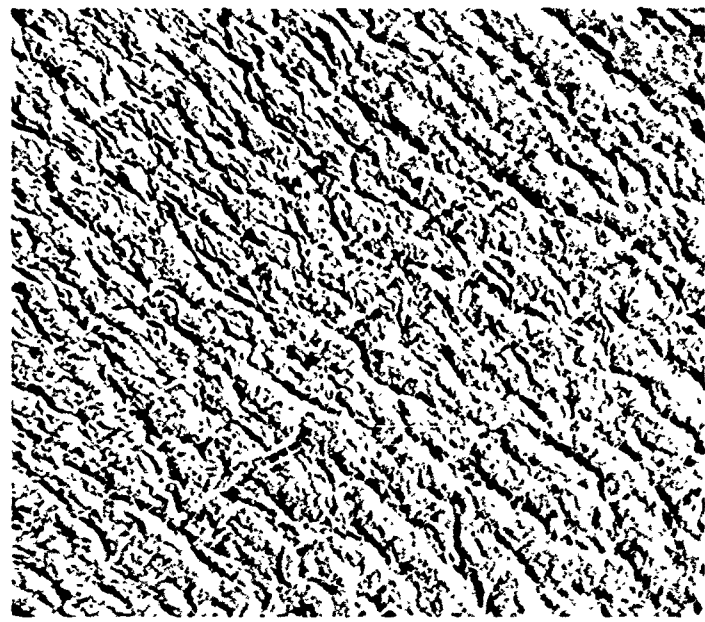


(a) Chromally "E" Boride Coating after 20 min. exposure

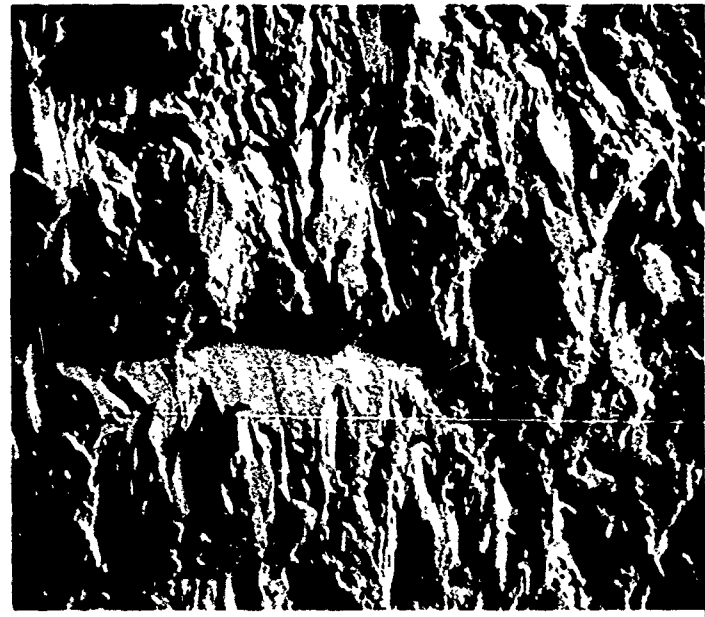


(b) Chromally "E" Boride Coating after 50 min. exposure

Figure 18. Erosion of Tip of Specimen in Sand at 880° ft/sec - 15X



(a) Boride coating before exposure



(b) Boride coating after 50 minutes exposure
to sand erosion at 880 ft/sec.

FIGURE 19. Boride coating on titanium 6Al-4V before and
after exposure to sand erosion SEM-650X



FIGURE 20. Electron micrograph-7000X view of fractured boride coating after 50 minutes exposure to sand particle impact at 880 ft/sec.

TABLE XIII
CHROMALLOY - BORIDE COATING ON Ti-6Al-4V
CUMULATIVE WEIGHT LOSS - MILLIGRAMS

880 ft/sec.

TIME MINUTES	SPECIMEN NO.		
	CAC-B-1	CAC-B-2	CAC-B-3
5	4	3	3
10	16	17	17
20	32	34	31
30	55	56	54
40	77	78	83
50	101	105	128

TABLE XIV

SAND EROSION - NRC BORON CARBIDE COATING ON Ti-6Al-4V

CUMULATIVE WEIGHT LOSS-MILLIGRAMS

880 ft/sec.

TIME MINUTES	SPECIMEN NO.				
	345-1	345-2	345-3	345-4	345-5
1	2	3	3	2	3
3	12	13	12	13	13
5	19	17	17	19	18
10	36	35	33	35	36
15	56	54	53	53	54
20	79	73	71	72	75
25	92	93	95	93	98
30	116	111	115	110	124

A proprietary boron carbide coating varying in thickness from 1.6 to 1.8 mils was applied by a vacuum deposition process to five standard turbine shaped Ti-6Al-4V alloy specimens by the National Research Corporation, Cambridge, Massachusetts. The coating was dark gray, smooth, nonporous and had a Knoop hardness of 3300.

The coating was applied and processed at temperatures below 1000°F which resulted in less than 10% loss in fatigue strength of the titanium alloy and negligible change (5%) to the microstructure and mechanical properties.

The boron carbide coating is relatively inert chemically and under average conditions does not react with the titanium alloy to form a corrosion cell.

The NRC boron carbide exhibited relatively high erosion resistance, however, the character of the erosion was brittle in nature and can be observed in Figure 21. Table XIV outlines the weight lost as a function of time.

Nine specimens of titanium 6Al-4V were nitrided at the Kolene Corporation plant using the "Tiduran" process in which the specimens were immersed in a molten cyanide bath at 1480°F for two hours and quenched. The surface of the nitrided titanium alloy was then shot peened with glass beads to reduce surface stresses.

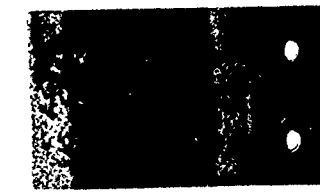
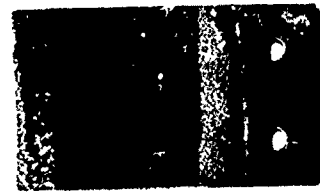
The results of the sand erosion tests on the "Tiduran" nitride coating are outlined in Table XV. The time to lose 100 milligrams in weight was eleven minutes. This time is compared with the other coatings in Figure 17

SAND EROSION TESTS

880 FT/SEC. SPECI MEN VELOCITY

660 FT/SEC. SAND-AIR VELOCITY

2.0 ± 0.1 LBS. SAND/MIN.



SPECIMEN NO.	345-1	345-2	345-3	345-4	345-5
MILLIGRAM WEIGHT LOSS	116	111	115	110	124

Figure 21. NRC Boron Carbide Coating on Ti-6Al-4V After 30 Minutes Exposure

TABLE XV
 SAND EROSION
 TIDURAN PROCESS - NITRIDE COATING ON Ti-6Al-4V
 CUMULATIVE WEIGHT LOSS - MILLIGRAMS

880 ft/sec.

TIME MINUTES	SPECIMEN NO.				
	KTN-1	KTN-2	KTN-3	KTN-4	KTN-5
1	9	7	6	8	7
2	18	15	11	13	12
3	26	24	20	22	20
4	37	33	32	30	29
5	45	42	41	39	38
6	56	50	48	47	46
7	64	59	57	55	54
8	75	67	66	64	64
9	84	74	75	73	72
10	95	82	86	82	81
11	102	91	95	90	90
12	113	100	103	99	98
14	-	-	-	105	96
16	-	-	-	113	110

High hardness coatings (Rockwell C78) consisting of mixtures of carbides and metallics applied by detonation gun process of Union Carbide's Materials Systems Division on Ti-6Al-4V standard test specimens were evaluated for sand erosion.

The following UCAR coatings 4-5 mils in thickness were tested.

1. LS-3 alloy of cobalt, nickel, tungsten, chromium
2. LN-3H 80% Ni- 20% Chromium
3. LW-5 25% WC - 5% Ni - balance tungsten and chromium

These coatings have exhibited good abrasion resistance in many industrial applications involving conditions of severe wear and were recommended for evaluation for impact erosion characteristics.

The influence of surface preparation on the adhesion of these coatings on titanium was evaluated as follows: two specimens of Ti-6Al-4V were coated in the as-received condition and two specimens were abraded with 600 wet and dry extra fine sand-paper just before coating by the UCAR process.

UCAR coating LW-5 was the hardest of the three coatings tested VHN-1075) and it showed brittle fracture on the leading edge of the standard test specimen under 20X and 50X optical microscopic examination during erosion evaluation.

Coatings LS-31 and LN-34 had Vickers hardness numbers of 360 and 700. These coatings did not show brittle fracture but only wear. However, as shown in Table XII the loss in weight due to erosion of the three coatings was not significantly different as the time to lose 100 milligrams ranged from 5-6 minutes.

Comparison of the erosion characteristics between the specimens that were abraded to remove the oxide on the surface of the titanium and the specimens that left the oxide film on the surface before coating with the UCAR materials failed to show any significant difference.

The five mil UCAR coating of alumina sprayed on the test specimens (A-12) and then densified in the isostatic hot press at Bell exhibited very low resistance to sand erosion losing 100 milligrams in 4-5 minutes. This was the poorest of the nine coatings tested for sand erosion resistance.

Two specimens (A-13, A-14) coated with the Bell alumina columbium coating were tested for sand erosion resistance at 880 ft/sec.

Specimen A-13 lost a portion of the outer alumina coating in nine minutes and specimen A-14 lost a portion of the outer coating of alumina in 22 minutes. Figure 22 is a 25X photomicrograph of the eroded areas which appear to have started at microcracks in the surface. The alumina coating on specimen A-13 was 79% dense and on specimen A-14 was 98% dense. Figure 23a is a 110X photomicrograph of a cross section of the two-phase coating of

TABLE XVI
SAND EROSION

UCAR COATINGS ON Ti-6Al-4V
CUMULATIVE WEIGHT LOSS-MILLIGRAMS

LN-3H
880 ft/sec.

TIME MIN.	SPECIMEN NO.			
	LS-31-1	LS-31-2	LS-31-3A*	LS-31-4A*
1	23	29	27	26
3	59	75	73	72
5	100	116	112	115
7	148	157	152	157

TIME MIN.	SPECIMEN NO.			
	LN-3H-1	LN-3H-2	LN-3H-3A*	LN-3H-4A*
1	29	29	27	27
3	65	65	63	66
5	91	96	90	91
7	113	120	113	111

LS-31
880 ft/sec.

TIME MIN.	SPECIMEN NO.			
	LW-5-1	LW-5-2	LW-5-3A*	LW-5-4A*
1	23	24	25	25
3	56	55	60	59
5	82	85	89	86
7	111	118	125	121

A* Specimens abraded before coating.

alumina on the metal substrate. The outer coating of 98% dense alumina is 4 mils thick and the inner layer of alumina particle in columbium matrix is 12 mils in thickness. Figure 23a is an 880X photomicrograph of the outer layer of 98% dense alumina showing the porosity and a typical microcrack.

It is believed if the porosity and microcracks can be reduced by improved processing techniques, a satisfactory sand erosion resistant coating system can be developed that will have little or no effect on the mechanical properties of the titanium alloy.

B. Tests on Airfoil Shaped Specimens

(1) Lead

Because no standard airfoil shaped specimen had been previously selected for the calibration of the sand erosion apparatus, a soft ductile isotropic, target material that would accurately reproduce and retain the craters formed upon impact, without distortion or smearing was desired. The use of soft copper and lead alloys was investigated as a means of observing and recording the nature of the damage resulting from the normal impact of quartz sand particles ranging in size from 5-1000 microns (Mikel's mix).

To determine the ability of the soft metals to accurately reproduce indentations of a solid upon impact a steel punch having a conical shaped point with a 10 mil radius (250 microns) was used to indent the surface of

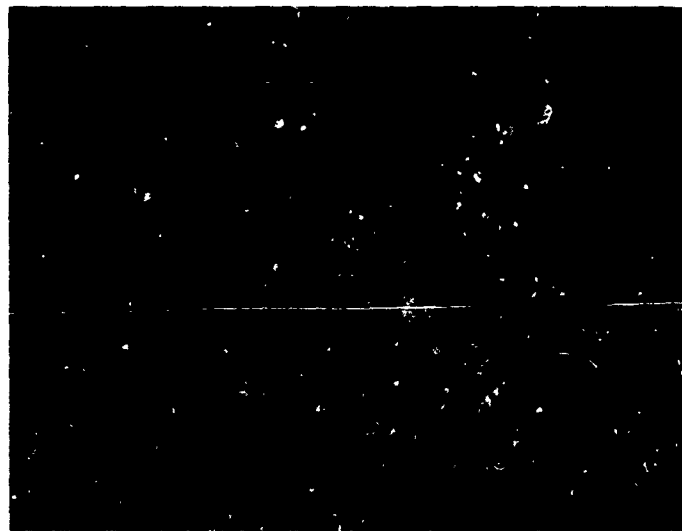
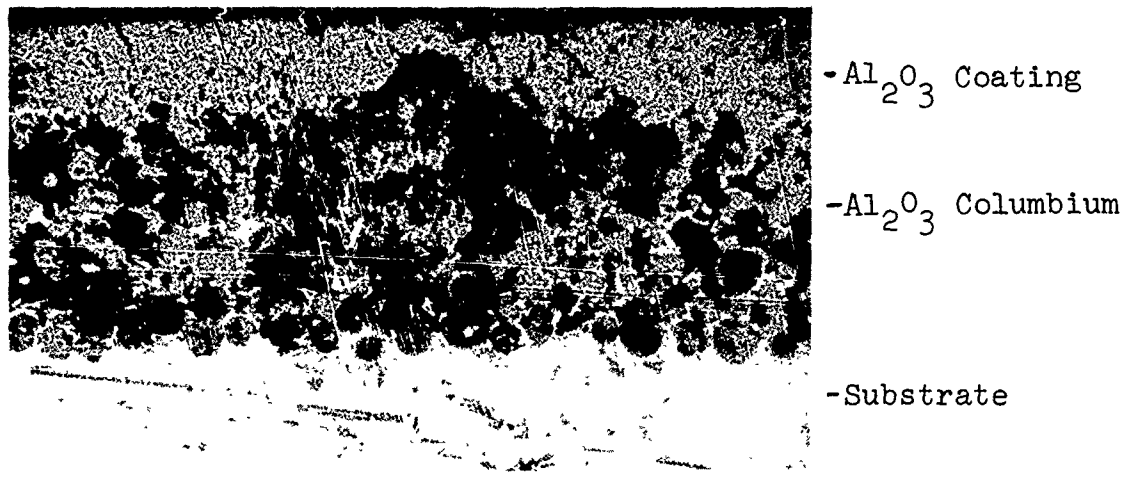
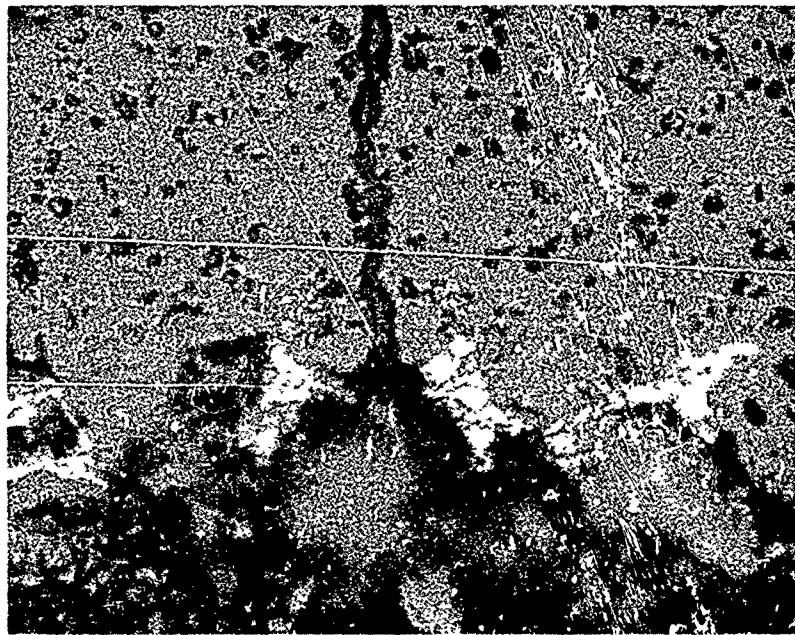


FIGURE 22. Sand eroded areas in alumina coating after
22 minutes of testing at 880 ft/sec -25X



(a) 110X View of alumina coating



(b) 880X View of coating

FIGURE 23. Photomicrographs of Bell alumina coating.

the metal alloy. Microscopic examination of the impression in the surface of two copper and three lead alloys that had been impacted with the steel punch revealed the fact that the lead alloy SAE13 gave the best replication of the conical steel point.

Cast sheets of the SAE13 lead alloy were obtained and erosion test specimens were prepared. The cast sheet of SAE13 lead alloy (85Pb - 10% Sb - 5% Sn) used for preparing the test specimens had an ultimate tensile strength of 9,800 psi, 5% elongation and a Brinell hardness of 19.

The airfoil shaped lead specimens were weighed and exposed to the standard sand environment at a velocity of 880 ft/sec for periods of 10, 30, and 60 seconds.

The general character of the craters or pits formed in the surface of the soft lead by the sand particles after short periods of exposure are shown in Figure 24.

As shown in Figure 25(a) (at 3X magnification) approximately fifty percent of the surface is pitted after 10 seconds exposure.

Additional impacts of sand particles occurring after longer exposure times resulted in the formation of large pits over the entire surface. The original small shallow pits which were formed initially are obliterated or enlarged as shown in Figure 25b and 25c.

SAND EROSION TEST
880 FT/SEC SPECIMEN VELOCITY
660 FT/SEC SAND-AIR VELOCITY
 2.0 ± 0.05 LB SAND/MIN

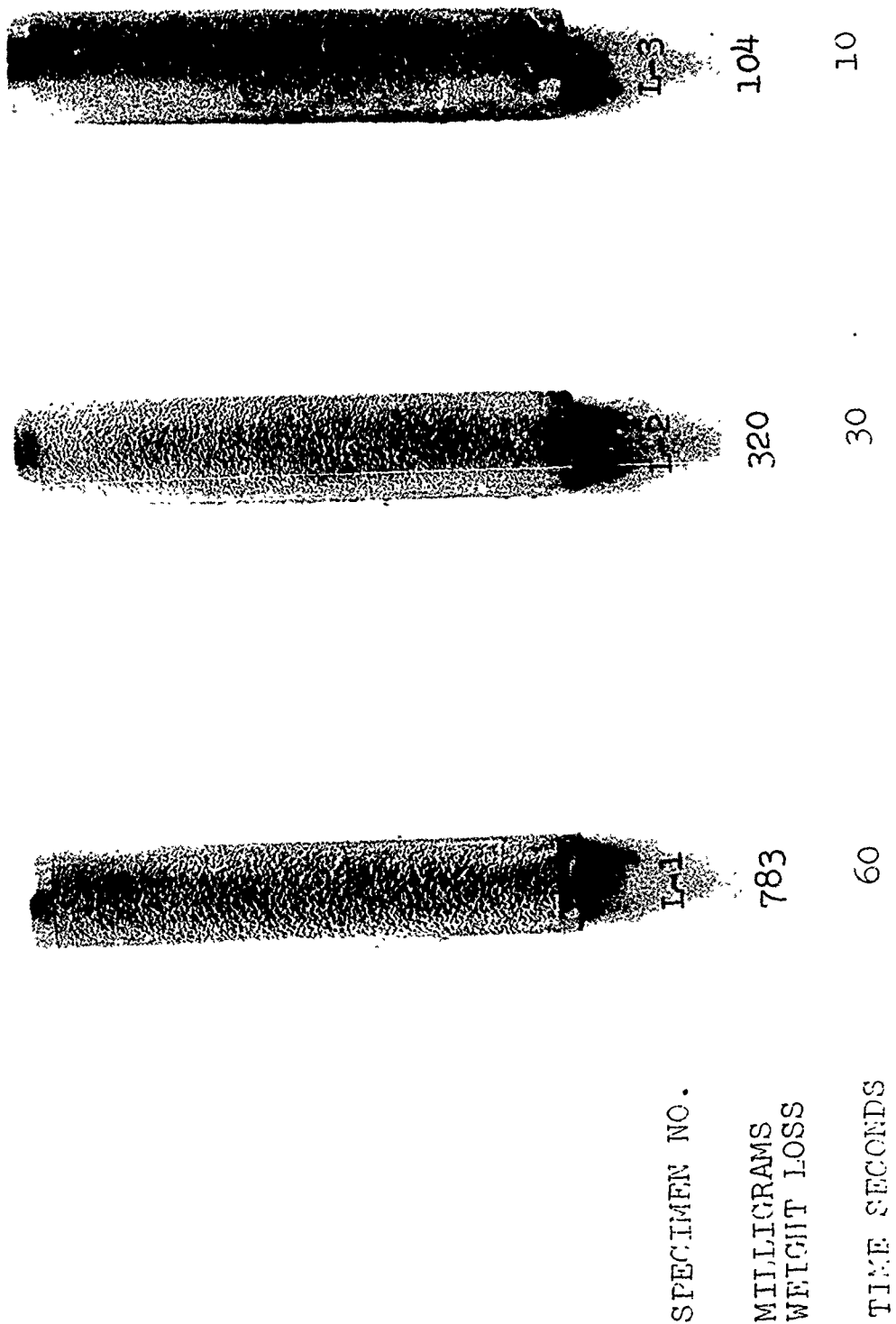
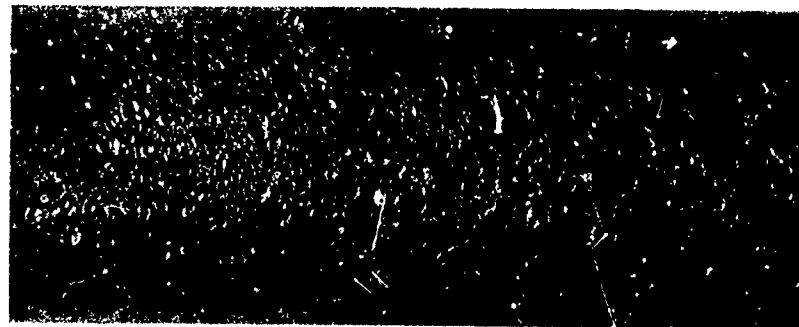


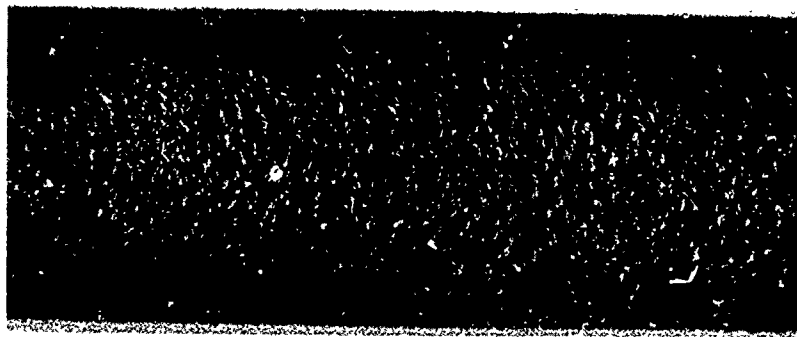
Figure 24. Erosion of Lead



(a) Specimen L-3 - 10 seconds



(b) Specimen L-2 - 30 seconds



(c) Specimen L-1 - 60 seconds

Figure 25. Sand Eroded Surface SAE 13 Lead Alloy
3X Magnification

The weight loss of six lead alloy specimens were determined at 880 ft/sec velocity and the results outlined in Table XVII.

The reproducibility of sand erosion or weight loss at 880 ft/sec specimen velocity and 2 lbs. of sand per minute with the SAE 13 lead alloy is within $\pm 10\%$ of the average value. Therefore, lead can be considered satisfactory as a standard material for the determination of the sand erosion characteristics of an airfoil shaped specimen.

2. Plastics

Two specimens of an AFML fluorocarbon coating 12 mils in thickness on aluminum substrate and heat aged at 400°F for 24 hours were tested. One specimen (FL-1) tested at 880 ft/sec eroded through the coating in 4 minutes. The second specimen FL-2 tested at 1100 ft/sec eroded through the coating in 1.5 minutes in the sand environment.

Airfoil shaped specimens were prepared for ultra high molecular weight polyethylene (Hostalen GUR) received from the Chemical and Plastics Division of American Hoechst Corporation. These specimens were coded MP-1 and 2 and were tested at 880 ft/sec.

Airfoil shaped specimens were machined from a copolymer of acrylic-polyvinyl chloride (Kydex) obtained from Rohm-Haas Company. The specimens were designated K-1, 2 and tested at 880 ft/sec.

TABLE XVII
 SAND EROSION SAE 13
 LEAD ALLOY
 CUMULATIVE WEIGHT LOSS MILLIGRAMS
 880 ft/sec.

TIME SECONDS	SPECIMEN NO.						
	L-1	L-2	L-3	L-4	L-5	L-6	Avg.
10	-	-	104	117	112	125	115
30	-	320	-	284	307	346	314
60	783	-	-	712	810	849	788

These two plastic materials were evaluated because they possess excellent resistance to wear by abrasion, good notched Izod impact properties and are very tough and have excellent stress relaxation properties under high impact rates offering good potential as erosion resistant materials that might be used as coatings.

The surface of the two types of plastic took on a scoured, roughened appearance, after one minute exposure, with only a small weight loss.

After five minutes exposure the weight loss for both types of plastic was approximately two hundred milligrams. After 20 minutes exposure the polyethylene was badly abraded and had lost 890 milligrams. After 15 minutes the acrylic-polyvinyl chloride (Kydex) copolymer was badly eroded and had lost 601 milligrams. Figure 26 shows the plastic specimens after test.

Figure 27a is a 15X photomicrograph of the surface of the acrylic-polyvinyl chloride surface after one minute of test. Figure 27b shows the surface after 15 minutes of erosion in sand and Figure 28 is a 160X SEM of the surface which has been highly abraded by sand particles.

Because the two plastic materials had a relatively high rate of sand erosion compared to nickel which is a good coating material, these plastics were not evaluated further.

Figure 29 graphically illustrates the high sand erosion rates of polyethylene and the acrylic copolymer.

SAND EROSION TEST

880 FT/SEC SPECIMEN VELOCITY

660 FT/SEC SAND-AIR VELOCITY

2.0 ± 0.05 LB SAND/MIN

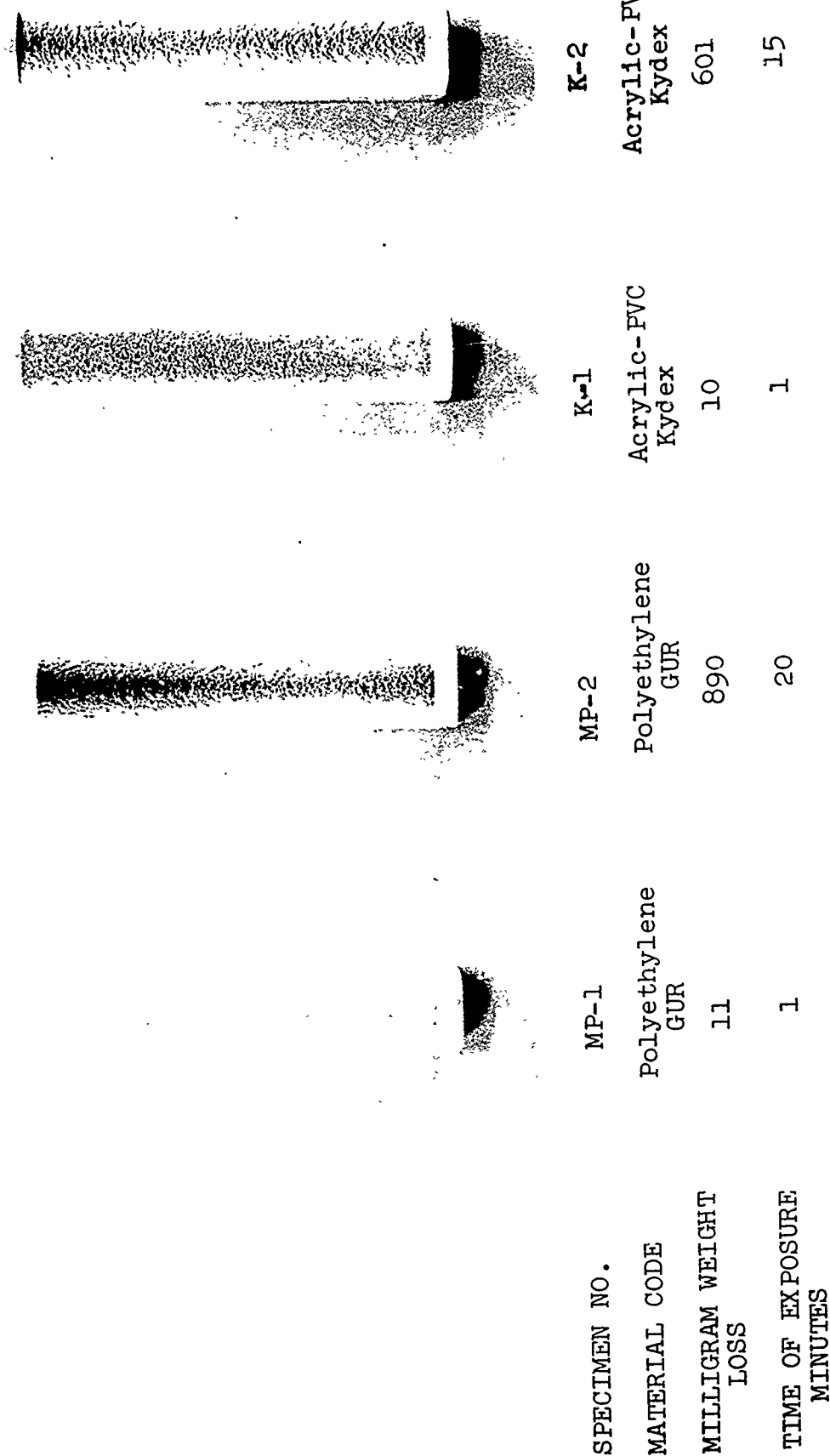
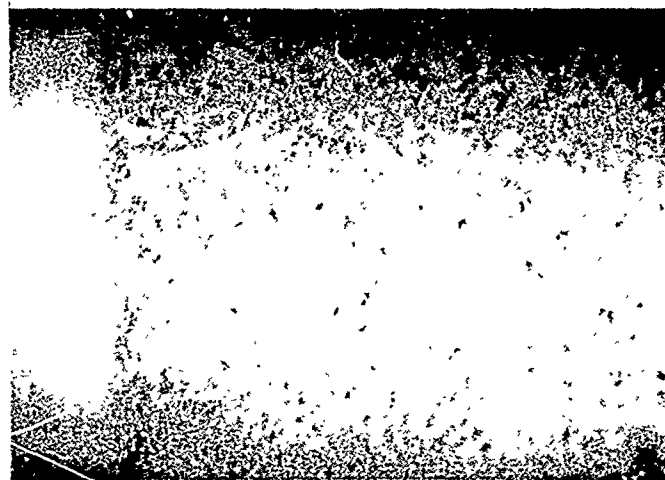
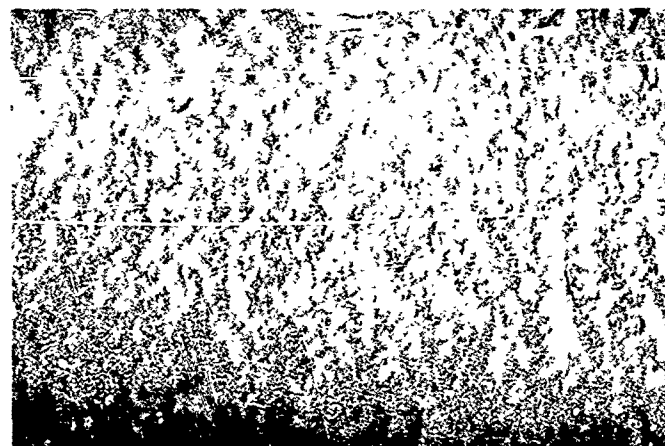


Figure 26. Erosion of Plastic Materials



(a) Surface of Kydex after 1 min. exposure - 15X



(b) Surface of Kydex after 15 min. exposure - 15X

FIGURE 27 Sand Erosion of Bulk Polymer (Kydex) at 880 ft/sec velocity.

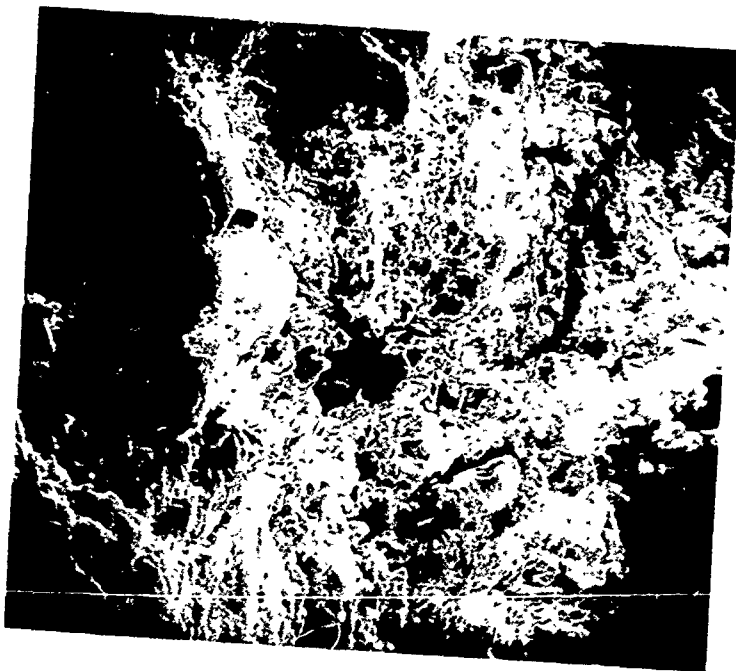


FIGURE 28 Scanning electron micrograph at 160X showing damage to surface of bulk polymer (Kydex) after 15 minutes exposure to sand erosion at 880 ft/sec.

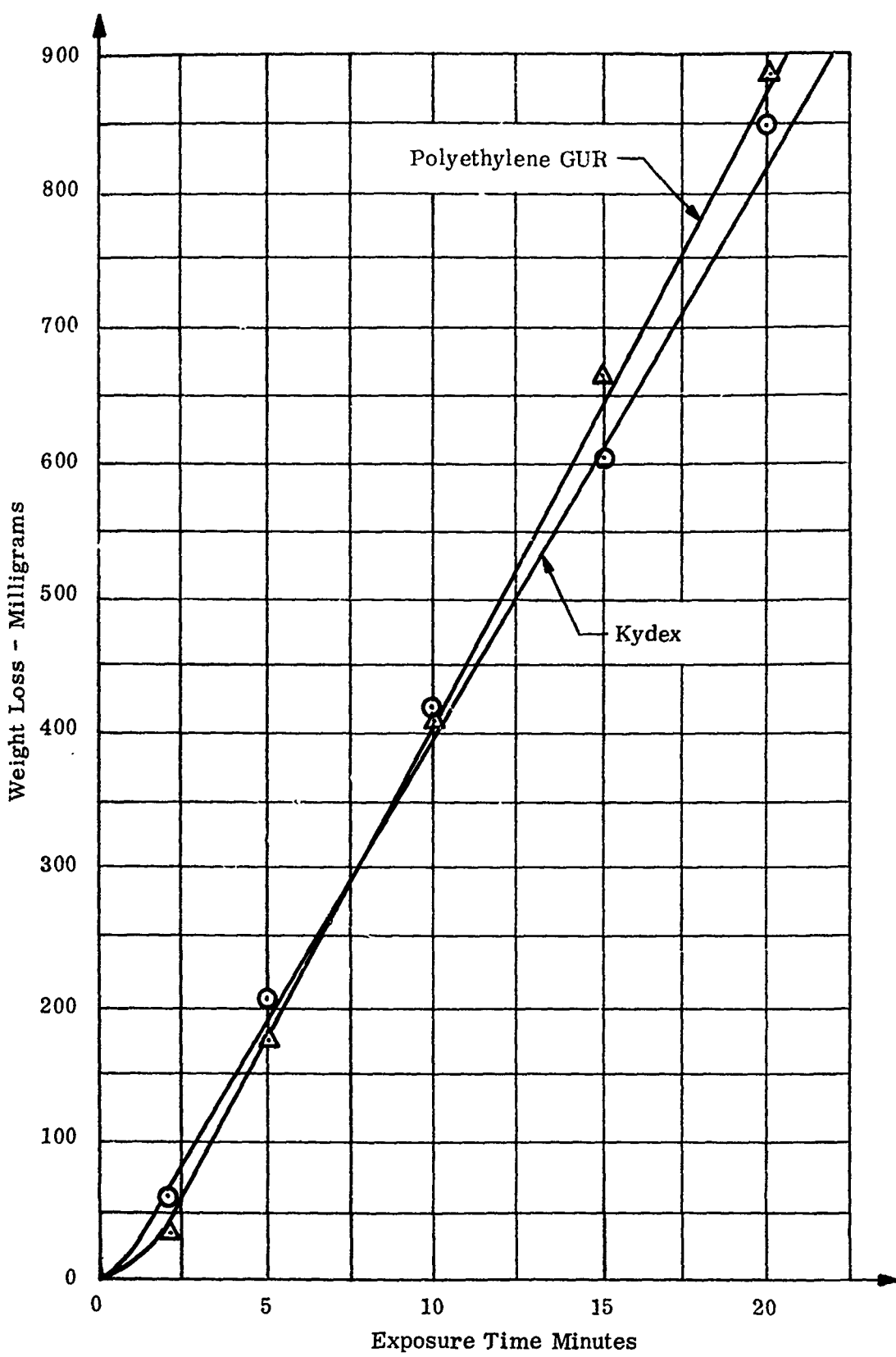


Figure 28. Rate of Sand Erosion of Materials at 880 ft/sec

3. Ceramics

Two ceramic materials, high density alumina and Pyroceram 9606 have exhibited satisfactory resistance to rain erosion but as far as it is known have not been evaluated for sand erosion. These materials were tested in the bulk to determine their relative sand erosion resistance.

Airfoil shapes of high density (99.5%) alumina 753 from American Lava Corporation were coded AL-6, 7, 8. A sample of Pyroceram 9606 from Corning Glass Company was designated PC-10.

These four ceramic specimens were tested at 1100 ft/sec.

The airfoil shaped specimens of alumina 753 tested at 1100 ft/sec exhibited very low rates of sand erosion as shown in Figure 30.

The samples of Pyroceram 9606 eroded very rapidly. After one minute the specimen had lost 342 milligrams and after five minutes had lost 2516 milligrams. The typical appearance of the eroded ceramics are shown in Figure 31.

4. Coatings

Airfoil shaped 181-glass fabric-phenolic laminate specimens coated with electroplated nickel by AFML personnel were tested at 770 ft/sec (530 mph) and 1100 ft/sec (Mach 1) in sand environment as requested.

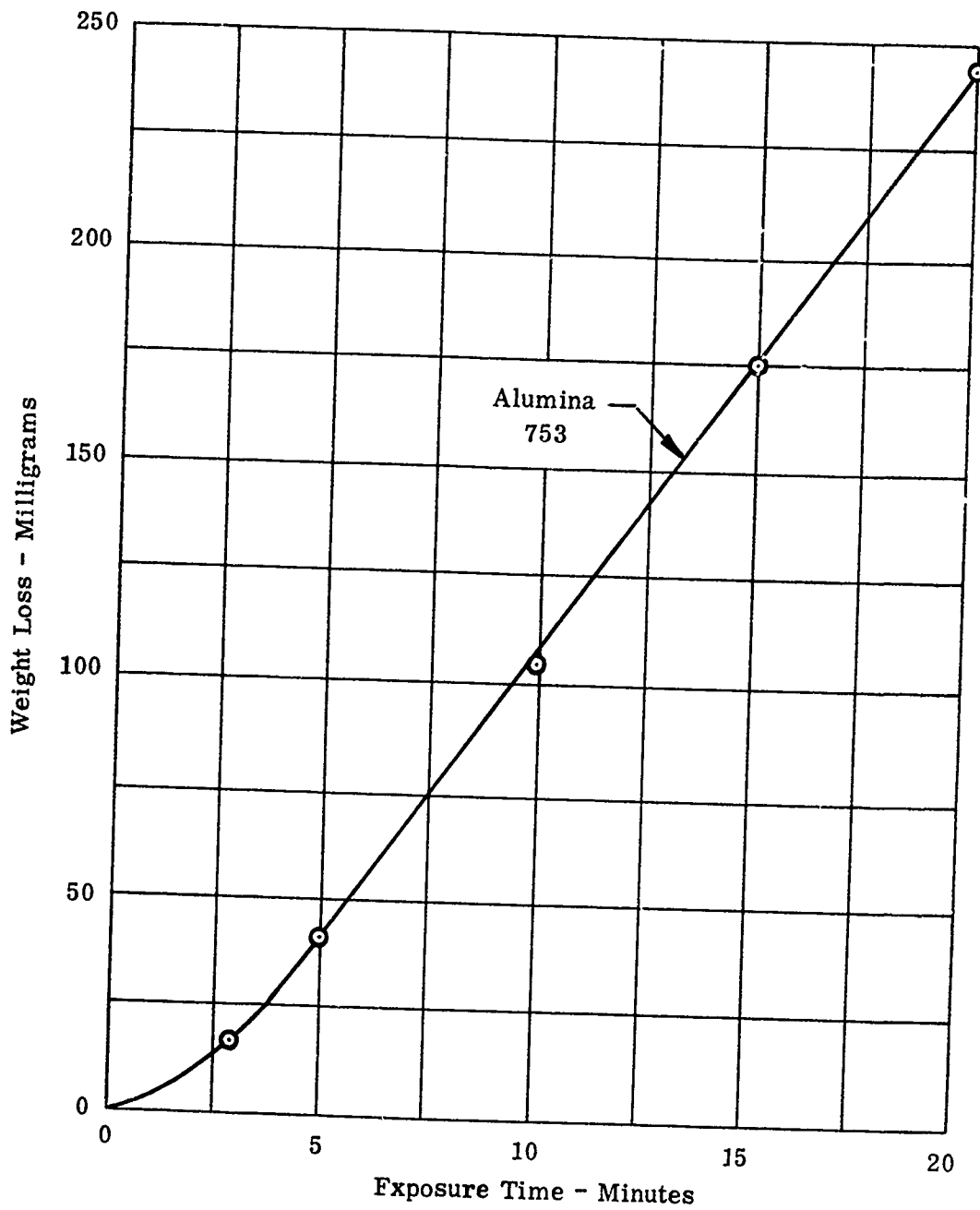


Figure 30. Rate of Sand Erosion of Alumina - Alsiniag 753 at 1100 ft/sec

SAND EROSION TEST
1170 FT/SEC SPECIMEN VELOCITY
660 FT/SEC SAND/AIR VELOCITY
 2.0 ± 0.05 LB SAND/MIN

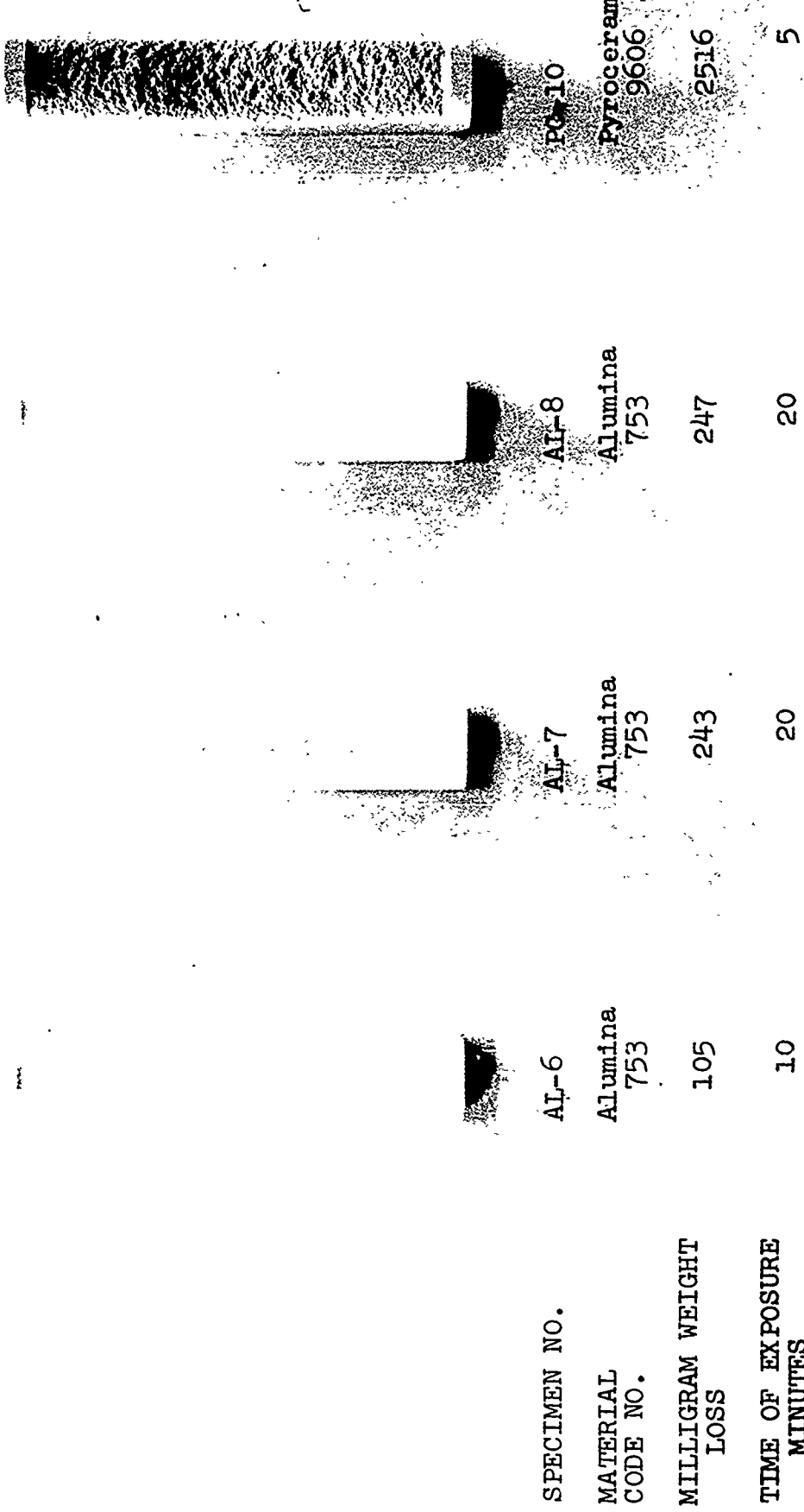


Figure 31, Erosion of Ceramic Materials

Two specimens (N-3 and N-4) one having a rough nickel surface (N-3) and one having a highly polished nickel surface (N-4) both having a coating thickness of 13 mils were compared for relative erosion resistance.

Specimen N-3 having the rougher surface lost 446 milligrams in weight compared to the smooth surfaced specimen N-4 which lost 587 milligrams. Both were exposed to sand environment at 1100 ft/sec for three minutes.

The nickel coatings all exhibited a wrinkling phenomenon. It was observed that the pattern of the wrinkles occurring at 770 ft/sec had a greater distance between the crest of the wrinkles as compared to the distance between the wrinkles occurring on the specimens tested at 1100 ft/sec. The reason for the wrinkling and different pattern at various speeds cannot be adequately explained at this time, but it was considered that the plastic flow was due to the combined effects of deformation by solid impact, centrifugal force and temperature of the coating.

Specimen N-5 tested at 770 ft/sec had a coating 18 mils in thickness that exhibited less wrinkling and weight loss than specimen N-2 which only had a 10 mil nickel coating.

Figure 32 illustrates the typical wrinkling and erosion observed with the nickel coating on glass laminate specimen.

SAND EROSION TESTS

770 or 1100 ft/sec Specimen Velocity

660 ft/sec Sand-Air Velocity

2.0 ± 0.05 lb Sand/Min

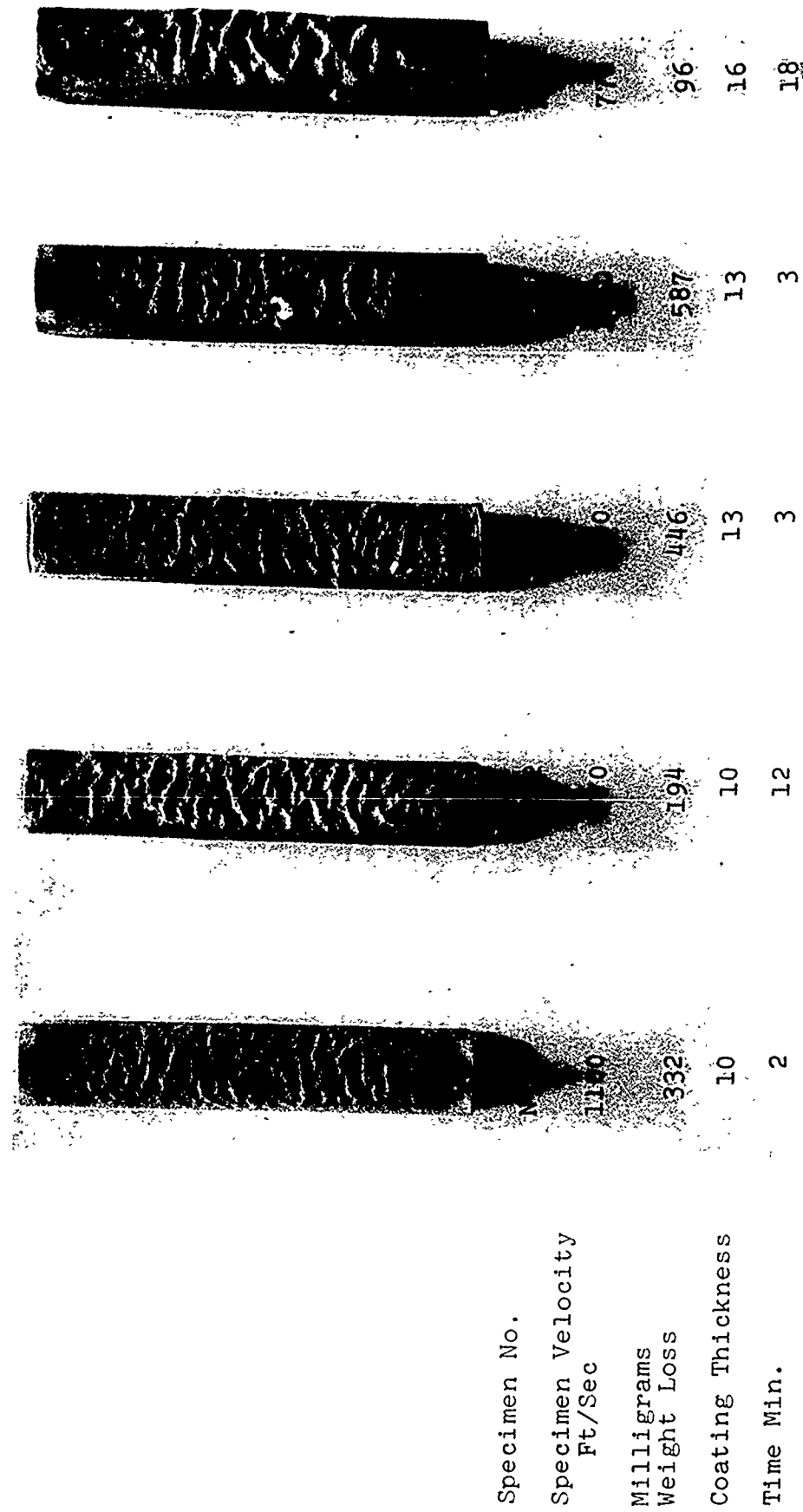


Figure 32 Erosion of Electroplated Nickel on Fiberglass Laminate

Ten airfoil shaped specimens of aluminum alloy 2024-T6 were coated with an 18 mil coating of Astrocoat polyurethane composite coating designed for sand erosion by Olin Research Center, New Haven, Connecticut.

Five of these specimens were tested for sand erosion at 880 ft/sec. until the coating eroded through in several spots. The time of exposure to sand erosion ranged from 12-18 minutes and the total weight loss noted.

Figure 33 shows how the coating eroded through in several spots on the leading edge of the specimens.

Microscopic observation of the surface of the composite polyurethane coating during tests showed that the coating was scouring off as if it were being abraded by sandpaper.

The surfaces of the polyurethane coating were roughened and exhibited microscopic tears. The tears would increase in length and width until several tears intersected at which time small chunks of rubber were removed from the coating surface forming a very pitted surface.

This removal of rubber and pitting increased until the coating was eroded through.

SAND EROSION TESTS

880 FT/SEC. SPECIMEN VELOCITY

660 FT/SEC. SAND-AIR VELOCITY

2.0 ± 0.1 LBS. SAND/MIN

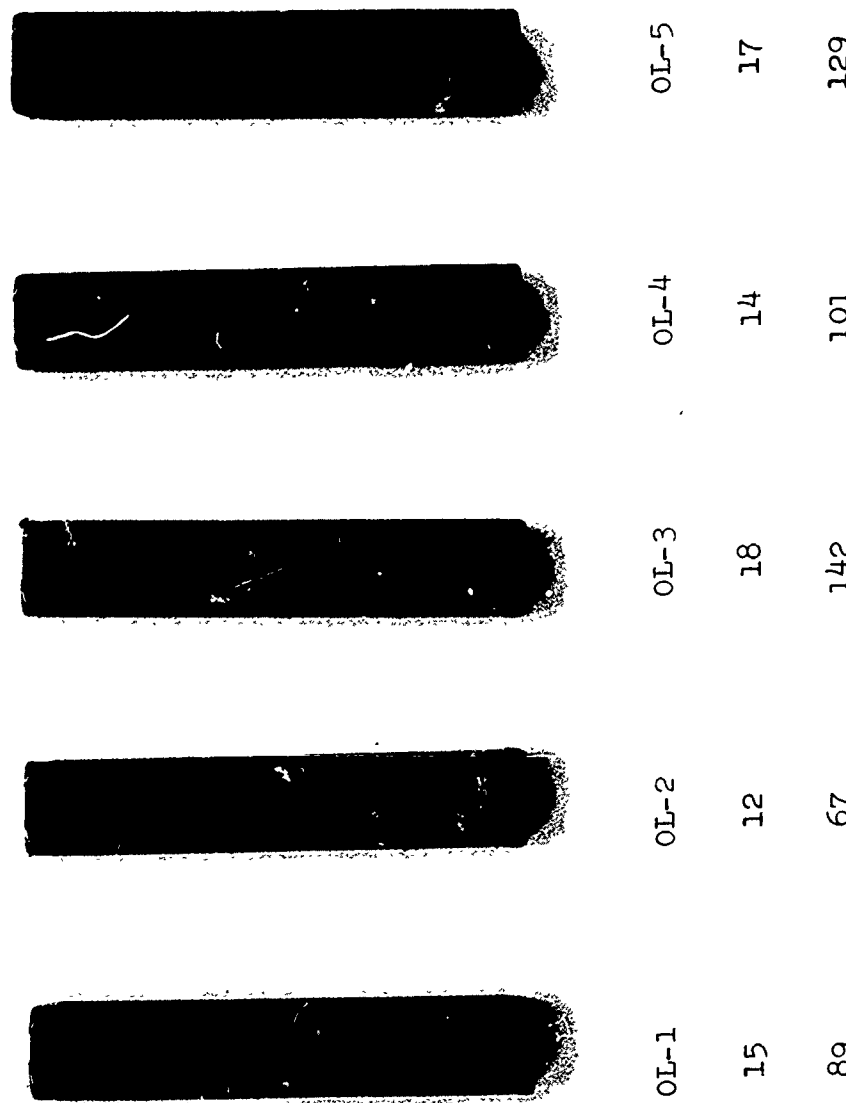


Figure 33 Astrocoat-Composite Polyurethane Coating System for Sand Erosion -
18 Mil Thickness on Aluminum Substrate

VII. MATERIALS CHARACTERIZED FOR RAIN EROSION BEHAVIOR

The following materials were tested at 730 ft/sec and/or at 1120 ft/sec in rainfall concentration of one inch/hr.

1. Aluminum Oxide Coatings
2. Nickel
3. AFML fluorocarbon coating
4. Polymers
5. Reinforced composites

1. Aluminum Oxide Coatings

Modified aluminum oxide (Al_2O_3) coatings, 20 mils in thickness, applied to two types of substrates (glass reinforced laminates and aluminum) were received from Georgia Institute of Technology for evaluation in a rain environment.

The coatings were applied by plasma spray and slip cast techniques and were identified as follows:

- (1) Six plasma sprayed alumina, epoxy impregnated coatings on 2024-T6 aluminum substrate.
- (2) Six, plasma sprayed aluminum oxide, polyimide impregnated coatings on polyimide/fiberglass laminate.
- (3) Six, slip cast aluminum oxide, epoxy impregnated caps on phenolic/fiberglass laminates.

These specimens were tested in 1" hour rainfall at 730, 880 and 1120 ft/sec velocity.

2. Nickel

Five airfoil shaped specimens of annealed nickel (Inco 270) were tested in standard rainfall of 1"/hr and 1120 ft/sec (Mach 1) velocity to aid in the study of the mechanism of erosion of ductile metals. The nickel containing 270 ppm of other metals is for all practical purposes pure nickel. The nickel had an ultimate tensile strength of 48,000 psi, 30% elongation and a Vickers hardness number of 160.

3. AFML Fluorocarbon coating

Sixteen specimens of AFML fluorocarbon coatings were applied to aluminum and glass reinforced substrates by AFML personnel.

Eight airfoil shaped 2024-T6 aluminum specimens were coated with 12 mil thickness of fluorocarbon coating. Four specimens had only room temperature cure (RT) and four were heat aged at 400°F for 24 hours.

Eight air foil shaped 181 glass fiber reinforced epoxy laminates were prepared by AFML, four of Type I and four of Type II coating. Two specimens were cured at 400°F for 24 hrs. and two for 100 hours at 400°F.

The fluorocarbon coatings on aluminum substrate were compared with polyurethane coating (Astrocoat 115P) and neoprene (Goodyear 1801-C) on aluminum substrate at 1"/hr rainfall and velocities of 730 and 1120 ft/sec.

The fluorocarbon coatings on glass fiber laminate were tested at 1"/hr rainfall and a velocity of 730 ft/sec.

4. Polymers

Two approaches to the determination of the resistance to wear and abrasion, caused by the high velocity impacts of small solid or liquid particles, on thermoplastic polymeric coating materials involves the following:

- (1) application of the coatings to a substrate and a comparison of the erosion characteristics
- (2) evaluation of relative resistance to erosion of the bulk material that might be used as a coating.

Each approach has merit; the first, takes into account factors such as adhesion, thickness of coating, methods of coating, effect of substrate support, etc. The second directly measures the relative resistance to impact erosion and deftly side-steps the complicating factors noted in the first approach.

Method (2) was selected for the rapid evaluation of the following thermoplastic polymeric materials that possessed outstanding abrasion, impact and wear resistance and offered a potential reduction in the erosion rates.

Oberst (20) in his report on rain erosion suggests that the erosion resistance of polymers is related to their viscoelastic properties and notched impact strength. He strongly implies that thermoplastic materials such as high molecular weight polyethylene which will not break in a standard Izod test (greater than 32 ft. lb/in. notch) should exhibit the ultimate in rain erosion resistance. With this in mind the following polymers which are regarded as extremely tough, wear resistant and having relatively high impact strengths were evaluated for relative rain erosion resistance at 730 and 1120 ft/second.

<u>TRADE NAME</u>	<u>SOURCE</u>	<u>CHEMICAL TYPE</u>
HOSTALGEN GUR	American Hoechst Corp.	ULTRA HIGH MOLECULAR POLYETHYLENE
KYDEX	Rohm & Haas	ACRYLIC POLYVINYL-CHLORIDE
LEXAN	General Electric	POLYCARBONATE
ASTREL 360	3M	POLYARYLSULFONE
ZYTEL-7110-13	DuPont	GLASS FILLED NYLON
NORYL 731	G. E.	MODIFIED POLYPHENYLENE OXIDE
NORYL GFN-3	G. E.	GLASS FILLED PPO
DELRIN 550	DuPont	ACETAL
WINTHANE 121, 134	Winthane Chemical Ind.	ETHER BASE POLYURETHANE
WINTHANE 612	Winthane Chemical Ind.	ESTER BASE POLYURETHANE

5. Reinforced Composites

Samples of unidirectional, end oriented, glass fiber-epoxy composite bar stock $1/2 \times 1/2 \times 3"$ long were obtained from UniRoyal and machined into standard hemi-cylinder airfoil shaped test specimens with the fibers end-oriented to the leading edge.

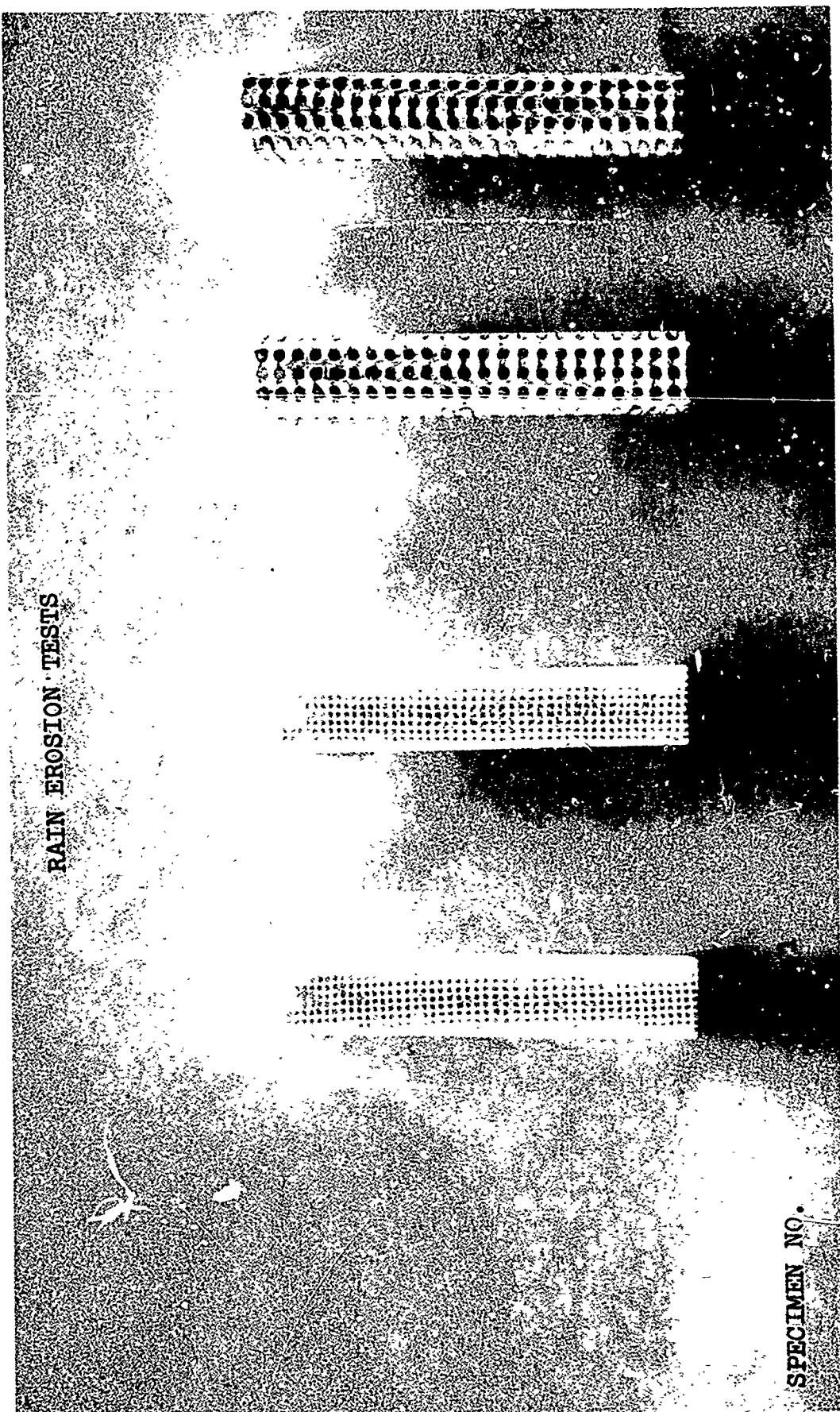
These specimens were compared for rain erosion resistance with standard airfoil shaped test specimens molded from 181 glass-epoxy laminates by the University of Dayton.

The end oriented glass fiber epoxy specimens were mounted so that the fibers were parallel to the plane of rotation of the blade.

Four specimens of 3D silica fiber reinforcement with silica binder were received from Philco-Ford Corporation for evaluation of their rain erosion resistance. The four specimens were not identified as to reinforcement configuration or binder content.

Two specimens numbered 108-6-1 and 108-6-2 had relatively fine fibers with a close 3D woven structure and specimens numbered 1855-57-1 and 1855-57-2 had coarse fibers with an open 3D woven structure. The nature of the specimens before testing shown in Figure 34.

Figure 34 Philco-Ford - 3D - Silica - Silica Fiber Composite
Specimens Before Test



VIII. RESULTS OF RAIN EROSION TESTS

1. Aluminum Oxide Coatings

The results of the tests on aluminum oxide coatings applied to aluminum and glass fabric reinforced laminates by Georgia Institute of Technology personnel indicate the importance of adhesion of coatings to a substrate and the general random failure that is experienced with a brittle coating material during water drop impingement at velocities of 730 ft/sec or above.

The plasma sprayed alumina on aluminum substrate when tested at 730 ft/sec exhibited fairly uniform erosion and weight loss for specimens 5-71-2 and 5-71-3; as outlined in Table XVIII.

During observation of specimen 5-71-2 in the T.V. monitor a fracture of the plasma sprayed coating was observed after 46 minutes and due to lack of adhesion of the coating a portion was lost at the tip as shown in Figure 35. Specimen 5-71-3 lost 70 milligrams after two hours of testing and exhibited fairly deep pits in the surface.

Two of the four specimens of plasma sprayed alumina on aluminum tested at 1120 ft/sec velocity showed fairly uniform erosion rates for the first eight minutes as shown in Table XIX, but during the next two minutes random large pieces of the coating were lost.

TABLE XVIII
PLASMA SPRAYED ALUMINA ON ALUMINUM
CUMULATIVE WEIGHT LOSS - MILLIGRAMS

730 ft/sec

TIME MINUTES	SPECIMEN NO.	
	5-71-2	5-71-3
3	5	6
5	12	17
10	16	20
15	18	21
25	20	23
40	23	25
60	-	26
80	-	30
100	-	47
120	-	70

TABLE XIX
PLASMA SPRAYED ALUMINA ON ALUMINUM
CUMULATIVE WEIGHT LOSS - MILLIGRAMS
1120 ft/sec

TIME MINUTES	SPECIMEN NO.			
	5-71-4	5-71-8	5-71-10	5-71-11
1	fractured	8	14	10
3	-	23	41	29
5	-	87	97	fractured
8	-	120	143	-
10	-	817	1274	-

Figure 35 Plasma Sprayed Alumina on Aluminum Substrate

SPECIMEN NO. 6-71-2
TIME OF EXPOSURE
MINUTES 100



After 30 seconds of testing a fracture was observed in the alumina coating on specimen 5-71-4 and a large portion of the coating lost adhesion. Specimen 5-71-11 began to erode uniformly but the coating fractured after 4.9 minutes of testing and was lost from most of the specimen surface as shown in Figure 36.

The four specimens of plasma sprayed alumina on polyimide glass fabric laminate exposed to rain at 730 ft/sec fractured after test periods ranging from 1.2 to 6 minutes. The fractured coatings lost adhesion with subsequent loss of portions of the coating as shown in Figure 37.

Weight losses of the polyimide and phenolic resin glass fabric reinforced laminates could not be successfully obtained because the laminates absorbed varying amounts of water during testing resulting in very drastic variations in weight changes.

Two of the plasma sprayed alumina specimens on polyimide glass laminates were tested in rain at 1120 ft/sec. After 12-15 seconds the coatings fractured and the coating lost adhesion and were completely removed after 18 seconds at which time the test was stopped.

Six slip cast alumina specimens on phenolic glass laminate were tested, two at each of three velocities 730, 880 and 1120 ft/sec.

RAIN EROSION TESTS
1 INCH/HR RAINFALL - 1.8 MM DROP SIZE
1120 FT/SEC - (MACH 1)

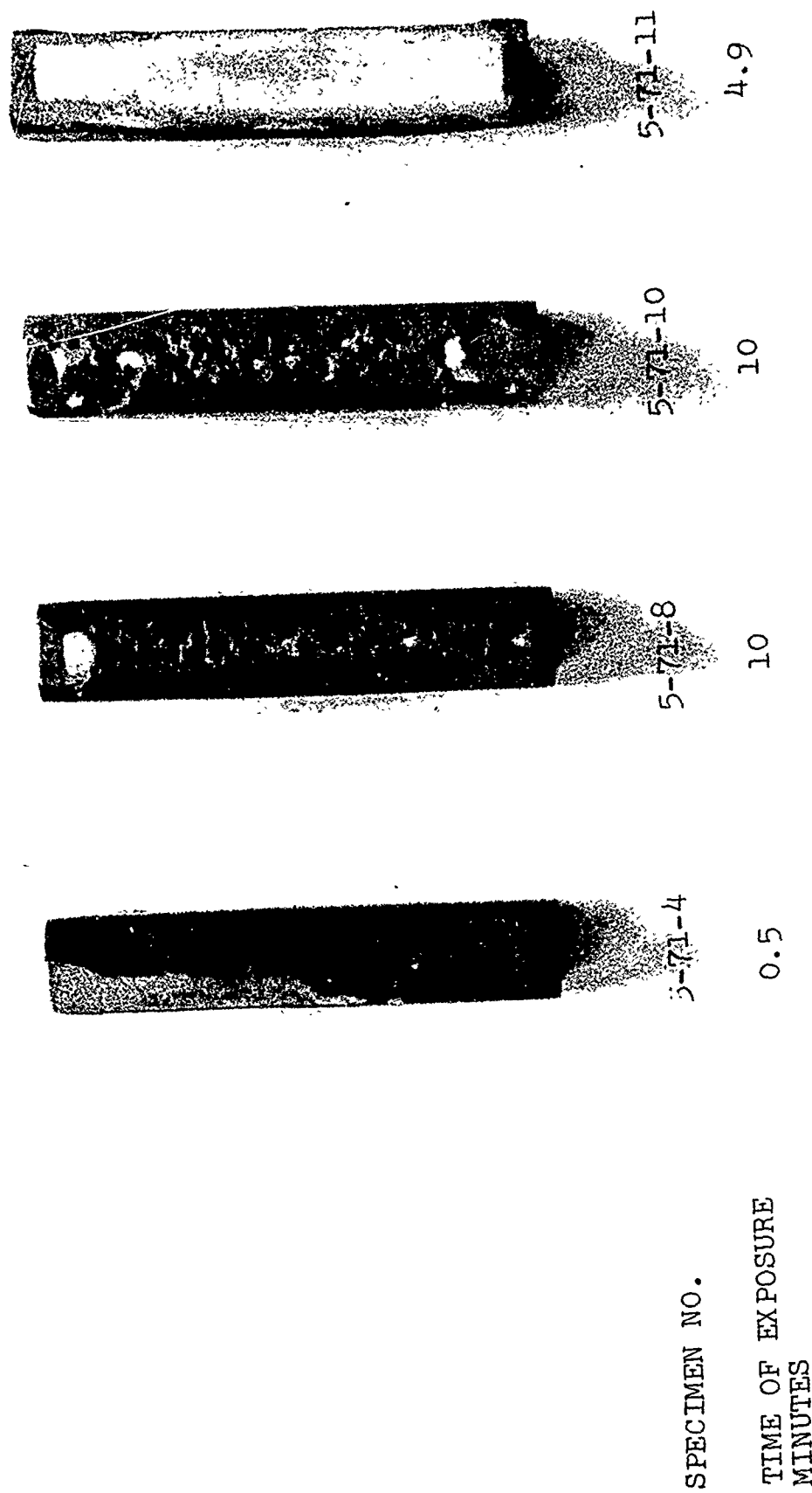


Figure 36. Plasma Sprayed Alumina on Aluminum Substrate

RAIN EROSION TESTS
1 INCH/HR RAINFALL - 1.8 MM DROP SIZE
730 FT/SEC VELOCITY

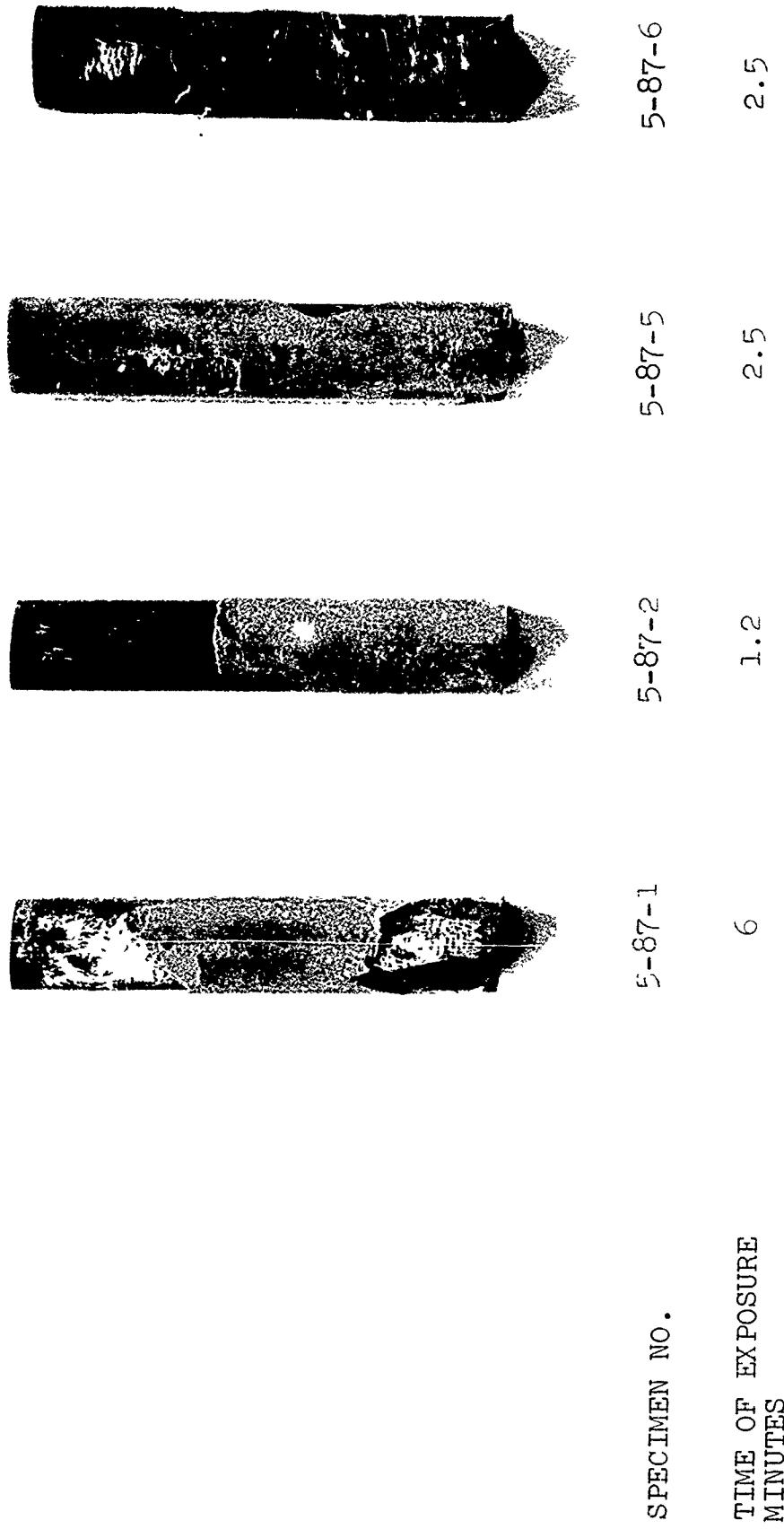


Figure 37. Plasma Sprayed Alumina on Polyimide-Glass Fabric Substrate

Because these coated laminate specimens absorbed water at varying rates, weight increases were noted after each test exposure. Actual weight loss data due to erosion of the alumina coating were therefore not obtained.

After two hours exposure to 730 ft/sec velocity in standard rainfall the surface of the slip cast alumina coating was only slightly roughened and pitted.

Exposure to standard rainfall at 1120 ft/sec of the slip cast alumina caused roughening and the formation of several large pits after one and two minutes. The nature of the pitting is shown in Figure 38.

Rain erosion tests on the slip cast alumina at 880 ft/sec indicated that a considerable amount of pitting occurred on specimen 2-107-12 after 19.7 minutes and pitting and microcracking of the alumina on specimen 2-107-11 after 28 minutes. The nature of the pitting in the alumina is shown in Figure 39.

The results of all the tests on aluminum oxide coating are summarized in Table XX.

These tests indicate that for velocities up to Mach 1 and at normal angles of incidence, the alumina shows considerable promise as a nonmetallic coating for rain erosion resistance.

RAIN EROSION TESTS
1 INCH/HR RAINFALL - 1.8 MM DROP SIZE
730 AND 1120 FT/SEC VELOCITY

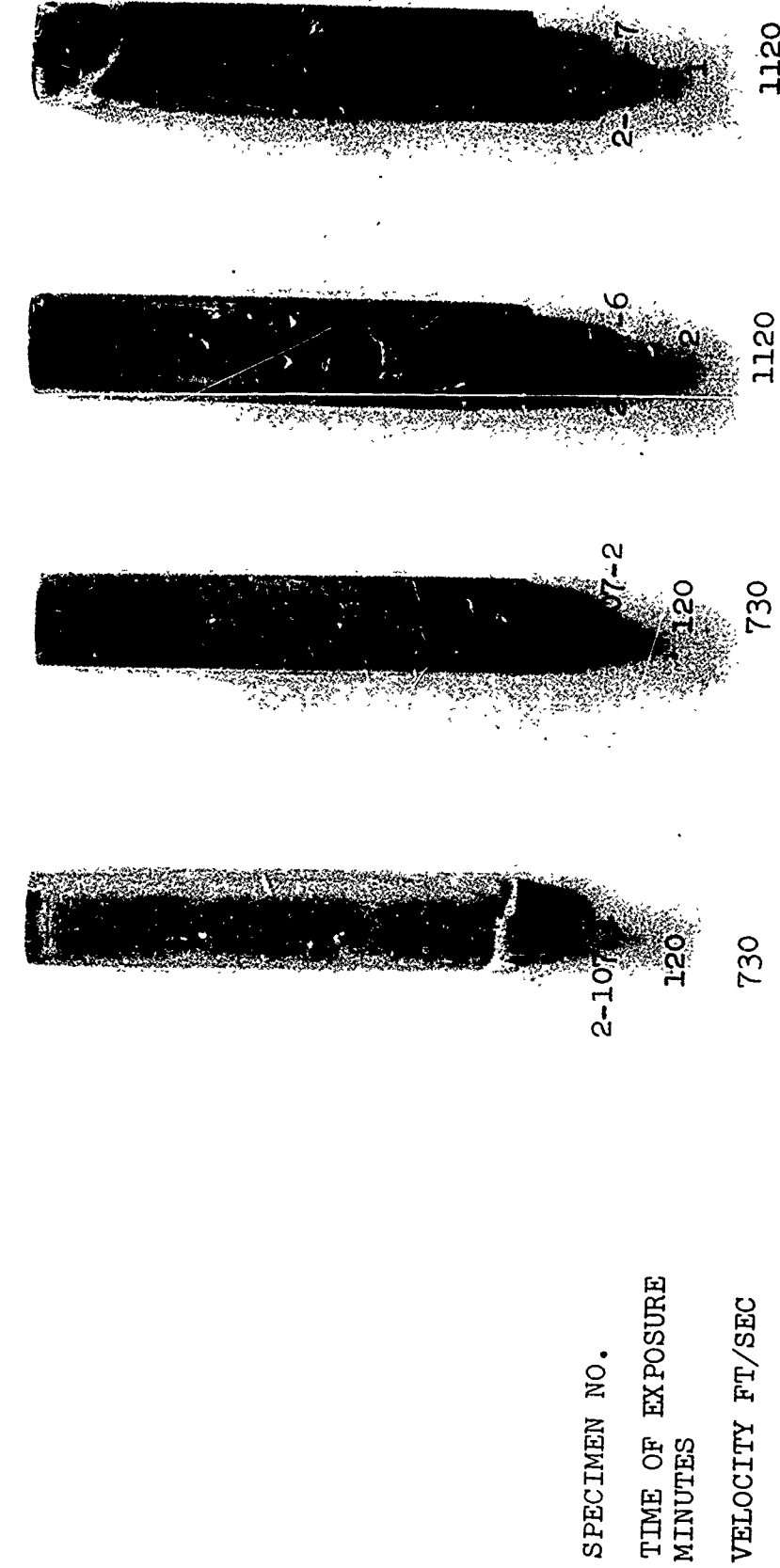
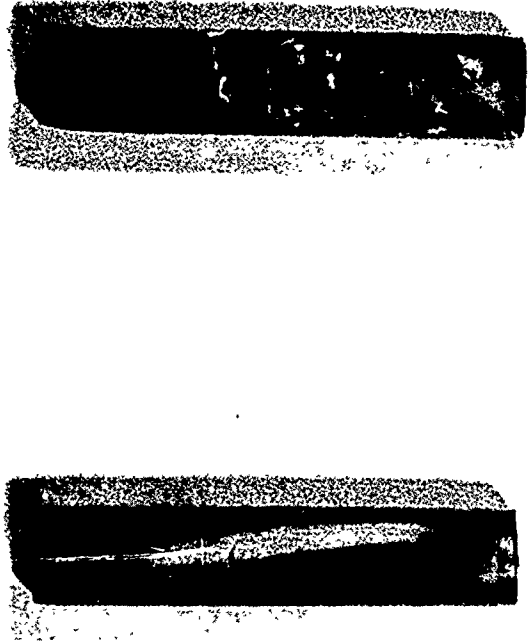


Figure 38 Slip Cast Alumina on Glass Reinforced Phenolic Substrate

RAIN EROSION TESTS

1 INCH/HR RAINFALL - 1.8 MM DROP SIZE
880 FT/SEC (600 MPH)



SPECIMEN NO.	2-107-11
TIME OF EXPOSURE	
MINUTES	28
	19.7

Figure 39 Slip Cast Alumina on Glass Reinforced Phenolic Substrate

TABLE XX
RAIN EROSION TESTS ON ALUMINA COATING

<u>PLASMA SPRAYED ON ALUMINUM</u>			
<u>Bell Specimen No.</u>	<u>Test Velocity Ft/sec</u>	<u>Time of Test Min.</u>	<u>Remarks</u>
5-71-2	730	46	Surface pitted coating fractured on end
5-71-3	730	120	Surface roughened
5-71-4	1120	0.5	Coating fractured lost adhesion on 30% of area
5-71-8	1120	10	Surface roughened after 5 min.
5-71-10	1120	10	No pits 1st pit through alumina in 8 min.
5-71-11	1120	4.9	Coating fractured and lost adhesion

<u>PLASMA SPRAYED ON POLYIMIDE LAMINATE</u>			
5-87-1	730	6	Coating fractured 4.5 min.
5-87-2	730	1.2	Coating fractured and lost adhesion
5-87-3	1120	0.3	Coating completely lost
5-87-4	1120	0.3	Coating completely lost
5-87-5	730	2.5	Coating fractured
5-87-6	730	2.5	Coating fractured and lost adhesion

<u>SLIP CAST ON PHENOLIC LAMINATE</u>			
2-107-1	730	120	Trace surface roughness
2-107-2	730	2	
2-107-6	1120	2	2 pits in coating
2-107-7	1120	1	Microcracks
2-107-11	880	28	Pitting & microcracks
2-107-12	880	19.7	Large Pits

2. Nickel

Five specimens of annealed pure nickel (Inco 270) were tested in standard rainfall of 1"/hr and 1120 ft/sec and the weight losses determined as noted in Table XXI. A plot of cumulative weight loss of the nickel as a function of time is shown in Figure 40. Erosion of these nickel specimens will be discussed in the section on mechanism of erosion.

3. AFML Fluorocarbon Coating

Four AFML fluorocarbon coatings on an aluminum substrate were tested in standard rainfall at 730 ft/sec until one or more pits had eroded through the 12 mil coating. Typical erosion patterns and pits occurring after exposure periods ranging from 10-13 minutes are shown in Figure 41.

A comparison of the erosion damage and typical times to erode through 12 mil coatings of the AFML fluorocarbon coating, 1801-C neoprene and 115P polyurethane on alumina substrate at 730 and 1120 ft/sec are shown in Figures 42 and 43. Eight specimens of AFML fluorocarbon coatings on 181-glass fabric-epoxy laminate were tested at 730 ft/sec in 1"/hr rainfall.

Four specimens had Type I radome coating applied. Two specimens had been heat aged for 24 hours at 400°F and two specimens had been heated for 100 hours at 400°F.

Specimens FI-5 and FI-6 heat aged for 24 hours eroded through the 11.5 mil coating after twelve minutes of exposure to rainfall. Specimens FI-7 and FI-8 heat

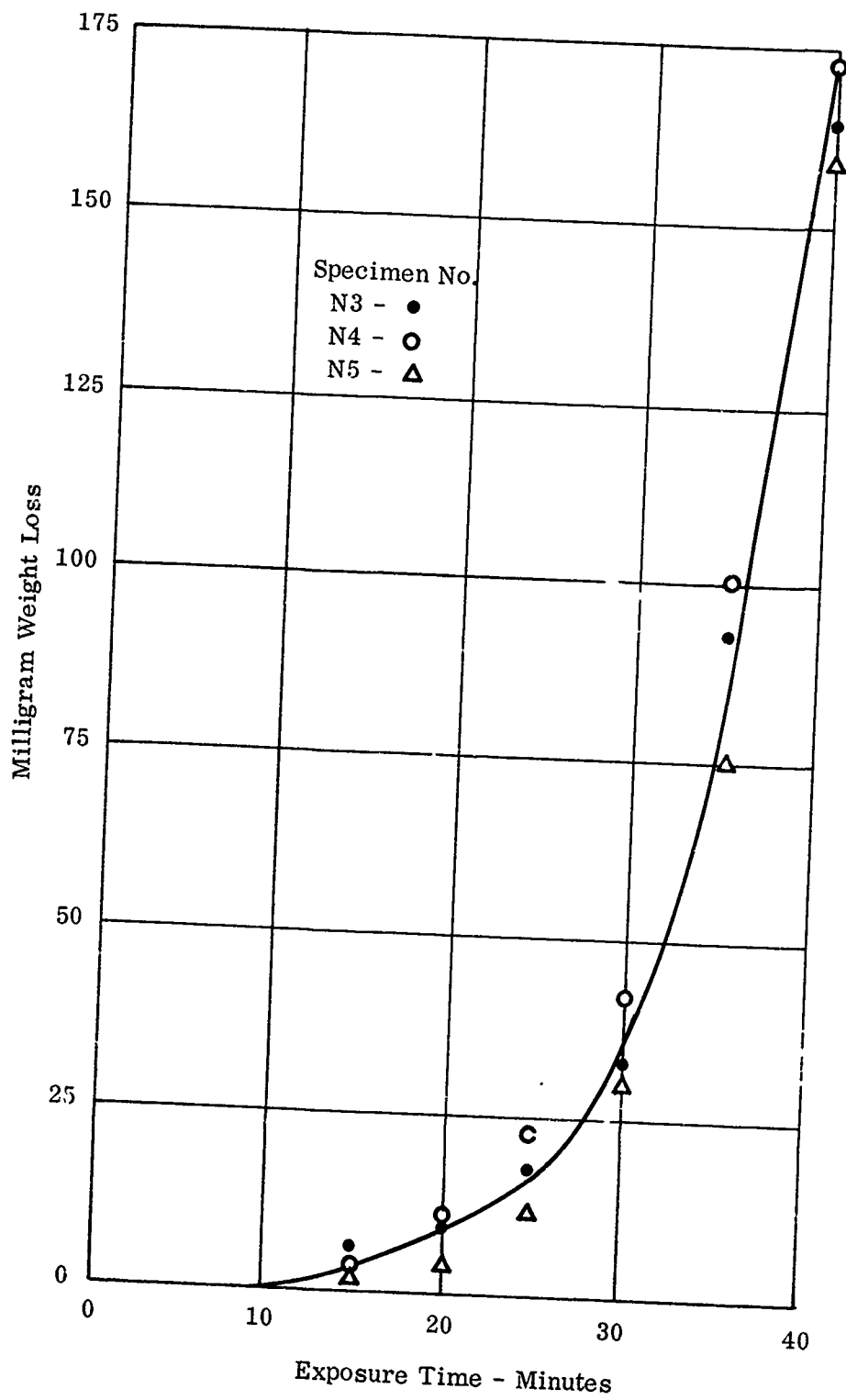


Figure 40. Rain Erosion of Pure Nickel 270 at 1120 ft/sec

TABLE XXI
RAIN EROSION TESTS ON PURE NICKEL (270)
CUMULATIVE WEIGHT LOSS - MILLIGRAMS

1120 ft/sec

TIME MINUTES	SPECIMEN NO.				
	N-1	N-2	N-3	N-4	N-5
5	0	0	0	0	0
10	2	3	2	3	2
15	-	-	5	4	3
20	-	-	8	10	5
25	-	-	16	23	11
30	-	-	33	42	30
35	-	-	86	99	75
40	-	-	163	172	157

RAIN EROSION TESTS
1 .INCH/HR RAINFALL - 1.8 MM DROP SIZE
730 FT/SEC - (500 MPH)

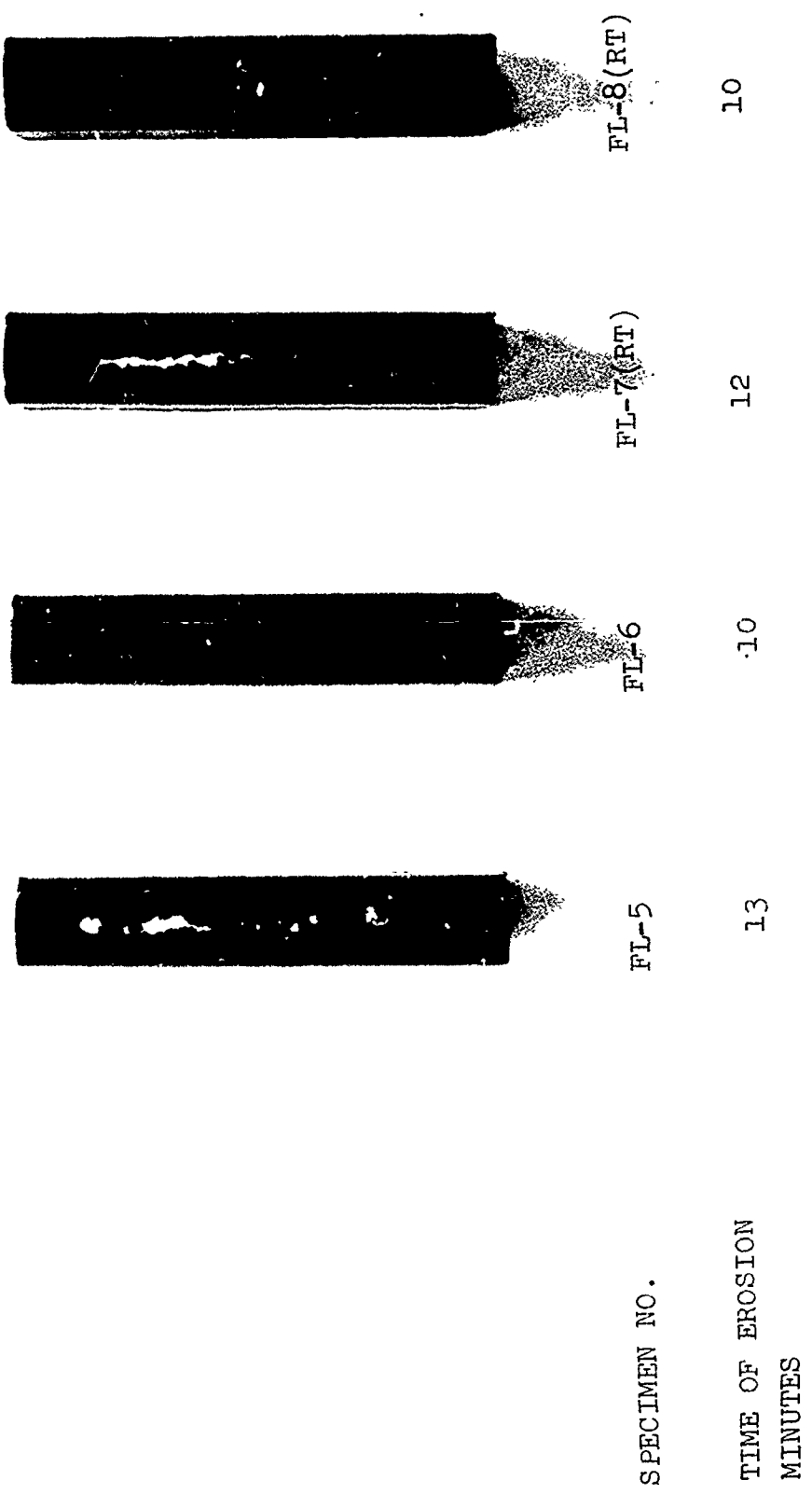


Figure 41 Erosion of 12 mil AF.MI. Fluorocarbon Coating on Aluminum Substrate

RAIN EROSION TESTS
1 INCH/HR RAINFALL - 1.8 MM DROP SIZE
730 FT/SEC - (500 MPH)

MATERIAL	SPECIMEN NO.	TIME OF EROSION MINUTES
Astrocoat - 115P	C-116	96
1801-C Neoprene	C-117	90
N-51	N-52	30
FL-8 (RT)	FL-6	39
AEMI Fluorocarbon		10
		10

Figure 42 Typical Erosion of Radome Coatings on Aluminum Substrate

RAIN EROSION TESTS
 1 INCH/HR RAINFALL - 1.8 MM DROP SIZE
 1120 FT/SEC (MACH 1)

MATERIAL	SPECIMEN NO.	TIME OF EROSION MINUTES		
Astrocoat-115P	C-119	9	7	-
1801-C Neoprene	C-120	4	3	1.0
AFML Fluorocarbon	N-53	4	3	1.25
	N-54			FL-4
	FL-3			FL-4

Figure 43 Typical Erosion of Radome Coatings on Glass-Epoxy Substrate

aged for 100 hrs. exhibited a slightly lower erosion rate of 7-8 minutes.

Figure 44 shows the character of the erosion observed on these Type I specimens.

Four Type II fluorocarbon and radome coating on glass fiber reinforced-epoxy laminate that were not heat aged eroded through in an average of eight minutes.

The typical erosion experienced with these four specimens tested at 730 ft/sec are shown in Figure 45. The AFML fluorocarbon elastomer coating tested had satisfactory rain erosion resistance and a temperature capability for use at temperatures of 500°F. This development represents a break-through in high temperature and rain erosion resistant coatings for radomes. Details of the development and testing of the coating are given in a recent report (21).

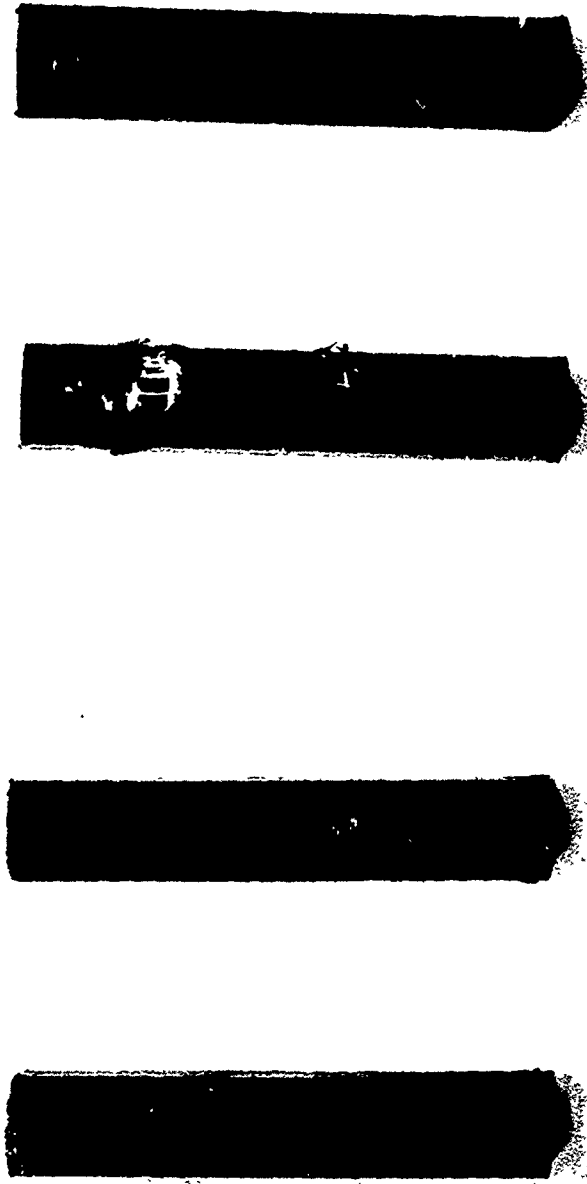
4. Polymers

The average izod impact strengths of the polymers tested are shown in Table XXII.

Hostalen GUR, ultra high molecular weight polyethylene when tested for rain erosion resistance of 730 ft/sec showed no signs of erosion for the first fifteen minutes of test after which time signs of minute cracking or small tears in the surface were observed. After twenty-five minutes of test these tears intersected which resulted in a very roughened surface as shown in

RAIN EROSION TESTS

1 INCH/HR. RAINFALL - 1.8 MM DROP SIZE
730 FT/SEC (500 MPH)



SPECIMEN NO.	FI-5	FI-6	FI-7	FI-8
TIME OF EROSION MINUTES	12	12	7	8
HEAT AGING	24 HOURS @ 400°F		100 HOURS @ 400°F	

Figure 44 Erosion of 11.5 mil AFML Fluoroelastomer Type I on Glass Fiber Reinforced Laminate

RAIN EROSION TESTS

1 INCH/HR. RAINFALL - 1.8 MM DROP SIZE

730 FT/SEC (500 MPH)

SPECIMEN NO.	FII-1	FII-2	FII-3	FII-4
TIME OF EROSION MINUTES	8	8	8	7
HEAT AGING	None	None	None	None

Figure 45 Erosion of 12 mil AFML Fluoroelastomer Antistatic Type II -
on Glass Fiber Reinforced Laminate

TABLE XXII
IZOD IMPACT STRENGTH OF POLYMERS

<u>TRADE NAME</u>	<u>SOURCE</u>	<u>CHEMICAL TYPE</u>	<u>AVERAGE IZOD IMPACT STRENGTH ft. lb./in. notch</u>
HOSTALGEN GUR	American Hoechst Corp.	ULTRA HIGH MOLECULAR POLYETHYLENE	> 32
WINTHANE	Winthane Chem. Ind.	POLYURETHANE	20
KYDEX	Rohm & Haas	ACRYLIC POLYVINYLCHLORIDE	15
LEXAN	General Electric	POLYCARBONATE	14
ASTREL 360	3M	POLYARYLSULFONE	5
ZYTEL-7110-13	duPont	GLASS FILLED NYLON	3
NORYL 731	G. E.	MODIFIED POLYPHENYLENE OXIDE	2.3
NORYL GFN-3	G. E.	GLASS FILLED PPO	2.6
DELRIN 500	duPont	ACETAL	2.3

Figure 46. After thirty-five minutes of testing the specimens exhibited approximately 100 milligrams of weight loss as outlined in Table XXIII.

The UHMW polyethylene tested at 1120 ft/sec in rain did not exhibit signs of erosion for the first two minutes after which time the surface began to roughen significantly. After six minutes the polyethylene specimens lost approximately 100 milligrams and were very rough and abraded in appearance as illustrated in Figure 47. The weight losses observed are noted in Table XXIV.

Kydex a copolymer of acrylic and polyvinyl chloride which had a slightly higher impact strength than polycarbonate was tested at 720 and 1130 ft/sec. As noted in Table XXV and XXVI the specimens lost approximately 100 milligrams in ten minutes at 720 ft/sec and in two minutes at 1130 ft/sec. The type of erosion experienced is shown in Figures 48 and 49.

Lexan a G.E. polycarbonate was tested and previously reported (8). Results indicated that this polymer lost approximately 100 milligrams in two minutes at 730 ft/sec and 100 milligrams at 1120 ft/sec in forty-five seconds. Polyurethane polymers tested were identified as Winthane No. 121 and 13⁴ which are ether based and No. 612 which is ester based. All three specimens were amine cured and cast in 1/2" sheets and were obtained from Winfield Chemical Industries, Buffalo, New York.

TABLE XXIII

RAIN EROSION TESTS ON HMW POLYETHYLENE
CUMULATIVE WEIGHT LOSS - MILLIGRAMS

730 ft/sec.

TIME MINUTES	SPECIMEN NO.		
	MP-3	MP-4	MP-5
10	0	0	0
15	1	2	1
20	9	12	8
25	42	52	46
30	73	80	71
35	98	108	88

TABLE XXIV

RAIN EROSION TESTS ON HMW POLYETHYLENE
CUMULATIVE WEIGHT LOSS - MILLIGRAMS

1130 ft/sec.

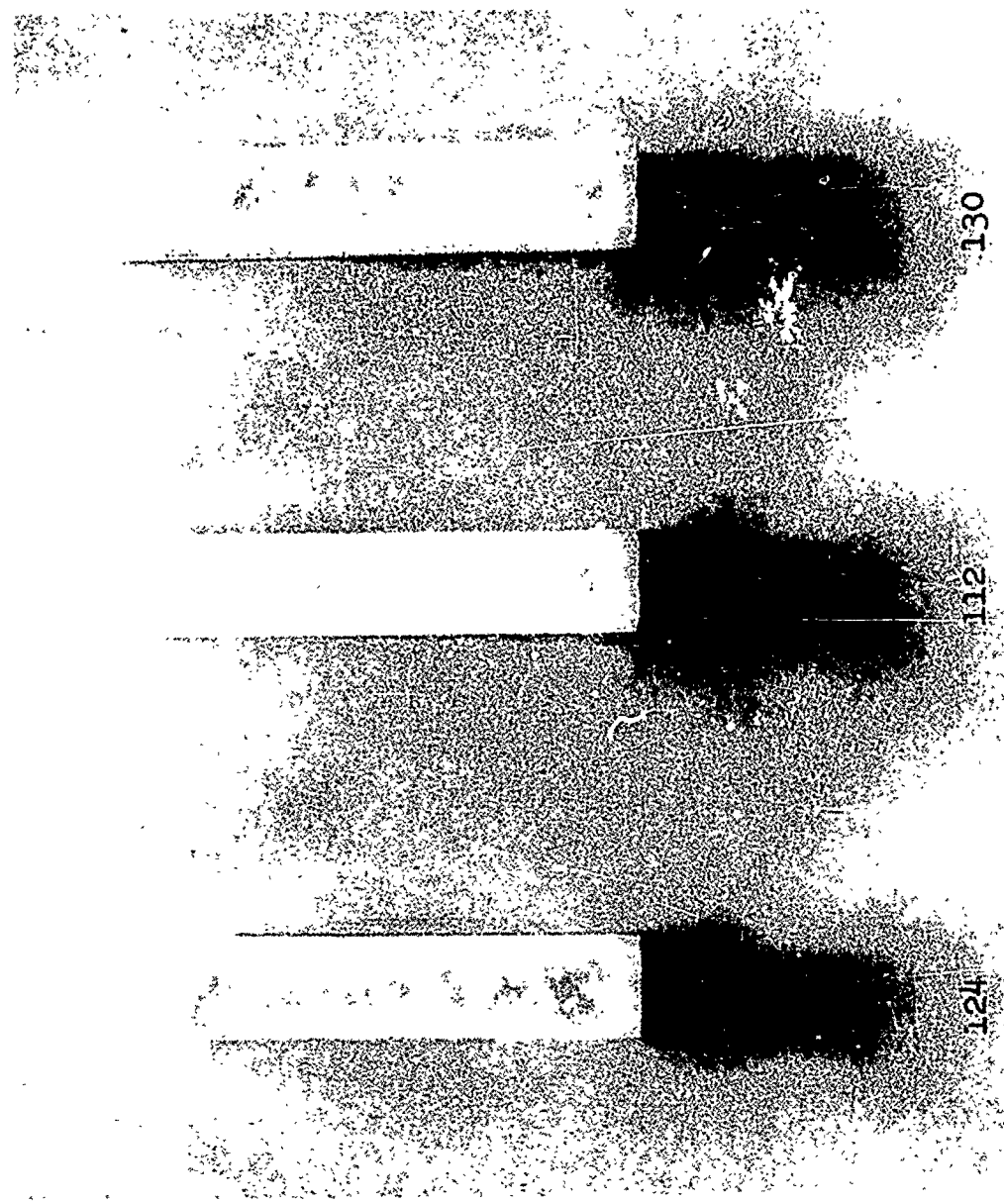
TIME MINUTES	SPECIMEN NO.		
	MP-6	MP-7	MP-8
1	0	0	0
3	22	11	32
5	79	62	87
7	124	112	130

RAIN EROSION TESTS
1 INCH/HR RAINFALL - 1.8 MM DROP SIZE
730 FT/SEC VELOCITY

SPECIMEN NO.	TIME OF EXPOSURE MINUTES	MILLIGRAM WEIGHT LOSS
108	35	35
98	35	35
88	35	35
75	35	35
63	35	35
55	35	35
45	35	35
35	35	35
25	35	35
15	35	35
5	35	35
1	35	35

Figure 46. Erosion of High Molecular Weight Polyethylene Plastic

RAIN EROSION TESTS
1 INCH/HR RAINFALL - 1.8 MM DROP SIZE
1130 FT/SEC VELOCITY



SPECIMEN NO.	TIME OF EXPOSURE MINUTES	MILLIGRAM WEIGHT LOSS
112	124	130
132	130	132

Figure 47 Erosion of High Molecular Weight Polyethylene Plastic

TABLE XXV

RAIN EROSION TESTS ON ACRYLIC-POLYVINYLCHLORIDE
CUMULATIVE WEIGHT LOSS - MILLIGRAMS

730 ft/sec.

TIME MINUTES	SPECIMEN NO.		
	K-3	K-4	K-5
2	3	5	3
4	26	34	29
6	49	56	50
8	76	82	78
10	98	120	115

TABLE XXVI

RAIN EROSION TESTS ON ACRYLIC-POLYVINYLCHLORIDE
CUMULATIVE WEIGHT LOSS - MILLIGRAMS

1130 ft/sec.

TIME MINUTES	SPECIMEN NO.		
	K-8	K-9	K-10
1	29	34	46
2	112	108	126
3	-	200	241

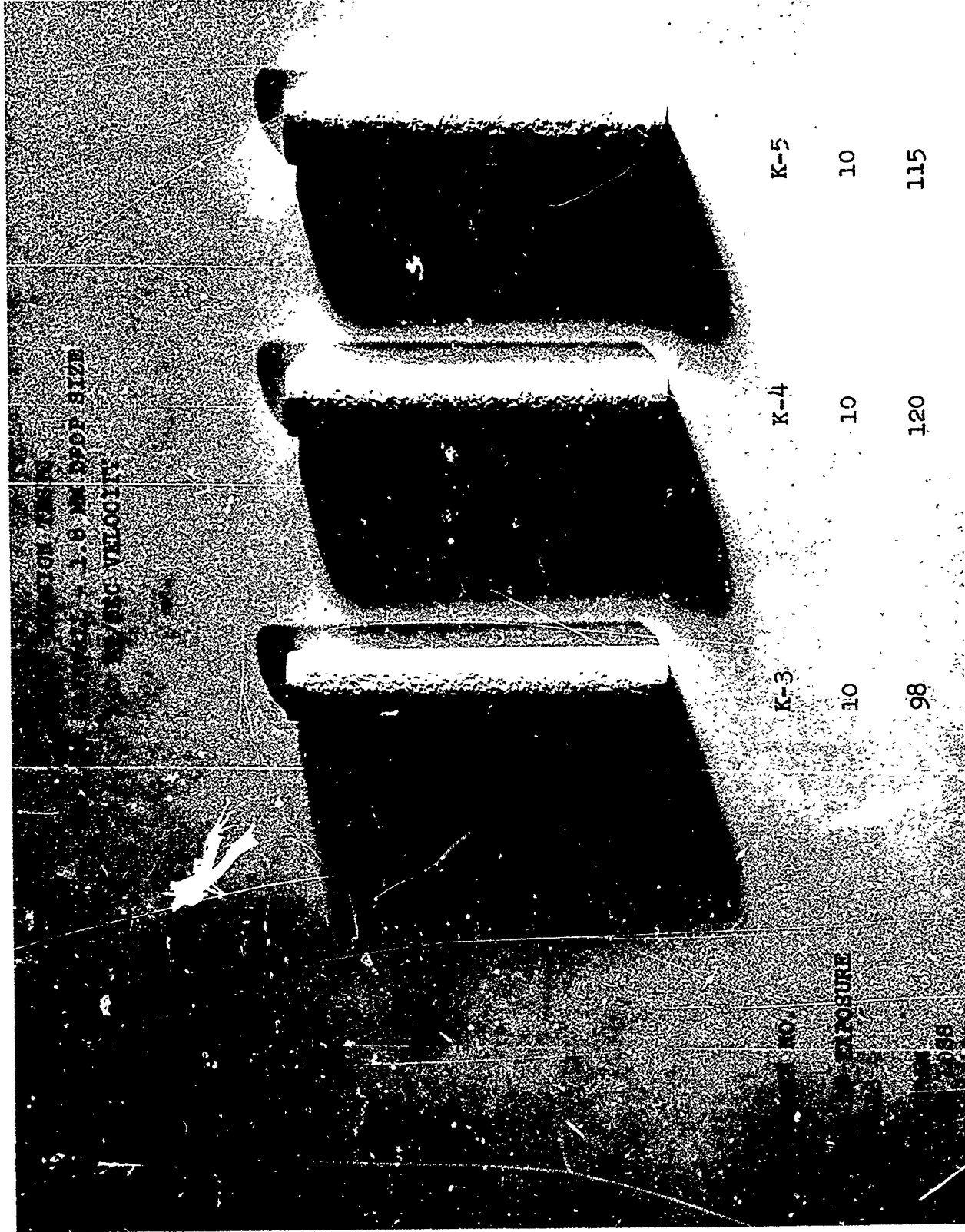


Figure 48 Erosion of Acrylic-Polyvinylchloride Plastic

RAIN EROSION TESTS
1 INCH/HR RAINFALL - 1.8 MM DROP SIZE
1130 FT/SEC VELOCITY

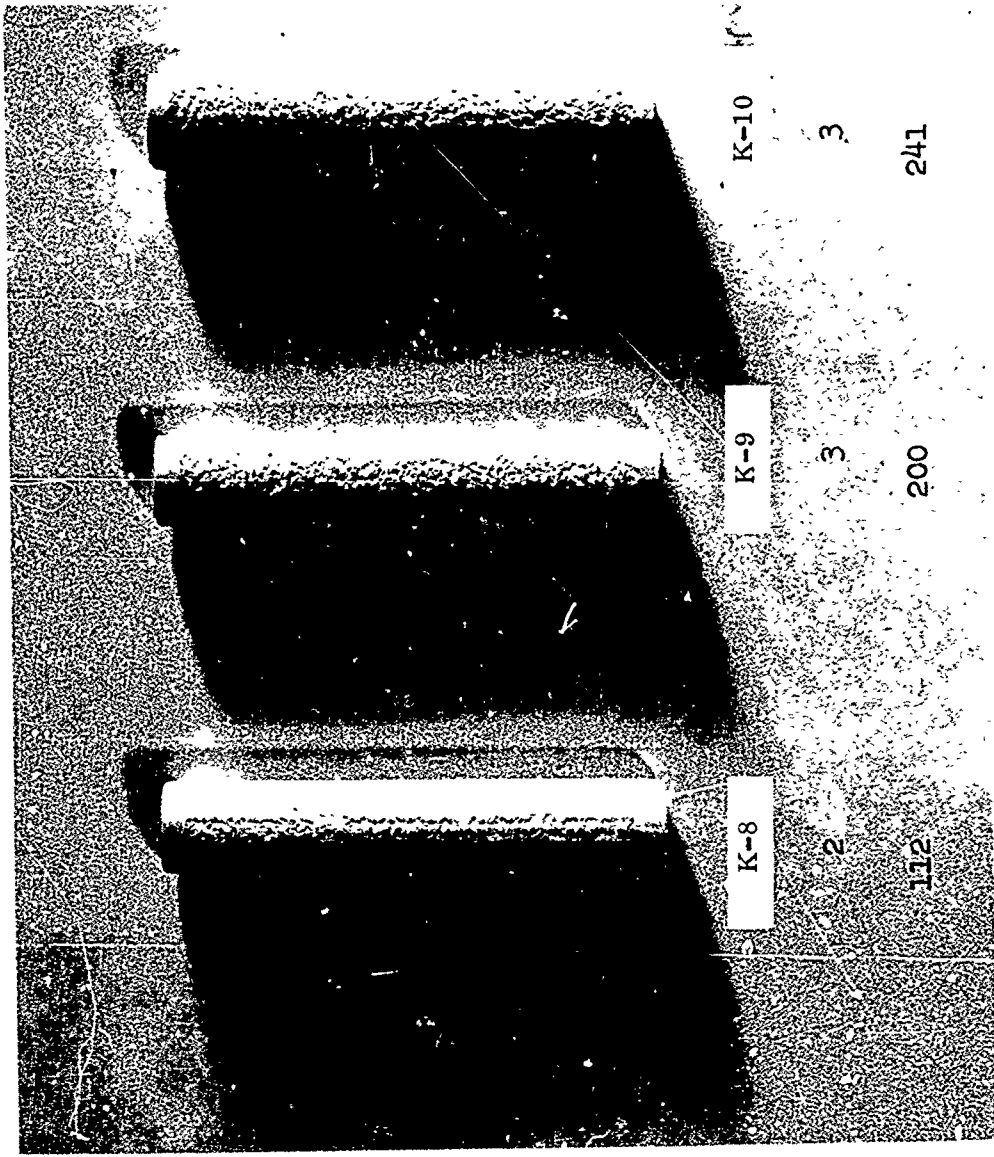


Figure 49 Erosion of Acrylic-Polyvinylchloride Plastic

Typical properties are as follows:

	#121	#134	#612
Hardness-Shore	55	70	55
Tensile PSI	6800	8000	8250
100% Modulus PSI	2000	4100	1650
300% Modulus PSI	5050	--	3500
Elongation %	350	260	410
Rebound Resilience %	43	46	35
Tear D624 Die C PLI	800	1050	845
Tear D470 PLI	145	115	180

Three specimens of polyurethane elastomers No. 121, 134 and 612 were tested in standard rainfall at 730 ft/sec and three specimens of polyurethane 612 was tested at 1120 ft/sec.

The weight losses experienced are outlined in Table XXVII through XXX.

The data on weight loss indicates a considerable variation between samples of the same polyurethane material for a given time of exposure, highlighting the fact that the formation of pits or tearing out of polyurethane surface, upon impact, proceeds in a random manner.

Polyurethane elastomers #121 and 612 have 2-3 times the erosion resistance of elastomer #134 in a standard rainfall at 730 ft/sec impact velocity. The typical erosion pattern experienced with the polyurethane elastomers is illustrated in Figures 50 through 53.

TABLE XXVII
RAIN EROSION TESTS ON POLYURETHANE (W-134)
CUMULATIVE WEIGHT LOSS - MILLIGRAMS

730 ft/sec

TIME MINUTES	SPECIMEN NO.		
	134-1	134-2	134-3
3	0	0	0
5	25	14	5
8	72	57	41
10	134	115	90

TABLE XXVIII
RAIN EROSION TESTS ON POLYURETHANE (W-121)
CUMULATIVE WEIGHT LOSS - MILLIGRAMS

730 ft/sec

TIME MINUTES	SPECIMEN NO.		
	121-1	121-2	121-3
10	1	0	2
15	6	8	6
20	19	75	37
25	92	182	123

TABLE XXIX
RAIN EROSION TESTS ON POLYURETHANE (W-612)
CUMULATIVE WEIGHT LOSS - MILLIGRAMS

730 ft/sec

TIME MINUTES	SPECIMEN NO.		
	612-1	612-2	612-3
5	9	5	3
10	18	20	10
15	30	46	19
20	48	98	27

TABLE XXX
RAIN EROSION TESTS ON POLYURETHANE (W-162)
CUMULATIVE WEIGHT LOSS - MILLIGRAMS

1120 ft/sec

TIME MINUTES	SPECIMEN NO.		
	612-4	612-5	612-6
2	6	7	3
3	-	60	30
5	-	106	-

RAIN EROSION TESTS
1"/HR RAINFALL - 1.8 MM DROP SIZE
730 FT/SEC - (500 MPH)

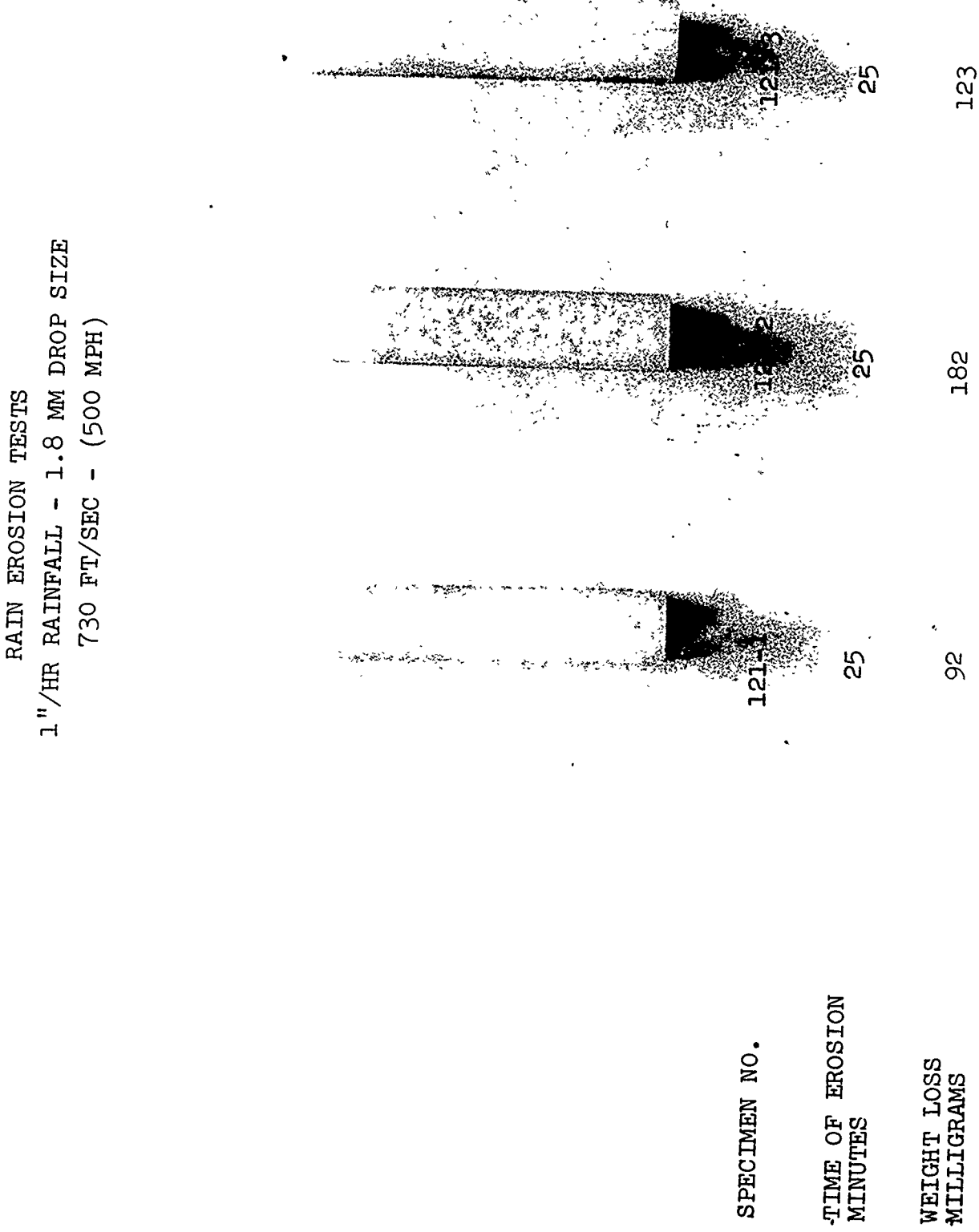


Figure 50 Erosion of Polyurethane W-121

RAIN EROSION TESTS
1"/HR RAINFALL - 1.8 MM DROP SIZE
730 FT/SEC - (500 MPH)

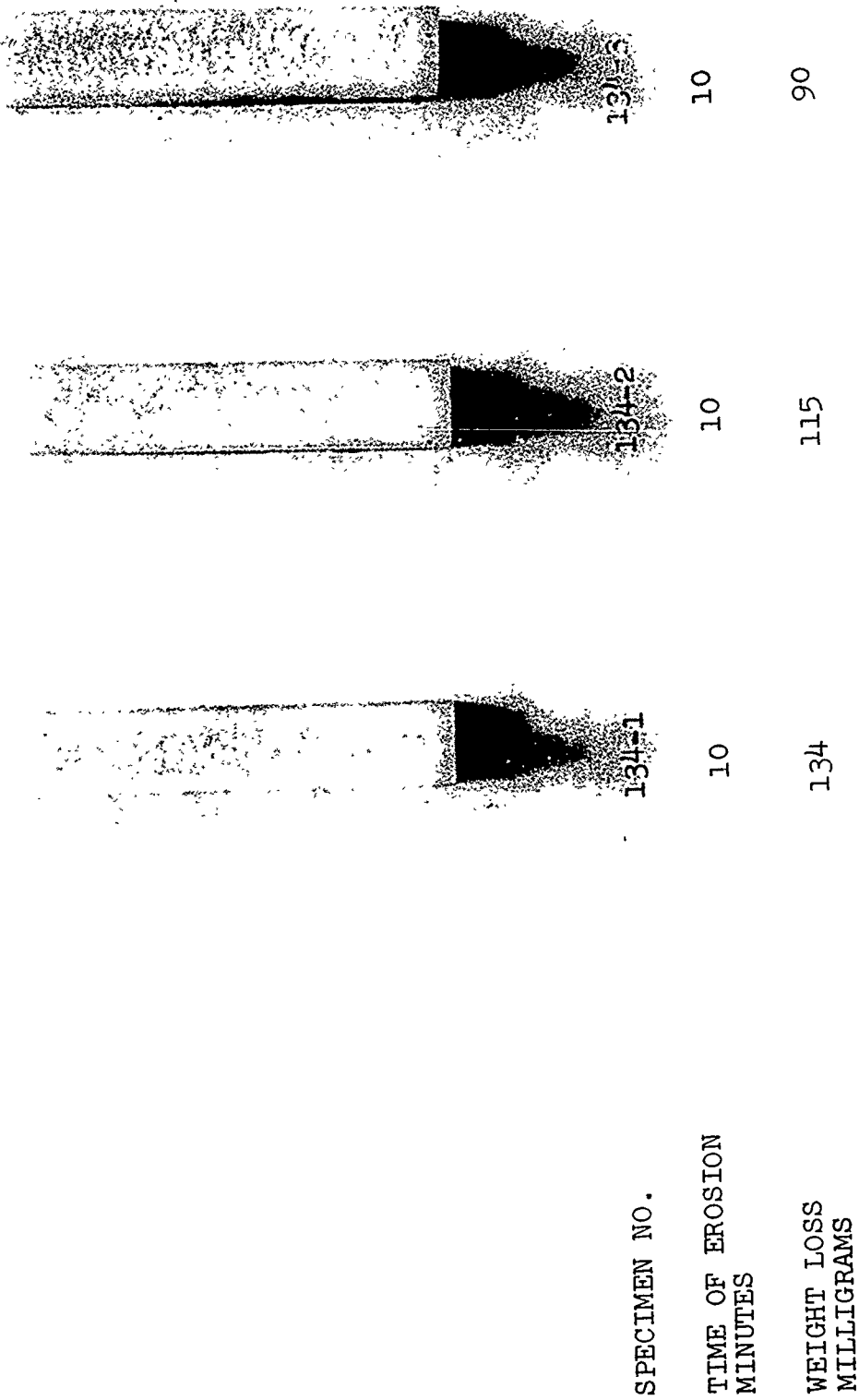


Figure 51. Erosion of Polyurethane W-134

RAIN EROSION TESTS
1" /HR RAINFALL - 1.8 MM DROP SIZE
730 FT/SEC - (500 MPH)

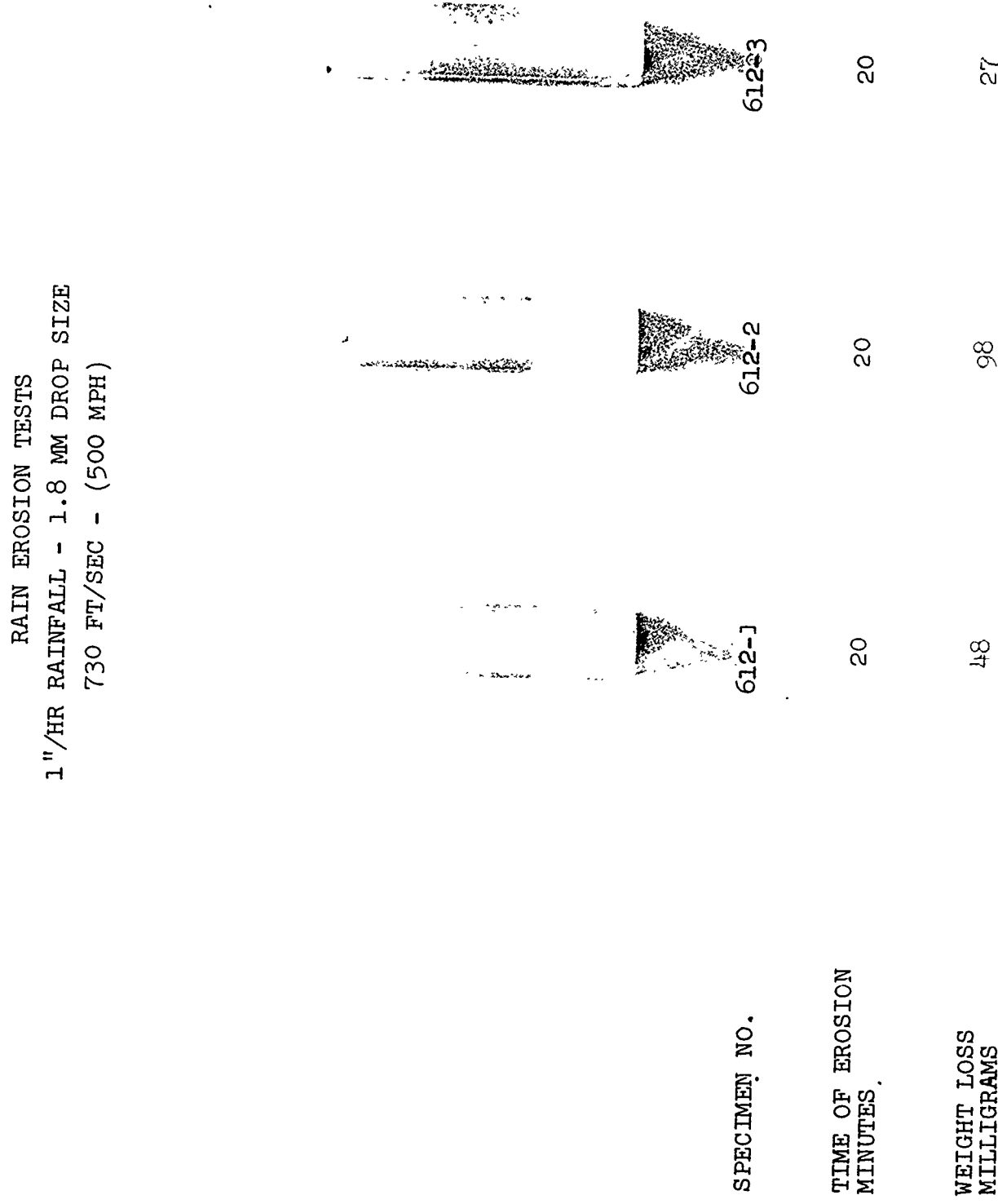


Figure 52 Erosion of Polyurethane W-612

RAIN EROSION TESTS
1 INCH/HR RAINFALL - 1.8 MM DROP SIZE
1120 FT/SEC (MACH 1)

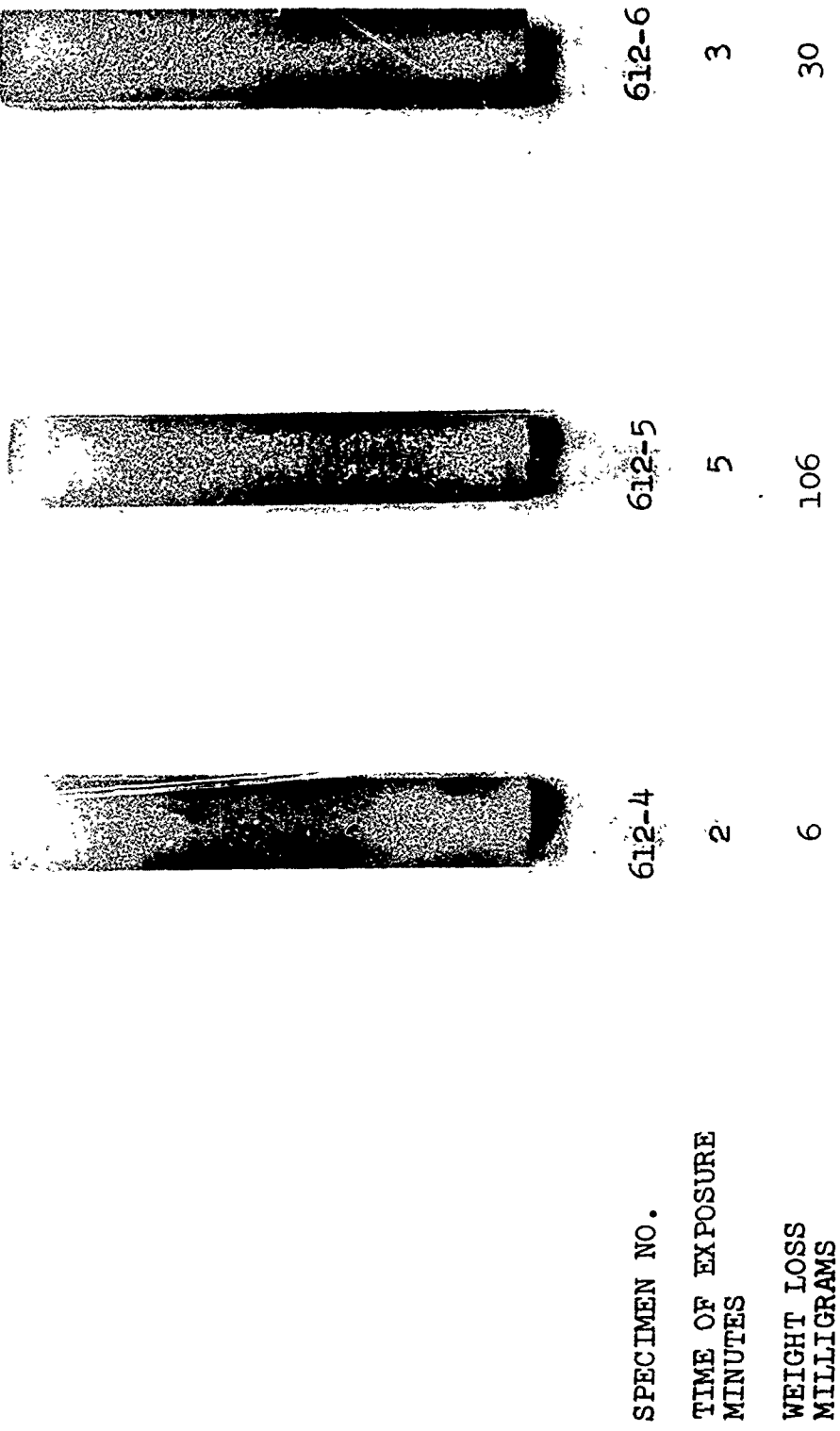


Figure 53 Erosion of Polyurethane W-612

Both elastomers 121 and 612 have a Shore hardness of 55 compared to 13⁴ having a hardness of 70. The percent elongation for elastomers 121 and 612 is approximately one and one half times that of elastomer 13⁴ and the modulus at 100% elongation for 13⁴ is twice that of elastomers 121 and 612.

Astrel 360 with the next highest impact strength, lost 100 milligrams in eight minutes at 730 ft/sec and approximately 100 milligrams in forty-five seconds at 1120 ft/second.

The nature of the erosion after testing at these two velocities can be observed in Figures 54 and 55. The weight loss as a function of time is given in Tables XXXI and XXXII.

Nylon reinforced with 33% by weight of long glass fibers (Zytel 7110-13) was evaluated for erosion weight loss at 730 and 1120 ft/sec as noted in Table XXXIII and XXXIV. The time to lose 100 milligrams was twenty minutes at 720 ft/sec and one minute at 1120 ft/sec. From the character of the erosion of the glass reinforced nylon shown in Figures 56 and 57 it would appear that the glass reinforcement aids in the fracture of large pieces of resin from the surface of the test specimens.

The modified polyphenylene oxide resin (Noryl 731) and glass fiber reinforced resin PPO resin with 33% by weight of glass (Noryl GFN-3) illustrates a fact that has been previously stated i.e., the erosion resistance of a straight unreinforced resin is greater than when the resin is reinforced.

RAIN EROSION TESTS
1" /HR RAINFALL - 1.8 MM DROP SIZE
730 FT/SEC (500 MPH)

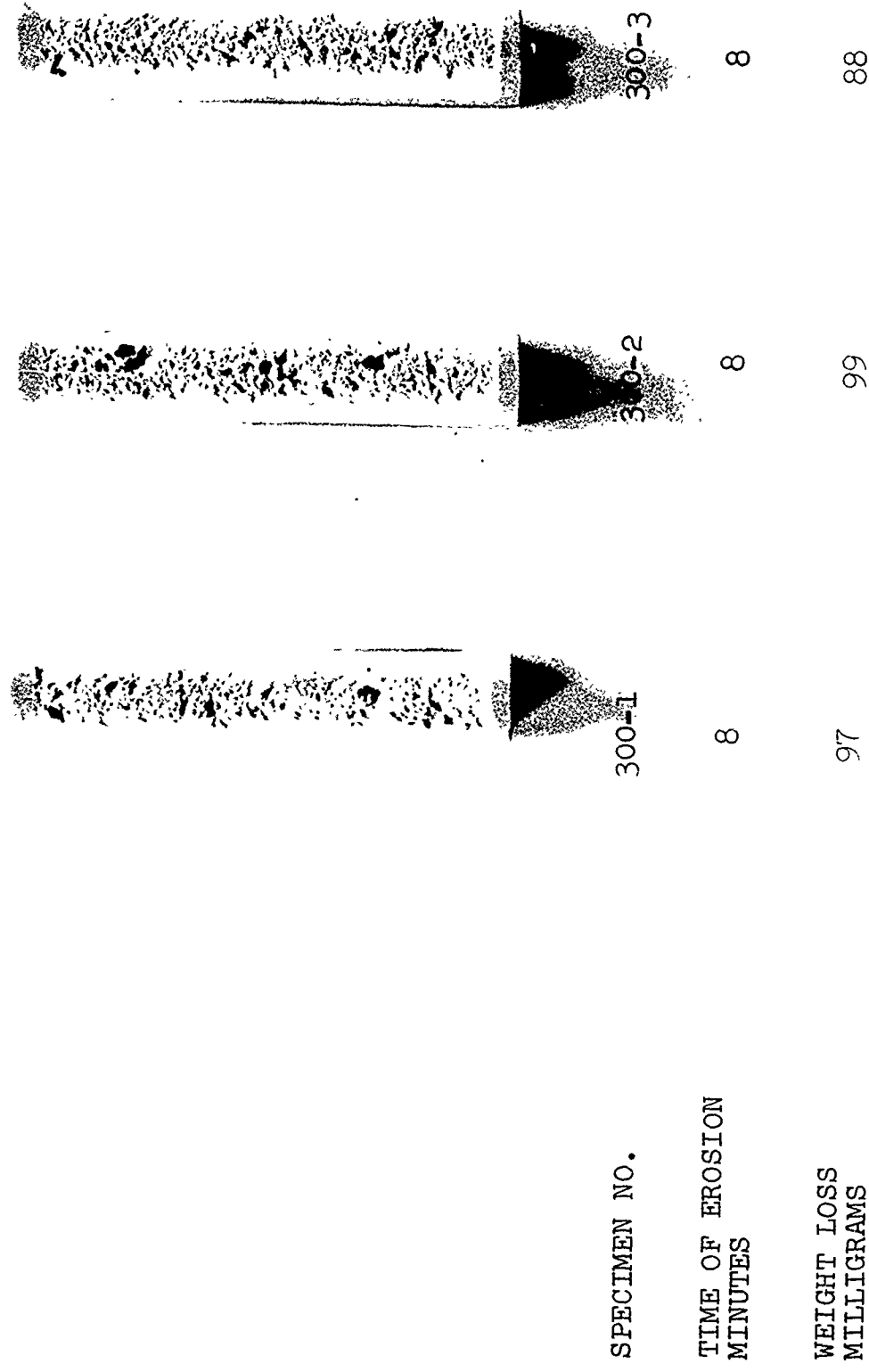


Figure 54 Erosion of Polyarylsulfone (Astral 360)

RAIN EROSION TESTS

1 INCH/HR RAINFALL - 1.8 MM DROP SIZE

1120 FT/SEC (MACH 1)

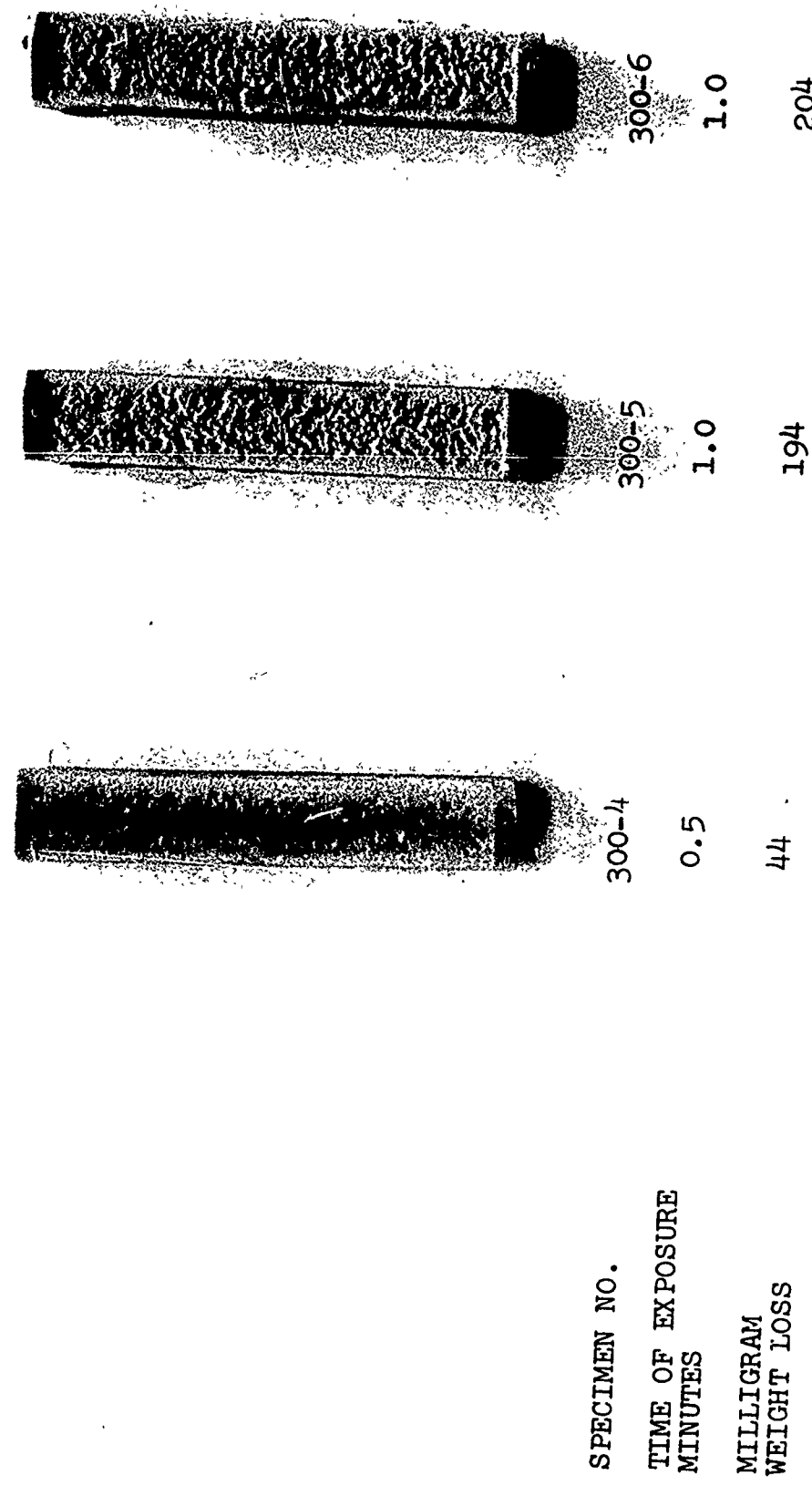


Figure 55 Erosion of Polyarylsulfone (Astral 360)

TABLE XXXI
RAIN EROSION TESTS ON POLYARYLSULFONE (ASTREL 360)
CUMULATIVE WEIGHT LOSS - MILLIGRAMS
730 ft/sec

TIME MINUTES	SPECIMEN NO.		
	300-1	300-2	300-3
2	9	3	5
3	21	19	20
5	49	38	48
8	97	99	88

TABLE XXXII

RAIN EROSION TESTS ON POLYARYLSULFONE (ASTREL-360)

CUMULATIVE WEIGHT LOSS - MILLIGRAMS

1120 ft/sec

TIME MINUTES	SPECIMEN NO.		
	360-4	360-5	360-6
0.25	4	6	7
0.50	44	56	63
1.0	-	194	204

TABLE XXXIII

RAIN EROSION TESTS ON NYLON (ZYTEL-7110-13)

CUMULATIVE WEIGHT LOSS - MILLIGRAMS

1120 ft/sec

TIME MINUTES	SPECIMEN NO.		
	Z-4	Z-5	Z-6
0.5	12	14	18
1.0	76	97	82
1.5	526	-	552

TABLE XXXIV

RAIN EROSION TESTS ON NYLON (ZYTEL-7110-13)
CUMULATIVE WEIGHT LOSS - MILLIGRAMS

730 ft/sec.

TIME MINUTES	SPECIMEN NO.		
	Z-1	Z-2	Z-3
3	2	1	1
5	4	3	3
10	10	8	8
15	42	37	37
20	109	72	68

RAIN EROSION TESTS
1 INCH/HR RAINFALL - 1.8 MM DROP SIZE
730 FT/SEC (500 MPH)

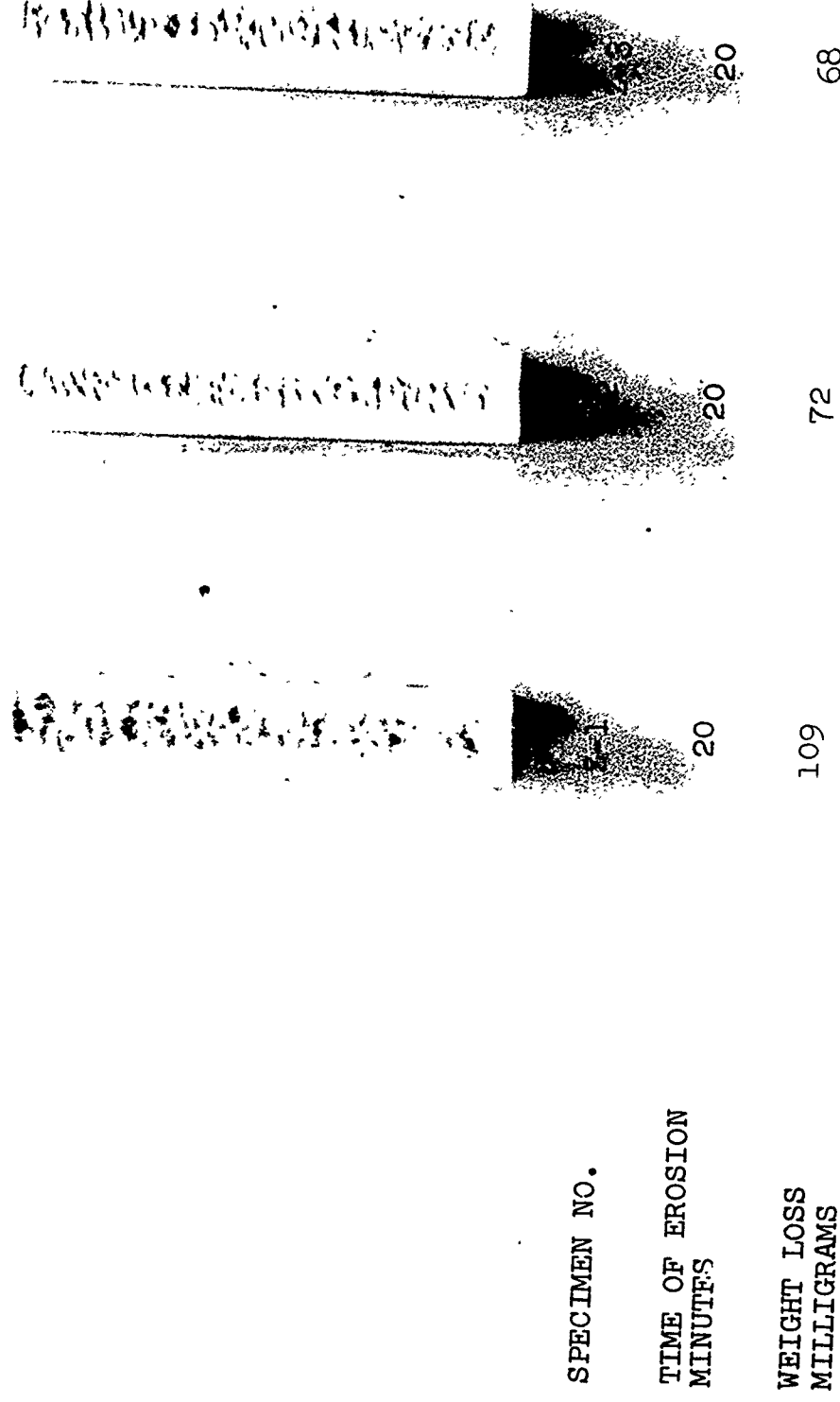


Figure 56. Erosion of Nylon (Zytel 7110-13)

RAIN EROSION TESTS
1 INCH./HR RAINFALL - 1.8 MM DROP SIZE
1120 FT/SEC (MACH 1)

SPECIMEN NO.	TIME OF EXPOSURE MINUTES	MILLIGRAMS WEIGHT LOSS
Z-4	1.5	526
Z-5	1.0	97
Z-6	1.5	552

Figure 57. Erosion of Nylon (Zytel 7110-13)

As outlined in Tables XXXV and XXXVI the erosion time for the unfilled PPO (Noryl 731) was approximately 12 minutes for 100 milligrams weight loss and for the glass reinforced PPO (Noryl GFN-3) 3 minutes at 730 ft/sec. The typical erosion experienced at 730 ft/sec with the reinforced and nonreinforced PPO resin (Noryl) is shown in Figures 58 and 59.

The weight losses observed for the PPO resin systems at 1120 ft/sec are outlined in Tables XXXVII and XXXVIII. The approximate time to erode 100 milligrams of Noryl 731 was one minute and for Noryl GFN-3 approximately 30 seconds. Figures 60 and 61 illustrate the character of erosion observed for the reinforced and nonreinforced PPO resin.

The acetal resin (Delrin 550) having fair impact strength and resistance to abrasion was evaluated at 730 and 1120 ft/sec and was found to be outstanding in comparison to the other polymers for rain erosion resistance.

The acetal resin specimen exhibited no significant signs of erosion until it had received 40 minutes of testing at 730 ft/sec at which time small tears were seen in the surface when observed at 20X magnification under an optical microscope.

After approximately 85 minutes of testing at 730 ft/sec the acetal resin lost 100 milligrams as noted in Table XXXIX.

TABLE XXXV

RAIN EROSION TESTS ON POLYIHENYLENE OXIDE (NORYL-731)
CUMULATIVE WEIGHT LOSS - MILLIGRAMS

730 ft/sec

TIME MINUTES	SPECIMEN NO.		
	N-731-1	N-731-2	N-731-3
2	17	8	12
5	34	17	31
10	101	45	42
12	-	74	87
15	-	160	167

TABLE XXXVI

RAIN EROSION TESTS ON GLASS FILLED PPO (NORYL-GFN-3)
CUMULATIVE WEIGHT LOSS - MILLIGRAMS

730 ft/sec

TIME MINUTES	SPECIMEN NO.		
	GFN-1	GFN-2	GFN-3
1	20	24	24
2	51	57	58
3	98	93	106
5	183	-	

TABLE XXXVII
 RAIN EROSION TESTS ON
 POLYPHENYLENE OXIDE (NORYL-731)
 CUMULATIVE WEIGHT LOSS - MILLIGRAMS

1120 ft/sec

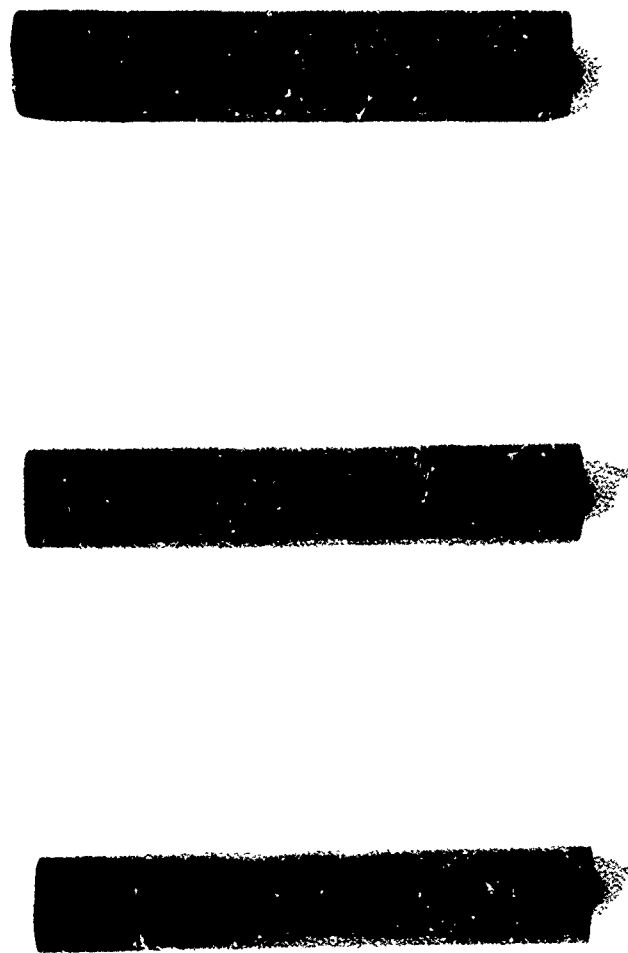
TIME MINUTES	SPECIMEN NO.		
	N-731-4	N-731-5	N-731-6
0.25	2	4	2
0.5	18	22	26
1.0	80	-	84

TABLE XXXVIII
 RAIN EROSION TESTS ON
 GLASS FILLED PPO (NORYL-GFN-3)
 CUMULATIVE WEIGHT LOSS - MILLIGRAMS

1120 ft/sec

TIME MINUTES	SPECIMEN NO.		
	GFN-4	GFN-5	GFN-6
0.25	12	16	19
0.50	102	113	124

RAIN EROSION TESTS
1" /HR RAINFALL - 1.8 MM DROP SIZE
730 FT/SRC (500 MPH)



SPECIMEN NO.	TIME OF EROSION MINUTES	WEIGHT LOSS MILLIGRAMS
N731-1	10	101
N731-2	15	160
N731-3	15	167

Figure 58 Erosion of Polyphenylene Oxide (Noryl-731)

RAIN EROSION TESTS
1" /HR RAINFALL - 1.8 MM DROP SIZE
730 FT/SEC (500 MPH)

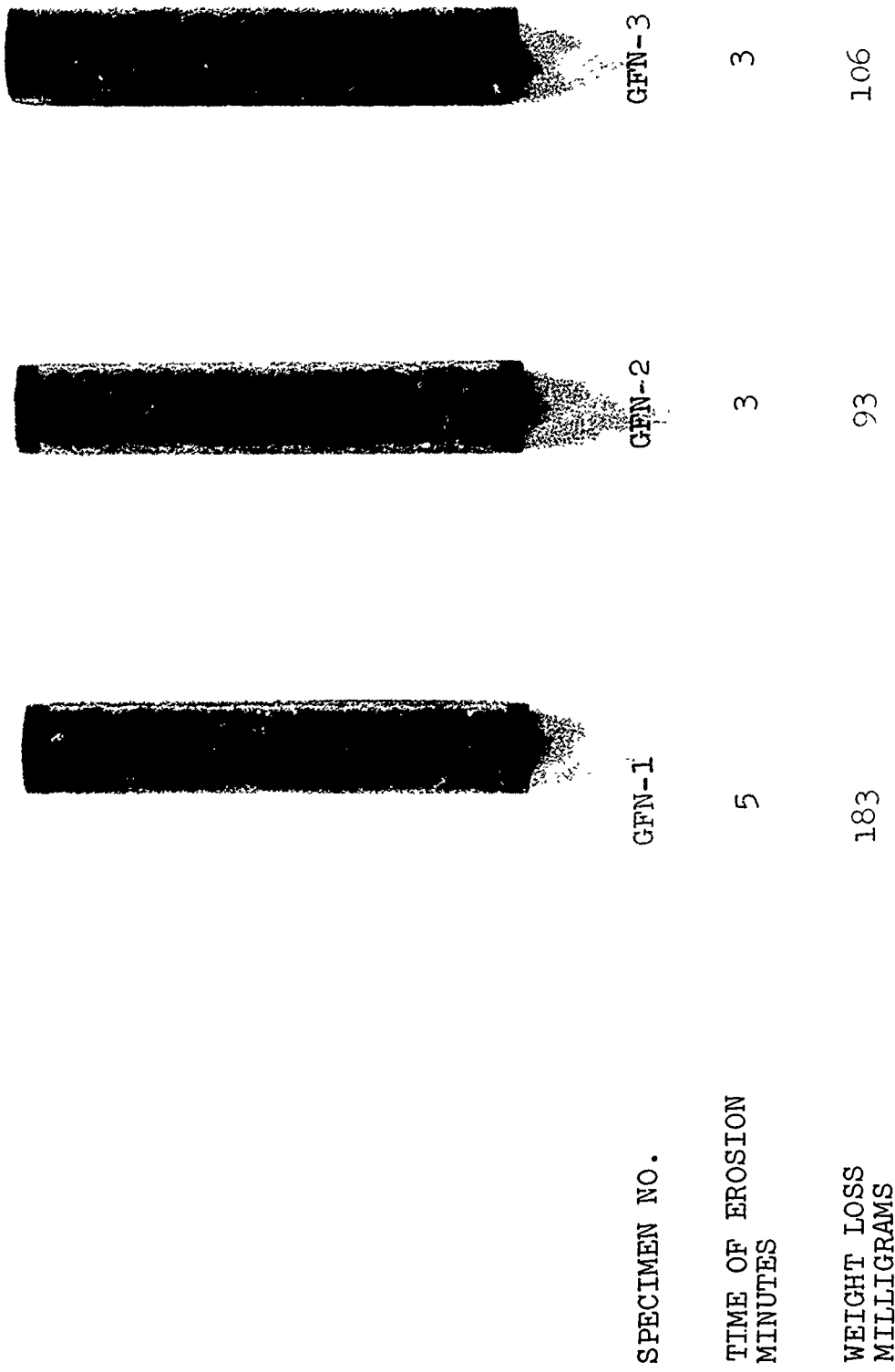


Figure 59. Erosion of Glass Filled PPO (Noryl-GFN-3)

RAIN EROSION TESTS
1 INCH/HR RAINFALL - 1.8 MM DROP SIZE
1120 FT/SEC (MACH 1)

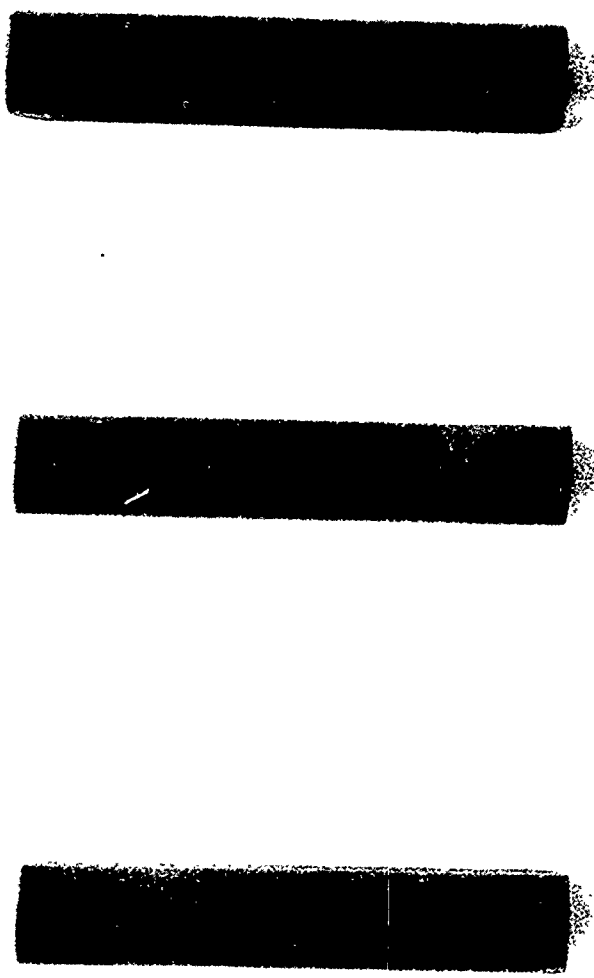


SPECIMEN	N-731-4	N-731-5	N-731-6
TIME OF EXPOSURE MINUTES	1.0	0.5	1.0
MILLIGRAM WEIGHT LOSS	80	22	84

Figure 60 Erosion of Polyphenylene Oxide (Noryl-731)

RAIN EROSION TESTS

1 INCH/HR RAINFALL - 1.8 MM DROP SIZE
1120 FT/SEC (MACH 1)



SPECIMEN NO.	TIME OF EXPOSURE MINUTES	GPN- 0.5	GPN- 0.5	11%	16%

Figure 61 Erosion of Glass Filled PPO (Noryl-GFN-3)

When tested at 1120 ft/sec the acetal resin lost 100 milligrams in five minutes and after approximately 8 minutes exposure 150 milligrams. The results are outlined in Table XL.

The nature of the damage due to rain erosion on the surface of the acetal resin is shown in Figures 62 and 63.

A comparison of the relative rain erosion resistance at 730 and 1120 ft/sec with the average Izod impact strength noted in Table XLI indicates that in general there is little correlation between the two properties.

The base polymer of acetal (Delrin 550) exhibits an erosion resistance comparable to the best polyurethane coating material (Astrocoat 115), however for the acetal resin to be useful as a coating some method of applying it to a substrate with suitable adhesion must be developed.

Because the acetal polymer is not significantly better than the polyurethane and a considerable amount of time and effort would be involved in the development of an acetal coating with good adhesion further work on the acetal polymeric material is not planned.

5. Reinforced Composites

The theory has been advanced that reinforced composites having the fibers end oriented or in a three dimensional configuration so that the solid or liquid

TABLE XXXIX

RAIN EROSION TESTS ON ACETAL (DELRIN 550)
CUMULATIVE WEIGHT LOSS - MILLIGRAMS

730 ft/sec.

TIME MINUTES	SPECIMEN NO.		
	D-550-1	D-550-2	D-550-3
20	0	0	0
30	2	3	5
40	4	5	8
60	33	29	35
80	79	71	80
90	112	125	133
100	163	172	181

TABLE XL

RAIN EROSION TESTS ON ACETAL (DELRIN 550)
CUMULATIVE WEIGHT LOSS - MILLIGRAMS

1120 ft/sec.

TIME MINUTES	SPECIMEN NO.		
	D-550-4	D-550-5	D-550-6
1	6	3	4
3	43	35	26
5	116	96	74
8	-	151	153

SPECIMEN NO.	TIME OF EROSION MINUTES	WEIGHT LOSS MILLIGRAMS
D-1	100	163
D-2	100	172
D-3	100	181

1 INCH/HR RAINFALL - 1.8 MM DROP SIZE
 730 ft/sec (500 MPH)

RAIN EROSION TESTS

Figure 62. Erosion of Acetal (Delrin 550)

RAIN EROSION TESTS
1 INCH/HR RAINFALL - 1.8 MM DROP SIZE
1120 FT/SEC (MACH 1)

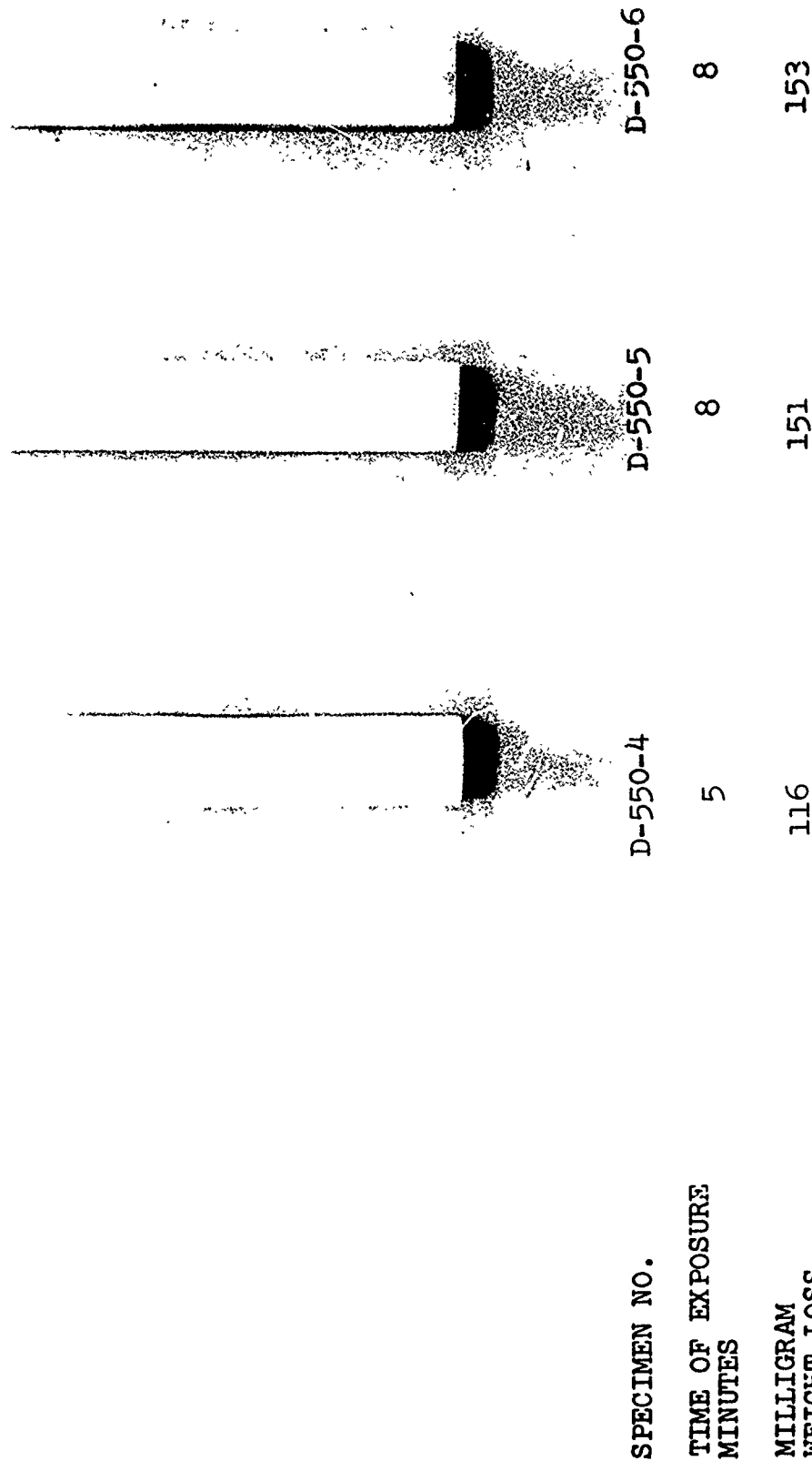


Figure 63. Erosion of Acetal (Delrin 550)

TABLE XLI

COMPARISON OF EROSION RESISTANCE OF THERMOPLASTIC POLYMERS

Trade Name	Average Izod Impact Strength ft. lb/in. notched	Approximate Time Min. to Erode 100 milligrams at 730 ft/sec.	Approximate Time Min. to Erode 100 milligrams at 1120 ft/sec.
Delrin 550	2.3	85	5
Hostalen GUR	>32	35	6
Winthane W-121	20	23	0
Winthane 612	20	2C	5
Zytel 7110-13	3	20	1
Noryl - 731	2.3	12	1
Kydex	15	10	2
Winthane W-134	20	10	-
Texan	14	10	0.75
Astrel 360	5	8	0.75
Noryl - GFN-3	2.6	3	0.5

particle impact would be on the ends of the fibers would result in composites with superior rain erosion resistance.

Preliminary comparisons were made with glass fiber epoxy composites.

Two unidirectional specimen G-1 and G-2 and two 181-glass fabric laminate specimen M-16-E and M-17-E were evaluated in a standard rainfall at 730 ft/sec velocity.

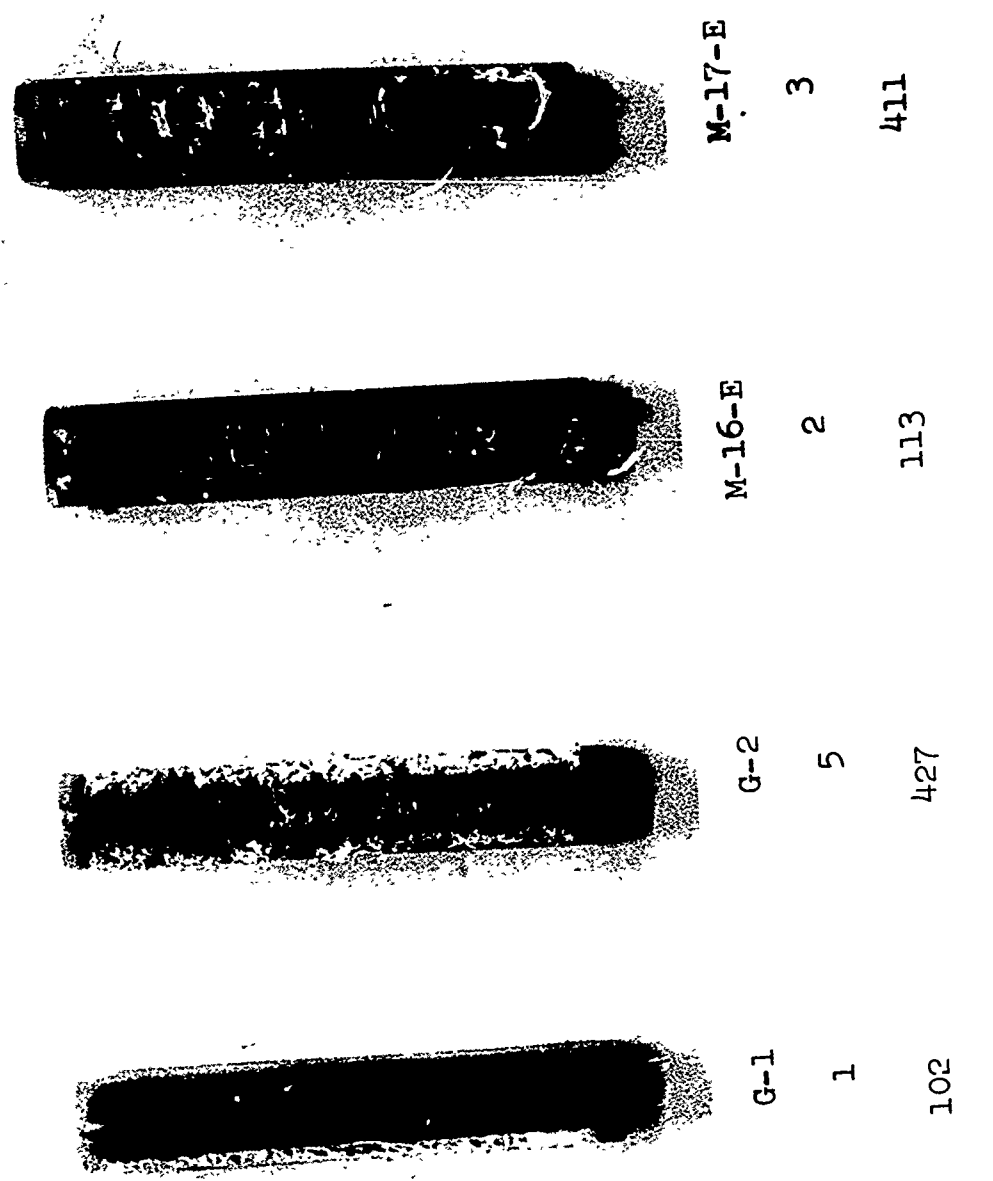
Specimen G-1 of the end oriented eroded on the upper side as shown in Figure 63.

After one minute of exposure to rainfall specimen G-1 lost 102 milligrams and showed a considerable amount of erosion on the upper side.

Optical microscopic examination of the specimen revealed small pits, at the bottom of which, the fractured ends of the fibers, damaged by the water drop impacts, could be observed.

Specimen G-2 was tested for five minutes and as shown in Figure 63 the erosion is the greatest on the upper surface but it had progressed so that the normal impacting surface and the bottom of the specimen are also eroded. After five minutes exposure the specimen had lost 427 milligrams in weight.

RAIN EROSION TESTS
1 INCH/HR RAINFALL - 1.8 MM DROP SIZE
780 FT/SEC (500 MPH)



SPECIMEN NO.	TIME OF EXPOSURE MINUTES	MILLIGRAM WEIGHT LOSS
G-1	1	102
G-2	5	427
M-16-E	2	113
M-17-E	3	411

Figure 54 Glass Reinforced Epoxy Laminates

Specimens of 181-glass fabric-epoxy laminate M-16-E and M-17-E showed no signs of erosion after one minute and after two minutes the resin surface was pitted and first layer of 181-glass fabric was exposed and the specimen had lost 113 milligrams in weight. After three minutes exposure to rain at velocity of 730 ft/sec specimen M-17-E showed erosion through two plies of the 181-glass fabric laminate and the specimen had lost 411 milligrams due to erosion.

Based upon the relative amount of erosion experienced by these two types of glass reinforced epoxy specimens it would appear that they are comparable in their resistance to erosion damage and that fiber orientation does not significantly influence the erosion rate.

The silica fiber composites were tested at 730 ft/sec in 1"/hour rainfall and the weight loss determined after thirty seconds and one minute.

The composites exhibited severe erosion > 1200 milligrams after thirty seconds and > 2600 milligrams after one minute exposure to rain at 730 ft/sec.

The character of the erosion of the 3D silica fiber composites is shown in Figure 65.

RAIN EROSION TESTS
1 INCH/HR RAINFALL - 1.8 MM DROP SIZE
730 FT/SEC (500 MPH)

SPECIMEN NO.	TIME OF EROSION MINUTES	WEIGHT LOSS MILLIGRAMS
100	1	0
100	2	0
100	5	0
1276	1	0
1276	2	0
1276	5	0
1214	1	0
1214	2	0
1214	5	0
18	1	0
18	2	0
18	5	0
3329	1	0
3329	2	0
3329	5	0

Figure 65 Philco-Ford Silica - Silica Fiber Composite

IX. MECHANICS OF EROSION STUDIES

A. The Mechanisms of Erosion

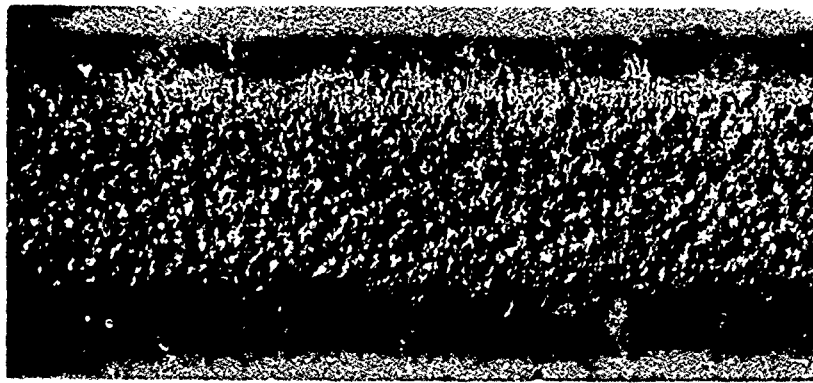
The mechanisms of material removal during erosion may be roughly divided into two categories: erosion through plastic deformation and erosion through progressive fracture. The category of erosion through plastic deformation includes erosion processes dominated by ductile pitting, by abrasion, and by polishing. Erosion through progressive fracture includes material removal via fatigue, tearing, and brittle fracture.

1. Ductile Pitting

If a ductile solid is impacted at near normal incidence by a solid or liquid particle traveling at sufficient velocity, a plastic indentation is formed at the point of impact. Such indentations may be deepened by subsequent impacts, isolating islands of materials which may be easily sheared off or driven from the surface. This ductile pitting erosion is particularly important in the rain erosion of ductile metals at moderate velocities and has been described in detail in AFML technical reports (8, 22). Erosion through ductile pitting is particularly likely when the impacting particles are liquid, since it may be shown that the deformability of the liquid particle leads to an intense preferential attack of pits in a roughened surface. An example of ductile pitting due to droplet impacts is shown in Figure 66. The material is pure nickel exposed to a 1 in/hr rainfall at 1120 ft/sec.



(a) 10 MIN. EXPOSURE, 4X



(b) 40 MIN. EXPOSURE, 4X



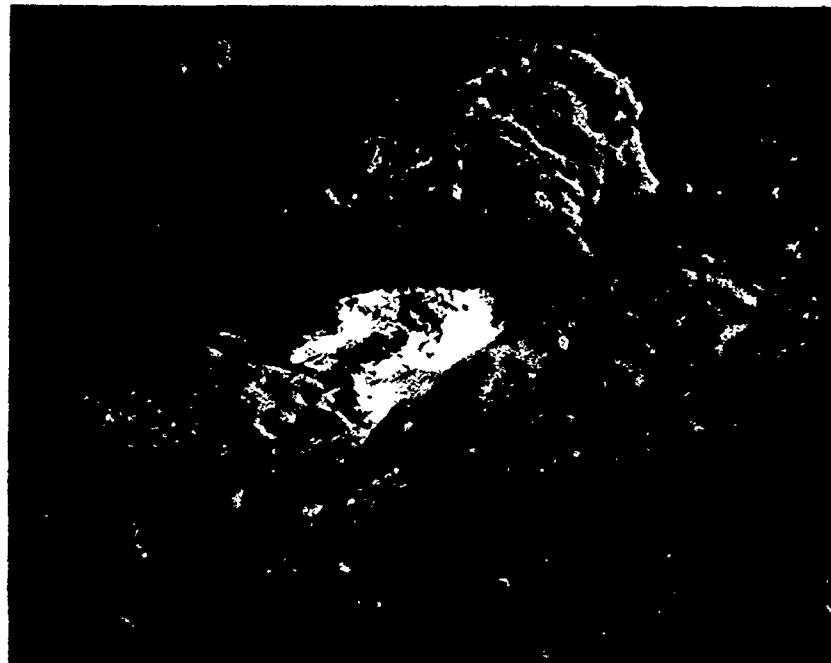
(c) 40 MIN. EXPOSURE, 15X

Figure 66 Rain Erosion of Nickel at 1120 ft/sec

Ductile pitting erosion is also observed in sand erosion of ductile metals at moderate velocity at and near normal incidence. An example is shown in the scanning electron micrograph of Figure 67 taken from recent work under this program. The material shown is a Ti-6Al-4V sample exposed to impact at approximately 900 ft/sec by a Mil-E-5007-C sand mixture in the rotating arm erosion apparatus. The large pits are apparently formed as single impact craters in this case. The resistance of a material to erosion by this mechanism will depend on its resistance to plastic deformation, which is expected to correlate roughly to its yield strength when impact velocity is low, to its hardness at intermediate velocities, and to its hardness and density at very high velocity when hyper-velocity cratering is important.

2. Abrasion

When a ductile material is scratched by a hard particle dragged over its surface under load, a small amount of material is cut or sheared away. This is the classic mechanism of abrasive wear of metals (23) and is also the apparent dominant mechanism of erosion by solid particles impacting a surface obliquely. This mechanism of erosion is illustrated in the scanning electron micrograph of Figure 68 taken from recent work under this program. The material is again the Ti-6Al-4V alloy, and the sample has been impacted by the standard test sand at a velocity of approximately 900 ft/sec at an angle approximately 35° to the plane of the surface. The scratch marks made during abrasive rubbing by the impacting sand particles can be seen clearly. The rate of material removal by abrasion is very sensitive to the size and shape of the abrading particles



Sand erosion of a ductile material at near normal incidence. The surface of a Ti-6al-4V sample exposed to sand erosion at ~ 900 ft/sec and at near normal incidence. The eroding sand was a specification MIL-E-5007-C mixture. The bright area of the figure is a sand particle embedded in the metal. Scanning electron micrograph: 1300X.

Figure 67. Micrograph of Sand Erosion of Ductile Material



Sand erosion of ductile material at oblique incidence. The surface of a Ti-6Al-4V alloy sample exposed to sand erosion at ~ 900 ft/sec and an angle of incidence near 35° . The eroding sand was a specification MIL-E-5007-C mixture. Scanning electron micrograph 1300X.

Figure 68. Micrograph of Sand Erosion of Titanium Alloy

and to the resistance of the solid to dynamic cutting which can be very roughly correlated to its static hardness. Under suitable simplifying assumptions, a simple relation may be derived for the rate of material removal during abrasive wear (24). The classic formula was modified by Finnie (26, 27) to apply to sand erosion of metals by angular particles. This relation predicts the correct dependence of the rate of erosion on velocity. An abrasive mechanism may also apply to rain erosion of ductile metals at oblique incidence and moderate to high velocity.

3. Polishing

If a ductile solid is wiped or polished by a suspension of fine particles, solid material is smeared over the surface to create a semi-amorphous polished layer. Some material will be lost as material is smeared off the surface or carried away through adhesion to the polishing particles. As shown in work summarized by Bowden and Tabor (24), the polishing process is largely governed by frictional heating of the solid surface. They concluded that the polished layer is progressively melted by frictional heating. More recent work indicated that the material need not necessarily be melted; the polished layer may be created and deformed through high temperature creep. In either case the melting point of the material is predicted to be a dominant variable governing the rate of polishing; this feature has been observed experimentally. The polishing mechanism may be important in the erosion of ductile materials moving through dense clouds of fine dust. Thus, Compton (25) found that the dominant material variable governing the rate

of erosion of metal alloys in dusts was the melting point of the alloy. Surface heating in dust erosion was studied by Laderman, et al, (28) who concluded that the surface temperature of Teflon eroded in a fine sand at a moderate velocity exceeded its melting point.

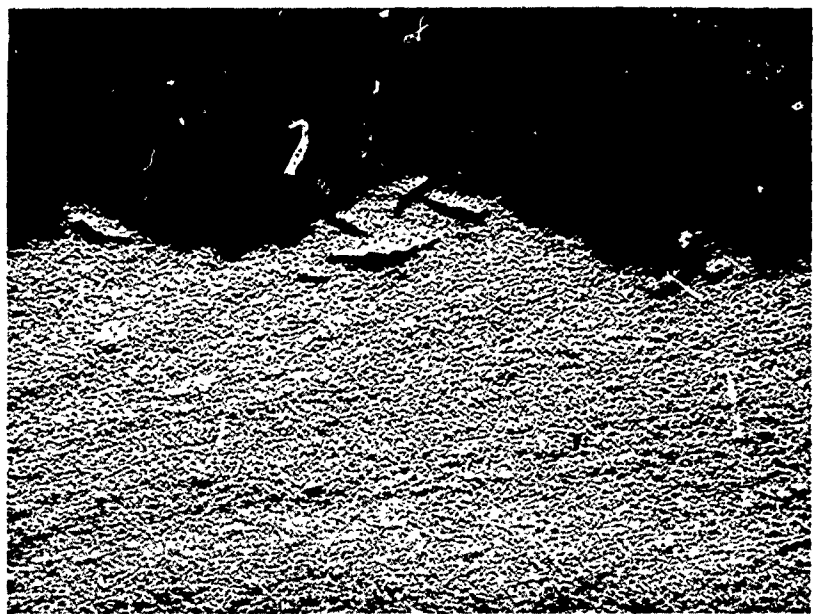
4. Fatigue

If a ductile polycrystalline body is subjected to repeated impacts on its surface which cause the yield strength to be exceeded over some part of the interior of the material, a subsurface layer of deformed material will gradually develop. Within this layer an inhomogeneous state of residual stress is developed. If the damage progresses far enough before this layer is removed through ductile erosion, fatigue cracks will nucleate and begin to propagate. The junction of fatigue fractures will cause material removal. Fatigue is found in all types of erosion of ductile materials and is particularly noted when the eroding particles impinge normally at low velocity. For example, Marriot and Rowden (29) identified and studied the progressive development of fatigue damage in several ductile metals exposed to multiple impact by a high speed water jet. Moore (3) noted the development of subsurface damage and the subsequent development of fatigue cracks in steel exposed to the normal impact of glass spheres at 250 ft/sec. Recent work, Morris (8) indicates the importance of subsurface cracking in the later stages of erosion of soft aluminum subjected to rain erosion at 730 ft/sec and to cavitation erosion in the standard field of a magnetostrictive oscillator (31). The nature of metal fatigue in

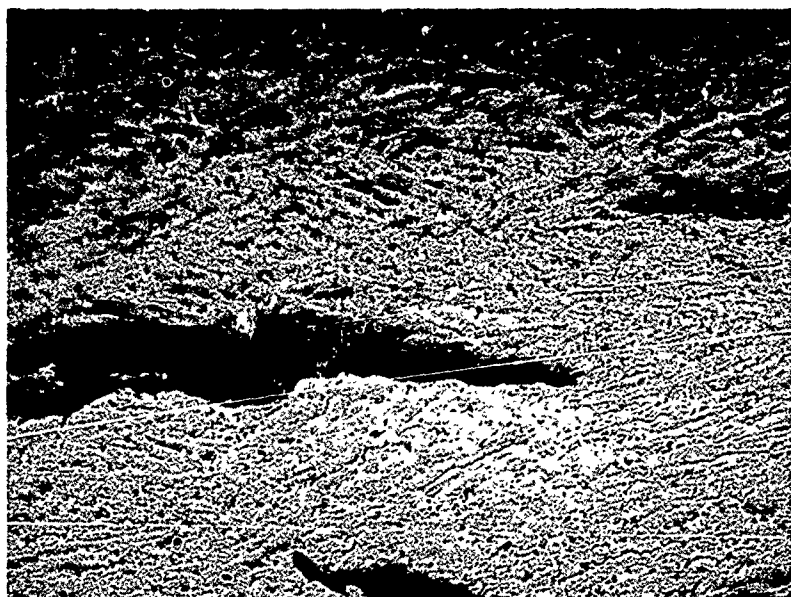
this dynamic environment is poorly understood. Attempted correlations of erosion rate with static fatigue properties have met with little success (32). Fatigue cracks have been found to be responsible for large-scale material removal in Ti-6Al-4V after an exposure time of one hour in a rainfall of 1 in/hr at 1120 ft/sec. These cracks are easily seen in the sectioned sample shown in Figure 69.

5. Tearing

Elastomeric materials subjected to repeated liquid impacts at moderate velocity fail through the propagation of tear-like fractures. Both the site of origin and the propagation characteristics of these fractures seem to be extremely sensitive to elastomer type. Thus a neoprene coating layer exposed to rain impact at 730 ft/sec rapidly develops a dense distribution of fine tears propagating in from its surface. The erosion of the coating is apparently governed by the junction of these tears. A typical urethane coating exposed to the same environment maintains the integrity of its outer surface. Tears originate in this case either at the coating-substrate interface or from voids or other included flaws in the body of the coating. The density of tears is typically very small, and initial damage to the coating is marked by the removal of a chunk of coating of appreciable area, presumably through the growth and accretion of one or only a few fractures. Examples of this mechanism will be described in more detail in the sections on bulk polyurethanes and urethane coatings.



(a) 350X



(b) 700X

Figure 69. Erosion of Ti-6Al-4V at 1120 ft/sec Showing Subsurface Cracks

6. Brittle Fracture

Brittle solids such as ceramics undergo little or no plastic deformation on impact at typical erosion velocities. On the other hand these materials usually have very low fracture toughness since their micromechanical yield strengths are so high that material near the tip of an embedded flaw will respond elastically to stresses. Material removal during erosion is observed to proceed through the junction of fractures generated from flaws, usually at the sample surface, where the tensile stresses imposed during impact are greatest.

Mechanisms of brittle erosion have been studied in the rain and sand erosion of brittle samples tested in the AFML-Bell rotating arm apparatus. The rain erosion of brittle samples in this research is complicated by the fact that the size of the impacting droplets is significant compared to the size of the sample. This, coupled with geometric intensification of droplet impact when the rain-drop impinges on a roughened surface, has the consequence that fractures are propagated deeply into the sample and erosion tends to proceed through the removal of large chunks. An interesting example of the sand erosion of brittle materials is the erosion of ceramic coated metals. Both carbide and boride coatings have been tested in the standard sand impacting at a velocity of approximately 900 ft/sec. The coatings erode through the nucleation of pits in the coating which expose portions of the metal substrate followed by the lateral spreading of these pits through preferential fracture along their periphery. An example of the periphery of such a pit is shown in the scanning electron micrograph of Figures 15b and 70. From the appearance of this surface

the erosion of the coating is largely governed by fractures due to discrete impact. Moreover, the fracture surface terminating the intact coating is oriented nearly perpendicular to the impinging stream of sand particles.

B. Mechanisms of Sand Erosion

Micrographic studies were carried out to identify the principal mechanisms of sand erosion in materials whose resistance to sand erosion had been characterized on the rotating arm. The materials studied included three ductile metals: 6061-T6 aluminum, the titanium alloy Ti-6Al-4V, and type 403 stainless steel; two types of ceramic coating on type 403 stainless steel: titanium carbide and a boride proprietary to Solar Aircraft; and two filament-reinforced composite materials: aluminum-borsic and graphite-epoxy.

The samples were all tested at a true velocity of incidence of approximately 900 feet per second. This velocity of incidence is the vector sum of the sample speed on the rotating arm and the finite velocity of the sand introduced into the chamber. Hence the sand impinges on the turbine shaped flat samples at a slight angle, simulating impact conditions within an operating turbine. The sand is in all cases a Mil-E-5007-C mixture.

1. Ductile Metals

The principal mechanism of erosion of the three ductile metals was the classic abrasion process described in the preceding section. However, the tip of the flat specimen was ductilly blunted so that impact was virtually

normal to the surface, and some evidence of ductile pitting erosion was observed, as illustrated in Figure 67. With respect to erosion by abrasion, three principal observations were made. (a) The markings of abrasion can be clearly seen on the sample surfaces: as in Figure 68, the abrasion tracks cut during sand impact were clear and evidence the surface irregularity of the sand particles. The sand particles are apparently neither pulverized nor appreciably deformed during the principal stages of erosive impact. An occasional sand particle had adhered to the surface. However, imbedded particles were not common, indicating that no significant adhered debris layer forms during erosion. The imbedded particles were in all cases severely fractured. It is not clear whether this particle damage occurs during impact or whether it is due to subsequent impacts of sand particles on the imbedded particles. (b) The depth and definition of the abrasion markings is a measure of the scratch hardness of the material; hence the appearance of typical sand tracks gives some indication of the relative hardness of these metals under the dynamic erosive load. If micrographs are compared, one sees that the abrasion tracks are most clearly defined on the aluminum alloy, that they are also clearly defined in those portions of the steel alloy which are free of precipitates, and that they are least marked on the titanium. Hence dynamic hardness apparently increases in the sequence aluminum/steel matrix alloy/titanium. (c) The erosion is markedly influenced by hard precipitates dispersed through the alloy matrix. This is particularly evident in the 403 steel where precipitate density is very high. Abrasion tracks on the steel surface are discontinued or terminate at regions of high precipitate density. These regions appear highly resistant to erosion through abrasion.

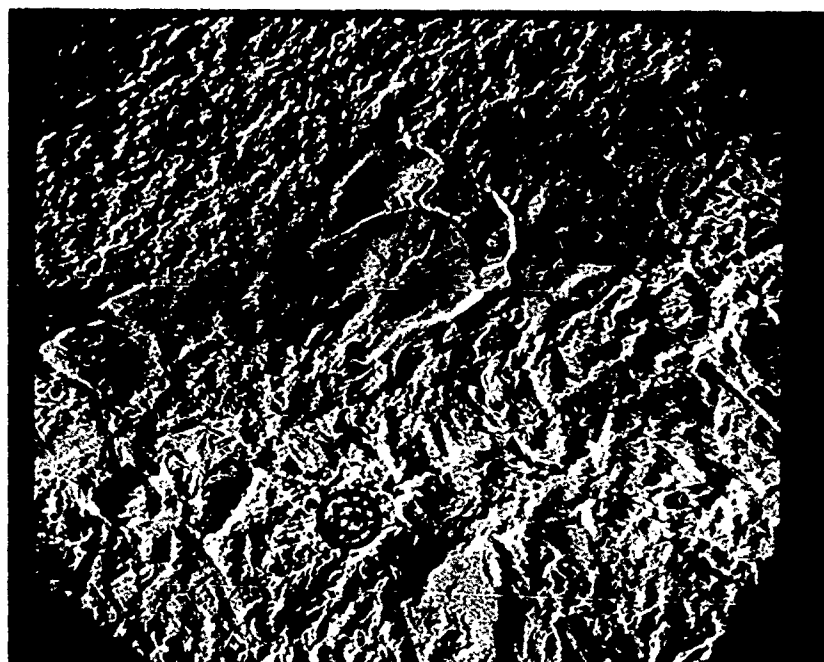
Regions within the alloy which have been dispersion-hardened by a distribution of precipitates which are small compared to the size of the more erosive sand particles seem particularly resistant. When precipitate size is larger, the precipitates tend to be fractured and broken out of the alloy surface. Precipitates in the titanium alloy are also effective in retarding local abrasion. However, the precipitates are so dispersed that their aggregate effect is not great.

These observations lead to the conclusion that dispersion hardening may prove an effective technique for increasing the resistance of ductile alloys to sand erosion, particularly if the hardening particles are densely arrayed and if they are small compared to the size of the grains of impacting sand.

2. Ceramic Coatings

The principal mechanism of erosion of the ceramic coating materials was brittle fracture. There were marked differences, however, in the appearance of erosion on the two coatings. Since the composition and method of application of the boride coating is unknown to us, it is hard to interpret these differences with any certainty.

The titanium carbide coating eroded through the propagation of rather large brittle fractures, which seemed to grow easily both perpendicular to the coating and along it. Erosion is most rapid around the periphery of areas where the coating has been removed. Such an area is shown in Figure 70. The terminus of the coating shows, in



Sand erosion of a ceramic coated metal. The figure shows the surface of a titanium carbide-coated 403 stainless steel sample exposed to sand impact at ~ 900 ft/sec at an angle of incidence near 35° . The dark area in the upper portion of the figure is the surface of the coating (Area A). The light area in the lower portion of the figure is exposed 403 steel (Area B). The greyish band (Area C) across the coating center of the figure is the fracture surface terminating the eroding coating. Scanning electron micrograph, 325X.

Figure 70. Micrograph of Sand Erosion of Titanium Carbide Coating

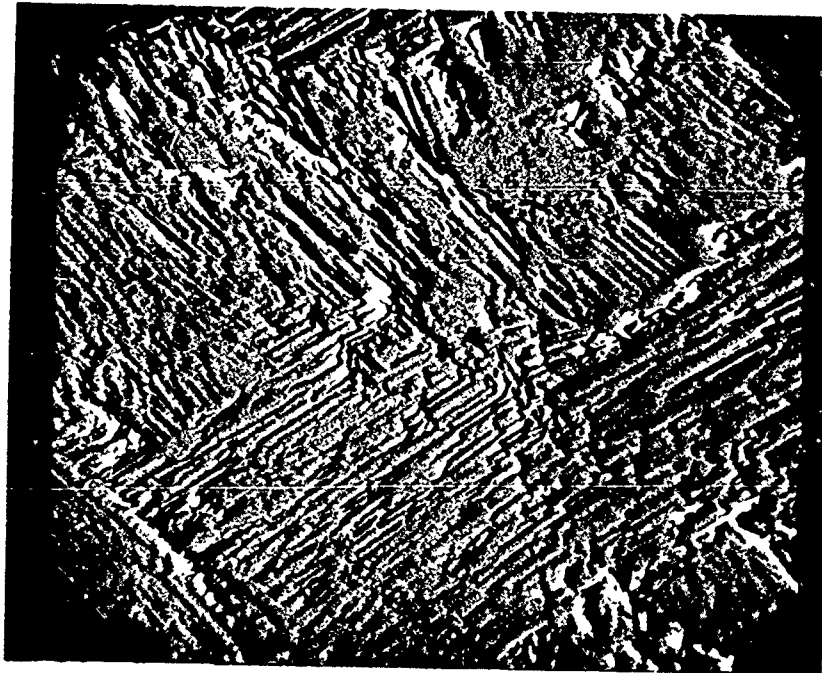
cross section, a dense array of through fractures. The portion of the coating which has not yet been eroded has locally rough surface laced by a network of microcracks of significant depth. Inspection of uneroded areas on the underside of the sample indicates that this is the original state of the coating surface. Erosion pits nucleate in the surface through local growth and juncture of these microflaws. Once nucleated, the pits grow rapidly.

The boride coating tested is significantly more resistant to sand erosion. The apparent rate of pit nucleation and growth are both appreciably lower than on the titanium carbide coating. While inherent differences between the two materials may account for this erosion resistance, a major cause is the better physical quality of the boride coating. The surface of the boride coating is very smooth compared to that of the titanium carbide coating. While the boride coating also shows a network of microflaws when inspected in the electron microscope, these inherent flaws are small compared to those seen in the titanium carbide coating. A further observation is that crack propagation over the surface of the boride coating seems to be retarded; flaws rather grow perpendicular to the coating. Erosion pits nucleate through the junction of nearly parallel flaws oriented toward the substrate, creating deep wedge-shaped pits. These grow by chipping at their periphery, but discrete chips are small and the rate of growth is comparatively slow. These observations give us the impression that the surface of the coating has been chemically or thermally treated to produce a residual compressive stress.

3. Fiber-Reinforced Composites

Observations on the erosion of composite materials are in many ways similar to our conclusions on the effect of dispersed precipitates. The brittleness of the filaments and their size and spacing relative to the size of the more erosive sand particles are important parameters. Comparative micrographs of the graphite-epoxy and aluminum-Borsic composites are shown in Figures 71 and 72. Figure 71 shows the appearance of a graphite-epoxy composite eroded at a velocity of incidence near 900 feet/second and an angle of incidence near 55° in the standard sand field. Fiber spacing is in this case small compared to the mean diameter of the more erosive sand particles, however the length of the filament is very large compared to the diameter of the impinging particles. Erosion progresses through brittle fracture across groups of fibers. Figure 72 shows the appearance of an aluminum-Borsic composite eroded under identical conditions. In this case fiber spacing, fiber size, and particle diameter are of roughly the same order of magnitude as one can see from the adhered sand particle appearing in Figure 72. The erosion of the composite specimen is controlled by ductile erosion of the aluminum matrix; the reinforcing fibers are fractured and removed from the surface almost as soon as they are exposed through matrix erosion. This behavior is more clearly seen in Figures 73-75. In light of these data it is not surprising that the rate of erosion of the aluminum-borsic composite is very close to that of the unreinforced aluminum alloy.

These observations reinforce the conclusion that the possibility of developing composite materials having desirable properties for structural optimization with



Sand erosion of a graphite fiber composite. The figure shows the surface of a graphite-epoxy composite sample exposed to sand erosion at an impingement velocity of ~ 900 ft/sec at an angle of incidence near 55° . The sand was a MIL-E-5007-C mixture. Scanning electron micrograph; 168X.

Figure 71. Micrograph of Sand Erosion of Graphite-Epoxy Composite



Sand erosion of an Aluminum-Borsic composite. The figure shows the surface of a Borsic filament-aluminum matrix composite exposed to sand erosion under conditions identical to those described in Figure IV-6. The bright object in the micrograph is a sand particle which has adhered to the surface. Scanning electron micrograph, 168X.

Figure 72. Micrograph of Sand Erosion of Aluminum-Borsic Composite



Figure 73. Scanning Electron Micrograph at 200X Showing Sand Erosion of a Composite of Boron Fibers in Aluminum Matrix

The surface of the composite shows the results of abrasive action of the sand particles as they traverse the specimen at an oblique angle of 55° at 1450 ft/sec velocity. The brittle fibers are fractured and abraded while the aluminum matrix being more ductile is scoured by the sand particles after one minute exposure to a sand concentration of 2.3 grams/ft³ of air.



Figure 74. View of Fractured Fiber of Boron in Aluminum Matrix After
1-Minute Exposure to Sand Impact



Figure 75. Scanning Electron Micrograph at 400X Showing Void in Surface
of Boron-aluminum Composite

simultaneous erosion resistance is not great. Candidate filament materials are brittle, and they are used in a geometry which virtually ensures filament fracture on sand impact. Sand erosion resistance can be improved by changing the matrix material, but the behavior of the matrix material must lead to desirable composite strength, and hence the available options in choice of matrix material are limited. It seems clear that erosion research should concentrate on the development of coating materials to protect composites rather than on material manipulation to improve the native erosion resistance of the composite.

C. Mechanisms of Rain Erosion

The rain erosion mechanism studies were concerned with ductile metals, ceramic and elastomeric coatings, bulk elastomers and thermoplastics, and fiber-reinforced composites. Generally, specimens for this research have been supplied after weight-loss data have been acquired, so the mechanism studies have investigated the mechanisms which predominate during the later stages of the erosion process. Under this program a series of tests were conducted on well characterized specimens of titanium alloy (Ti-6Al-4V), three formulations of bulk polyurethane, and a 181 glass-fiber reinforced epoxy. The purpose of these tests was not to obtain weight-loss data, but to investigate the evolution of the initial erosion mechanisms before the occurrence of measurable weight-loss. The information acquired from these tests indicates that the erosion mechanisms during the very early stages of the rain erosion process can be different from those observed in the later stages when large-scale material

removal takes place. The initiation of the later stage mechanisms can be correlated roughly with a fairly abrupt change in the plots of weight-loss as a function of time.

1. Erosion of Ductile Metals

Initial research on the rain erosion of ductile metals which concentrated on aluminum and its alloys has been reported in a previous report (8). During the current period this research was extended through examination of the erosion of pure nickel (INCO 270), type 403 stainless steel, and titanium alloy Ti-6Al-4V.

Some static mechanical properties of four alloys are shown in Table XLII, where these mechanical properties are compared to those of an erosion-resistant aluminum alloy 7075-T6. The erosion behavior of these four alloys is compared in Figure 76, which shows erosion measured as total volume lost as a function of time of exposure for tests conducted at a speed of 1120 ft/sec (Mach 1.0) in a one-inch per hour rain field, 1.8 mm. mean droplet size. A comparison of Table XLII with Figure 76 shows no obvious relation between mechanical properties and erosion resistance. In particular, the high erosion resistance of pure nickel is anomalous. Some probable explanations of the relative erosion resistance of these alloys does emerge, however, from a close examination of the eroded samples interpreted in light of previous work reported (8) on the mechanism of rain erosion of ductile metals.

TABLE XLII
MECHANICAL PROPERTIES OF METALS TESTED

	YIELD STRENGTH (KSI)	TENSILE STRENGTH (KSI)	ELONGATION %	HARDNESS (BRINNELL)
Al7075-T6	73	83	11	150
Ni (99.9)	8.5	48	30	75
403 Steel	85	110	24	225
Ti-6Al-4V	130	135	15	250

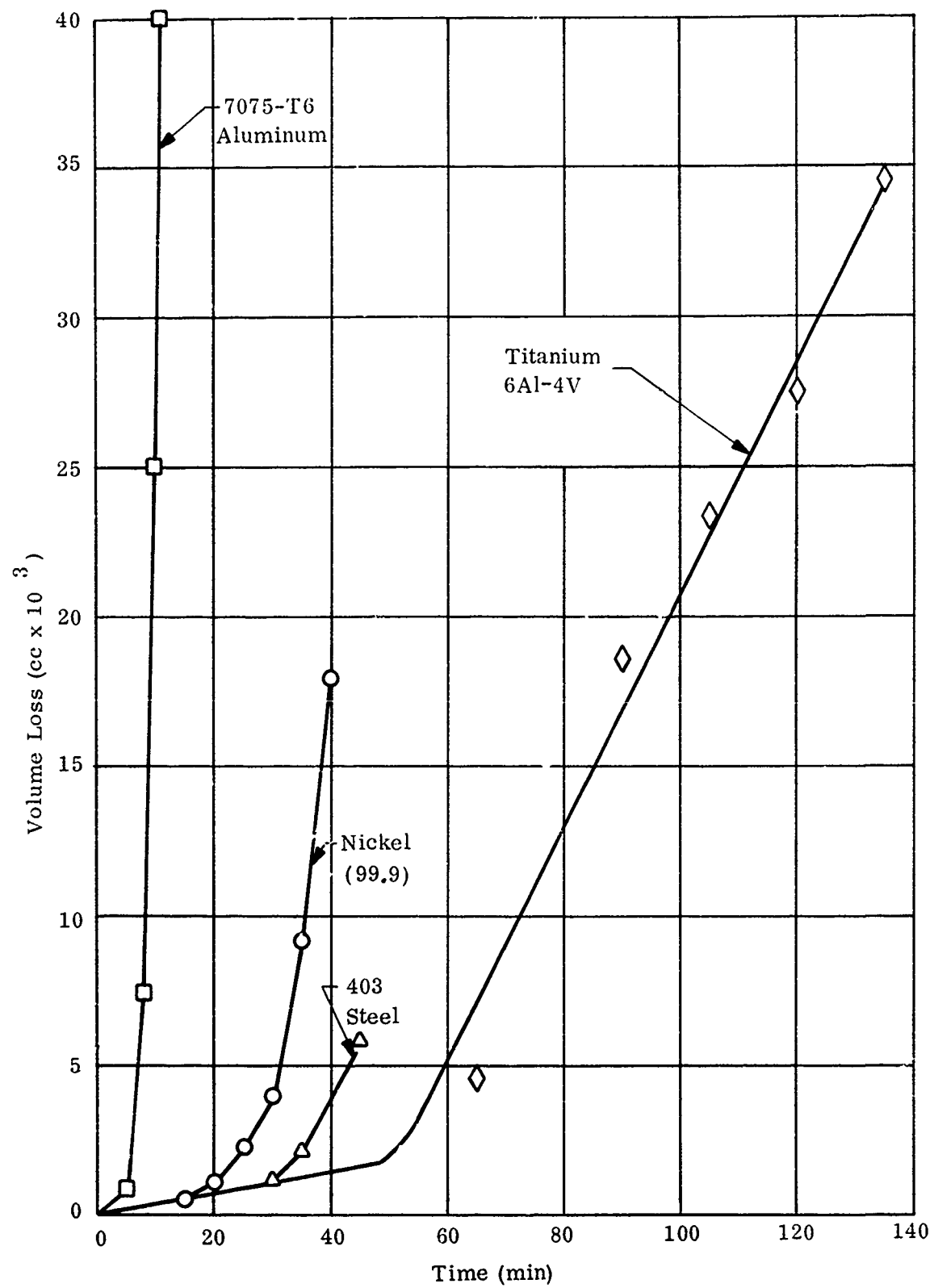


Figure 76. Rain Erosion of Four Ductile Metals at 1120 ft/sec

a. Erosion of Pure Nickel

The pure nickel samples erode via the mechanisms of ductile erosion previously identified in studies of aluminum alloys. The surface of the nickel sample is gradually roughened on exposure to rain through accumulating plastic deformation. As the surface roughens, the loads imposed in droplet impact are intensified at the base of surface pits. These pits sustain substantial plastic deformation. Material is removed from the surface through shear of the lips of surface pits, and in chunks as adjacent pits grow to overlap one another.

The mechanism of erosion of pure nickel is illustrated in Figures 66 and 77. Figure 66a shows the surface of a sample exposed at 1120 ft/sec for 10 minutes. A few isolated surface pits are visible. Figure 66b shows the surface of a sample exposed for 40 minutes. The pits have increased in depth and number, and the surface has taken on an appearance generally similar to that of aluminum alloys which have begun to erode severely. The rate of erosion accelerates markedly over this time interval, as can be seen from Figure 76. Figure 66c shows a cross section of the nickel sample after 40 minutes exposure. The ductile nature of the damage process is evident in this cross section. If these pits are compared to those typically found in aluminum alloys (8) they are seen to be somewhat shallower and broader.

Figure 77a shows micrographs of etched cross sections of the 40-minute nickel sample. The severe ductile flow which occurs as the nickel samples are eroded is evident in these micrographs. Surface features like those in the



(a)



(b)



(c)

Figure 77. Micrographs of Erosion Damage on Etched Nickel Sample

micrograph of Figure 77b seem to indicate that some material is removed from the lips of erosion pits through shear flow. Figures 77a and 77c illustrate the process of pit accretion as ductile pit growth occurs.

While the overall mechanism of erosion of pure nickel is clear its high erosion resistance (relative to that of aluminum) is not easy to explain. As one can see from the data given in Table XLII the mechanical properties of nickel 270 compare unfavorably to those of the aluminum alloy 7075T6. Nonetheless the nickel is far more resistant to erosion.

Morphologically, the high erosion resistance of the nickel seems attributable to the fact that the pits formed in the nickel are broad and shallow. Such pits tend to minimize the likelihood that high velocity water jets will be formed in raindrop impact, and the velocity of those jets which do form. Both factors are expected to give a significant reduction in the rate of ductile erosion.

The mechanical interpretation of the observed morphology of nickel erosion is unclear, but two factors seem particularly important: the high elongation of the nickel in tension tests, indicative of a high ductility and tendency toward necking and the high density. The high ductility of the nickel has the consequence that the alloy surface should be able to withstand considerable plastic shearing action by water outflow without forming deep cracks or asperities. The high density of the nickel has the consequence that the material is very resistant to "tunneling" on collision with very high velocity outflows of water drops. In fact, when the velocity of impact

of a jet of water is so high that the stagnation pressure it imposes is large compared to the yield strength of the impacted solid, one may show that the density of the solid is the primary determinant of the depth of damage. In the high velocity region the depth of penetration due to jet impact tends to vary as $\rho^{-\frac{1}{2}}$, where ρ is density. Since nickel is slightly more than three times as dense as aluminum, a true high velocity jet will penetrate only about 0.6 as far into it. It is hence not too surprising that the pits formed in nickel are broad and shallow compared to those in aluminum exposed at the same velocity.

b. Erosion of 403 Stainless Steel

The mechanical properties of 403 stainless steel are much closer to those of the titanium alloy than to those of nickel, yet the erosion resistance exhibited by the steel in these tests is not much greater than that of nickel and is not comparable to the erosion resistance of titanium. A closer examination of the samples tested shows that the poor performance of the steel is due in large part to microstructural flaws in the samples that were tested, which cause elements of the sample surface to be particularly liable to erosive attack.

The overall appearance of the eroded steel samples is shown in Figure 78. The sample surfaces are marked by deep pits which show evidence of considerable plastic deformation. But these pits appear only along a few discrete lines along the length of the specimen. Virtually all material removed has come from the vicinity of these rolling marks or lines.

RATE: 0.000311: TRSTS
1" /HR. RAINFALL - 1.8 MM DROP SIZE

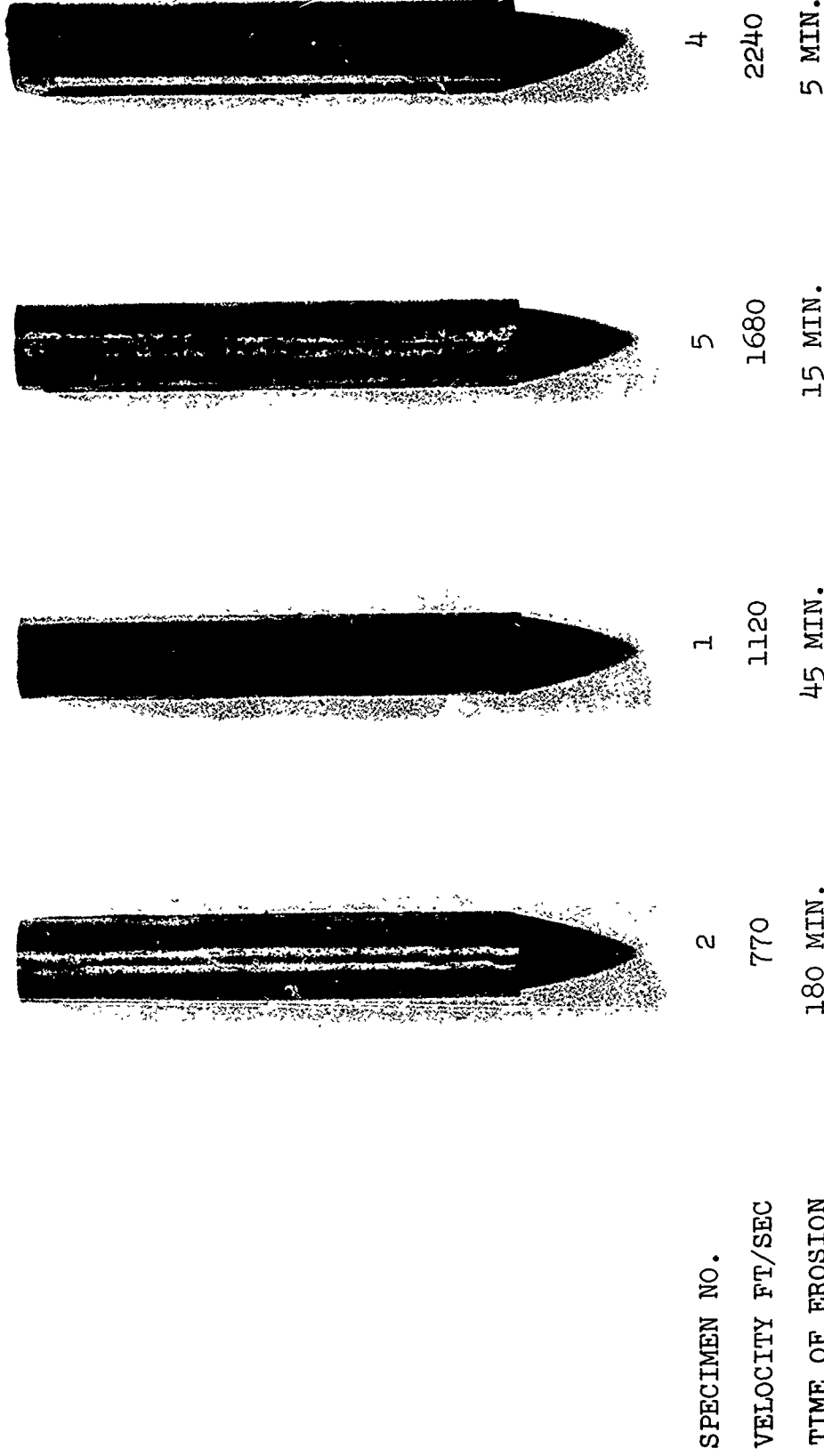


Figure 78. Rain Erosion Tests of 403 Stainless Steel

An examination of sample cross sections reveals the source of these erosion features. The 403 steel samples tested were machined from rolled stock. As shown in the typical micrograph in Figure 79, the rolling operation left planar distributions of brittle precipitates and cracks through the bulk of the material. These planar flaws intersect the exposed face of the samples along lines parallel to sample length. On exposure to rain the lines of intersection are attacked by flowing water to open deep, narrow pits. An example is shown in Figure 80a which exhibits a portion of a cross section of a sample exposed to rain at 1120 ft/sec for 45 minutes. The lip of the planar crack intersecting the surface in this micrograph has been bent back to open a pit. Pits of this shape are particularly liable to attack via high speed jetting on water impact. The pit shown in Figure 80b has undergone this attack. The material near the pit is severely deformed with apparent loss of material.

Reference to Figures 80a and 80b shows that portions of the 403 steel surface somewhat removed from these planar flaws are not seriously eroded even after 45 minutes exposure at Mach 1.0. It seems clear from this evidence that 403 stainless steel samples prepared to have unflawed, homogeneous surfaces would have substantially greater erosion resistance.

c. Erosion of Titanium-6Al-4V

The titanium alloy samples tested showed outstanding resistance to erosion in rain. The major cause of material removal in the titanium samples is through progressive cracking, apparently in a fatigue-like mechanism.

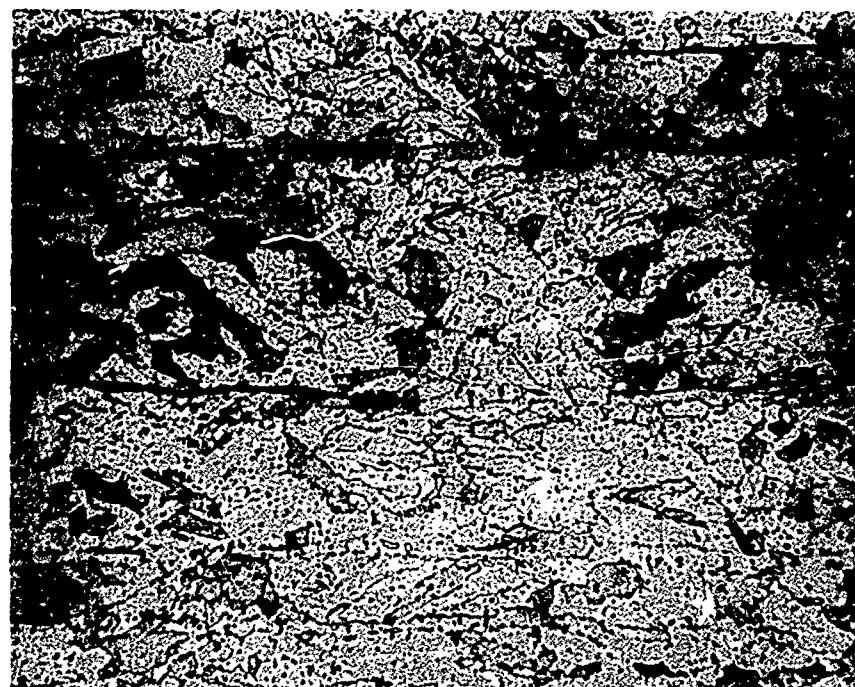
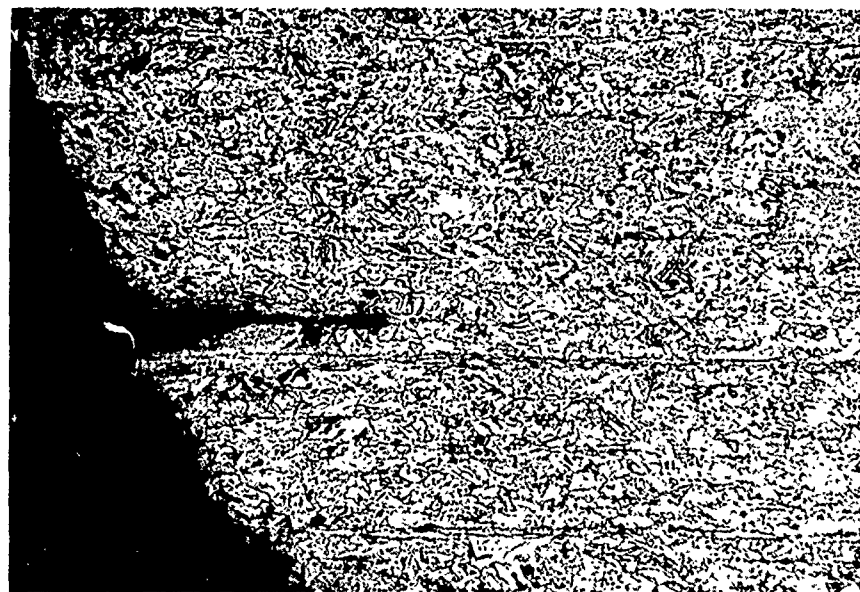
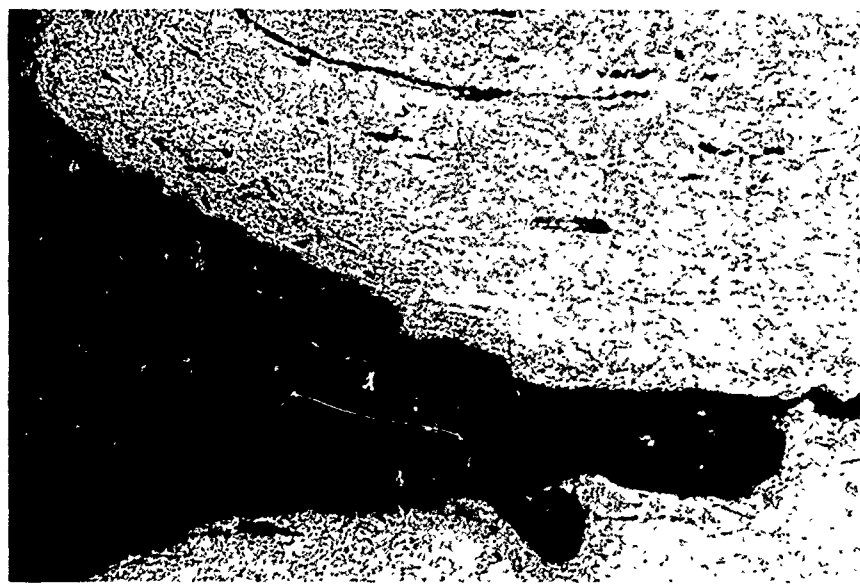


Figure 79. Structure of 403 Stainless Steel Showing Planar Precipitates and Flaws



(a) SURFACE PIT, AT 250X



(b) PIT AFTER EROSION ATTACK 400X

Figure 80. Pits in Surface of 403 Stainless Steel Exposed at 1120 ft/sec for 45 Minutes

Material is removed through the junction of these cracks. The morphology of erosion is such that the surface remains relatively smooth during the early stages of erosion, and hence the titanium is less subject to the intense jetting impacts involved in water out-flow on a rough surface. The strength of the titanium alloy reduces erosion of smooth surfaces, and the type of erosion experienced tends to keep the surface relatively smooth as material is removed; the result of these two effects is outstanding erosion resistance.

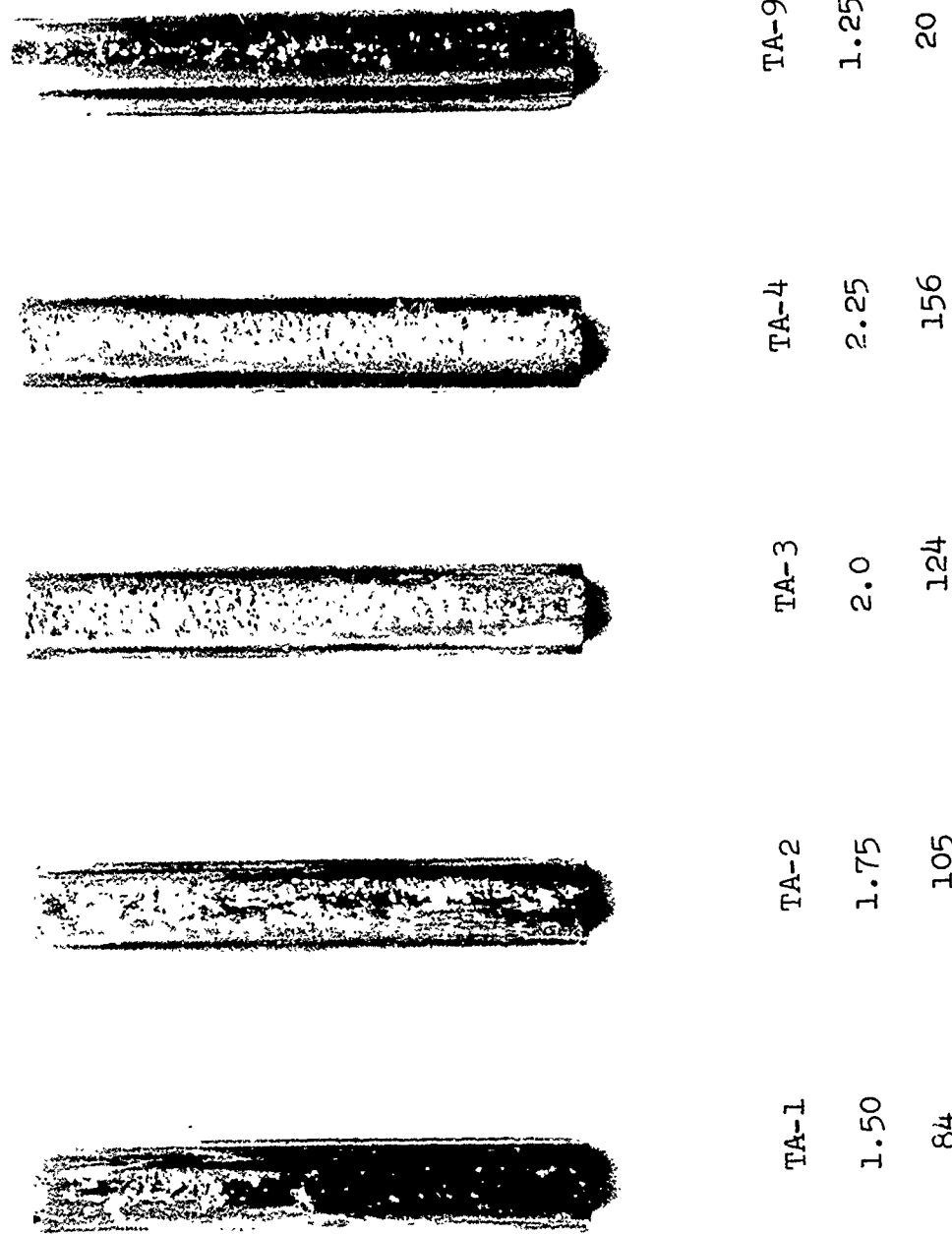
The overall appearance of the Ti-6Al-4V alloy samples exposed to rain at 1120 ft/sec is shown in Figure 81. The eroded surfaces of three of these samples are shown in Figure 83 at higher magnification. An additional titanium specimen was run for an exposure time of 30 minutes in order to observe the early development of the erosion damage. The condition of the surface is shown in Figure 82. The small pits developing on this specimen can also be identified on the specimens shown in Figure 83; however, the sequence of photographs in Figure 83 indicates that the very small pits develop into shallow, flat-bottomed pits. On further exposure the number and the mean lateral size of the broad, shallow pits increase. On this scale the pits appear to extend laterally without deepening appreciably.

The specimen with an exposure time of only 30 minutes was particularly informative. The surface of the specimen was polished before testing in order to differentiate between surface features which are produced by droplet impacts and those which are already present on the surface. The polishing procedure was to grind the surface

RAIN EROSION TESTS

1" /HR RAINFALL - 1.8 MM DROP SIZE

1120 FT/SEC - 250 TORR



SPECIMEN NO.	TIME OF EXPOSURE HOURS	WEIGHT LOSS MILLIGRAMS
TA-1	1.50	84
TA-2	1.75	105
TA-3	2.0	124
TA-4	2.25	156
TA-9	1.25	20

Figure 81. Erosion of Ti-6Al-4V at 1120 ft/sec

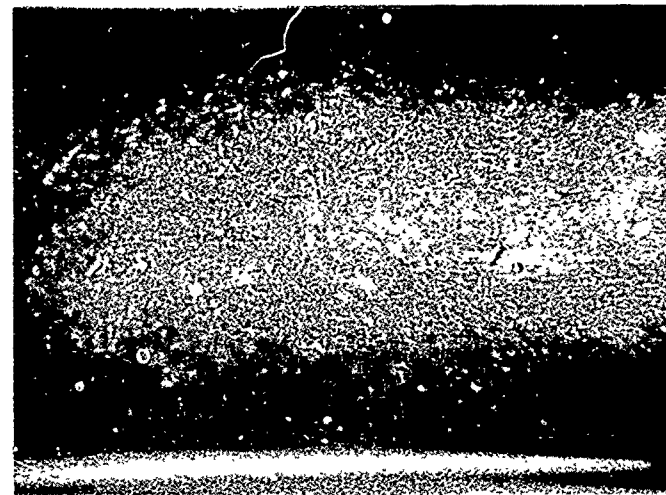
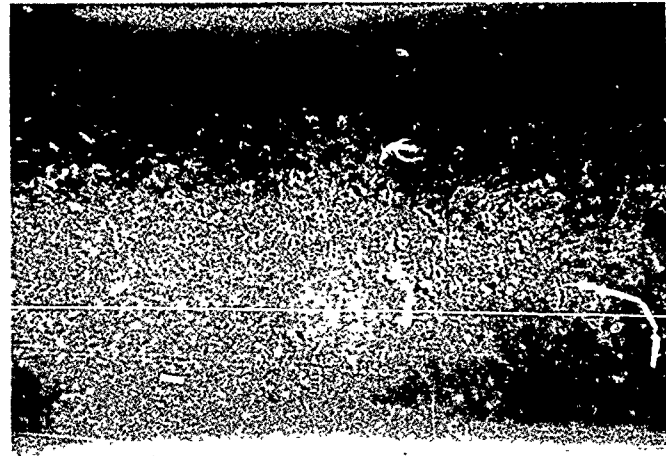


FIGURE 82. Erosion damage on Ti-6Al-4V after 30-minute exposure to 1 in/hr rainfall at 1120 ft/sec.

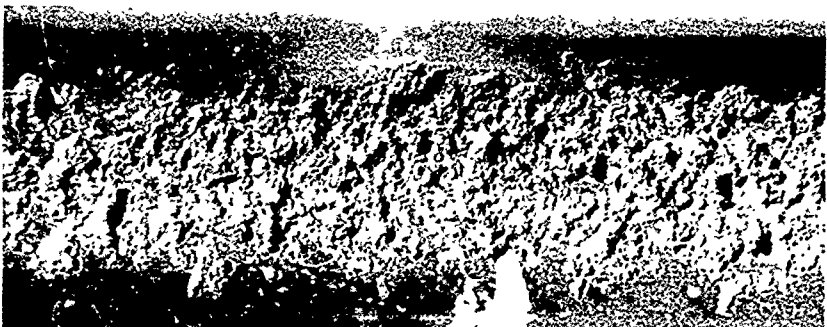
7 X



(a) AFTER 75 MIN. EXPOSURE



(b) AFTER 105 MIN. EXPOSURE



(c) AFTER 135 MIN. EXPOSURE

Figure 83. Erosion of Ti-6Al-4V at 1120 ft/sec - 4X

on 200 through 600-grit SiC wet paper and fine grind with diamond paste. The surface was then polished with a 0.05μ alumina. Examination of the as polished surface using surface replication and transmission electron microscopy with magnification up to 20,000X showed the original surface was extremely smooth with a very low density of surface disruptions. After 30 minutes exposure, replicas were made of the eroded surface. Microscopic examination of regions away from the primary damage zones, which were already too gross for the effective use of surface replication, revealed extensive ductile indentations and localized cracking. The indentations were extremely shallow with lateral dimensions ranging from ten to fifty microns. Cracking of the surface was generally very localized and appears to be due to the presence of brittle precipitates at or near the surface. It was relatively rare when surface cracking could not be ascribed to the presence of precipitates. The ductile indentations and localized cracking are the dominant features on the surface before the initiation of material removal.

Optical microscopic examination of the eroded surface indicates that there are three distinct pit configurations which contribute to removal of material. One form is a relatively shallow, smooth-bottomed pit. The rims of these pits are level with the surrounding region and are generally less than five mils in diameter. The specimen was sectioned for better observation of the pit formations. The transverse sections were polished and etched with a general purpose etchant consisting of one part hydrofluoric acid, one part nitric acid, and two parts glycerine. Additional metallograph examinations will be

required before an accurate evaluation of the grain size in this titanium alloy can be made; however, from preliminary observations it appears that the Ti-6Al-4V is a very fine-grained material with a mean grain size on the order of one mil. From the form of the smallest pits seen in Ti-6Al-4V and this preliminary information on the grain size, it is conjectured that the initial mechanism for material removal is the cracking of precipitates which eventually results in the removal of very small fragments of material. Cracking of the surrounding granular material is also observed in the pits which subsequently develop.

The cracking and fragmentation process continues throughout the period of exposure to the erosive environment. Once shallow pits are formed, subsequent droplet impacts initiate tunneling within them. An explanation is still being sought for the preferential erosion of certain areas within the shallow pits: brittle fracture of precipitates and the development of localized cracking within grains may be major contributors to the tunneling phenomenon. Evidence in support of this cracking and fragmentation mechanism is the rounded appearance of the ends of the tunnels and the absence of distortion within the local grain structure. Tunneling into the interior of the material eventually becomes very extensive. This is a common pit configuration on the surface of the sample.

As the tunnels deepen, the droplet impacts produce intense pressures within them which ultimately bend the overlying material outward from the surface for tunnels running nearly parallel to the surface. The elevation of these regions above the surface will increase

with additional droplet impacts, until they are removed from the surface by lateral jetting and localized cracking. Sizable fragments of material were found protruding from the surface. Raised lips were also observed around a large number of pits representing the completion of the process described above. This is a third type of pit configuration which was well-represented on the surfaces of the titanium specimens.

The erosion mechanisms identified in Ti-6Al-4V during the early stages of the erosion process are:

1. Cracking and fragmentation which results in the removal of subgrain and possibly grain-size pieces. This mechanism is continually operative on the surface and within the pitted regions.
2. Preferential tunneling into the material within shallow pits presumably initiated by localized cracking within the pits. Material removal from the tunnels is by the mechanism described in (1).
3. Upheaval of regions of material due to the intense pressure applied to cracks and tunnels during droplet impacts and subsequent removal of raised sections by lateral jetting and cracking. This mechanism causes material removal on a larger scale than the mechanism of cracking and fragmentation listed in (1).

As already stated, the effectiveness of the third mechanism is dependent on cracks or tunnels which run essentially parallel to the surface of the specimen.

The material removed from tunnels extending toward the longitudinal axis of the specimen is at a much slower rate than that due to upheaval of larger fragments. It is for this reason in conjunction with the mechanism of progressive fatigue cracking (to be described) that the pits at the later stages of the erosion process appear broad and shallow as shown in Figure 89.

The description of the erosion mechanisms in Ti-6Al-4V during the very early stages of the erosion process required extensive microscopic investigations employing electron and optical microscopy. The informative observations made with the optical microscope could not be photographed in detail due to the limited depth of field at the magnifications required. Some examples, although lacking in photographic quality, are provided in support of the general descriptions already given of erosion mechanisms in Ti-6Al-4V.

The lightly eroded surface areas on the specimen with a 30 minute exposure time were found to consist of shallow, ductile indentations generally under one mil in diameter and a moderate density of localized cracking (estimated to be on the order of one thousand cracked zones per square inch). The general form of these cracked regions are shown in Figures 84-85. The existence of these regions indicates the presence of brittle precipitates at or near the surface.

The micrographs in Figures 86 and 87 show the details of pits which are approximately 3 to 4 mils in diameter. Cracks are clearly visible along the walls of these pits which tends to support the cracking and fragmentation mechanism.

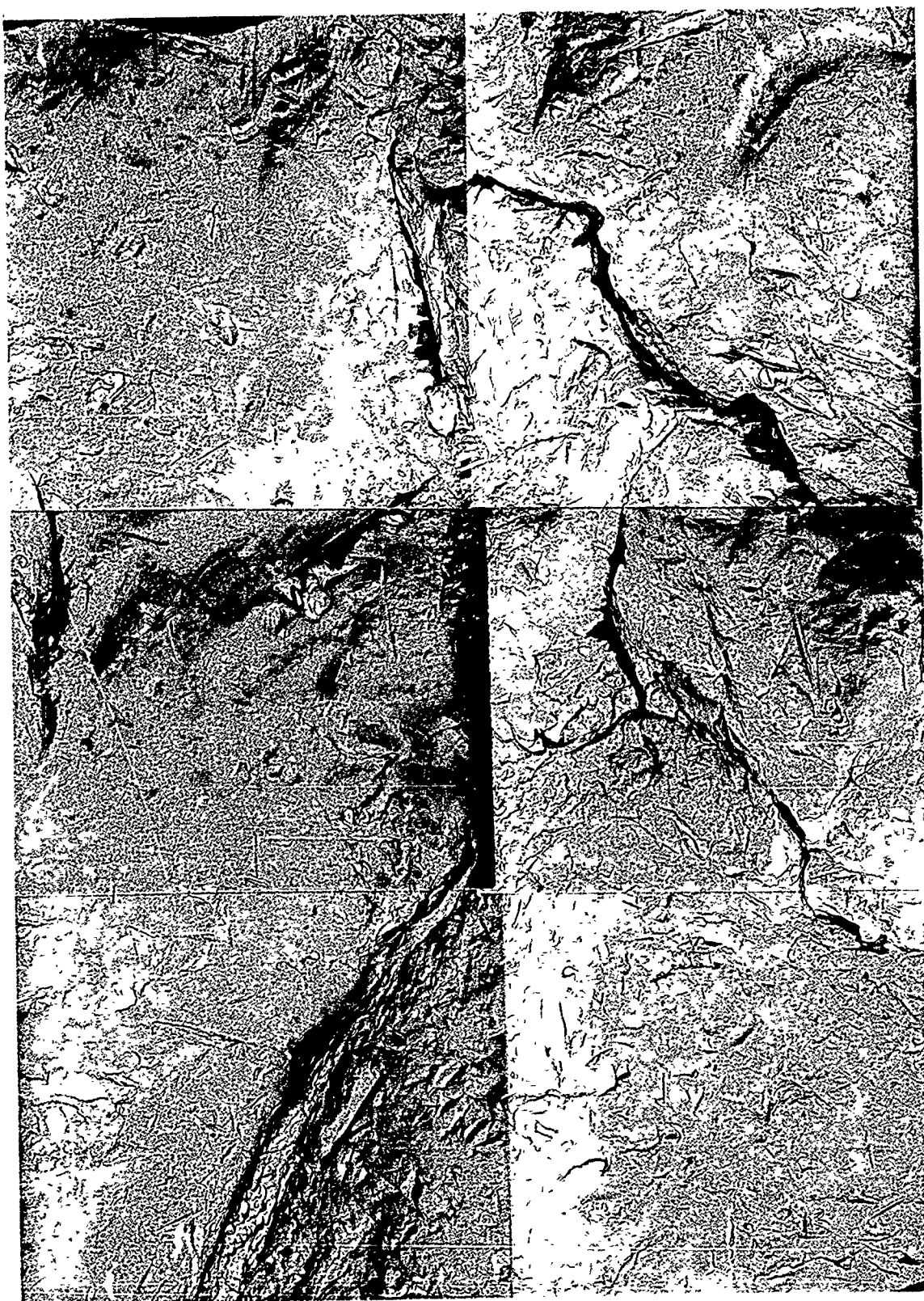


FIGURE 84. Cracking on surface of Ti-6Al-4V - 2000 X

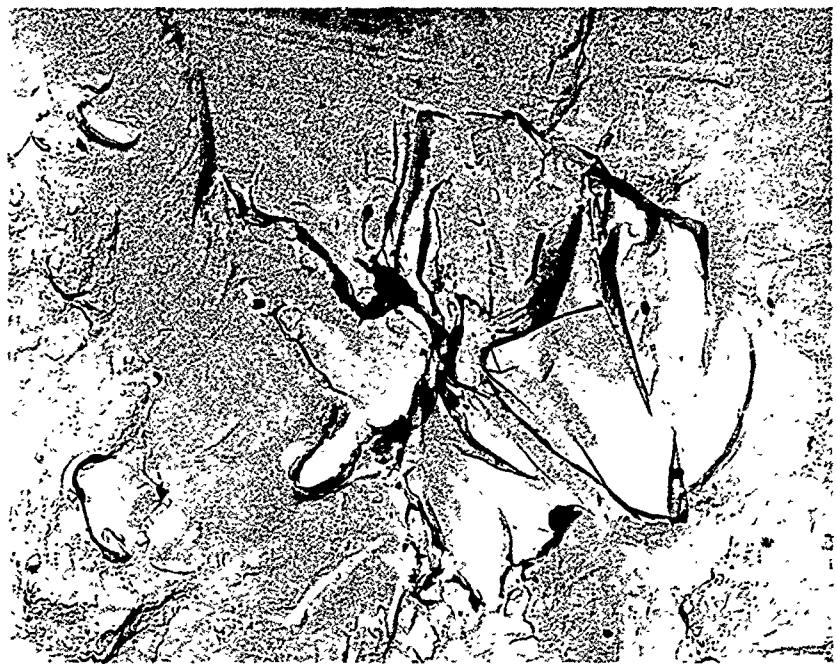
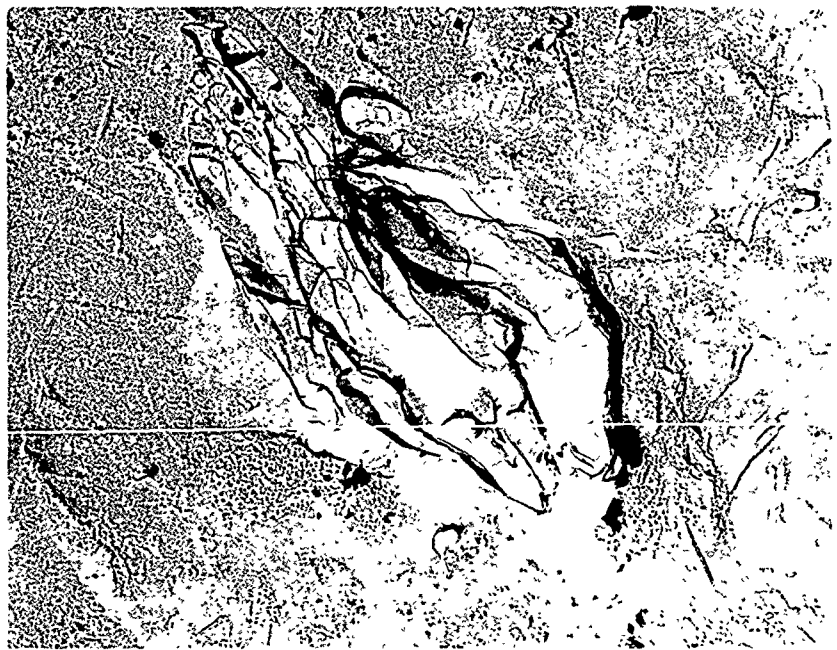
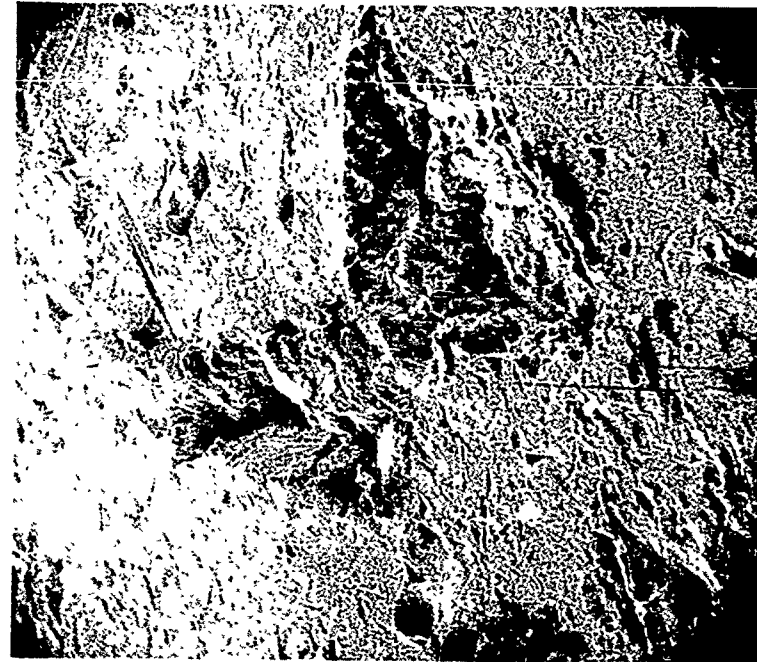


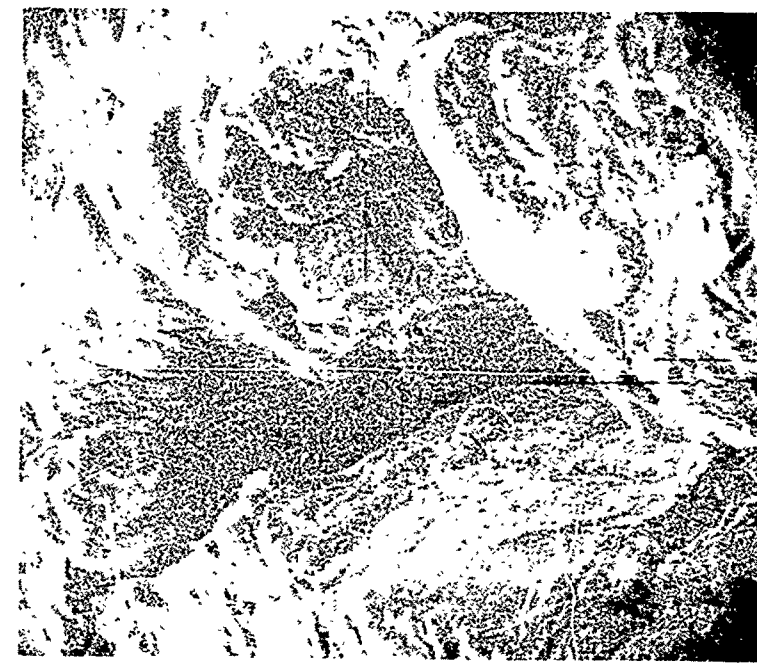
FIGURE 85. Localized cracking at precipitates on surface of Ti-6Al-4V - 3000X

The general form of the pits can be seen most easily on the sectioned specimens. Figure 88 shows a shallow pit with a lateral dimension of approximately 3 mils. Figure 89 shows shallow pits with fairly well-developed tunnels. The pit pointed out on the surface shown in Figure 90 shows a more advanced stage of the tunneling and upheaval process. Unfortunately, the quality of the photograph is such that it is not as illustrative as direct observation in the optical microscope. A tunnel has developed in the pit which is roughly 3 mils in surface area. The region just above the existing pit with a surface area of 4.5 mils is being elevated above the surrounding surface. A similar situation, though not on such a grand scale, is shown in Figure 91. The etched cross-section provides a clue as to the formation of the raised section on the right-hand side of the pit. The horizontal tunnel may have originated as a crack. The walls of the crack are then separated by the applied water pressure forcing the overlying region upward. The tunnel directed toward the surface bifurcating from the main tunnel was also due to a crack as evidenced by the local distortion in the region. The cracking and fragmentation mechanism will also continue to be operative in these tunnels which accounts for the blunted appearance of the ends of the tunnels.

Occasionally cracks could be seen in the erosion pits on the specimen with an erosion time of 30 minutes using optical microscopy at magnifications around 100 times, however such observations were rare. All of the titanium specimens with longer exposure times exhibited more extensive cracking within pits under the conditions mentioned above;



(a) General surface features .. 230X



(b) Detail of pit - 920X

FIGURE 86. Scanning electron micrographs of small pits configurations on
 $Ti-6Al-4V$ after 30-minute exposure to rain at 1120 ft/sec.



FIGURE 87 Scanning electron micrograph showing detail of small pit in Ti-6Al-4V - 650X

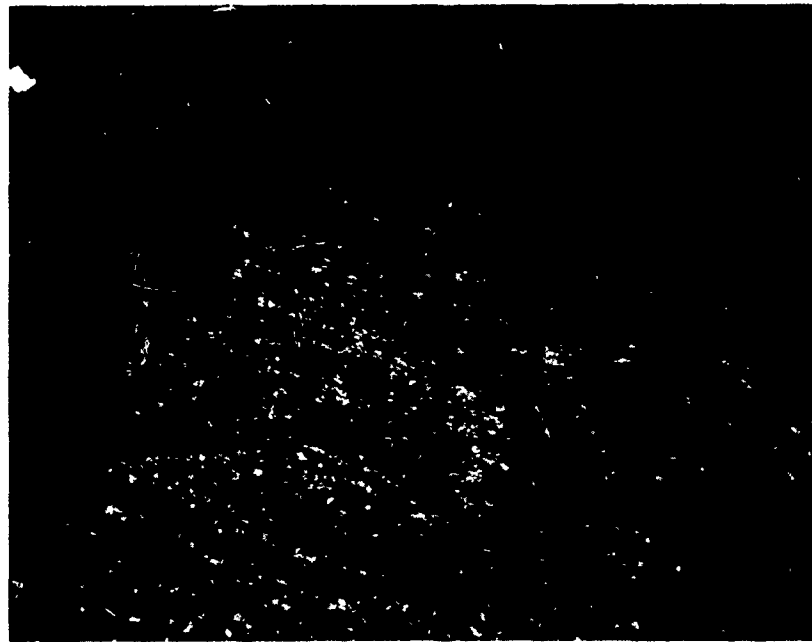


FIGURE 88 Etched cross-section of shallow pit in Ti-6Al-4V - 110X

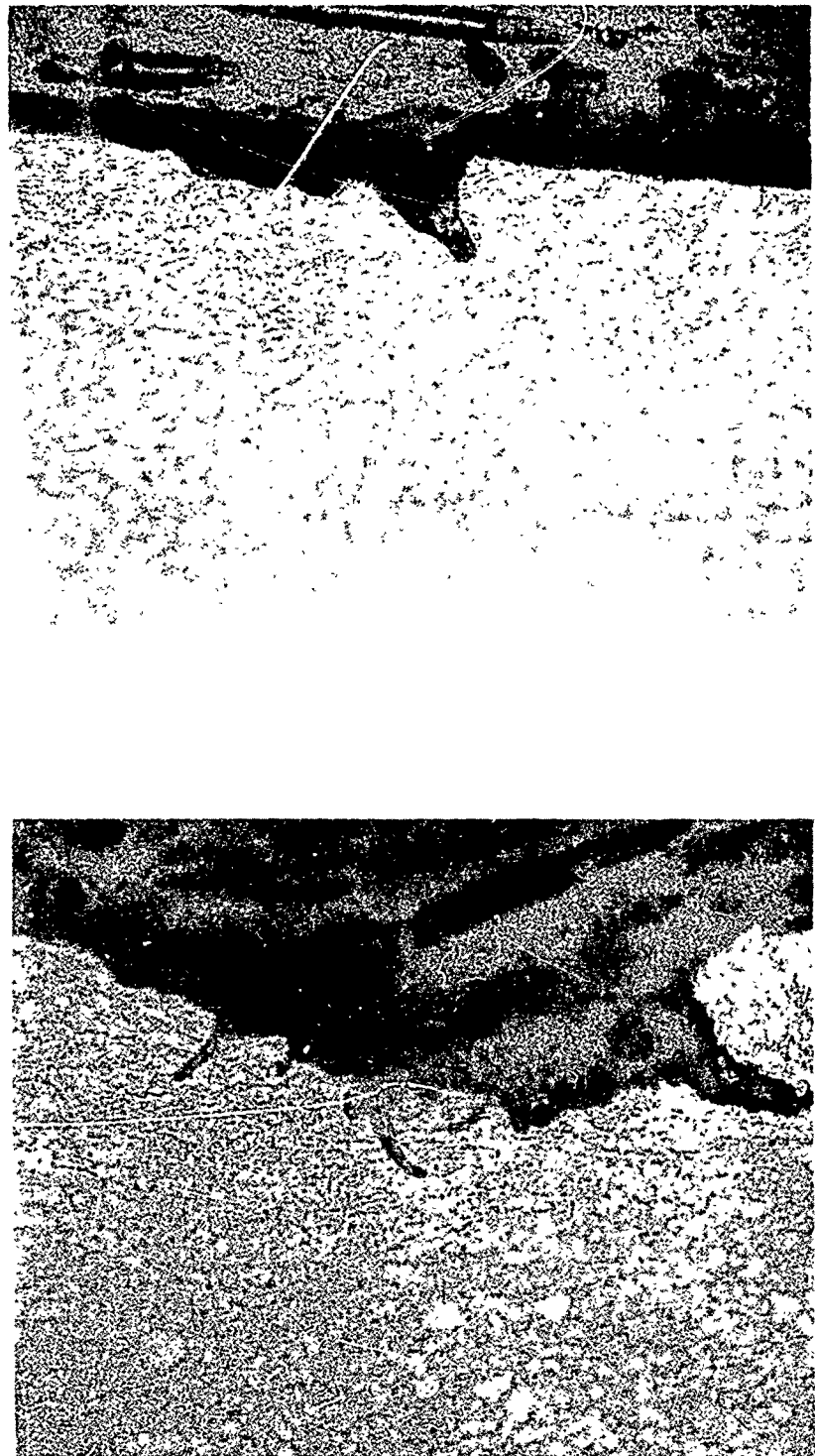


FIGURE 89. Etched cross-section of tunneling within shallow pits in Ti-6Al-4V - 440X.

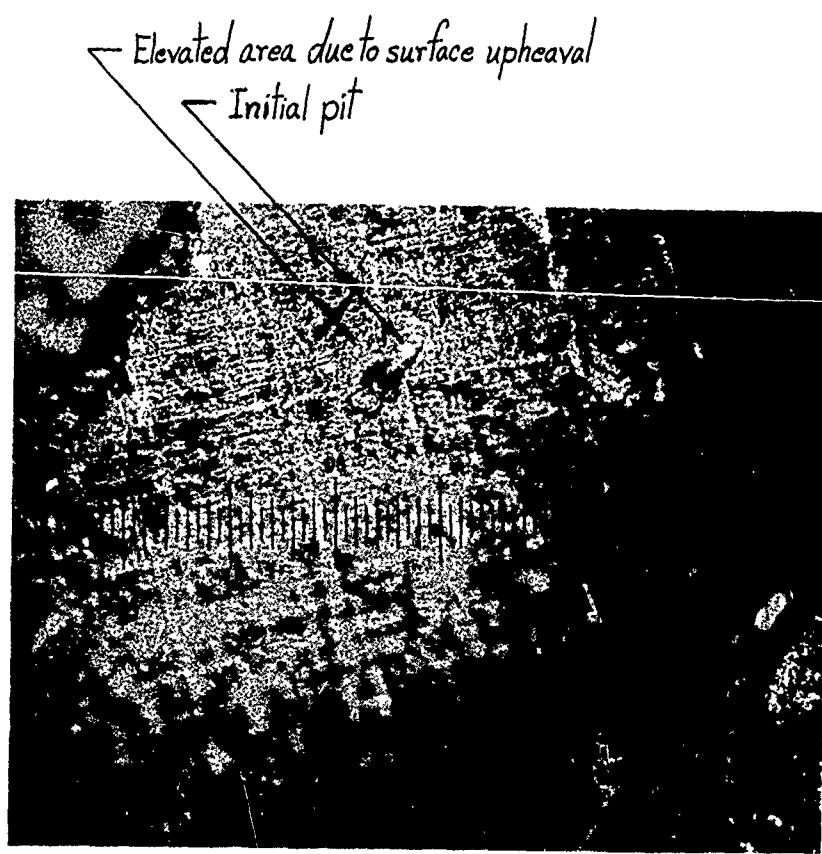


FIGURE 90. Surface upheaval in Ti-6Al-4V - 110X

the severity of the cracking increased with increasing exposure time. The more highly eroded specimens still displayed evidence of tunneling and upheaval as an operative erosion mechanism. However, at longer exposure times it is evident from the specimen cross-section in Figures 69 and 92 that another mechanism becomes operative by which material is removed through junction of progressive cracking on a large scale. As shown in Figure 69, cracks appear within the pitted regions and are also nucleated in the bulk material slightly beneath the surface. These cracks do not penetrate appreciably into the material, but rather tend to run parallel to the surface. In this regard these cracks differ from the fine random cracking described in conjunction with the shorter exposure times. Figure 92 is a view of the interior of a pit as seen from the opposing wall. Horizontal cracks are visible at several locations within the pit. Due to the limited depth of focus of the optical microscope, the sequence of micrographs focuses on different cross-sections beginning at the back wall of the pit.

The jagged appearance (Figure 69) and apparently progressive growth of the large erosion cracks in titanium indicates that there are probably true fatigue cracks, growing under the load imposed by successive impacts. If this is so, then the mode of growth of the cracks makes sense; since the alloy will be progressively more severely worked as it lies closer to the eroding surface. The fatigue crack has a tendency to propagate through the most severely deformed material, and hence tends to run parallel to, or bend toward, the free surface. The erosion rate is greatly accelerated once this erosion mechanism becomes effective as shown in Figure 76.



(a) Overall view of pit - 360X



(b) Detail of undermining - 940X

FIGURE 91. Etched cross-section of tunneling and surface upheaval in Ti-6Al-4V.

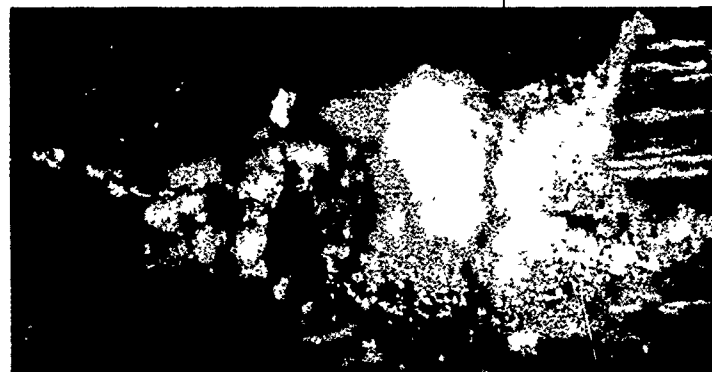
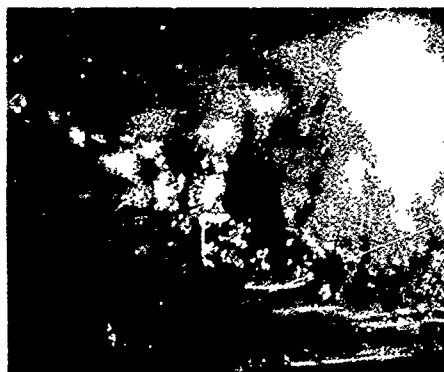
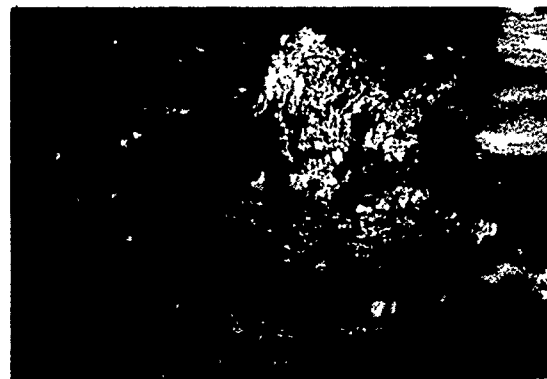


FIGURE 92. Subsurface cracking in Ti-6Al-4V. Optical micrographs of cracks within a sectioned pit after an exposure time of 135 minutes.
110X

The erosion mechanisms in titanium are influenced by its microstructure, consisting of fine grain size and dense distribution of fine precipitates apparent in the micrographs of Figure 69. The fine scale of the microstructure helps in two ways. First, the material will behave as a working homogeneous body to imposed loads of more than a few microns in area of application, and hence the full strength of the alloy is brought to bear to resist more effectively the damage by fine-scale water jets during impact. This accounts for the low rate of erosion for an exposure time of almost one hour. Secondly, there is little tendency for the alloy to develop extensive flawed areas which are easily eroded to give (as in the case of the 403 steel samples) a severe local roughening of the surface.

The results of these tests on steel and titanium seem to indicate profitable direction for the development of other rain erosion resistant alloys, particularly steel and nickel-base alloys. Drawing on these results, the rain erosion resistant metal should have the yield strength and hardness to resist the accumulation of plastic damage. Results to date indicate that a yield strength of about 90 ksi is sufficient to resist damage at Mach 1.0 if the surface is free of gross flaws. One must, however, ensure that this strength is available to resist fine fluid flows, which dictates a fine grain size and thorough dispersion of hardening agents. In the case of high strength steels or titanium alloys it appears that one can profitably trade some bulk strength for fracture toughness. If we begin from the position that it is mandatory to prevent surface roughening, the material must have the toughness

to resist quasi-brittle crack propagation normal to the surface and should have an effective fatigue limit high enough to ensure that only the material in the immediate surface layer is liable to fatigue failure.

2. Erosion of Polymeric Materials

The technical objective of this research was to qualitatively identify the mechanism of erosion for various classes of materials which typify different modes of mechanical response to multiple droplet impact. To accomplish this, air-foil shaped specimens of a bulk elastomer (cast polyurethane), urethane coatings on an aluminum substrate, a group of nine thermoplastics, and a 181 glass-fiber reinforced epoxy were eroded on the rotating arm apparatus at 730 ft/sec in a 1 in/hr rainfall (1.8 mm drop size). The specimens were then studied micrographically in order to identify dominant erosion processes. A reasonably complete picture of the erosion process has been constructed for a homologous series of urethanes and the glass-fiber reinforced epoxy. The diversity of molecular structure and general microstructural characteristics of the thermoplastics coupled with the fact that only highly-eroded specimens were available for detailed study made it difficult to provide a qualitative description of the initiation and evolution of the erosion of these materials. Erosion mechanisms of selected thermoplastics will be examined in detail in the future.

a. Rain Erosion of Polyurethane Elastomers

Erosion studies of three urethane elastomers, cast in bulk form, were carried out in order to clarify the erosion behavior of urethane coating materials without the interpretational difficulties introduced by the presence of a substrate. The cast urethanes studied were Winthane #121 and #134 (ether based, amine cured) and Winthane #612 (ester based, amine cured). The supplied mechanical properties of these urethanes are compared on page 132. The three urethanes were tested in the standard rain field at 730 ft/sec. Photographs of the eroded specimens are included as Figures 49-51. The erosion of these urethanes as a function of exposure time is shown in the graph in Figure 93. The weight-loss data clearly shows that there are significant differences in the erosion characteristics of the urethanes tested. The #134 eroded at a very high rate. The #121 had the best erosion resistance at exposure times less than 15 minutes, however at longer exposure times the #612 was the most erosion resistant of this group of elastomers.

The Winthane #121 and #134 are nearly opaque. The #134 has a milky appearance, but the opacity of the #134 was only slightly greater than that of the #121. The #612 was much more transparent than either of these urethanes. Markings on the base of the #612 specimen could be seen easily up to a distance of three-quarters of the width of specimen when viewed through the side of the specimen, while the maximum distance that markings could be seen on the base of the two other urethanes was only one-quarter width. Opacity in thermoplastics is often a measure of their relative crystallinity, however the relation between the opacity of these elastomers and their molecular structure has not been established.

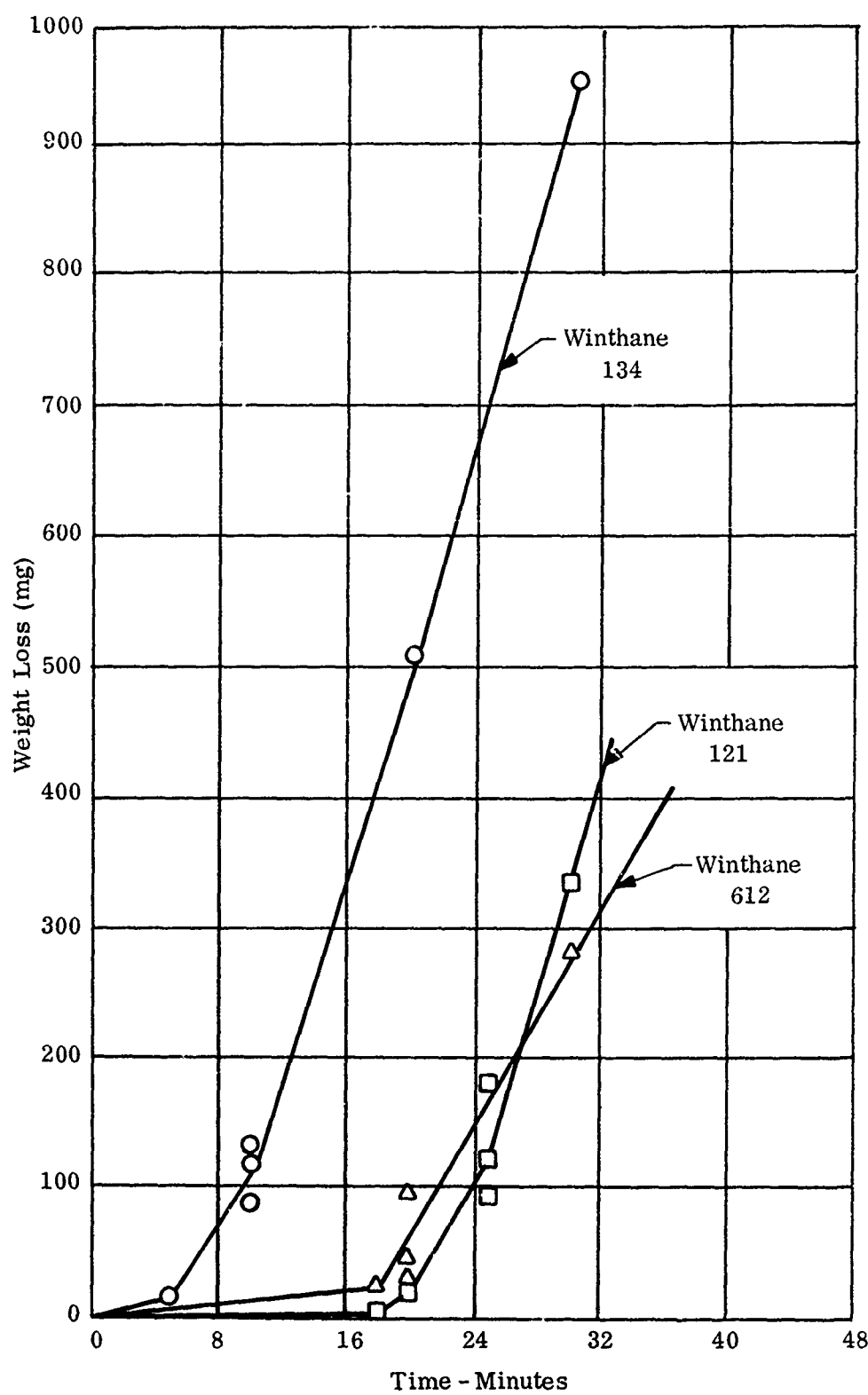
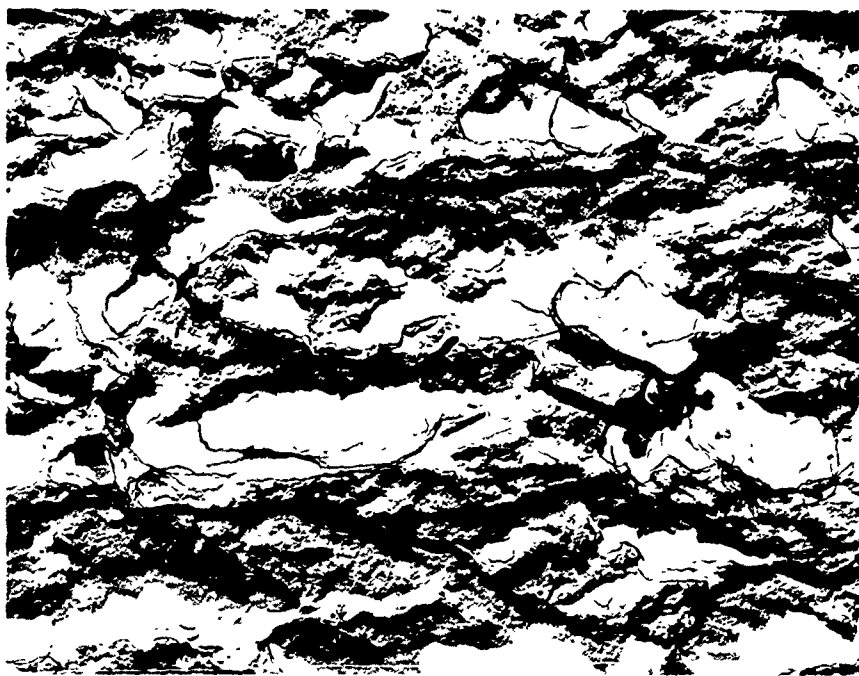


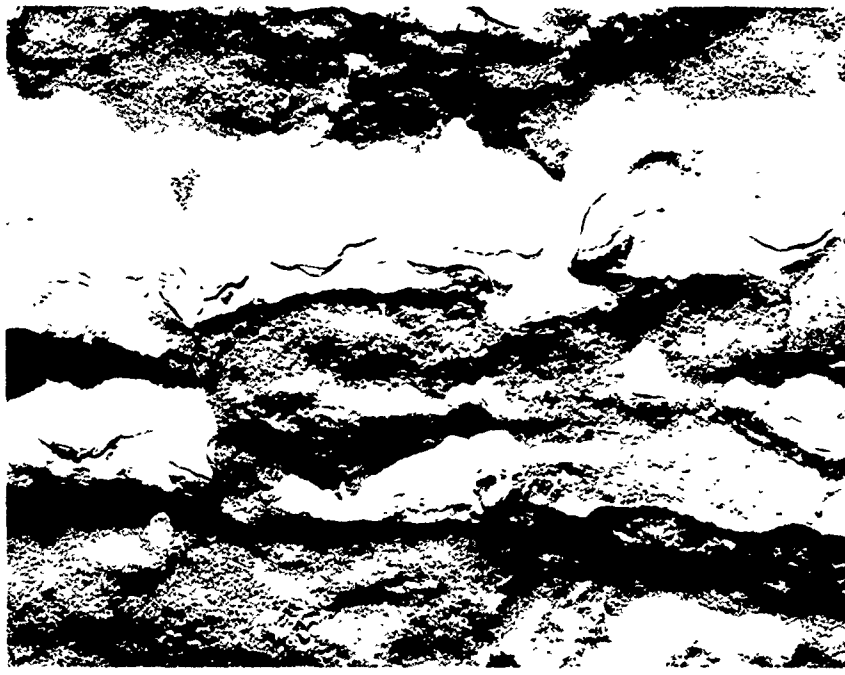
Figure 93. Erosion of Cast Urethane in 1 in./hr Rainfall at 730 ft/sec

Specimens of #121 and #612 were prepared for detailed investigations of the initiation of damage at very short exposure times. An attempt was made to polish the surface of each specimen, but the inherent material characteristics of the elastomers prevented the attainment of a very smooth surface. Replicas were taken of the surfaces before exposure to the standard rain field at 730 ft/sec. Transmission electron micrographs of typical areas of the original surfaces are shown in Figure 94 and 95. It can be seen that the surface is essentially a series of fine grooves which run parallel to the axis of the specimen. Closer examination of the surface reveals a distribution of hairline cracks which also run parallel to the axis of the specimen as shown in Figures 94b and 95b. The orientation of the grooves and presence of the hairline cracks are probably due to the preparation of the specimen. The defect distribution within the bulk of the specimens is not known.

The Winthane #612 was eroded for a total of 6 minutes, the #121 for 9 minutes, and a specimen of #134 used in previous tests on the polyurethanes was eroded for only 2 minutes. The extent of the damage at these exposure times is shown in Figure 96. Comparison of Figure 96 with Figures 49-51 provides some idea of the limited amount of damage considered in these investigations. Visual inspection of the lightly eroded surfaces shows very little evidence of removal of pieces of the surface for the #612; the surface still appears relatively smooth. The surface of the #121 is beginning to exhibit some degree of coarseness with a few pieces of material which have been partially freed from the surface clearly



(a) Replicated surface with shadowing - 3000X



(b) Replicated surface with shadowing - 15,000X

FIGURE 94. Typical surface condition of polyurethane W-121 before testing.

detectable. The #134 has the same degree of surface roughness as the #121 with a fairly uniform distribution of damage, however there are no visually observable areas of localized damage.

On the basis of the detailed studies on the erosion mechanisms in polyurethane it was found that the erosion process in the #121 and #612 was almost identical. Specimen #134 displayed an erosion behavior which appears distinctly different than specimens #121 and #612, but the same process is taking place at an accelerated rate. The initiation of damage in #612 will be discussed first supplemented by observations on #121.

The optical microscope was used extensively in constructing the progression of damage in these specimens. However, due to the limited depth of field of the instrument and the curvature of the airfoil shapes, it was not possible to obtain many photographs of publishable quality. Gold has to be vapor deposited on the polymeric specimens for viewing in the scanning electron microscope. This made it more difficult to detect areas of the surface which were being freed from the bulk material, but did provide excellent micrographs of the fracture surfaces. Replicas of the eroded surfaces were made at intermediate stages of the total exposure time; however, the replica would tear in moderately damaged areas, so this technique was only applicable to the very earliest stages of the erosion process. Again, the carbon replica when viewed in the transmission electron microscope does not show regions which are being freed from the surface as can be seen using optical microscopy due to the difference in reflectivity

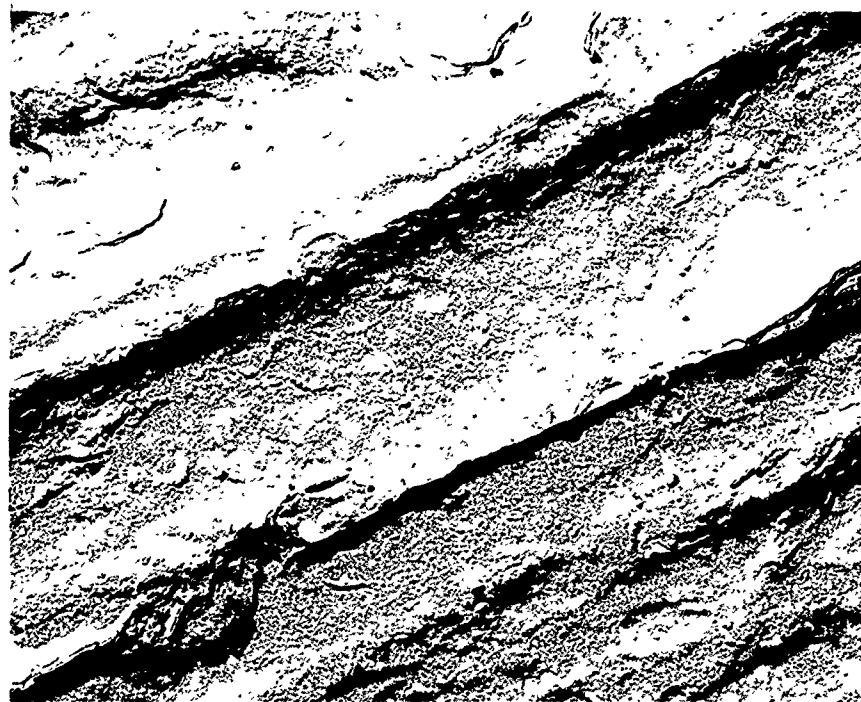
at subsurface fractures. The following description of the rain erosion process in Winthane #612 is constructed using all three forms of microscopy.

Viewing the Winthane #612 in the optical microscope indicated that the impacts on the surface propagate the initial flaws on the surface shown in Figure 95. It also seems reasonable to expect the impacts to be capable of producing additional tears in the surface. The propagation of surface flaws nucleate sites for the initial removal of material. Using the optical microscope, regions with linear dimensions ranging from one mil to less than a tenth of a mil can be found on the eroded surface which has a reflectivity which is different than that of the surrounding area. These regions are found in undamaged areas of the surface and the difference in reflectivity is believed to be due to the coalescence of cracks extending into the bulk material. Subsequent impacts in the area finally results in the removal of extremely small pieces of material. Several pits produced in this way are shown in the transmission electron micrographs in Figure 97. The average lateral dimensions of the pits in Figure 97 are approximately 1 mil. There is also evidence that a small percentage of the initial grooves on the surface are expanded, since striations begin to develop and can be seen on the surface at relatively low magnification.

It is conjectured that the small pits produced in the manner described above now serve as nuclei for the next phase of the erosion process. Rain particles striking these small pits will impose an intense pressure pulse on the walls of the pit which will cause lateral



(a) Replicated surface with shadowing - 3000X



(b) Replicated surface with shadowing - 15,000X

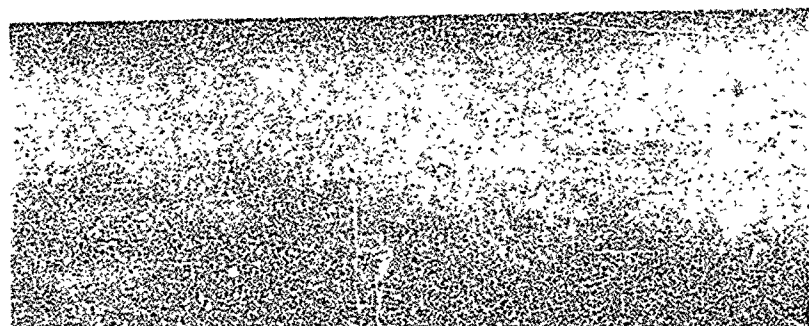
FIGURE 95. Typical surface condition of polyurethane W-612 before testing.



(a) Polyurethane W-121 after 9-minute exposure - 4X



(b) Polyurethane W-612 after 6-minute exposure - 4X



(c) Polyurethane W-134 after 2-minute exposure - 4X

FIGURE 96 Eroded surfaces of cast urethane in 1 in/hr rainfall at 730 ft/sec.



FIGURE 97. Transmission electron micrographs showing the initiation of pitting in polyurethane W121 after an exposure time of 5 minutes. 3000X.

extension of the pit walls and initiate or propagate cracks within the pit. The configuration of the initial site and the location of a preexisting or induced flaw must be such that the impacting droplets can force apart the two walls of the crack. However, since the force intensity required to propagate the fracture acts only for a short period of time, it rapidly becomes ineffectual in propagating the crack further. Hence a single impact will not be sufficient to remove material from the surface. Another droplet impact on the pit will supply the force necessary to continue propagating the crack. The material between the surface and the crack offers much less resistance to deformation than the bulk material as idealized in Figure 98. When the crack propagates to the point that the material above the crack offers very little resistance to the deformation, the crack begins to turn toward the surface. A small hinged piece of material forms as shown in Figures 98 and 99. Although Figure 99 is actually at a more advanced stage of the erosion process, the mechanism described here is the same. The change in reflectivity of the severed material is clearly seen in Figure 99. Material removal takes place when the hinged piece, which is now very flexible, is torn loose by a fluid jet of sufficient intensity or the propagating crack encounters a deep groove in the material which terminates the fracture surface with a straight-line as shown in most cases in Figure 99.

The process described above results in the scalloped configuration shown in Figure 100, which is a surface replica of one of the regions where small pits of this type can be seen and in the scanning electron

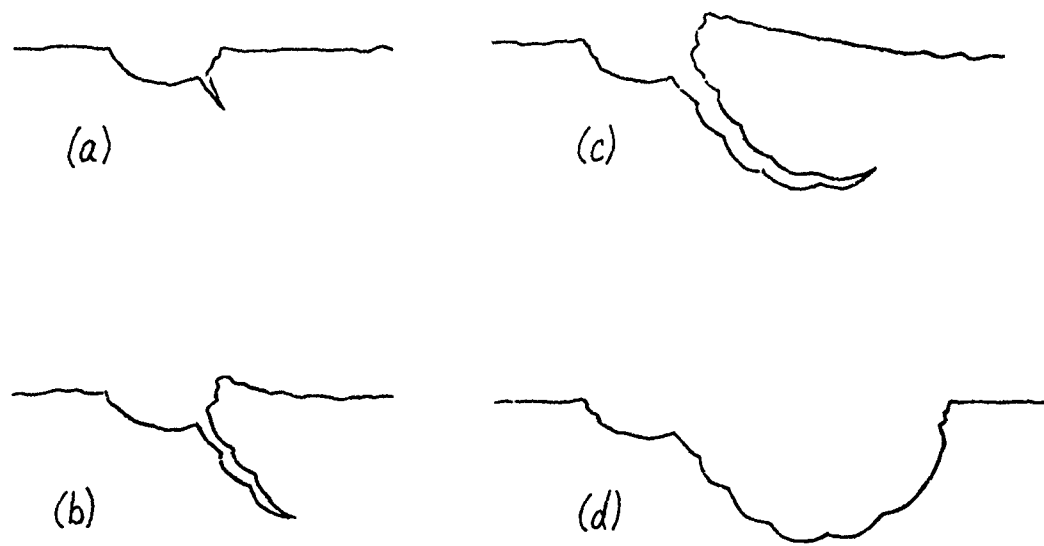


FIGURE 98. Idealization of hinge mechanism in polyurethane.

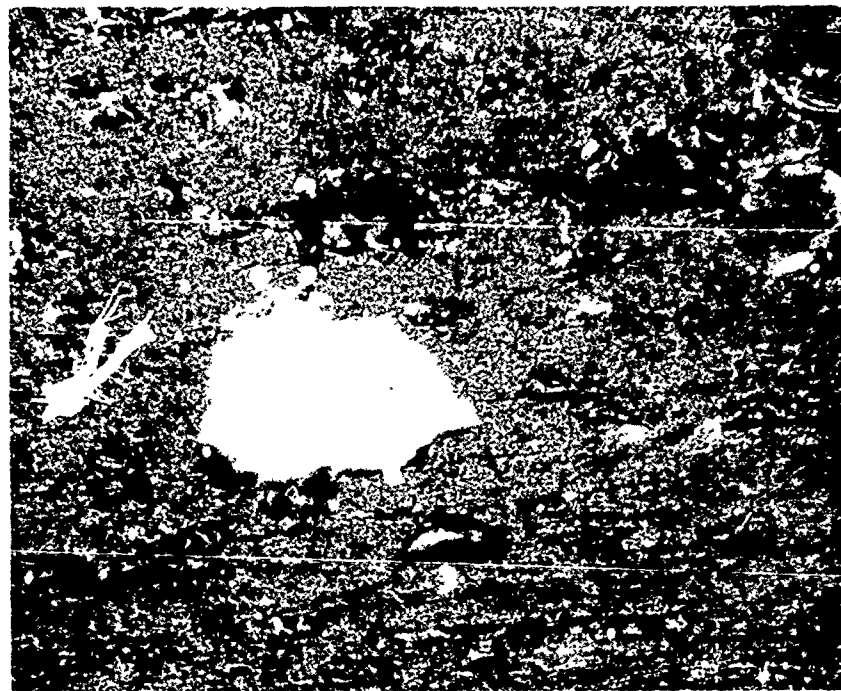


FIGURE 99. Example of hinge mechanism in polyurethane
W-612 - 150X

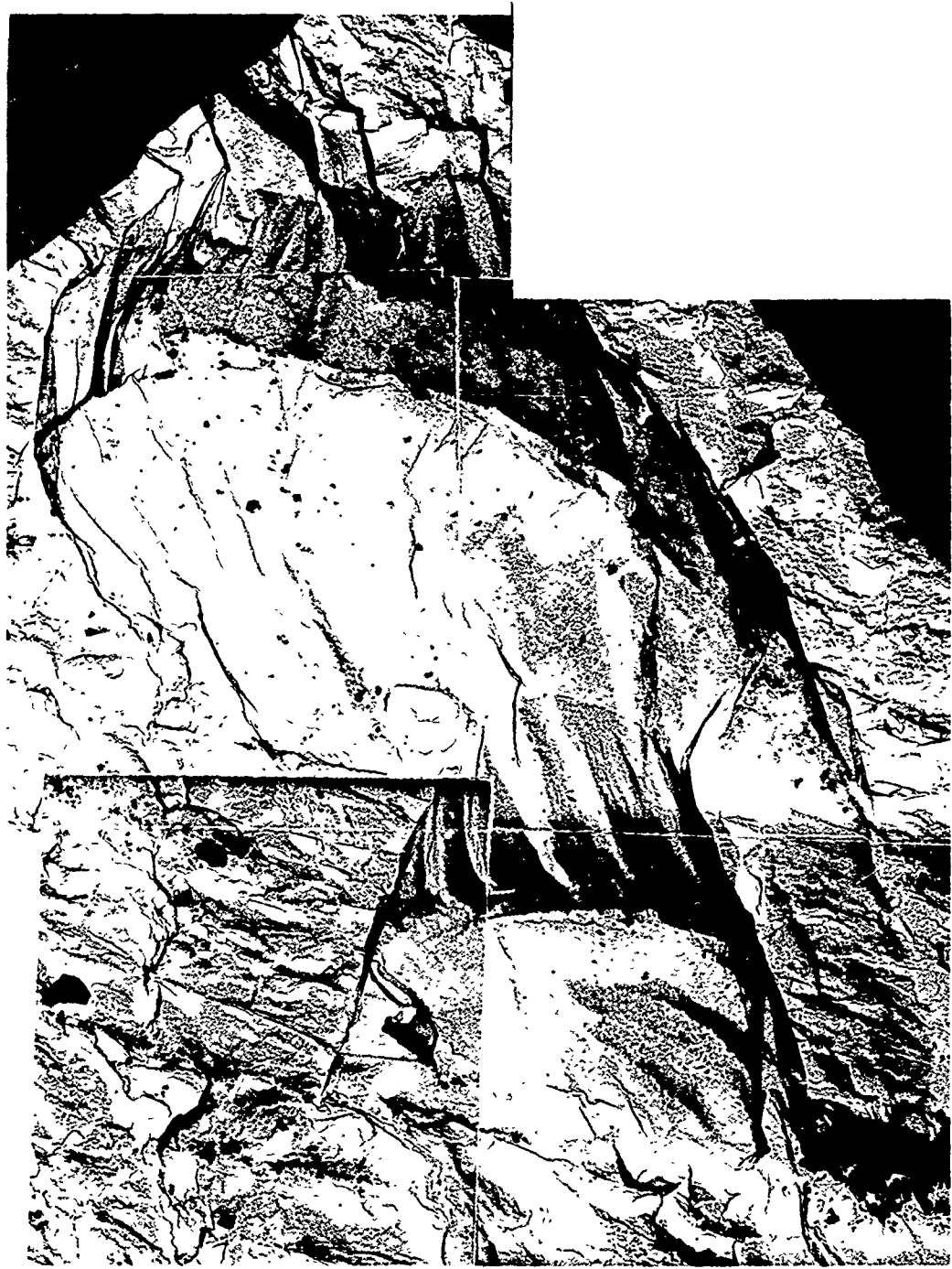
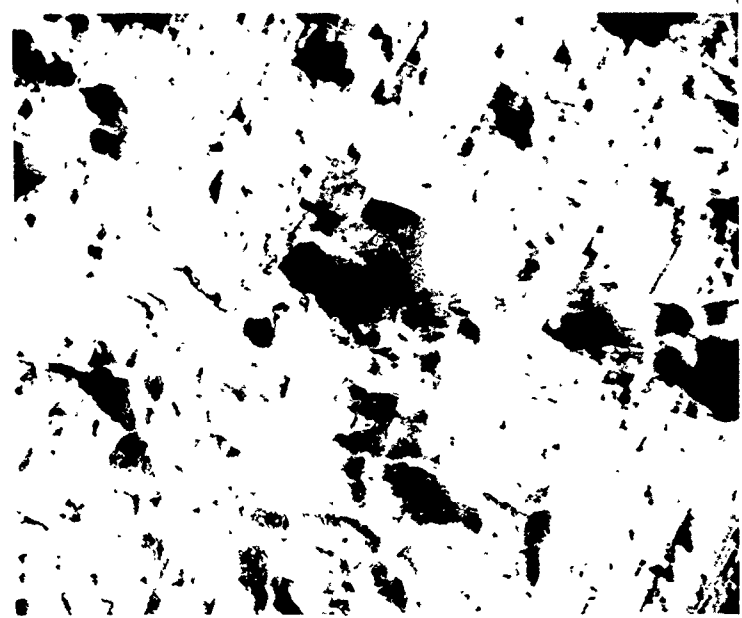


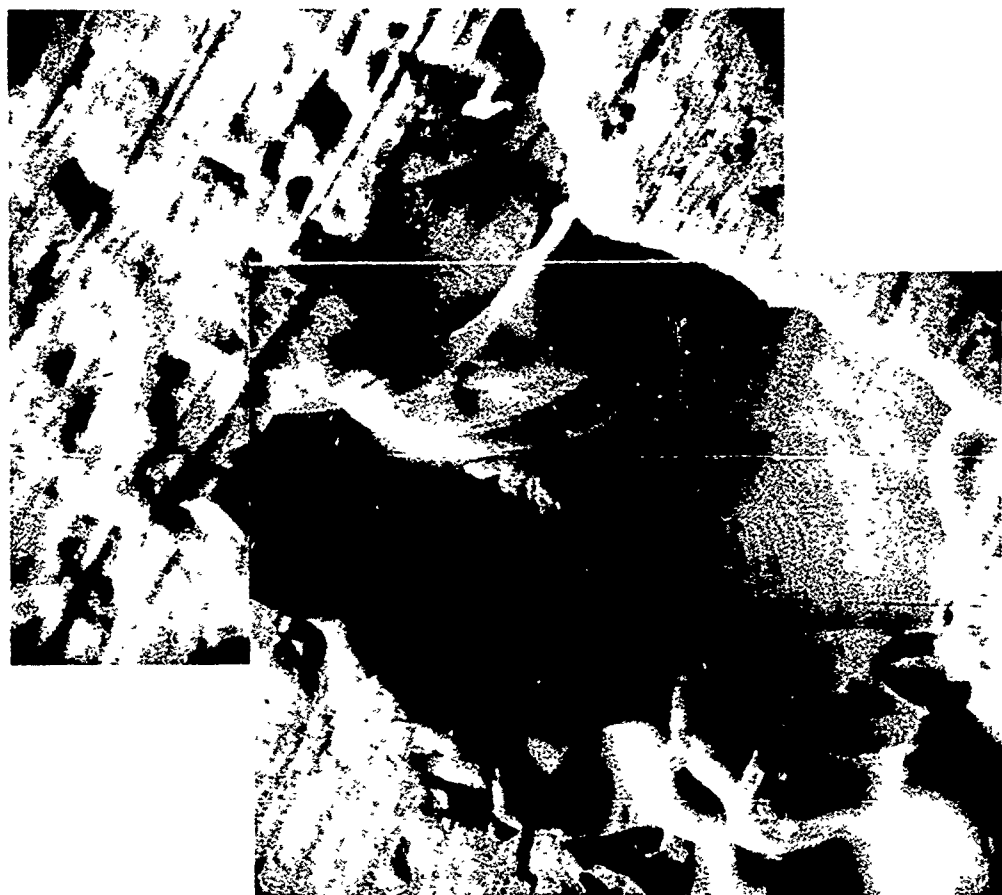
FIGURE 100. Scalloped fracture surfaces in polyurethane W121 after an exposure time of 5 minutes. (Shadowed surface replica - 2000X).

micrographs (Figure 101) taken at a later stage of the erosion process. According to the reasoning given above, the pits shown in Figure 100 took three or four successive impacts to produce. They are very shallow and a negligible amount of material has been removed. The large pit in Figure 101b required at least fifteen successive droplet impacts. Tearing of material around the rim of the pits is evident, as well as the remnants of the hinged area which intersects the smaller pit in the lower right-hand corner of the figure. The scalloped appearance shows where the crack stopped and was subsequently extended. The dark lines parallel to the front of the propagating crack are the result of the change in the speed of propagation as the applied force is reduced to zero. Figure 102 shows the same fracture surfaces in Winthane #121. The conchoidal features are the predominant mode of material removal from the surface of these elastomers.

Referring again to Figures 99 and 101a, the range in pit sizes is clearly evident. The sites for the nucleation of conchoidal fractures are distributed over the surface. Some of the very small pits already show conchoidal characteristics. The next step in the material removal process is the development of larger pits which originate within these small scalloped regions. The initial scalloped region generates a larger and deeper pit. Numerous examples of this cascade process can be seen in Figures 99 and 101a. In most cases the smaller pit or pits at which the larger pit originated can still be seen. This is a basic erosion mechanism in Winthane #121 and #612.



(a) 163 X



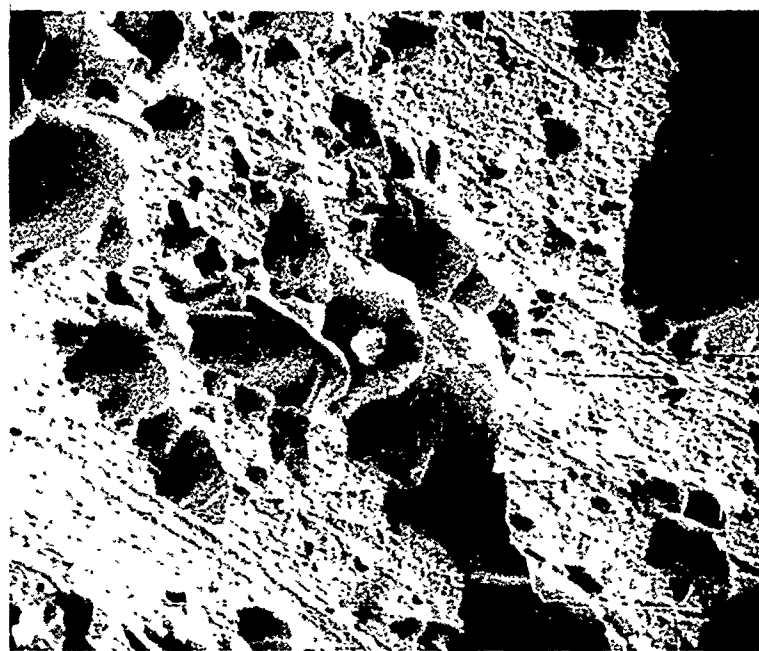
(b) 650 X

FIGURE 101. Scanning electron micrograph of general surface features and detail of scalloped fracture surface in polyurethane W-612 after 6-minute exposure.

As the exposure time increases, the size of the pits increases in accordance with the cascade process. However, the pit density eventually becomes so great that relatively large flaws develop on the surface. Examples of these large flaws are shown in Figure 103. The walls of these cracks will be separated by the force of the impacting droplets. The process of progressive fracture described earlier now continues on a larger scale with much larger pieces of the material, which also contain a number of smaller pits and flaws, being torn free. The large pit in the center of Figure 101a was probably a result of this mechanism for material removal. The initiation and subsequent development of this stage of the erosion process is responsible for the increased rate of erosion which according to Figure 93 takes place around an exposure time of 16 minutes. The total exposure time of 9 minutes for the specimen of Winthane #121 under examination is approaching this level of exposure. The erosion mechanisms become very difficult to follow as more of these large conchoidal fractures overlap and the rate of material removal is accelerated; however, it seems reasonable to believe that no new mechanism for material removal develops after the initiation of the increased rate of erosion.

In summary, the erosion mechanisms in Winthane #121 and #612 are:

1. The development of very small pits due to the coalescence of inherent or induced hairline fractures on the surface.



(a) 460 X



(b) 920 X

FIGURE 102. Scanning electron micrograph of scalloped fracture surfaces in polyurethane W-121.

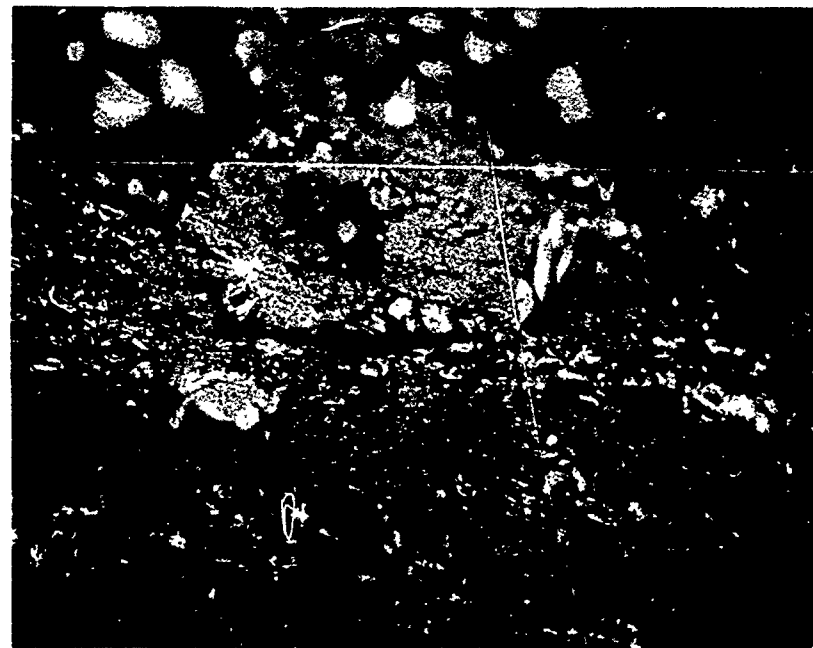
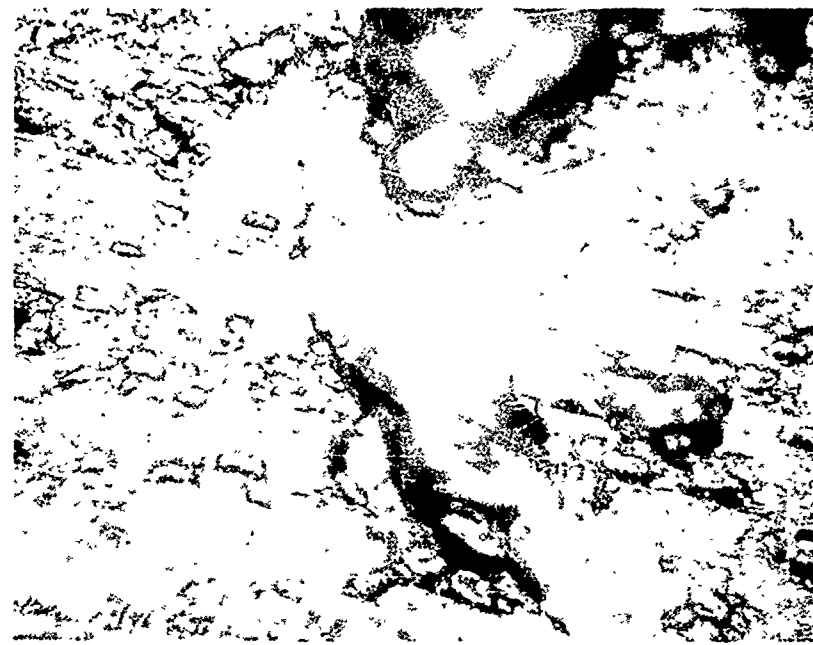


FIGURE 103. Development of large-scale surface cracking in polyurethane W-121 after 9-minute exposure to 1 in/hr rainfall at 730 ft/sec. Optical micrographs - 110X.

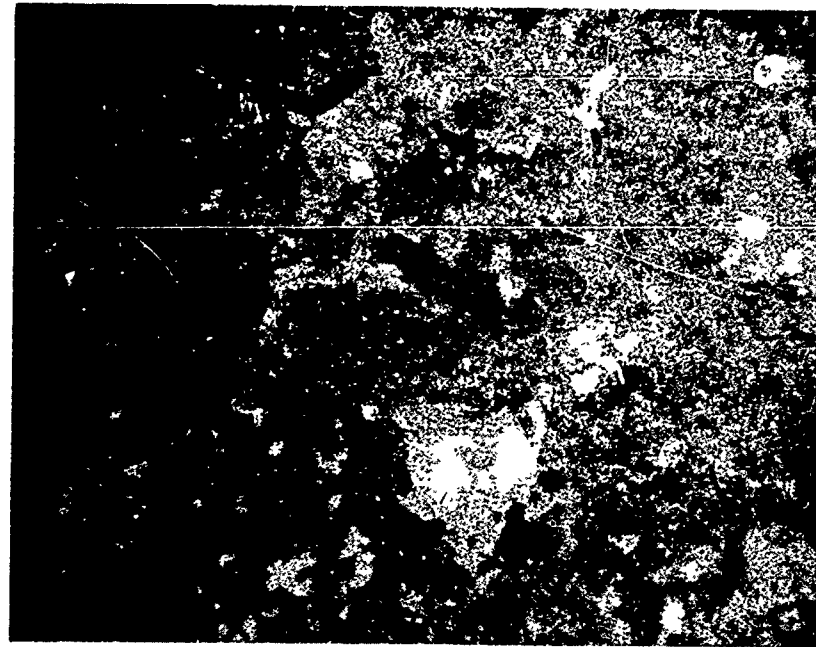


FIGURE 104. General appearance of polyurethane W-134 after 2-minute exposure to 1 in/hr rainfall at 730 ft/sec. Optical micrograph - 110 X.

2. The development of small conchoidal pits produced by a number of independent droplet impacts which propagate fractures nucleated at the minute pits in (1). The multiple impacts required for eventual removal of material account for the scalloped appearance of the fracture surface within these pits.
3. The development of larger conchoidal pits with smaller conchoidal pits serving as nucleation sites. The size of the conchoidal pits increases by a cascade process.
4. The development of relatively large cracks on the surface. When the density of conchoidal pits is large, there is a high probability for the development of large cracks. Direct droplet impacts cause these cracks to propagate in the same manner as the smaller conchoidal pits. These very large conchoidal pits are responsible for the removal of considerably larger pieces of material and are related to the increased rate of erosion observed in the weight-loss data.

The Winthane #134 exhibited a greatly accelerated rate of erosion compared to Winthane #121 and #612 as shown in Figure 93. The eroded surface of #134 after an exposure time of two minutes appeared more brittle than the other two urethane formulations. This can be seen by comparing Figure 104 with Figure 99. Extensive surface cracking was observed on the surface of the #134, and numerous

fragments of various sizes are partially freed from the surface. Although scalloped fracture surfaces were observed in many of the larger pits, the heavy bands which were previously associated with progressive crack propagation were not as prevalent in #134. The difference in the form of the fracture surfaces should be indicative of the difference in microstructural characteristics in the polyurethanes, however the microstructural characteristics influencing crack initiation and growth have not been identified. The apparent brittleness of #134 accelerates the erosion processes described in #121 and #612, but in general it seems that the same erosion mechanisms are operative in this elastomer.

The erosion resistance of the elastomers tested show a direct correlation with the tensile stress-strain data listed on page 132. The erosion resistance of the #612 was slightly better than the #121, but these two urethane formulations exhibited a much higher erosion resistance than #134. This same trend is seen in the flexibility and capacity for these urethanes to withstand large deformations. The high rates of loading do not appear to affect the relative ordering of the quasi-static stress-strain behavior.

b. Rain Erosion of Elastomer Coating Materials

Elastomeric coating materials have been developed for the principal purpose of protecting composite aircraft radomes exposed to rain at subsonic speeds. Previous research has indicated that the success of such coatings is dependent on two factors: the erosion resistance of the coating and the protection offered the composite substrate. Research to date in this program

has concentrated on the native erosion resistance of candidate urethane coating materials. The samples studied used aluminum substrates to eliminate effects associated with substrate pulverization when glass fiber-resin composite substrates are tested.

The principal conclusion from the microstructural study of these coatings is a confirmation of earlier results that failure of the urethane coatings is due almost entirely to the propagation of isolated flaws. One or a few breaks in the coating form shortly after exposure to raindrop impacts. These breaks enlarge during further exposure, but new pits rarely form. An examination of the sample surfaces indicates that these early pits form from flaws beneath the surface of the urethane coating; surface damage to the urethane is rarely observed. The samples examined during this period were a pigmented Astrocoat, and it was not possible to identify the nature of imbedded flaws leading to pitting. There is, however, indirect micrographic evidence that the more severe early pits form from sites at which the coating is not properly bonded to the substrate. In the core areas of several such pits there is no evidence of residual bonding, while patches of primer material remain attached to the substrate surface during subsequent pit growth. Previous visual study of transparent coatings has indicated that bubbles or embedded particles in the coating may also act as sites for flaw initiation.

The growth of nucleated flaws in the urethane coating occurs through progressive chipping of material from the periphery of the delaminated area. The surface of

the delaminated area has the appearance usually associated with conchoidal impact fractures in brittle materials; there is no evidence of plastic deformation of the urethane and only minor evidence of the irregular fracture surfaces which would result from a ductile tearing. The conchoidal fractures initiate at the bottom of the pit near the substrate. The cause of the fracture is presumably fluid flow against the periphery of the pit during water droplet impact.

Some slight surface damage at isolated points on the urethane surface has been observed. Included particles in the surface are occasionally ripped out. The resulting pits undergo some growth over the surface due to conchoidal chipping, but the rate of growth is slow. On those coatings which show outstanding resistance to rain erosion, pits will eventually nucleate in the surface of the coating near the ends of the sample where the coating is restrained by metal guards. The pitted areas form via erosion from the surface through the coating. The mode of nucleation of these pits has not been established but is probably through the ripping out of small particles in the surface.

The native erosion resistance of the urethane coatings tested is extremely impressive. Even after exposure to high velocity rain drop impacts for over an hour, large areas of coating surface show almost no evidence of damage, and coating removal is through the growth of one or only a few pits. Since conchoidal fractures seem to propagate rapidly through the urethane once they have formed, we attribute this outstanding erosion resistance

to the virtual absence of native flaws in the urethane surface. This absence of flaws is confirmed through high magnification inspection of the coating in the electron microscope.

The implication of these results for the development of improved elastomeric coatings seems clear. Coating improvement may be achieved through advances in coating procedure and subsequent inspection, to eliminate or detect coating flaws which are likely to lead to erosion pits, or through material changes which impart some fracture toughness to the urethane and cause it to be more tolerant of imbedded flaws. There seems no reason to seek improvement in the properties of unflawed urethane; available coatings seem to have adequate strength and resistance to deformation under raindrop impact to sustain very long exposures to rain. The problem is that strength is not being fully utilized.

The problem will be studied in more detail in subsequent research. In particular, clear urethane coatings on aluminum substrates will be examined in detail so as to more closely specify the coating flaws which lead to early pitting. Based on these results, the feasibility of improving coating practices to achieve greater erosion resistance in engineering applications will be assessed. Should such an improvement appear impractical, research to improve the flaw tolerance of urethane elastomers will be considered.

c. Rain Erosion of Thermoplastics

Useful erosion data (reported on pages have been acquired for a series of nine thermoplastics: Delrin 550 (a polyformaldehyde), ultra high molecular weight polyethylene, Zytel 7110-13 (a glass-fiber reinforced nylon), Noryl 731 and Noryl GFN-3 (modified polyphenylene oxides), a copolymer of an acrylic ester and polyvinyl chloride (Kydex), an aromatic polycarbonate (Lexan), polyarylsulfone (Astrel 360), and polymethyl-methacrylate. Considering the diversity of material characteristics represented by this group of thermoplastics, it was desirable to explore the possible correlations which could be established between the mechanical properties for these thermoplastics and their erosion behavior. It was found that no general correlations evolved, but this may be due in part to the sparseness of the data for several relevant mechanical properties.

Qualitative descriptions of the evolution of the erosion process in the thermoplastics tested will require additional testing and micrographical studies. The successful identification of erosion mechanisms in urethanes has demonstrated the importance of controlled tests employing well-characterized specimens. A similar approach for selected thermoplastics is anticipated to yield similar results.

(1) Problems in Correlating Mechanical Properties with Erosion Resistance

The selection of a material for a particular application is based in part on the properties of suitable materials obtained from standard tests. An attempt has

been made to correlate the erosion resistance of representative classes of bulk thermoplastics with their thermo-mechanical behavior under standard conditions; however, the rain erosion problem presents a unique loading condition which is not closely allied with the usual mechanical property evaluations. A limited number of experimental investigations have shown that the response of thermoplastics to multiple impact loadings is different than in single impact tests. The results of Heater and Lacey (33) for example, illustrate this point. The ratings of six materials based on their tensile impact strength are shown to be quite different under repetitive tensile impacts at different impact velocities and frequencies. Representative results from their investigation are listed in Table XLIII.

The standard ASTM impact tests are the only universally employed measure of mechanical behavior under dynamic loadings; however, the results from these tests have been severely criticized (34-35). Dynamic loadings are used extensively in describing the rheological behavior of visco-elastic materials, but these are small-amplitude, steady-state vibrations, transient torsional motions, and low constant strain rates. Dissipation mechanisms within the material are identified by these procedures. An important consideration in understanding the energy absorption characteristics of the polymers investigated would be to identify potential dissipation mechanisms for the loading rates encountered in raindrop impacts at low mach numbers. Work of this nature has been initiated by Oberst (20), who attempted to relate relaxation times for a number of thermoplastic and elastomers to the impact phenomena associated with rain erosion through arguments based on order-of-magnitude comparisons.

TABLE XLIII COMPARISON OF TENSILE IMPACT STRENGTHS WITH REPEATED IMPACT DATA

Tensile Impact Strength ^b (ft-lb/in ²)	Rank	Number of Impacts to Failure at Various Impact Velocities ^c						Rank
		40 in/sec	Rank	60 in/sec	Rank	85 in/sec	Rank	
Polycarbonate	400	1	12	5	19	4	37	4
Nylon 6/6 (Zytel 101) ^a	200	2	250	1	250	1	250	1
Die-cast zinc (SAE 903)	80	3	40	3	14	5	7	5
ABS-impact grade	75	4	10	6	11	6	50	3
Delrin 550	50	5	18	4	38	2	185	2
Die-cast aluminum (SAE 306-1% Zn)	40	6	50	2	23	3	5	6

^aConditioned to equilibrium moisture content at 50% relative humidity

^bImpact velocity of pendulum, 136 in/sec.

^cImpact energy constant at 30 ft-lb/in². Impact frequency was 6 blows/minute.

Oberst, along with Hoff, et. al (36), supports the view that the rain erosion resistance of thermoplastics and elastomers can be assessed from their visco-elastic properties and impact tests on notched samples. The universality of this hypothesis appears tentative.

General trends in the dynamic behavior of materials can be obtained from high-speed tensile tests and studies of stress-wave propagation. However, it is extremely difficult to relate the impact strength to strength measurements under more controlled conditions of loading due to the rate-sensitivity of the stress-strain and fracture properties of polymers. High rates of loading alter the values of the moduli, yield stress, and fracture stress. Dispersion of the elastic waves occurs due to strain-rate sensitivity of the elastic moduli, and in some instances slower moving plastic waves may also be encountered. It is impossible in practice to separate the two basic effects of impact loading: the complex stress distribution arising from travelling stress waves giving rise to high maximum stress, and the actual change in material-properties under high rates of strain. One-dimensional constitutive equations have been proposed which account for strain-rate effects in materials based on experimental observations, however the problem of evaluating the influence of changing material behavior during transient loadings on the surface of a semi-infinite half-space does not seem to have received attention.

(2) Mechanical Properties of Thermoplastics Tested

The mechanical properties of the eight bulk polymers used in the erosion tests are based exclusively on standard ASTM tests and are recorded in Table XLIV. The values given are only relative measures, since the value of a mechanical property appearing in several published listings was not always properly identified and information on some of the specific polymers used could not be found. The ASTM does allow some latitude in the procedure employed but does provide a definite form in which the results are to be reported. For example, some tables provided the tensile strength at yield instead of at break (depending on the toughness of the polymer), but generally it was not stipulated which value was being recorded. The rate of loading was seldom indicated, so the tensile strength for one polymer found in one listing may not be obtained under the same set of test conditions as for another polymer to which it is being compared. One factor which was totally neglected was the method of preparation and microstructure of the polymer, unless this information was developed in conjunction with a study of the effect of the internal structure on a particular mechanical property. These descriptions would be helpful when more refined correlations are considered subsequently. Under these prevailing circumstances, definitive studies of

the eight bulk polymers used in the erosion tests based on their mechanical properties and internal constitution were not possible.

In erosion processes the fatigue endurance limits are often cited in the literature as an important mechanical property (38), however not enough data were found for comparison purposes. Also, thermal properties of the polymers were not included, since little variance was found in the values of the thermal conductivity, specific heat, and thermal expansion coefficient. However, this does not mean that temperature effects are unimportant. In the case of rain erosion the temperature at the surface of the specimen is influenced by aerodynamic heating, evaporative cooling of the raindrops, and the heat generated at the surface of the repetitive collisions with the raindrops. Due to the low values of the thermal conductivity for thermoplastics, localized heating (or cooling) may be more significant than in metals. The mechanical properties of thermoplastics display a strong temperature-dependence which can produce significant losses in strength at moderate temperature increases beyond room temperature. Therefore the properties at 72°F listed in Table XLIV may not be at all indicative of the temperature field near the impacted surface of the specimen. It was discovered some time ago that fatigue tests on plastics had to be conducted at loading frequencies much lower than those used when working with metals due to the large temperature rises which would result.

The glass-transition temperature, T_g , is also included in Table XLIV. In an amorphous thermoplastic resin (represented by Astrel 360) the glass transition

occurs with increasing temperature when the state of the polymer changes from a brittle, glassy material to a flexible, rubbery material. This transition usually occurs within a narrow temperature range with accompanying abrupt changes in several of the physical and mechanical properties. Amorphous thermoplastics below Tg have low elongation, a high tensile strength, a high modulus of elasticity, and low impact strength; above Tg they often have the reverse of these properties. Noryl is believed to be an amorphous form of polyphenylene oxide with a Tg around 410°F. Despite this, the polymer exhibits ductile behavior at room temperature with substantial elongation. The brittle point of poly (2,6-dimethylphenylene oxide) is -275°F. Several of the polymers considered here are semicrystalline: polyethylene, Zytel 7110-13, Lexan, Delrin 550, and Kydex. This means they behave as though they were a mixture of amorphous and crystalline material. The amorphous portion of the polymer will have a glass transition and again abrupt changes in material properties will occur. Crystalline thermoplastics exhibit mechanical properties which are functions of the amount of crystallinity present. A crystalline thermoplastic generally has better impact strength when well-above its Tg than when it is at or below Tg. Increased crystallinity (among samples of the same polymer) tend generally to give a higher modulus, lower elongation, higher tensile strength, greater resistance to creep, and correspondingly a lower impact strength.

The range of polymer types tested for rain erosion resistance is relatively broad and not conducive to exploring the changes which might occur in the erosion

resistance by changes in the structure of the same type of polymer. Loosely stated, Astrel 360 and Noryl 731 are amorphous; Lexan, Hostalen CUR, and Delrin 550 are crystalline; Kydex is a semicrystalline copolymer; Noryl-GEN-3 is a glass-fiber reinforced amorphous resin; and Zytel 7110-13 is a glass-fiber reinforced crystalline resin. It is seen that reinforcement in Noryl does not improve its erosion resistance but lessens it: the strength of the Noryl is greatly increased, but apparently the material is more susceptible to brittle fractures. The nylon is reinforced and shows good erosion resistance; however, data for unreinforced nylon-6,6 are not available in order to evaluate the influence of the reinforcement in this case. The highly crystalline thermoplastics tested are significantly more erosion resistant at 730 ft/sec than the more amorphous polymers.

In reviewing the mechanical properties listed in Table XLIV, no general trends can be established corresponding to the relative ranking of the thermoplastics based on their erosion resistance at 730 ft/sec. A similar conclusion was reached by Garcia, et al, (39) in a slightly different context. The reordering of this ranking at 1120 ft/sec would lead one to suspect that the erosion resistance of some of these polymers is velocity-dependent.

Admittedly the evaluation and scope of the mechanical properties provided in Table XLIV leaves much to be desired, however these are the data which are readily available. The direct correlation of erosion resistance with the quasi-static stress-strain behavior for polyurethane reported in another section is encouraging. Presumably correlations of this type can be established for homologous series of other polymers.

TABLE XLIV. PROPERTIES OF SELECTED THERMOPLASTIC RESINS

	Delrin 550 ^a	Hostalen GUR ^b	Zytel 7110-13 ^d
Specific Gravity	1.425	0.94	1.34 (approx.)
Glass transition temperature, °F	-40 to -76	-184	120
Hardness	M94, R120	R55	R118-120
Tensile strength, psi			
at yield	10,000	3,365	19,500-28,000
at break	25 injection molded); 75 extruded)	525	5-10
Tensile modulus, psi	520,000	102,000	1,000,000-1,250,000
Poisson's ratio	0.35		
Compressive strength, psi			
at yield	5,200		18,500-20,000
1% deformation	18,000		
10% deformation	670,000	110,000	
Compressive modulus, psi	14,100		
Flexural strength, psi (yield)	410,000		
Flexural modulus, psi			
Impact strength, Izod, ft-lb/in ²			
1/2 x 1/2 in. notched bar	1.4 (injection molded; 2.3 (extruded))	32 ^c	
1/2 x 1/4 in. notched bar			
1/2 x 1/8 in. notched bar			
1/2 x 1/8 in. unnotched bar			

1.7-2.1

^aValues listed are for Delrin in general and not Delrin 550, although it is stated that the properties considered here do not change appreciably for the different compositions available.

^bValues listed correspond to an ultra-high-molecular-weight polyethylene (AC-1220) produced by Allied Chemical Corporation.

^cSpecimen will bend but does not break.

^dValues listed are for a generic 30% glass-filled nylon-6, 6.

TABLE XLIV. PROPERTIES OF SELECTED THERMOPLASTIC RESINS (continued)

	Noryl-731	Kydex ^f	Lexan ^g	Astrel	360	Noryl-GFN3
Specific gravity	1.06	1.35	1.20		1.36	1.27
Glass transition temperature, °F	R119	R99-R105	M73-78, R115-125	M110	550	L108
Hardness	9,360	6,500	8,000-9,500	13,000		17,000
Tensile strength, psi						
Tensile elongation, %						
at yield	20-60	100	5-7	8		
at break	355,000	335,000	60-130	10-13	4-6	
Tensile modulus, psi			300,000-350,000	370,000	1,200,000	
Poisson's ratio						
Compressive strength, psi						
at yield	8,400	12,000				
1% deformation	16,400					
10% deformation			17,900			
Compressive modulus, psi						
Flexural strength, psi (yield)	13,500	400,000	345,000	340,000		
Flexural modulus, psi	360,000	10,700	12,200-12,700	17,200	20,000	
Impact strength, Izod, ft-lb/in ²		400,000	320,000-350,000	395,000	1,100,000	
Impac ²⁴⁹						
1/2 x 1/2 in. notched bar						
1/2 x 1/4 in. notched bar						
1/2 x 1/8 in. notched bar						
1/2 x 1/8 in. unnotched bar						

^eRange specified covers two different values found in General Electric publications.^fValues listed are for a generic acrylic-PVC copolymer.^gData for a generic unfilled polycarbonate and injection-molded bisphenol-A derived polycarbonate.

(3) Microscopic Investigation of Thermoplastics

The series of eight thermoplastics were tested primarily for evaluation of their relative erosion resistance. The specimens were not examined microscopically until after the completion of the tests, however the only feature that could be distinguished with optical microscopy at this advanced stage of the erosion process was that all the thermoplastics eroded in a brittle manner. The specimens were sectioned and polished in order to observe the characteristics of the pits on the surface. The form of the pits in each thermoplastic was distinct as shown in Figures 45-48 and Figures 53-62, however the reasons for the differences have not yet been assessed.

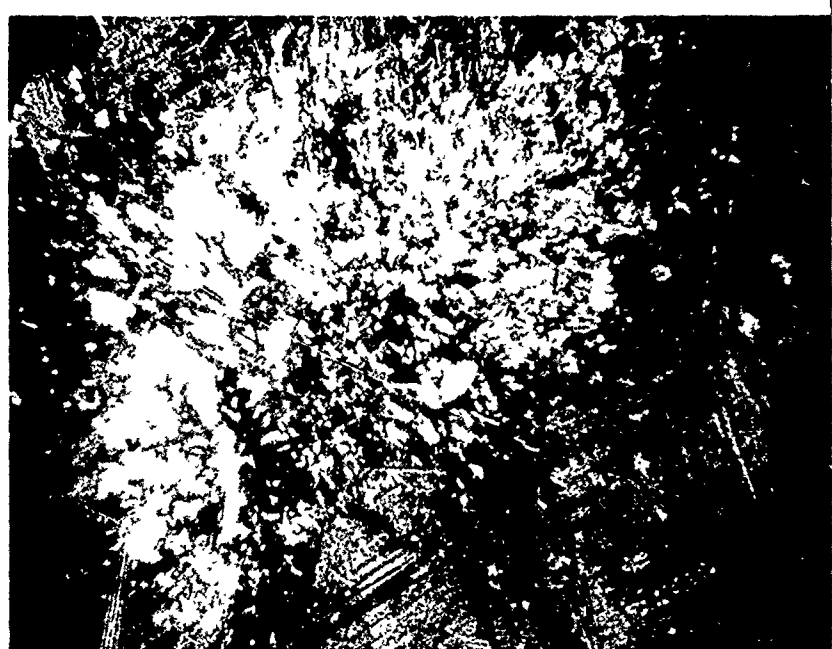
A series of three specimens of polymethyl-methacrylate were eroded for 15, 30, and 45 seconds in a 1 in/hr rainfall at 730 ft/sec in order to observe the initiation of the erosion process. The initial surfaces were polished before testing. The replication technique generally used in this laboratory involves dissolving thin sheets of cellulose acetate with acetone on the surface to be replicated. However acetone will also dissolve the surface layer of the polymethylmethacrylate, so a replication technique using a non-reactive solvent was sought. One of the replication techniques used for polymers is polyvinylalcohol with water as the solvent. The taking of replicas with polyvinylalcohol was not perfected before the polymethylmethacrylate specimens were scheduled to be tested on AFML-Bell rotating-arm apparatus, so the condition of the surfaces before testing could not be investigated in the transmission electron microscope. Replication of polymeric material surfaces with polyvinyl-alcohol is now available for future studies.

The typical forms of damage observed on the surface in the very early stages of the erosion process are locally abraded areas and initial development of pits. Figures 105 and 106 show some of the patterns that are found in the damage regions. The reason for the type of damage observed has not been discovered.

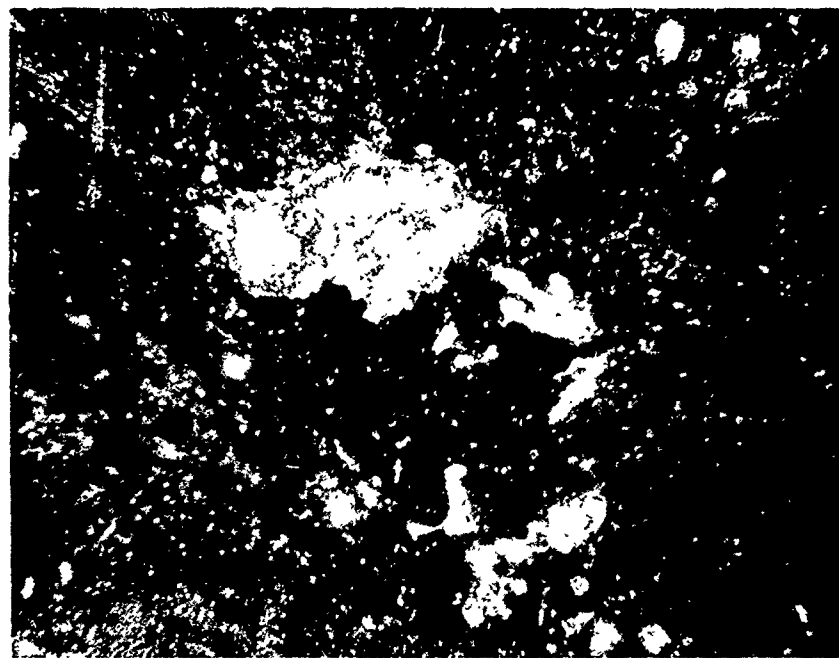
The specimen of polymethylmethacrylate with an exposure time of 45 seconds was prepared for viewing in the scanning electron microscope. It was found that at the higher magnifications required the electron beam would preferentially remove material from the surface. Over a period of five minutes a microstructure was uncovered which maintained the general features of the deformed area but displayed rather unusual subsurface features in essentially undisturbed adjoining regions of the surface. The interaction of radiation with polymeric materials will have to be investigated further before it can be determined if this condition can be avoided or if this phenomenon can be beneficial to the erosion mechanism studies. The results obtained are questionable and will have to be reported after the difficulties mentioned above have been resolved.

d. Erosion of 181 Glass-Fiber Reinforced Epoxy (4617)

A series of controlled tests were conducted on three glass-fiber reinforced epoxy specimens which provided information on their erosion behavior up to an exposure time of 70 seconds in 10 second intervals. The specimens were exposed to a 1 in/hr rainfall at 730 ft/sec.



(a) 100X



(b) 60X

FIGURE 105. Rain erosion of polymethylmethacrylate after 15-second exposure at 730 ft/sec. Optical micrographs.

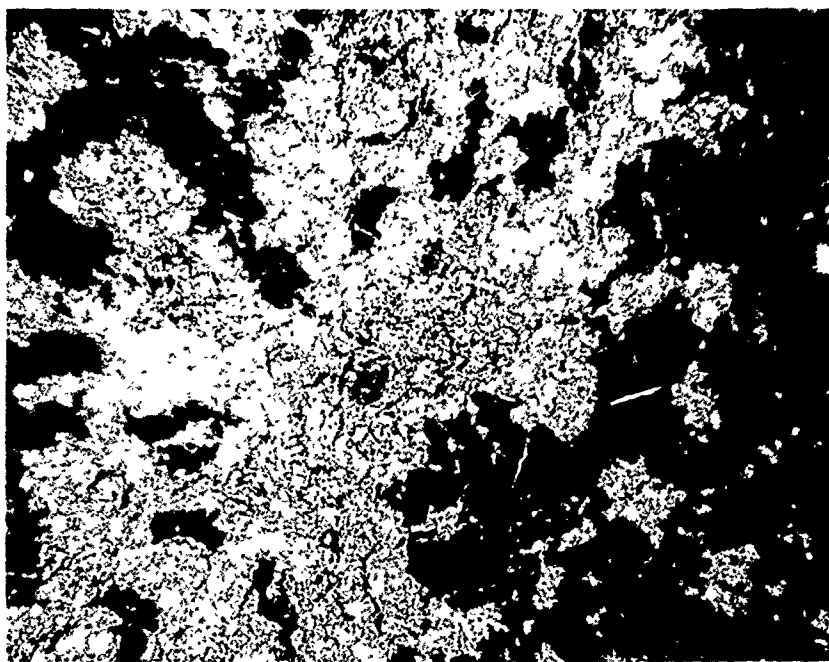


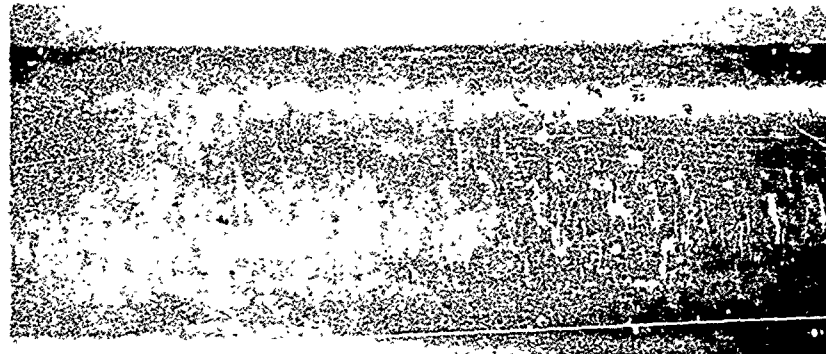
FIGURE 106. Rain erosion of polymethylmethacrylate
after 45-second exposure at 730 ft/sec.
Optical micrograph - 100 X.

Large white areas are found on the specimens (Figure 107) where the droplet impacts have freed a length of a complete fiber bundle from the surface, but the fibers are still strong enough to adhere to the bulk material. Several areas of this kind with lengths up to one-quarter inch and including four layers of the woven fabric could be found on the specimens after an exposure time of approximately one minute. Subsequent stages of the erosion process appear to worsen this situation until these sections of the weave are torn free in addition to the brittle chipping of the epoxy matrix.

These studies indicate that from the stand-point of erosion resistance the epoxy matrix is the weakest component in the composite. The droplet impacts preferentially remove the epoxy from areas which form interstices in the woven fabric; brittle chipping of the epoxy continues down to the underlying fiber bundles. The composite fractures at the epoxy/fiber interface; however, the glass fibers resist the initial failure mode and exhibit minimal fracturing of the fibers in a fiber bundle. Even after several layers of fiber bundles are exposed to direct droplet impacts, relatively few pits can be found along the exposed fibers. A limited number of fibers are removed by localized cracking in one area with subsequent removal from the fiber bundle by lateral jetting. The primary erosion mechanism is the progressive removal of epoxy from around entire fiber bundles. Segments of the fiber bundles are removed when they can be fractured in bending or shear.



(a) After 50-second exposure.



(b) After 60-second exposure.



(c) After 70-second exposure.

FIGURE 107. Rain erosion of 181 glass-fiber reinforced epoxy (4617) at 730 ft/sec. - 4X

Replicas were made of the surface of each specimen at the beginning, during, and at the end of each test. The extent of the damage produced on these specimens at the completion of the tests is shown in Figure 107. The erosion damage at longer exposure times can be seen in Figure 63. The accumulated damage appears to be greater in the specimen with the least overall time of exposure, however this may be due to the fact that the specimen surfaces were polished before testing following the procedure outlined on page 200. General inspection of the uneroded surfaces showed that the depth of the glass fibers below the surface was variable and dependent on the weave of the fabric. Due to the polishing some of the fibers were at the surface and did not have a layer of epoxy over them as can be seen in Figure 108. Observation of the uneroded surfaces using the transmission electron microscope did indicate that there were a small number of disruptions in the epoxy matrix which could nucleate cracking. There was very little evidence of surface cracks, and, in general, the bonding between the fibers and the matrix is sound.

A number of different failure modes which are a function of the proximity of the glass fibers to the surface of the specimen could be identified. When the fibers are at the surface as in Figure 108, the fibers are exposed to direct impacts. There is evidence that both cracking of the fibers and brittle chipping of the epoxy takes place (Figure 109). Figure 110 is a detail of the form of typical fracture surfaces in the epoxy during the very early stages of the erosion process. An overall view of the removal of material from the fibers

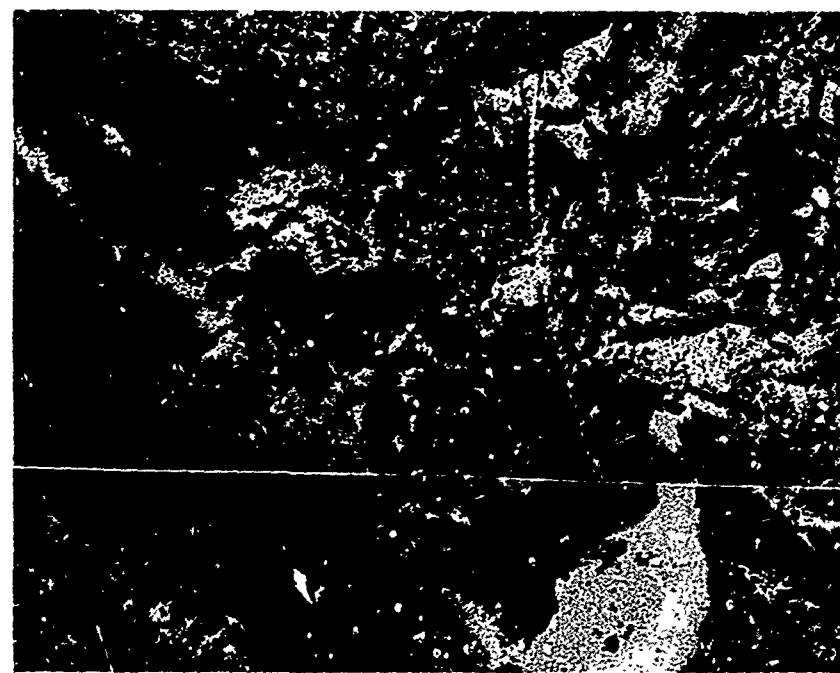
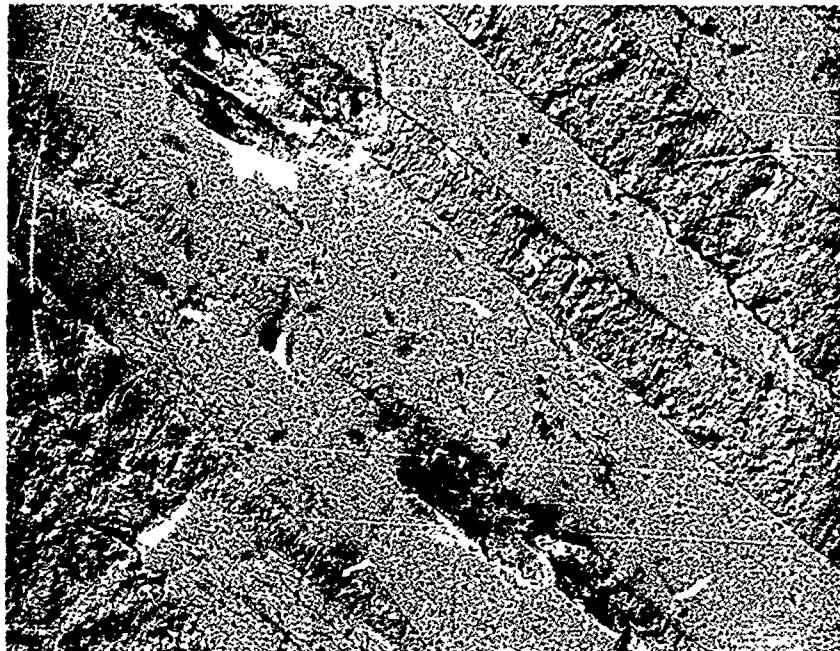
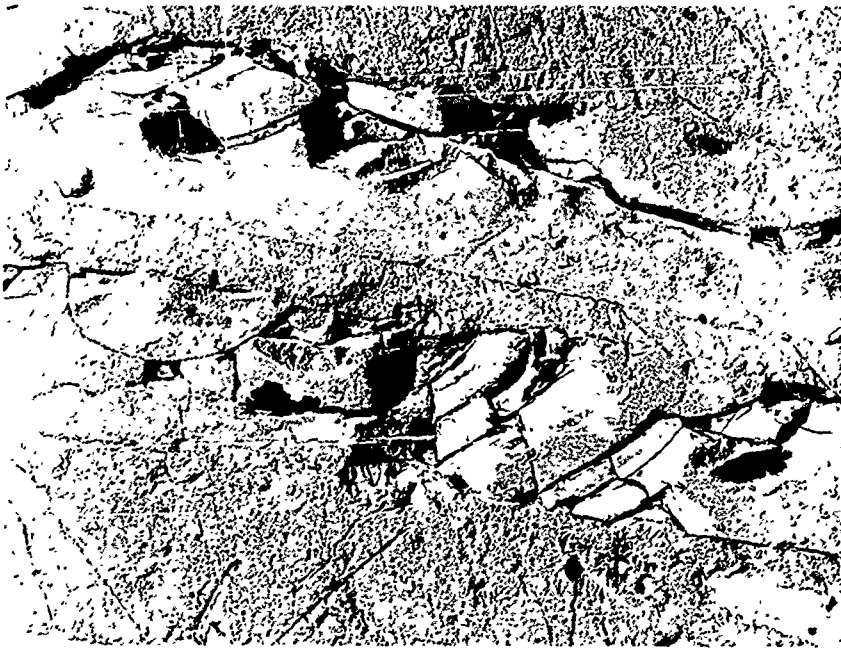
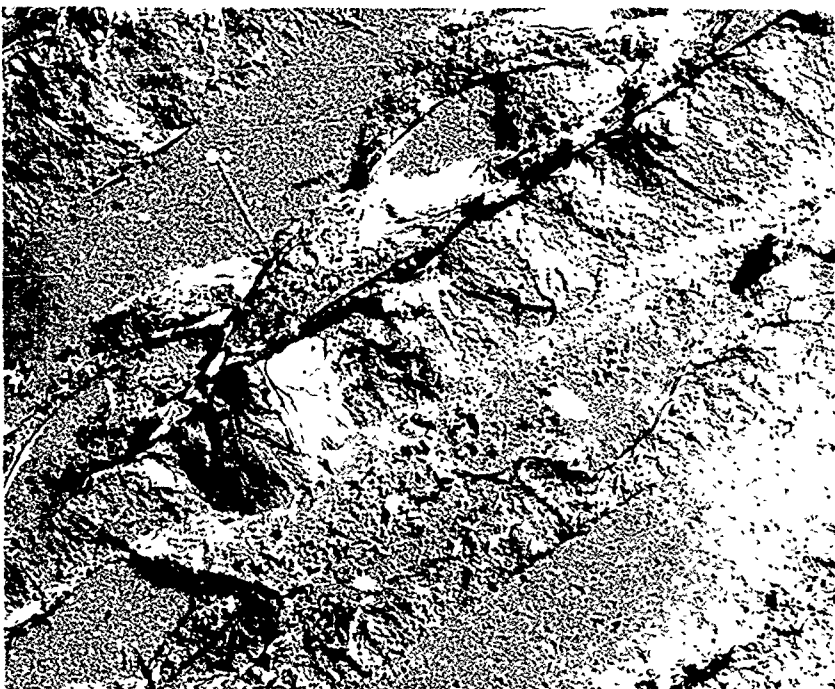


FIGURE 108. Uneroded surface of glass-fiber reinforced epoxy. - 3000X.

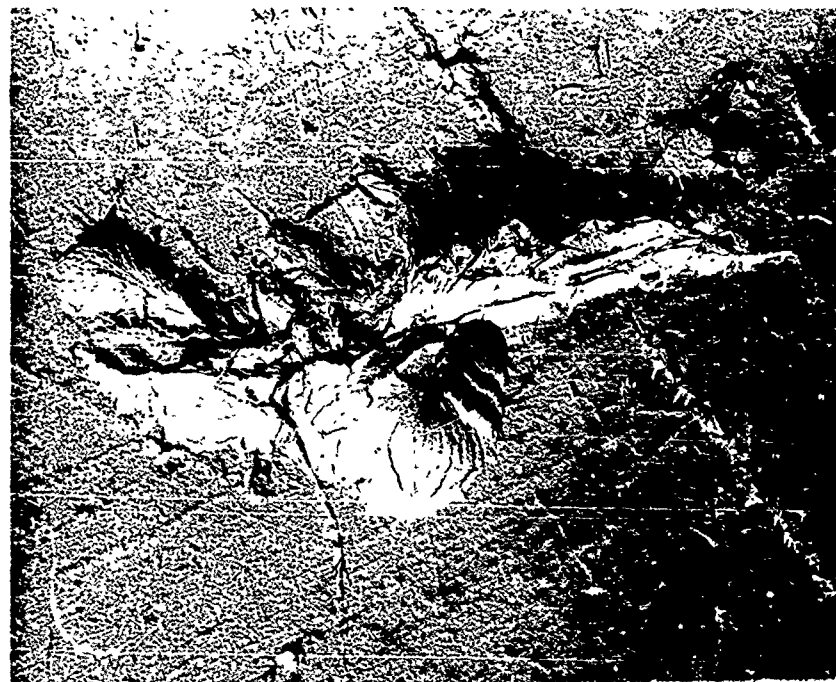


(a) Fracturing of glass-fibers at surface
after 40-second exposure - 3000X



(b) Intrafiber fracture in epoxy after
10-second exposure - 4500X

FIGURE 109. Rain erosion of glass-fiber reinforced
epoxy at 730 ft/sec.



(a) Replica - 3000X



(b) Replica - 5100X

FIGURE 110. Characteristic fracture surfaces in glass-fiber reinforced epoxy after 10-second exposure to rain at 730 ft/sec.

near and at the surface is shown in Figure 111. In general, the glass fiber bundles were more resistant to direct droplet impacts than the epoxy matrix. The matrix appears to fail in a brittle manner and small chips are removed as a single event. The fibers on the other hand undergo extensive cracking before pieces are removed, so a series of impacts are required.

Figure 112 shows the initiation of material removal in regions where the glass fibers are one or two mils from the surface. In this case the epoxy is being removed from around the fibers with negligible damage to the fibers. The scanning electron micrograph in Figure 113 shows a more advanced stage of this process. The erosion of the overlying epoxy follows along the path of the fiber bundle. After a region of the overlying epoxy has been removed, the process of material removal is due to high intensity jets which are directed along the trough produced in the surface. This process is inhibited when transverse fibers are encountered. There is evidence of some cracking of the fibers along these paths; but in general the fibers do resist direct impacts. When pieces are removed from a fiber due to localized cracking, a length of the fiber is subsequently removed from the bundle by jetting from successive droplet impacts. Usually the isolated length breaks off, however a number of twisted but still attached fibers can be found along these cleared paths. This behavior can be seen in the sectioned specimen in Figure 114.

The fiber bundles are woven into a fabric, so large-scale material removal depends on the efficiency of

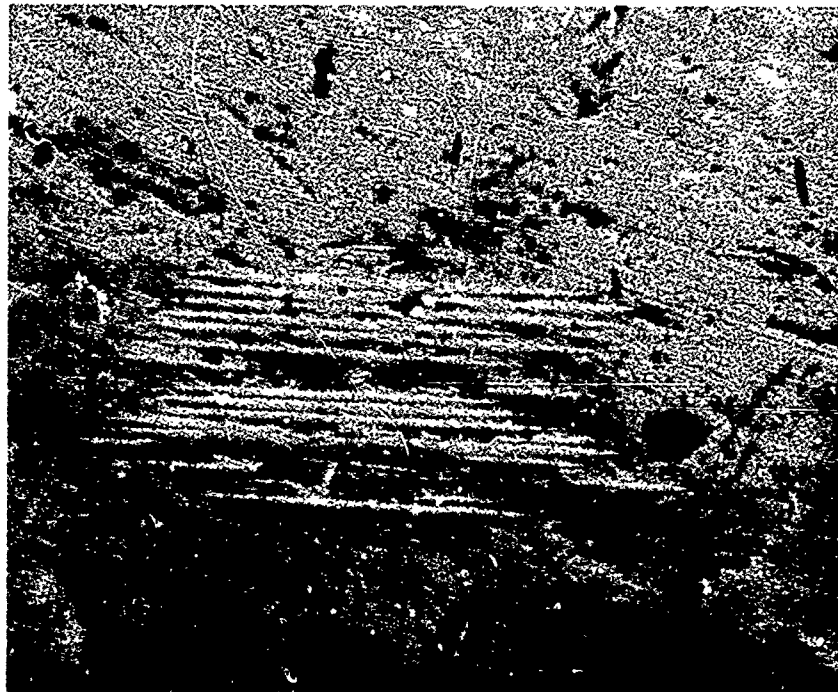
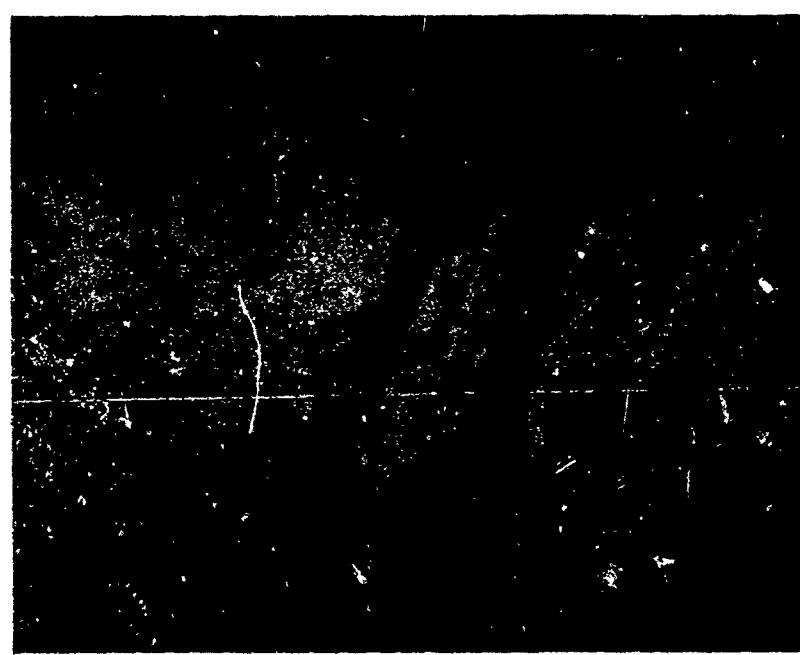


FIGURE 111. Material removal from fibers at surface
and matrix in glass-fiber reinforced epoxy.
Optical micrograph - 200X.



(a) Optical Micrograph - 320X



(b) Scanning electron micrograph - 325X

FIGURE 112. Exposure of glass fibers lying near the surface of glass-fiber reinforced epoxy specimens.

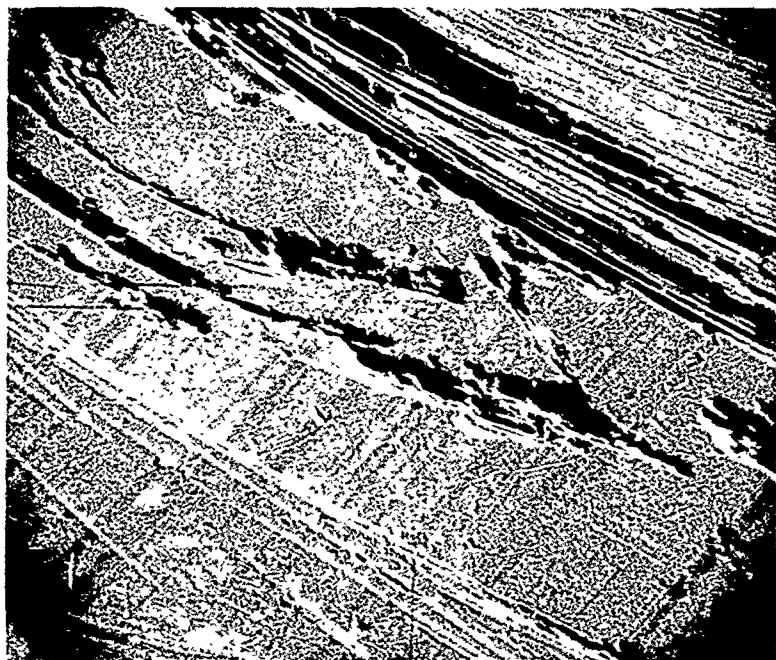


FIGURE 113. Advanced stage of exposure of glass fibers lying near the surface of glass-fiber reinforced epoxy specimens.
Scanning electron micrograph - 163X.

the impacting droplets to attack subsequent layers of the weave. The fiber bundles form an interlocking array as shown in cross section in Figure 115. The fibers which are near the surface in one area extend into the bulk material in another. A very prevalent type of material removal was brittle chipping of the epoxy in regions between fiber bundles where an intervening fiber bundle at the surface penetrates the bulk material. The initiation and development of this process can be seen in Figure 116 and 117. The erosion of the overlying layer of epoxy takes place without much difficulty. Figure 118 shows a larger area which has been cleared of the overlying epoxy with very little indication of disruptions in glass-fiber fabric.

Studying the evolution of the erosion mechanisms with time has shown that the epoxy is removed easily from the surface, however the transverse fiber bundles are a deterrent to continuation of this process. The influence of the high intensity water jets moving along the troughs created in the surface has been observed to separate the transverse fiber bundles along their path from the bulk material (Figure 114) and to occasionally break the fibers in the transverse fiber bundles (Figure 119). Generally a transverse fiber bundle will terminate the erosion process along a previously established path as can also be seen in Figure 119. As fibers are fractured and freed from the bundle lying along a line from the lower left to the upper right corner of Figure 119, they are broken in the vicinity of the transverse bundle due to the rigidity provided at that point.



FIGURE 114. Cross-section of glass-fiber reinforced epoxy - 150X.

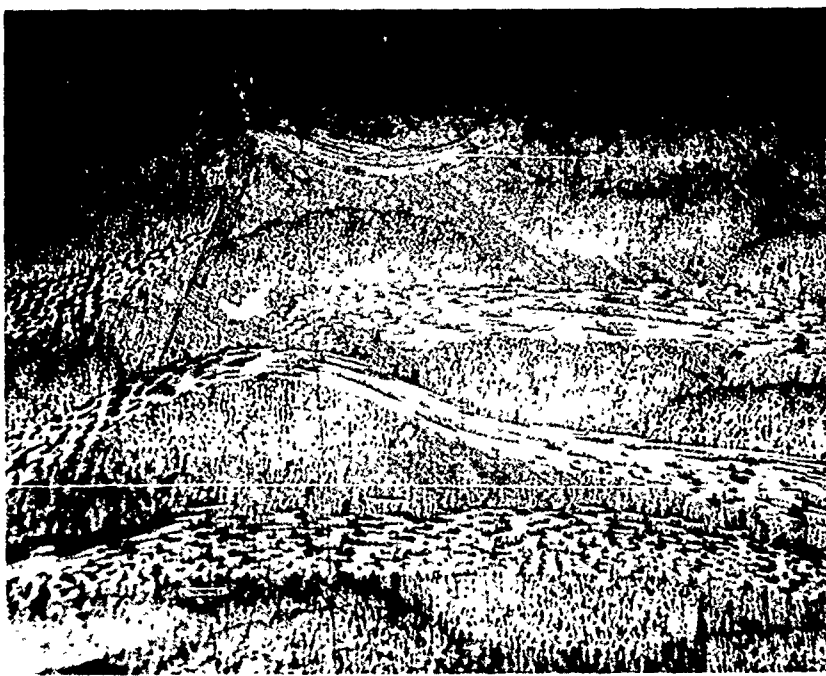


FIGURE 115. Cross-section of glass-fiber reinforced epoxy showing twill weave pattern - 110X.

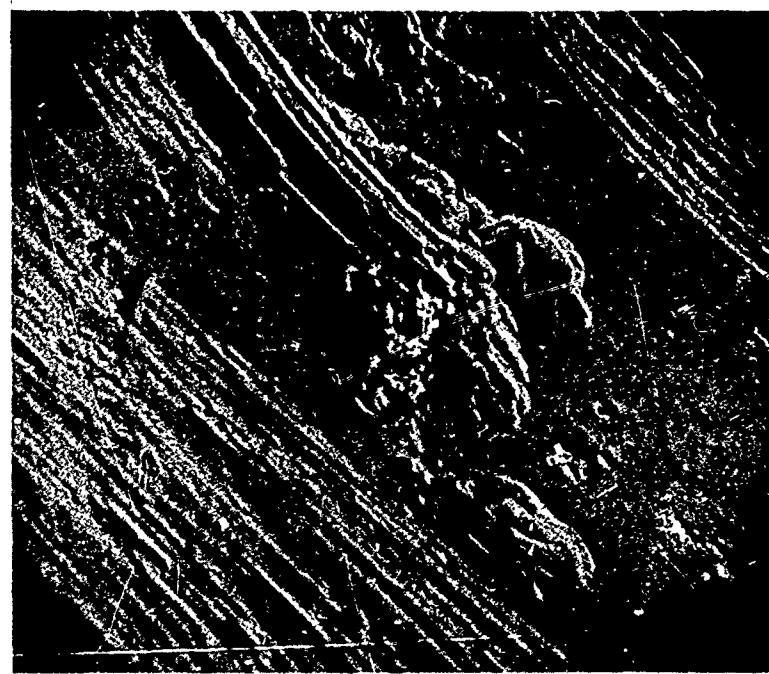
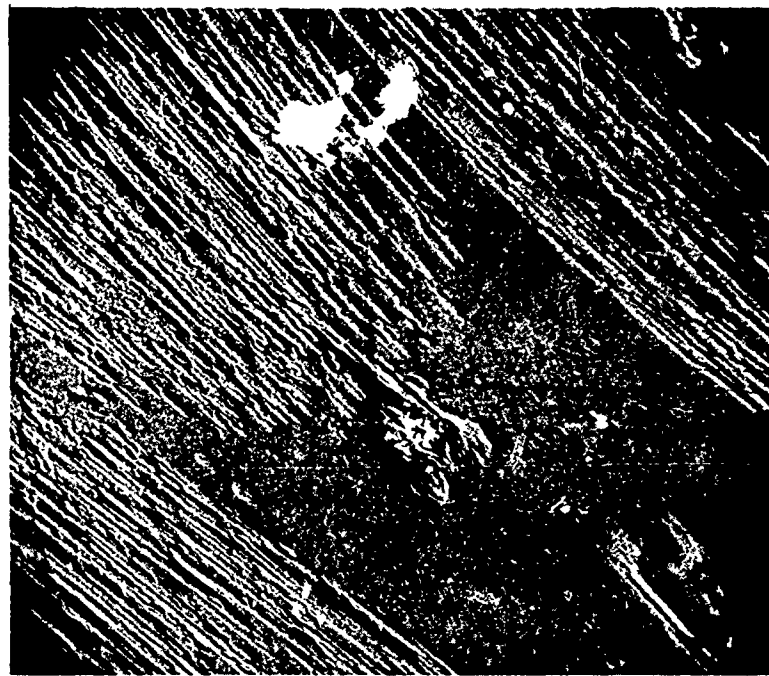
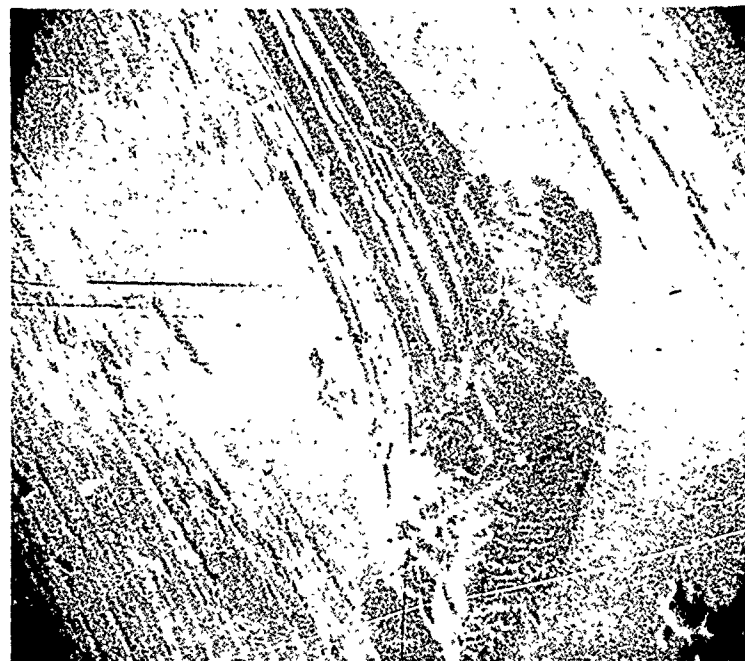
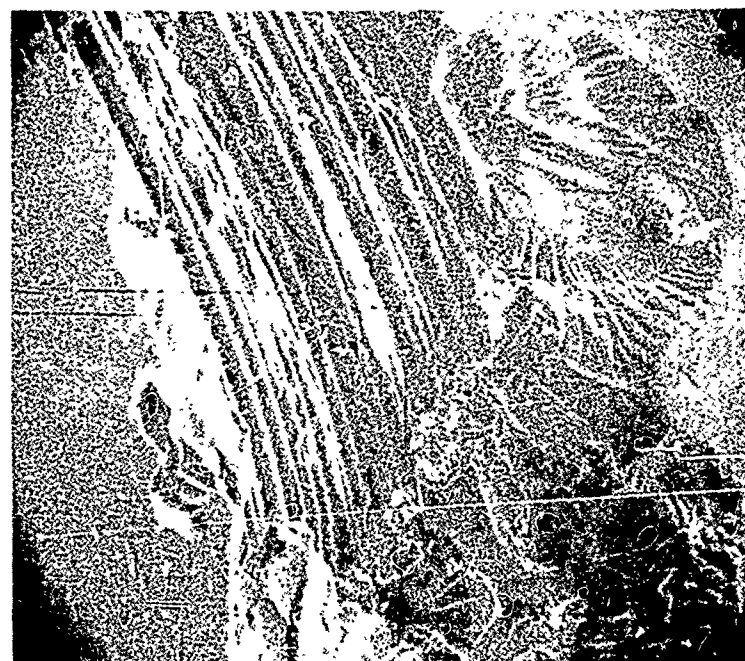


FIGURE 116. Initiation of material removal below the surface layer in glass-fiber reinforced epoxy. Scanning electron micrographs - 230X.



(a) General view of interfiber erosion -
230X.



(b) Detail of pit in (a) - 460X.

FIGURE 117. Intermediate stage of material removal
below surface layer in glass-fiber reinforced epoxy. Scanning electron micrographs.

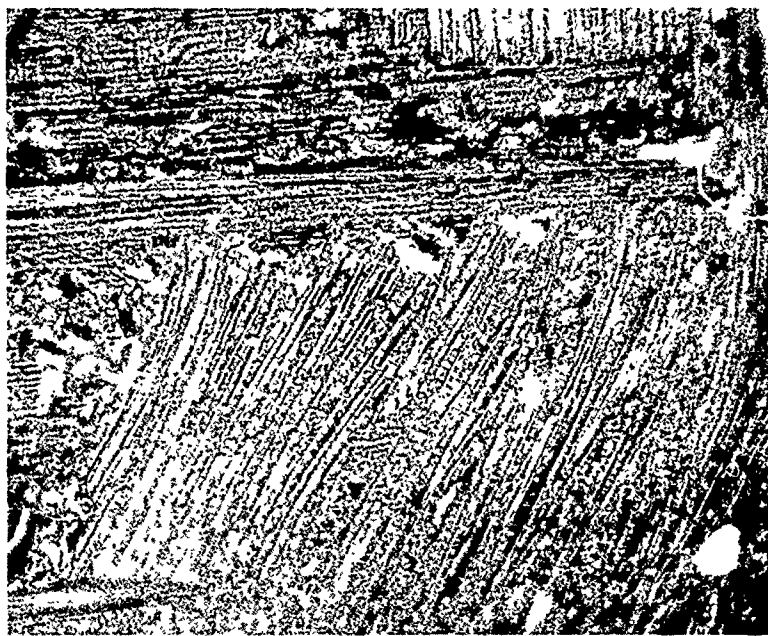


FIGURE 118. Advanced stage of separation of epoxy from fibers in glass-fiber reinforced epoxy - 110X.

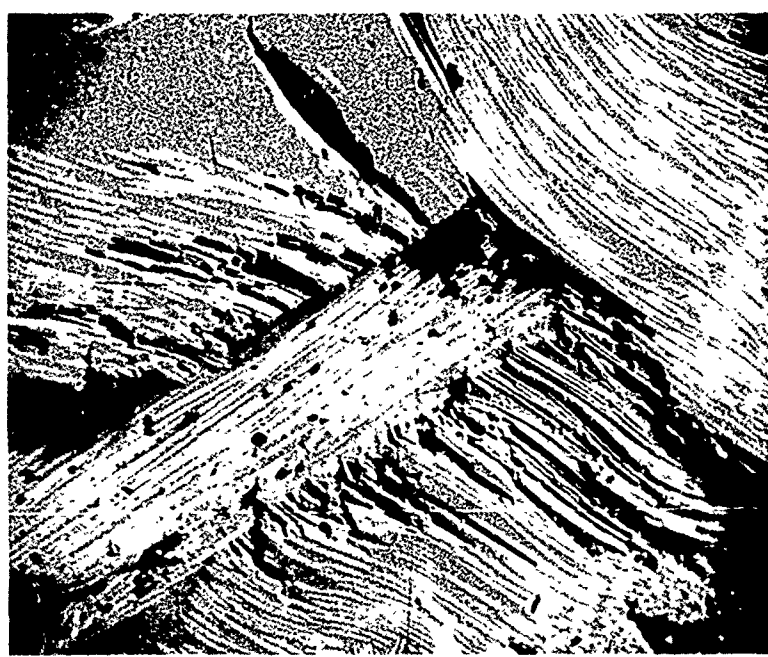


FIGURE 119. Fracturing of transverse fibers in glass-fiber reinforced epoxy. Scanning electron micrograph - 163X.

From these investigations it is clear that the erosion resistance of fiber-fabric reinforced composites could be increased if the bonding between the fibers and the matrix material could be improved in order to avoid delamination at the matrix/fiber interface and if the matrix material had more inherent erosion resistance than the brittle epoxy used in the specimens tested.

X. MAINTENANCE WORK

The following major maintenance items required attention during the last year.

1. After approximately 125-150 hours of operation at blade tip velocities of 1120 ft/second and above the bolts in the superstructure supporting the drive shaft and the bolts in the drive shaft pedestal became loosened due to vibration in spite of the fact that lock washers and nuts have been used. This fact requires retightening of the bolts at intervals of once a month.

2. The specimen holders which were fabricated from maraging steel (Vascalloy 300) exhibit a considerable amount of sand erosion along the leading edge and at the base of the flat turbine shaped specimens as shown in Figure 120. Approximately 1/8" to 3/16" of the maraging steel (Rockwell hardness C-50-52) erodes away at the base of the specimens in four hours at blade tip velocities of 880 ft/sec., in 2 - 2 1/2 hours at 1100 ft/sec and after 50-60 minutes at 1450 ft/sec and sand injection rates of 2 lbs/minute.

To repair the specimen holders the leading edge is rebuilt with maraging steel welding rod in the area of the leading edge and then machined with a 1/2" diameter radius cutter to form a new leading edge.

The holder is then heat treated at 900-920°F for four hours and quenched to obtain a Rockwell hardness of C-50 or above.

Figure 120b shows the refurbished holder.

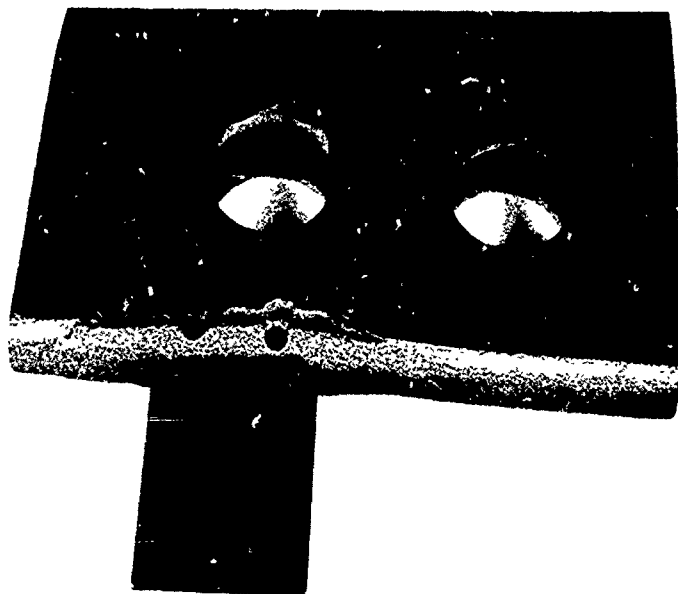
3. A large water leak occurred in the case of the vacuum pump.

The sand is evacuated through the vacuum pump and is carried through the impeller as a slurry since the impeller is sealed to the case by a continuous flow of water. The slurry of sand and water is driven at high velocity through a discharge port at the top of the pump.

The slurry of sand and water eroded through the 1/4" thick cast iron portion of the pump in the area of the discharge port.

Upon removal of the vacuum pump from the pit and disassembly, it was found that not only had the casing eroded through but the impellers were badly worn.

New impellers were purchased and installed and the worn area in the pump casing welded. To prevent wear, a centrifugal tank trap was fabricated and installed between the sand exhaust system and the vacuum pump to remove the sand before it gets to the pump.



(a) Specimen Holder Eroded by Sand



(b) Specimen Holder Refurbished

Figure 120 Specimen Holder Before and After Repair

XI. RECOMMENDATIONS

Future development of erosion resistant materials should include studies of:

1. The influence of coating thickness on the sand erosion rate of a hard coating on titanium alloys.
2. The effect of hardness and density on the erosion resistance of multilayer hard coatings on titanium alloys.
3. Microstructural analysis of the progressive failure of coatings on bulk metal and composite substrates.
4. Determination of the dynamic properties of materials which influence the erosion resistance of various classes of materials, i.e. metals, ceramics, plastics.
5. Determination of the effect of fracture toughness, strain hardening and phase transformation in metals on their erosion properties.
6. Determination of the influence of grain size and precipitate size and density on the erosion characteristics of metals.
7. Micrographic analyses of homologous series of generic materials in order to identify the dominant erosion mechanisms as a function of exposure time.
8. Analytical modeling of material removal rates in the initial and later stages of the erosion process in metals, plastics, and composites.

XII. REFERENCES

1. Wahl, N. E., "Investigation of the Phenomena of Rain Erosion at Subsonic and Supersonic Speeds," AFML-TR-65-330, October 1965.
2. Schmitt, G. F., Jr. and Krabill, A. H., "Velocity-Erosion Rate Relationships of Materials in Rain at Supersonic Speeds," AFML-TR-70-44, October 1970.
3. Hurley, C. J., and Schmitt, G. F., Jr. "Development and Calibration of a Mach 1.2 Rain Erosion Test Apparatus," AFML-TR-70-240, October 1970.
4. Weaver, James H., "Electrodeposited Nickel Coatings for Erosion Protection," AFML-TR-70-111, July 1970.
5. Schmitt, G. F., Jr. "Rain Erosion Behavior of Graphite and Boron Fiber-Reinforced Epoxy Composite Materials," AFML-TR-70-36, March 1971.
6. Sales, A. T., and Murphy, J. A., "Exploratory Development of Supersonic Rain Erosion Coating Materials," AFML-TR-68-364 Part III, January 1971.
7. Moraveck, J. F. and Guervin, P. R., "Rain and Sand Erosion Resistant Polyurethane Protective Coatings," AFML-TR-67-227 Part II, October 1969.
8. Morris, J. W. Jr., and Wahl, N. E., "Supersonic Rain and Sand Erosion Research," AFML-TR-70-265, November 1970.
9. Wood, R. A., "Surface Treatment of Titanium," DMIC Technical Note, AD 463016, March 1965.
10. Levy, M. and Morrossi, J. L., "Wear and Erosion Resistant Coatings for Titanium Alloys in Army Aircraft," AMMRC-TR-70-36, December 1970.

11. Currie, D. P., "Detailed Design of 2000 SHP Propeller System," USAAVLABS-TR-69-59, September 1969.
12. Green, H. M., "Manufacturing Techniques for Application of Erosion Resistant Coatings to Turbine Engine Components," AFML-TR-70-114, May 1970.
13. Brenner, A., Couch, D. F., and Williams, E. K., "Electrodeposition of Alloys of Phosphorous and Nickel or Cobalt," Plating 37 36 1960.
14. Brenner, A., and Gutzert, G., "Electroless Nickel Plating," ASTM Technical Publication 265, 1959.
15. Brenner, A., and Stanley, C., "Adhesion of Electroplated Coatings to Titanium," 43rd Annual Proceedings of American Electroplaters Society, p. 123, 1956.
16. Indria, K., Sampath, D., "Preparing Titanium for Plating," Metal Finishing, July 1969.
17. Yoskiska, S., Yamamoto, K., "Journal Metal Finishing Society of Japan," 21, 276-280, 1970.
18. Brenner, A., "Electrodeposition of Alloys," Vol. II Academic Press, New York 1963.
19. Max, A. M., "Metal Finishing Guidebook," Metals and Plastics Publications Inc., New Jersey, 1971.
20. Oberst, H., "Rain Erosion and Molecular Properties of Synthetic Materials," Royal Aircraft Establishment Library Translation No. 1335, December 1968.
21. Schmitt, G. F., Jr. et al. "High Temperature Rain Erosion Resistant Fluoroelastomer Coating," AFML-TR-71-196, November 1971.

22. Morris, J.W. Jr., "Mechanistic Investigation of Rain Erosion," AFML TR-69-287, Part II, (1969).
23. Rabinowitz, E., Friction and Wear of Materials, J. Wiley: New York. (1965).
24. Bowden, F.P., and Tabor, D., The Friction and Lubrication of Solids, Clarendon Press, Oxford. (1959).
25. Compton, W.A., "Study of the Mechanisms of Metal Removal by Impacting Dust Particles," USAF Materials Symposium, Miami Beach, (1970).
26. Finnie, I., "Erosion of Surfaces by Solid Particles" Wear, 3, (1960).
27. Bitter, J.G.A., "A Study of Erosion Phenomena" Parts I and II, Wear, 6, (1963).
28. Laderman, A.J., Lewis, C.H., and Byron, S.R., "Two Phase Plume Impingement Forces," SAMSO TR-68-308, (1968).
29. Marriott, J.B. and Rowden, G., "The Erosion of a Cobalt-Chromium Alloy by Liquid Impact," Phil. Trans. Roy. Soc. (London), A(260), 114 (1966).
30. Moore, M.B., "Mechanisms of Erosion of Ductile Metals by Solid Impingement," Rutgers, The State University, Tech. Rept. NYO-3477-12. (1968).
31. Morris, J.W. Jr., and Arndt, R.E.A., "Cavitation Erosion on Surface Effect Ships," Bell Aerospace Co. Tech. Rept. 9500-920188, (1970).
32. Heymann, F. J., "Erosion by Cavitation, Liquid Impingement, and Solid Impingement," Westinghouse Electric Co., Engineering Report E-1460. (1968).
33. Heater, J.R., and Lacey, E.M., "Repeated Impact Tests," Modern Plastics, 42, 123 (May, 1964).
34. Vincent, P.I., "Strength of Plastics, Part 5: The Effect of Notches," Plastics, 27, 116 (April, 1962).
35. Wolstenholme, W.E., et al, "Factors Influencing Izod Impact Properties of Thermoplastics Measured with the Autographic Impact Test," High Speed Testing, Volume 4, New York: Interscience Publishers, 1964, p. 119.

36. Hoff, G., Langbein, G., and Rieger, H., "Material Destruction Due to Liquid Impact," Erosion by Cavitation or Impingement, ASTM Special Technical Publication 408, 1967, p. 42.
37. Starkweather, Jr., H.W., and Brooks, R.E., "Effect of Spherulites on the Mechanical Properties of Nylon 66," J. Appl. Polymer Sci., 1, 236 (1959).
38. Thomas, G.P., "Repeated Liquid Impact as a Fatigue Process," 2. Forschungskonferenz Regenerosion, Meersburg, West Germany, 1967, p. 158.
39. Garcia, R., Hammitt, F.G., and Nystrom, R.E., "Correlation of Cavitation Damage with Other Material and Fluid Properties," ASTM Special Technical Publication 408, 1967, p. 239.

Unclassified

Security Classification

DOCUMENT CONTROL DATA - R & D

(Security classification of title, body of abstract and indexing annotation must be entered when the overall report is classified)

1. ORIGINATING ACTIVITY (Corporate author) Bell Aerospace Company PO Box 1 Buffalo New York 14240		2a. REPORT SECURITY CLASSIFICATION Unclassified
2b. GROUP		
3. REPORT TITLE "Supersonic Rain and Sand Erosion Research: Characterization and Development of Erosion Resistant Materials"		
4. DESCRIPTIVE NOTES (Type of report and inclusive dates) Final Summary January 1971 .. January 1972		
5. AUTHOR(S) (First name, middle initial, last name) Adler, William F. Morris, John W., Jr. Wahl, Norman E.		
6. REPORT DATE May 1972	7a. TOTAL NO OF PAGES 276	7b. NO OF REFS 39
8a. CONTRACT OR GRANT NO. F33615-71-C-1219	9a. ORIGINATOR'S REPORT NUMBER(S)	
b. PROJECT NO 7340	9b. OTHER REPORT NO(S) (Any other numbers that may be assigned this report) AFML-TR-72-85	
c. Task No. 734007		
d.		
10. DISTRIBUTION STATEMENT Distribution limited to U.S. Government agencies only; (test and evaluation). May 1972. Other requests for this document must be referred to Air Force Materials Laboratory, Nonmetallic Materials Division, Elastomers and Coatings Branch, AFML/LNE, Wright-Patterson AFB, Ohio 45433		
11. SUPPLEMENTARY NOTES	12. SPONSORING MILITARY ACTIVITY Air Force Materials Laboratory Air Force Systems Command Wright-Patterson AFB, Ohio 45433	
13. ABSTRACT Development and evaluation studies on electrodeposited, sprayed and diffusion coatings capable of providing erosion protection for titanium turbine engine blades were carried out. Recently developed hard coatings of carbides and borides exhibited sand erosion resistance 2.5 - 5 times that of uncoated titanium.		
Results are outlined on comparative erosion characteristics of thermoplastic polymers that might be used as coatings and might possess satisfactory rain erosion resistance. Correlation of the physical and mechanical properties of these polymers with erosion resistance, are discussed.		
The mechanism of erosion damage caused by plastic deformation and progressive fracture is discussed in detail.		
The erosion process occurring by these two methods considers ductile pitting, abrasion, polishing, fatigue, tearing and brittle fracture.		

Unclassified
Security Classification

14 KEY WORDS	LINK A		LINK B		LINK C	
	ROLE	WT	ROLE	WT	ROLE	WT
Supersonic Rain Erosion Sand Erosion Engine Compressor Blades Erosion Mechanisms						